

SEARCH FOR WEAKLY-PRODUCED SUPERSYMMETRY IN
THE SAME-SIGN DI-LEPTON FINAL STATE AT $\sqrt{s} = 8$ TEV
WITH THE ATLAS DETECTOR

Elizabeth J. Hines

A DISSERTATION

in

Physics and Astronomy

Presented to the Faculties of the University of Pennsylvania

in

Partial Fulfillment of the Requirements for the

Degree of Doctor of Philosophy

2015

Evelyn Thomson, Associate Professor, Physics
Supervisor of Dissertation

Marija Drndic, Professor, Physics
Graduate Group Chairperson

Dissertation Committee

I. Joseph Kroll, Professor, Physics

Burt Ovrut, Professor, Physics

Masao Sako, Associate Professor, Physics

Evelyn Thomson, Associate Professor, Physics

H. H. Williams, Professor, Physics



SEARCH FOR WEAKLY-PRODUCED SUPERSYMMETRY IN THE SAME-SIGN
DI-LEPTON FINAL STATE AT $\sqrt{s} = 8$ TEV WITH THE ATLAS DETECTOR

COPYRIGHT
2015
Elizabeth J. Hines

Acknowledgements

First, for my family— my parents Susan and Bill, and my sister Sarah. Thank you for always pushing me to achieve everything I've wanted and for nurturing my innate curiosity, love of learning, and interest in science.

For Dick Cleary, Robert Moreland, and particularly Mark Ilyes, for fostering my love of science and learning in general at an early age. To have such dedicated, intelligent, and engaging science teachers prepared me greatly for all of my studies and research since then.

For the University of Pittsburgh Honors College and particularly the late G. Alec Stewart. Thanks Doc, for inspiring me to always live “life above the neck” and reminding me to always remain irreverent.

I am eternally grateful to Jim Mueller and Joe Boudreau who allowed me to start on this journey at Pitt. To be able to travel and work at CERN as an inexperienced undergraduate was an amazing opportunity for which I can not thank you enough.

For my classmates at Penn, thanks for making the long hours of problem sets in the Zoo as collaborative and enjoyable as they could be. For Josh Kunkle, in particular, thanks for being my partner in crime and my cooper pair for so many years.

My heartfelt thanks go out to the entire group of Atlas Penn students, former and current, particularly those who spent extended periods in Geneva with me: Mike Hance, John Alison, Dominick Olivito, Ryan Reece, Josh Kunkle, Jon Stahlman, Chris Lester, Brett Jackson, Doug Schaefer, Rami Vanguri, Kurt Brendlinger, Jamie Saxon, and Alex Tuna. Our collective knowledge and expertise

of the Atlas Experiment is staggering. Thank you for the many nights of intelligent discussions on every topic imaginable. Thank you also for the nights of nonsense that made our time at CERN some of the best.

Also to all the rest of my friends from CERN and Geneva, particularly Emily Thompson, Phil Lawson, Ted Laird, Preema Pais, Mia Liu, Devin Harper, John Penwell, Jahred Adelman, Jared Sturdy, Ryan Carroll, Anna Sims, Rita Gomel, Hillery Midkiff, Susan Johnson, Jess Shannon, and Maria Lazarte, thank you for being wonderful travel partners and dinner companions. Good company always makes being far away from home easier. You all kept me sane and happy during my four years in Geneva.

For the Penn post-docs, particularly Mauro Donega, Jim Degenhardt, Sasa Fratina, Peter Wagner, Tae Min Hong, and Sarah Heim. Thank you for your excellent mentorship, patience and knowledge.

I would also like to thank Thomas Koffas and Kerstin Tackmann for providing excellent support and guidance during my first years at CERN. My work during the first few months of Atlas data was some of the most rewarding during my entire graduate student career.

For my collaborators on this thesis analysis, Lea Gauthier and Jean-Francois Arguin, thank you for being a pleasure to work with. Without you, this would not have been possible.

Thank you to Jean O'Boyle and Millicent Minnick for keeping me organized and helping to deal with the complications of working on a Ph.D. 4000 miles away from home.

And finally, thank you to the Penn professors: Brig Williams, Elliot Lipeles, Joe Kroll, and Evelyn Thomson. Over the past years, I can honestly say that I have had innumerable conversations with all of you that have made me the scientist I am today. Thank you for fostering such a welcoming, supportive and hard-working group. For Evelyn, in particular, though the path has been longer than expected, without you, I would not be here. Thank you.

ABSTRACT

SEARCH FOR WEAKLY-PRODUCED SUPERSYMMETRY IN THE SAME-SIGN
DI-LEPTON FINAL STATE AT $\sqrt{s} = 8$ TEV WITH THE ATLAS DETECTOR

Elizabeth J. Hines

Evelyn Thomson

A search for weakly-produced $\tilde{\chi}_1^\pm \tilde{\chi}_2^0$ supersymmetric particles decaying to two final state electrons or muons with the same electric charge is presented. The analysis is performed on 20.3fb^{-1} of integrated luminosity collected in 2012 with the Atlas Detector at the Large Hadron Collider, running at $\sqrt{s} = 8$ TeV. Pairs of like-sign leptons are collected and discriminated against background using Boosted Decision Trees trained on compressed supersymmetric simplified models. No significant excesses above background expectations are observed. The 95% confidence limits are placed on $\tilde{\chi}_1^\pm \tilde{\chi}_2^0$ pairs decaying via W and Z bosons and via intermediate sleptons with two different assumptions on the relative slepton mass. In the most optimistic scenarios considered, $\tilde{\chi}_1^\pm$ below 410 GeV are excluded assuming a massless $\tilde{\chi}_1^0$. In the compressed scenario, $\tilde{\chi}_1^\pm < 180$ GeV are excluded, with $\Delta M \tilde{\chi}_1^\pm, \tilde{\chi}_1^0 > 20$ GeV. Results from this analysis are also combined with those from a complementary search in the three lepton final state.

Contents

Acknowledgements	iii
Abstract	v
Contents	vi
List of Tables	x
List of Figures	xii
1 Introduction	1
2 Theoretical Motivations	3
2.1 The Standard Model	3
2.1.1 Structure of the Standard Model	3
2.1.2 Open questions of the Standard Model	4
2.1.2.1 The Hierarchy Problem	4
2.1.2.2 Dark Matter and Dark Energy	6
2.2 Supersymmetry	7
2.2.1 Motivation for Supersymmetry	7
2.2.1.1 The hierarchy problem	7
2.2.1.2 R-parity and Dark Matter	8

2.2.1.3	Unification of the Gauge Couplings	9
2.2.2	Supersymmetric Particles in the MSSM	9
2.2.3	The Case for Weakly-produced Supersymmetry	12
3	The ATLAS Detector	13
3.1	Trackers	14
3.1.1	Pixel Detector	15
3.1.2	Semi-Conductor Tracker	17
3.1.3	Transition Radiation Tracker	17
3.1.3.1	Design	18
3.1.3.2	Tracking	20
3.1.3.3	PID	21
3.2	Calorimetry	22
3.2.1	ElectroMagnetic Calorimeter	22
3.2.2	Hadronic Calorimeter	24
3.2.3	Forward Calorimeter	25
3.3	Muon System	25
3.4	Trigger	26
4	Physics Object Reconstruction and Identification in ATLAS	28
4.1	Identification of Electrons	28
4.1.1	Reconstruction	28
4.1.2	Identification	29
4.1.3	Electron Identification in the TRT	31
4.1.3.1	Quantifying Pion Rejection	34
4.1.3.2	Validating Hardware High-threshold Settings	37
4.2	Identification of Muons	38

4.3	Identification of Jets	40
4.4	Identification of Missing Transverse Energy	41
5	Analysis Overview	42
6	Signal Models	47
7	Background Estimation	54
7.1	Standard Model Same-sign Leptons	54
7.1.1	W/Z + γ^*	55
7.2	Charge Misidentification	58
7.2.1	Method	59
7.2.2	Results	61
7.2.3	Uncertainties	62
7.3	Lepton Misidentification	64
7.3.1	Matrix Method	65
7.3.2	Real efficiency measurements	66
7.3.3	Fake rate extraction	67
7.3.4	Uncertainties for fake rate extractions	69
8	Event Selection	71
8.1	Object Selection	71
8.1.1	Isolation	73
8.2	Trigger	73
8.3	Event Level Selection	75
8.4	Signal Selection using Boosted Decision Trees	76
8.4.1	Boosted Decision Trees	76
8.4.2	BDT Training	78

8.4.3	Discriminating Variables	81
8.4.4	BDT Output and testing	85
8.4.5	Signal Region definitions	86
9	Systematic Uncertainties	87
9.1	Systematic Uncertainties for background estimates	87
9.2	Systematic Uncertainties for Signal Models	89
9.3	Initial State Radiation	89
10	Validation of Background Estimates	90
10.1	General Same-sign Validation Regions	90
10.2	Dedicated Regions for Validation of Diboson Background	97
11	Results	102
12	Limits	106
12.1	Limit Setting Procedure	106
12.2	Limits on Simplified Models	110
12.2.1	$x=0.50$ Intermediate Slepton Grid	110
12.2.2	$x=0.95$ Intermediate Slepton Grid	111
12.2.3	WZ Grid	112
12.3	Model independent limits	113
12.4	Combined Limits	115
13	Conclusions	117
A	Kinematic plots for same-sign validation region	119
	Bibliography	145

List of Tables

2.1	Chiral Supermultiplets in the MSSM.	10
2.2	Gauge Supermultiplets in the MSSM.	11
4.1	Electron ID variables	32
4.2	Current high-threshold cut values for isEM tight electron selection (2010) and <i>medium</i> + + and <i>tight</i> + + (2012)	36
6.1	Cross-section and Relative uncertainty for simplified model with sleptons $x=0.50$. $\tilde{\chi}_1^\pm$ and $\tilde{\chi}_2^0$ are assumed to be mass degenerate and pure wino. The $\tilde{\chi}_1^0$ is the LSP and is assumed to be pure bino.	49
6.2	Cross-section and Relative uncertainty for additional simplified models with sleptons $x=0.50$. $\tilde{\chi}_1^\pm$ and $\tilde{\chi}_2^0$ are assumed to be mass degenerate and pure wino. The $\tilde{\chi}_1^0$ is the LSP and is assumed to be pure bino.	50
6.3	New signal samples used in 2LSS analysis : simplified model with sleptons $x=0.95$. $\tilde{\chi}_1^\pm$ and $\tilde{\chi}_2^0$ are assumed to be mass degenerate and pure wino. The $\tilde{\chi}_1^0$ is the LSP and is assumed to be pure bino.	51
6.4	Cross-section and Relative uncertainty for Simplified models with WZ bosons. $\tilde{\chi}_1^\pm$ and $\tilde{\chi}_2^0$ are assumed to be mass degenerate and pure wino. The $\tilde{\chi}_1^0$ is the LSP and is assumed to be pure bino. Cross sections do not include the branching fraction to leptons.	52
6.5	Cross-section and Relative uncertainty for additional simplified models with WZ bosons. $\tilde{\chi}_1^\pm$ and $\tilde{\chi}_2^0$ are assumed to be mass degenerate and pure wino. The $\tilde{\chi}_1^0$ is the LSP and is assumed to be pure bino. Cross sections do not include the branching fraction to leptons.	53
7.1	Diboson background samples.	56
7.2	Triboson background samples.	57
7.3	Top+Vector boson samples.	57
7.4	Higgs background samples.	57
7.5	SM $V\gamma$ samples used for the the analysis. The integrated luminosities corresponding to the total statistics in each sample are also given.	57
7.6	Uncertainties on the electron fake rate. In the first row, the first and second of set of numbers give the p_T (in GeV) and η range of the bin. For the last three bins there is only one η bin used.	70
7.7	Uncertainties on the muon fake rate. The p_T range of the bin is provided in the first row (in GeV).	70

8.1	Comparison of the analysis sensitivity before and after optimizing the isolation selection for leptons.	73
8.2	The list of lowest p_T un-prescaled di-lepton triggers.	74
8.3	Di-lepton triggers used in different regions of lepton p_T phase space. The definition of the regions for different channels is shown in Fig. 8.1. The trigger efficiencies shown are meant to be informative rather than exact, and are based on the single lepton trigger efficiencies. Label b-b (e-e) stands for both leptons being in the barrel (end-cap) detector region.	74
8.4	Importance of the variables used for the BDT training	85
8.5	Signal Region BDT cuts	86
9.1	Correlation Type (CT) : None=0, Regions=1, Processes=2, Regions and Processes=3. HistFitter Type (HFT) : Tree or weight.	88
9.2	Breakdown of uncertainty on background estimates	88
9.3	Systematic applied to signal models to account for modeling of Initial State Radiation	89
10.1	Validation Region BDT cuts	91
10.2	Signal contamination (in %) in each validation region for each channel.	91
10.3	Expected and observed number of events in the validation regions with $\Delta M = 20$ GeV and with or without ISR jets. The first uncertainty is statistical and the second is from systematics.	92
10.4	Expected and observed number of events in the validation regions with $\Delta M = 35$ GeV and with or without ISR jets. The first uncertainty is statistical and the second is from systematics.	92
10.5	Expected and observed number of events in the validation regions with $\Delta M = 65$ GeV and with or without ISR jets. The first uncertainty is statistical and the second is from systematics.	93
10.6	Expected and observed number of events in the validation regions with $\Delta M = 100$ GeV and with or without ISR jets. The first uncertainty is statistical and the second is from systematics.	93
10.7	Validation Region BDT cuts.	97
11.1	Expected and observed number of events in the signal regions with $\Delta M = 20$ GeV and with or without ISR jets. The first uncertainty is statistical and the second is from systematics.	102
11.2	Expected and observed number of events in the signal regions with $\Delta M = 35$ GeV and with or without ISR jets. The first uncertainty is statistical and the second is from systematics.	103
11.3	Expected and observed number of events in the signal regions with $\Delta M = 65$ GeV and with or without ISR jets. The first uncertainty is statistical and the second is from systematics.	103
11.4	Expected and observed number of events in the signal regions with $\Delta M = 100$ GeV and with or without ISR jets. The first uncertainty is statistical and the second is from systematics.	103
12.1	Model Independent Limits for SR dM20.	114
12.2	Model Independent Limits for SR dM35.	114
12.3	Model Independent Limits for SR dM65.	115
12.4	Model Independent Limits for SR dM100.	115

List of Figures

2.1	Summary of ATLAS Run 1 Standard Model measurements	5
2.2	One loop corrections to the Higgs mass due to top quark (top) and scalar top (bottom) proposed in SUSY.	8
2.3	Running of the coupling constants in the Standard Model and the MSSM	9
3.1	The full Atlas Detector with its individual sub detector elements visible	14
3.2	The Atlas Inner Detector Barrel	16
3.3	The Atlas Inner Detector End-caps	16
3.4	Transition radiation absorption length for potential gases in the TRT.	19
3.5	Illustration of a particle signal in one TRT straw.	20
3.6	Illustration of a particle signal in one TRT straw.	21
3.7	The Atlas Calorimeters	22
3.8	Schematic of Barrel Liquid Argon Calorimeter	24
3.9	The Atlas Muon Spectrometer	26
4.1	Diagram of the transverse view of a section of the Atlas detector. Interactions with the various sub-detectors are shown for common particle types. The distinct interactions for different types of particles are used for identification.	29
4.2	Efficiency for real isolated electrons using the new plusplus selection menu.	31
4.3	Demonstration of typical energy deposits for pions, electrons without TR, and electrons with TR	33
4.4	TRT high-threshold fraction	34
4.5	TRT high-threshold turn-on curves	35
4.6	Efficiency for electrons and pions to pass varying HT ratio cuts	36
4.7	Pion Rejection factors for the TRT	37
4.8	Results from special runs with differing TRT high-threshold hardware settings	38
4.9	TRT pion rejection power for differing hardware setting	39
5.1	Feynman diagram for $\tilde{\chi}_1^\pm \tilde{\chi}_2^0$ decaying via W and Z bosons (left) and previous limits on this signature from the three lepton search[1]	43
5.2	Previous limits on the direct production of $\tilde{\chi}_1^\pm \tilde{\chi}_2^0$, decaying via W and Z bosons	44
5.3	Previous limits on the direct production of $\tilde{\chi}_1^\pm \tilde{\chi}_2^0$, decaying via W and Z bosons (left) and sleptons (right) from the 2L opposite-sign analysis. The two lepton opposite-sign searches are not able to extend the trilepton search in the compressed region.	45

5.4	Effect of varying the intermediate slepton mass on acceptance for the 2L opposite sign analysis. The assumption that the slepton is halfway between the $\tilde{\chi}_1^\pm$ and $\tilde{\chi}_1^0$ maximizes the analysis acceptance for the majority of phase space.	46
7.1	(Left) The d0 significance distribution for opposite-sign (red) and same-sign (blue) $Z \rightarrow ee$ events, normalized to equal area. The same-sign events show a much broader distribution do to the poorly measured track coming from the trident process. (Right) Charge-flip rate for varying cut values of d0 significance.	59
7.2	Sideband regions used to remove background from the charge-flip extraction region. . .	60
7.3	Charge-flip rate for signal electrons as a function of p_T and η	61
7.4	Charge flip rate for baseline electrons as a function of p_T and η . These rates are used to remove the charge flip contribution to the matrix method estimate of fake leptons. . . .	62
7.5	Charge-flip rate closure test results.	63
7.6	η (left) and p_T (right) spectrum for the ee validation regions and the charge-flip extraction region.	64
7.7	Real lepton identification efficiency from loose to tight selection measured in data (top) and MC (bottom), for electrons (left) and muons (right).	67
7.8	Lepton fake rate from loose to tight selection for electrons (left) and muons (right). This rate is presented for different (p_T, η) bins for electrons and p_T bins for muons. Only the statistical uncertainties are shown.	69
8.1	Phase space requirements for the dilepton triggers in the ee (left), $e\mu$ (center), $\mu\mu$ (right) channels	75
8.2	Illustration of Decision Tree structure	77
8.3	Signal points with identical mass splitting are combined for BDT training	80
8.4	Cartoon depicting E_T^{miss} in the case of no ISR (left) and ISR (right). For the no ISR case, the two escaping LSPs are produced nearly back to back, so their E_T^{miss} sums to near 0. In the ISR case, their E_T^{miss} adds constructively.	80
8.5	Distribution of m_{T2} (left), $p_{T,u}$ (center) and $E_T^{\text{miss,rel}}$ (right) for ISR region.	82
8.6	BDT kinematic variables in ISR region	83
8.7	BDT kinematic variables in the No ISR region	84
8.8	Results of the Kolmogorov-Smirnov test for the BDT on the training and testing samples	85
10.1	BDT output distribution inside the Validation Region for $\Delta M=20$ GeV with (top) and without (bottom) an ISR jet for the three channels (ee at left, $e\mu$ in the middle and $\mu\mu$ at right).	94
10.2	BDT output distribution inside the Validation Region for $\Delta M=35$ GeV with (top) and without (bottom) an ISR jet for the three channels (ee at left, $e\mu$ in the middle and $\mu\mu$ at right).	94
10.3	BDT output distribution inside the Validation Region for $\Delta M=65$ GeV with (top) and without (bottom) an ISR jet for the three channels (ee at left, $e\mu$ in the middle and $\mu\mu$ at right).	95
10.4	BDT output distribution inside the Validation Region for $\Delta M=100$ GeV with (top) and without (bottom) an ISR jet for the three channels (ee at left, $e\mu$ in the middle and $\mu\mu$ at right).	95
10.5	Pull plot per channel for all the 8 validation regions for the ee channel (top left), $e\mu$ channel (top right) and $\mu\mu$ channel (bottom).	96
10.6	WZ Validation region for $\Delta M=20$ GeV	98
10.7	WZ Validation region for $\Delta M=35$ GeV	99
10.8	WZ Validation region for $\Delta M=65$ GeV	100
10.9	WZ Validation region for $\Delta M=100$ GeV	101

11.1	Output of Boosted Decision Tree for $\Delta M=20\text{GeV}$ for the ISR (top) and not ISR jet region (bottom) for the ee (left), $e\mu$ (middle) and $\mu\mu$ (right) channel.	104
11.2	Output of Boosted Decision Tree for $\Delta M=35\text{GeV}$ for the ISR (top) and not ISR jet region (bottom) for the ee (left), $e\mu$ (middle) and $\mu\mu$ (right) channel.	104
11.3	Output of Boosted Decision Tree for $\Delta M=65\text{GeV}$ for the ISR (top) and not ISR jet region (bottom) for the ee (left), $e\mu$ (middle) and $\mu\mu$ (right) channel.	105
11.4	Output of Boosted Decision Tree for $\Delta M=100\text{GeV}$ for the ISR (top) and not ISR jet region (bottom) for the ee (left), $e\mu$ (middle) and $\mu\mu$ (right) channel.	105
12.1	Illustration of p_b and p_{s+b} , values to the left of the plot are more signal-like, while values to the right are more background-like.	107
12.2	Exclusion contour for $\tilde{\chi}_1^\pm, \tilde{\chi}_2^0$ pair production with $x=0.50$ sleptons in the decay (left). Signal region with best expected CLs value used for each grid point (right).	111
12.3	Exclusion contour for $\tilde{\chi}_1^\pm, \tilde{\chi}_2^0$ pair production with $x=0.95$ sleptons in the decay (top left) and the expected Zn value from the trilepton search (top right) for comparison. Signal region with best expected CLs value used for each grid point (bottom).	112
12.4	Exclusion contour for $\tilde{\chi}_1^\pm, \tilde{\chi}_2^0$ pair production with WZ bosons in the decay chain (left). Signal region with best expected CLs value used for each grid point (right).	113
12.5	Exclusion contour for $\tilde{\chi}_1^\pm, \tilde{\chi}_2^0$ pair production with $x=0.50$ sleptons in the decay (left) and $x=0.95$ (right) sleptons in the decay, using the combination of the 2LSS analysis and the 3L analysis.	116
A.1	Lepton η in the validation regions with $\Delta M=20$ GeV and with ISR (top) or without ISR jet (bottom), for ee (left), $e\mu$ (middle), and $\mu\mu$ (right) channel.	119
A.2	Lepton η in the validation regions with $\Delta M=35$ GeV and with ISR (top) or without ISR jet (bottom), for ee (left), $e\mu$ (middle), and $\mu\mu$ (right) channel.	120
A.3	Lepton η in the validation regions with $\Delta M=65$ GeV and with ISR (top) or without ISR jet (bottom), for ee (left), $e\mu$ (middle), and $\mu\mu$ (right) channel.	120
A.4	Lepton η in the validation regions with $\Delta M=100$ GeV and with ISR (top) or without ISR jet (bottom), for ee (left), $e\mu$ (middle), and $\mu\mu$ (right) channel.	121
A.5	Lepton p_T in the validation regions with $\Delta M=20$ GeV and with ISR (top) or without ISR jet (bottom), for ee (left), $e\mu$ (middle), and $\mu\mu$ (right) channel.	121
A.6	Lepton p_T in the validation regions with $\Delta M=35$ GeV and with ISR (top) or without ISR jet (bottom), for ee (left), $e\mu$ (middle), and $\mu\mu$ (right) channel.	122
A.7	Lepton p_T in the validation regions with $\Delta M=65$ GeV and with ISR (top) or without ISR jet (bottom), for ee (left), $e\mu$ (middle), and $\mu\mu$ (right) channel.	122
A.8	Lepton p_T in the validation regions with $\Delta M=100$ GeV and with ISR (top) or without ISR jet (bottom), for ee (left), $e\mu$ (middle), and $\mu\mu$ (right) channel.	123
A.9	Subleading lepton p_T in the validation regions with $\Delta M=20$ GeV and with ISR (top) or without ISR jet (bottom), for ee (left), $e\mu$ (middle), and $\mu\mu$ (right) channel.	123
A.10	Subleading lepton p_T in the validation regions with $\Delta M=35$ GeV and with ISR (top) or without ISR jet (bottom), for ee (left), $e\mu$ (middle), and $\mu\mu$ (right) channel.	124
A.11	Subleading lepton p_T in the validation regions with $\Delta M=65$ GeV and with ISR (top) or without ISR jet (bottom), for ee (left), $e\mu$ (middle), and $\mu\mu$ (right) channel.	124
A.12	Lepton p_T in the validation regions with $\Delta M=100$ GeV and with ISR (top) or without ISR jet (bottom), for ee (left), $e\mu$ (middle), and $\mu\mu$ (right) channel.	125
A.13	Azimuthal angle between leptons in the validation regions with $\Delta M=20$ GeV and with ISR (top) or without ISR jet (bottom), for ee (left), $e\mu$ (middle), and $\mu\mu$ (right) channel.	125
A.14	Azimuthal angle between leptons in the validation regions with $\Delta M=35$ GeV and with ISR (top) or without ISR jet (bottom), for ee (left), $e\mu$ (middle), and $\mu\mu$ (right) channel.	126
A.15	Azimuthal angle between leptons in the validation regions with $\Delta M=65$ GeV and with ISR (top) or without ISR jet (bottom), for ee (left), $e\mu$ (middle), and $\mu\mu$ (right) channel.	126

A.16	Azimuthal angle between leptons in the validation regions with $\Delta M=100$ GeV and with ISR (top) or without ISR jet (bottom), for ee (left), $e\mu$ (middle), and $\mu\mu$ (right) channel.	127
A.17	Invariant mass of the 2 leptons in the validation regions with $\Delta M=20$ GeV and with ISR (top) or without ISR jet (bottom), for ee (left), $e\mu$ (middle), and $\mu\mu$ (right) channel.	127
A.18	Invariant mass of the 2 leptons in the validation regions with $\Delta M=35$ GeV and with ISR (top) or without ISR jet (bottom), for ee (left), $e\mu$ (middle), and $\mu\mu$ (right) channel.	128
A.19	Invariant mass of the 2 leptons in the validation regions with $\Delta M=65$ GeV and with ISR (top) or without ISR jet (bottom), for ee (left), $e\mu$ (middle), and $\mu\mu$ (right) channel.	128
A.20	Invariant mass of the 2 leptons in the validation regions with $\Delta M=100$ GeV and with ISR (top) or without ISR jet (bottom), for ee (left), $e\mu$ (middle), and $\mu\mu$ (right) channel.	129
A.21	Total transverse momentum of the 2 leptons in the validation regions with $\Delta M=20$ GeV and with ISR (top) or without ISR jet (bottom), for ee (left), $e\mu$ (middle), and $\mu\mu$ (right) channel.	129
A.22	Total transverse momentum of the 2 leptons in the validation regions with $\Delta M=35$ GeV and with ISR (top) or without ISR jet (bottom), for ee (left), $e\mu$ (middle), and $\mu\mu$ (right) channel.	130
A.23	Total transverse momentum of the 2 leptons in the validation regions with $\Delta M=65$ GeV and with ISR (top) or without ISR jet (bottom), for ee (left), $e\mu$ (middle), and $\mu\mu$ (right) channel.	130
A.24	Total transverse momentum of the 2 leptons in the validation regions with $\Delta M=100$ GeV and with ISR (top) or without ISR jet (bottom), for ee (left), $e\mu$ (middle), and $\mu\mu$ (right) channel.	131
A.25	Metrel in the validation regions with $\Delta M=20$ GeV and with ISR (top) or without ISR jet (bottom), for ee (left), $e\mu$ (middle), and $\mu\mu$ (right) channel.	131
A.26	Metrel in the validation regions with $\Delta M=35$ GeV and with ISR (top) or without ISR jet (bottom), for ee (left), $e\mu$ (middle), and $\mu\mu$ (right) channel.	132
A.27	Metrel in the validation regions with $\Delta M=65$ GeV and with ISR (top) or without ISR jet (bottom), for ee (left), $e\mu$ (middle), and $\mu\mu$ (right) channel.	132
A.28	Metrel in the validation regions with $\Delta M=100$ GeV and with ISR (top) or without ISR jet (bottom), for ee (left), $e\mu$ (middle), and $\mu\mu$ (right) channel.	133
A.29	H_T in the validation regions with $\Delta M=20$ GeV and with ISR (top) or without ISR jet (bottom), for ee (left), $e\mu$ (middle), and $\mu\mu$ (right) channel.	133
A.30	H_T in the validation regions with $\Delta M=35$ GeV and with ISR (top) or without ISR jet (bottom), for ee (left), $e\mu$ (middle), and $\mu\mu$ (right) channel.	134
A.31	H_T in the validation regions with $\Delta M=65$ GeV and with ISR (top) or without ISR jet (bottom), for ee (left), $e\mu$ (middle), and $\mu\mu$ (right) channel.	134
A.32	H_T in the validation regions with $\Delta M=100$ GeV and with ISR (top) or without ISR jet (bottom), for ee (left), $e\mu$ (middle), and $\mu\mu$ (right) channel.	135
A.33	m_{T2} in the validation regions with $\Delta M=20$ GeV and with ISR (top) or without ISR jet (bottom), for ee (left), $e\mu$ (middle), and $\mu\mu$ (right) channel.	135
A.34	m_{T2} in the validation regions with $\Delta M=35$ GeV and with ISR (top) or without ISR jet (bottom), for ee (left), $e\mu$ (middle), and $\mu\mu$ (right) channel.	136
A.35	m_{T2} in the validation regions with $\Delta M=65$ GeV and with ISR (top) or without ISR jet (bottom), for ee (left), $e\mu$ (middle), and $\mu\mu$ (right) channel.	136
A.36	m_{T2} in the validation regions with $\Delta M=100$ GeV and with ISR (top) or without ISR jet (bottom), for ee (left), $e\mu$ (middle), and $\mu\mu$ (right) channel.	137
A.37	$m_{T_{r1}}$ in the validation regions with $\Delta M=20$ GeV and with ISR (top) or without ISR jet (bottom), for ee (left), $e\mu$ (middle), and $\mu\mu$ (right) channel.	137
A.38	$m_{T_{r1}}$ in the validation regions with $\Delta M=35$ GeV and with ISR (top) or without ISR jet (bottom), for ee (left), $e\mu$ (middle), and $\mu\mu$ (right) channel.	138
A.39	$m_{T_{r1}}$ in the validation regions with $\Delta M=65$ GeV and with ISR (top) or without ISR jet (bottom), for ee (left), $e\mu$ (middle), and $\mu\mu$ (right) channel.	138

A.40	m_{Tr1} in the validation regions with $\Delta M=100$ GeV and with ISR (top) or without ISR jet (bottom), for ee (left), $e\mu$ (middle), and $\mu\mu$ (right) channel.	139
A.41	m_{Tr2} in the validation regions with $\Delta M=20$ GeV and with ISR (top) or without ISR jet (bottom), for ee (left), $e\mu$ (middle), and $\mu\mu$ (right) channel.	139
A.42	m_{Tr2} in the validation regions with $\Delta M=35$ GeV and with ISR (top) or without ISR jet (bottom), for ee (left), $e\mu$ (middle), and $\mu\mu$ (right) channel.	140
A.43	m_{Tr2} in the validation regions with $\Delta M=65$ GeV and with ISR (top) or without ISR jet (bottom), for ee (left), $e\mu$ (middle), and $\mu\mu$ (right) channel.	140
A.44	m_{Tr2} in the validation regions with $\Delta M=100$ GeV and with ISR (top) or without ISR jet (bottom), for ee (left), $e\mu$ (middle), and $\mu\mu$ (right) channel.	141
A.45	The azimuthal angle between the leading jet and the missing transverse energy in the validation regions with ISR jet and $\Delta M=20$ GeV (top row), 35 GeV (second row), 65 GeV (third row), and 100 GeV (bottom row), for ee (left), $e\mu$ (middle), and $\mu\mu$ (right) channel.	142
A.46	The ratio of the p_T of the leading lepton and the p_T of the leading jet in the validation regions with ISR jet and $\Delta M=20$ GeV (top row), 35 GeV (second row), 65 GeV (third row), and 100 GeV (bottom row), for ee (left), $e\mu$ (middle), and $\mu\mu$ (right) channel.	143
A.47	The ratio of the missing transverse energy and the p_T of the leading jet in the validation regions with ISR jet and $\Delta M=20$ GeV (top row), 35 GeV (second row), 65 GeV (third row), and 100 GeV (bottom row), for ee (left), $e\mu$ (middle), and $\mu\mu$ (right) channel.	144

CHAPTER 1

Introduction

This thesis documents a search for the existence of weakly-produced supersymmetric particles in the same-sign dilepton channel. The analysis is carried out on 20.3 fb^{-1} of $\sqrt{s} = 8 \text{ TeV}$ proton-proton collisions taken with the Atlas Detector at the Large Hadron Collider (LHC) in 2012.

The current understanding of the Standard Model and the theoretical motivation for searches for theories beyond the standard model, specifically those for supersymmetry, are given in Chapter 2.

The experimental apparatus is described in Chapter 3, detailing the Atlas particle detector. The reconstruction and identification of recognizable particle physics objects from the detector response is given in Chapter 4.

The analysis search procedure is described in Chapters 5-9. An overview of the motivation for this particular search and its relationship to existing Atlas weakly-produced supersymmetry searches is given in Chapter 5. This analysis concentrates on the pair production of $\tilde{\chi}_1^\pm$ and $\tilde{\chi}_2^0$, the possible decays of which and the corresponding signal samples are described fully in Section 6. The three sources of backgrounds to this analysis: Standard Model same-sign events, electrons with a misidentified charge, and misidentified or non-prompt leptons, are discussed in Chapter 7, including the techniques used for their estimation and the associated uncertainties. The methods used to reduce these backgrounds and select possible signal events are described in Chapter 8, including a description of the Boosted Decision Trees used. The additional uncertainties associated with this analysis are discussed in Chapter 9.

Checks on the background estimation techniques in dedicated validation regions are given in Chapter 10 and the results in the selected signal regions are shown in Chapter 11. Interpretations of these results are then given in Chapter 12 for model dependent and model independent scenarios. Conclusions and prospects for the future are given in Chapter 13.

CHAPTER 2

Theoretical Motivations

This chapter attempts to present the theoretical background for a search for Supersymmetric particles. It begins with presenting the current best understanding in particle physics, the Standard Model. The open questions of the model, particularly those that motivate Beyond the Standard Model (BSM) theories are then presented. A brief overview of one of these BSM theories, Supersymmetry (SUSY), is then given, concentrating on the phenomenology and how SUSY attempts to answer some of the open questions in the Standard Model. A more detailed description can be found in references such as [2]. Finally, the motivation to look for weakly-produced SUSY in the Run 1 data from the LHC is given.

2.1 The Standard Model

2.1.1 Structure of the Standard Model

The Standard Model of particle physics [3, 4, 5] represents the field’s best knowledge of the contents and interactions of the universe. The particles of the Standard Model can be easily classified into two groups, the fermions and the bosons. Fermions have half-integer spin (intrinsic angular momentum), and are the matter particles. They can be further sub-divided into quarks, which also carry color charge and thus interact via the Strong force, and leptons, which do not. Both the quarks and the leptons can be arranged into three “generations” with increasing mass. Bosons have integer spin, and are the force carriers of the model.

The Standard model follows a $SU(3)_C \times SU(2)_L \times U(1)_Y$ gauge symmetry. $SU(3)$ is the group of Quantum ChromoDynamics (QCD) or the strong force. The $SU(2)_L \times U(1)_Y$ represent the Electroweak force, where L denotes left-handedness and Y is the weak hypercharge:

$$Y = 2(Q - I_3) \tag{2.1}$$

where Q is the electric charge and I_3 is the third component of weak isospin ($\pm\frac{1}{2}$ for left-handed fermions, 0 for right-handed fermions).

The final piece of the Standard Model is the Higgs Boson, which breaks the Electroweak symmetry, and gives mass to the gauge bosons (W and Z). Fermions also acquire their mass through the Yukawa interactions with the Higgs Field.

With the recent discovery of the Higgs Boson[6, 7], the theory can be considered “complete”, in that all of the predicted particles have been observed. However, several outstanding questions remain.

2.1.2 Open questions of the Standard Model

The Standard Model has been an extremely successful theory, working over many orders of magnitude in production rate and describing a wide variety of phenomena. A summary of the wide range of SM results from Atlas Run 1 and their comparison to theory predictions is given in Figure 2.1. However, it can not be the complete description of the universe as it does not include gravity. Additional open questions have also arisen, such as the inclusion of the very small neutrino masses after the observation of neutrino oscillations. Two other remaining issues for the Standard Model as it currently is formulated help to motivate a search for Supersymmetry and so they are described in more detail in the next sections.

2.1.2.1 The Hierarchy Problem

Perhaps the largest open question in the Standard Model is why the difference in strength is so large between the weak force and gravity [8, 9, 10, 11]. This can also be expressed as a question of why

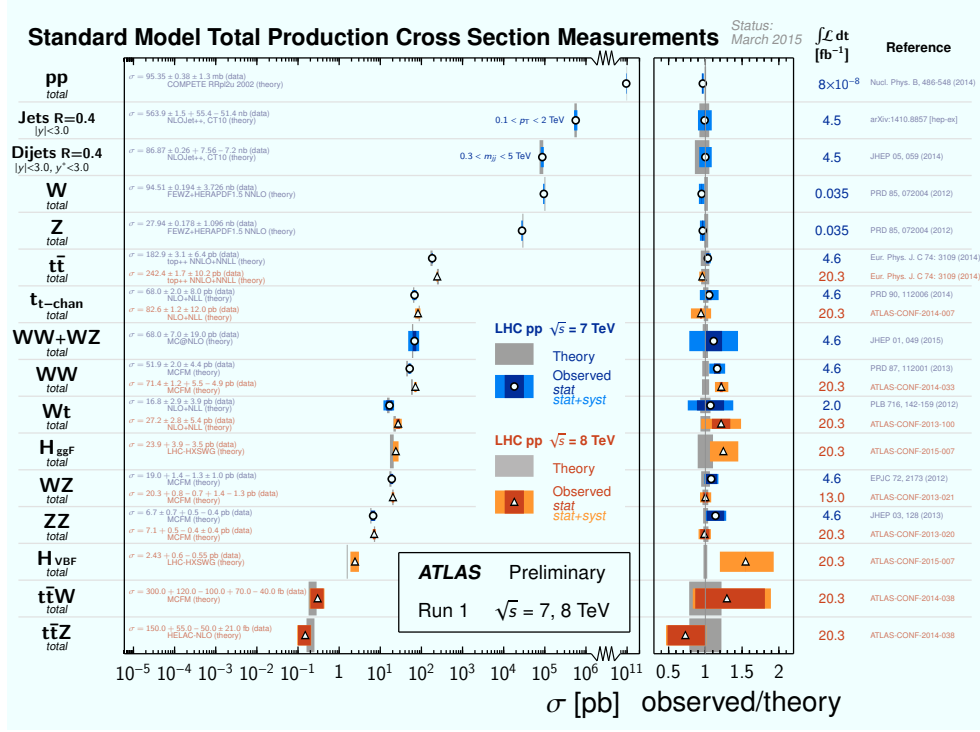


Figure 2.1: Summary of ATLAS Run 1 Standard Model measurements

the Higgs Boson mass is so low compared to the Planck Scale, where the effects of quantum gravity must be included and it is known that the Standard Model would no longer be valid. This arises from the Higgs field itself, as a complex scalar with the potential:

$$V = m_H^2 |H|^2 + \lambda |H|^4 \quad (2.2)$$

With the discovery of the Higgs Boson with a mass near 125 GeV, a problem arises that the quantum corrections to the bare Higgs mass can be very large. For fermions, these are of the form:

$$\Delta m_H^2 = \frac{|\lambda_f|^2}{8\pi^2} \Lambda_{UV}^2 + \dots \quad (2.3)$$

where Λ_{UV} is the ultraviolet momentum cutoff, usually interpreted as the energy scale at which the theory is not longer valid. The largest of these terms is for the top quark, since Higgs couplings to the fermions are proportional to their mass. If Λ_{UV} is on the order of the Planck Scale, the corrections are about 30 orders of magnitude larger than the value of m_H^2 . Thus, in the Standard

Model, the bare mass (which is not measurable) must be able to cancel these correction terms almost exactly to the observed Higgs mass near 125 GeV. In the Standard Model, this is a problem unique to the scalar Higgs; the quantum corrections to the fermions and bosons do not have these quadratic divergences with Λ_{UV} . As will be further explained in Section 2.2.1.1, Supersymmetry provides a natural cancellation of these terms, stabilizing the Higgs mass without a need for an absurdly large “fine-tuning” of the bare mass parameter.

2.1.2.2 Dark Matter and Dark Energy

Though the Standard Model represents our best understanding of the structure of the universe, it fails to quantify roughly 95% of the matter-energy content. Cosmological evidence shows that only about 5% of the observable universe is made up of ordinary matter described by the standard model; the remainder is made up of dark matter (27%) and dark energy (68%).

Dark matter was postulated as an explanation for discrepancies in the observed mass of astronomical objects and their apparent mass through gravitational effects, such as galaxy rotational curves. It is postulated that the additional matter is not seen because it does not interact with the electromagnetic radiation. Further evidence comes from weak gravitational lensing measurements, particularly observations of the Bullet Cluster[12] and anisotropies in the Cosmic Microwave Background (CMB). One of the leading explanations for dark matter is postulating a new type of particle that only interacts through the gravitational and the weak force, going by the name Weakly-Interacting Massive Particles (WIMPs).

Dark Energy is theorized as an unknown form of energy that allows for the acceleration of the expansion of the universe. Evidence for dark energy primarily comes from measurements of Type 1A supernovae, a standard candle used to measure distances and redshifts. Other evidence comes from CMB measurements that indicate that the geometry of space is close to flat. The ordinary matter and dark matter content of the universe is not enough to allow this, implying an additional source.

2.2 Supersymmetry

Perhaps the leading candidate for extension of the SM is Supersymmetry[13, 14, 15, 16, 17, 18, 19, 20, 21]. This symmetry posits a relationship between the fermions and bosons and causes an effective doubling of the number of fundamental particles, predicting “superpartners” for each known SM particle, differing only in spin. If the symmetry were exact, these superpartners, or sparticles, would have the same mass as their Standard Model counterparts. However, since no such superpartners are found to exist, it is theorized that the symmetry must be broken, leading to mass differences between the SM particles and SUSY particles. SUSY was first proposed to solve the hierarchy problem, but it has several other features that make it a very attractive BSM theory.

2.2.1 Motivation for Supersymmetry

2.2.1.1 The hierarchy problem

Supersymmetry provides the additional symmetry needed to naturally cause the cancellation on the large corrections to the Higgs mass mentioned in the previous section [22, 23, 24, 25, 26, 27]. In the calculation of the corrections to the Higgs mass, fermionic components and bosonic components enter with opposite signs, such that a Standard Model particle and its superpartner will cancel. So for the top quark, its contribution will be exactly balanced by that of the stop.

However, as mentioned previously, SUSY, if it exists, must be a broken symmetry as no particles with identical masses have been found. This fact can lead to some tension in the loop cancellation just described. Because of the relative contributions of the different standard model particles, it is more important for certain SUSY particles to be closer in mass to their SM partners, otherwise a similar hierarchy problem arises. This requirement for only a small amount of fine-tuning is generally referred to as “naturalness” and will be further mentioned in Section 2.2.3.

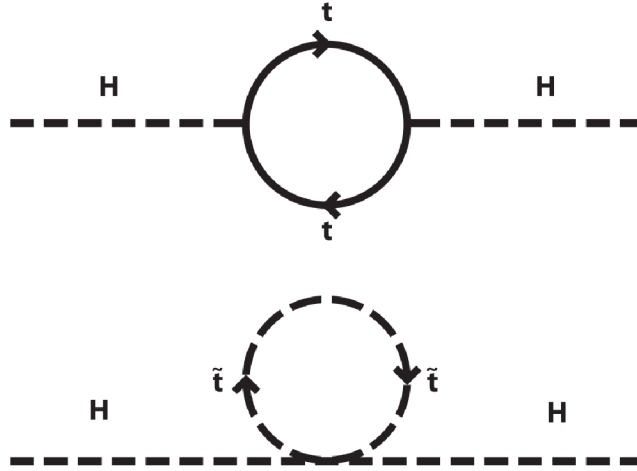


Figure 2.2: One loop corrections to the Higgs mass due to top quark (top) and scalar top (bottom) proposed in SUSY.

2.2.1.2 R-parity and Dark Matter

The most general supersymmetric potential includes terms that would allow for violation of lepton number and baryon number. This would lead to several processes that have not been seen experimentally, most importantly proton decay, on which there are very strict limits set[28].

One way to protect against this is to introduce an additional symmetry, called R-parity. R-parity is defined as:

$$P_R = (-1)^{3(B-L)+2s} \quad (2.4)$$

where B is the baryon number, L is the lepton number and s is the spin. This gives all Standard Model particles $P_R = +1$ and all SUSY particles $P_R = -1$.

If R-parity is conserved, there are several important consequences. First, at colliders such as the LHC, SUSY particles must always be produced in pairs. Additionally, in order for R-parity to be conserved, the lightest SUSY particle (LSP) must be stable. If the LSP has no electric charge, this means it can then only interact through the weak force, making it a WIMP. This particle then

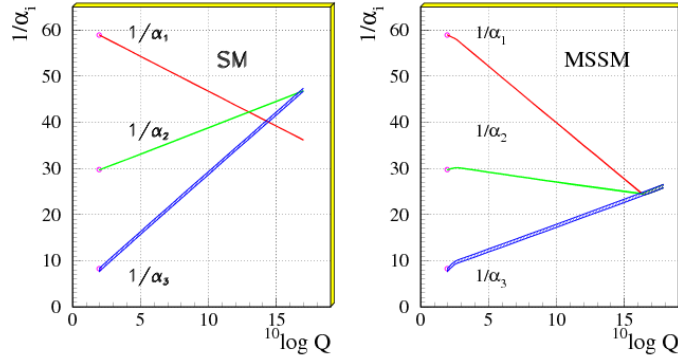


Figure 2.3: Running of the coupling constants in the Standard Model and the MSSM

provides a natural candidate for the dark matter observed in the universe [29, 30].

2.2.1.3 Unification of the Gauge Couplings

Supersymmetry, at least in its minimal version, also has the intriguing property that it allows for the unification of the gauge couplings [31, 26, 32, 33, 34, 35, 36, 37, 38]. With the Standard Model, if the three fine structure constants from the $SU(3)$, $SU(2)$, and $U(1)$ are allowed to run at higher energy scales, as shown in the left plot of Figure 2.3, the three lines do not share a common intersection point. However, in the MSSM, shown in the right plot, the three lines intersect at a single point within errors. This is an interesting hint for Supersymmetry playing a part in Grand Unification Theories (GUTs).

2.2.2 Supersymmetric Particles in the MSSM

The most commonly studied SUSY model is the Minimal Supersymmetric Standard Model (MSSM). The MSSM contains the fewest new particles required. Superpartners of the fermions will be scalars and are named with an 's' preceding their SM names. So, the SUSY equivalents of quarks and leptons are squarks and sleptons. It is important to note that the left and right handed SM fermions have different gauge transformations, and so must have different scalar partners. These proposed scalar particles and their quantum numbers can be seen in Table 2.1

In the Higgs sector in the Standard Model, only one complex Higgs doublet is required, manifest-

Names		spin 0	spin 1/2	$SU(3)_C, SU(2)_L, U(1)_Y$
quarks, squarks ($\times 3$ generations)	Q	$(\tilde{u}_L, \tilde{d}_L)$	(u_L, d_L)	$(\mathbf{3}, \mathbf{2}, \frac{1}{6})$
	\bar{u}	\tilde{u}_R^*	u_R^\dagger	$(\bar{\mathbf{3}}, \mathbf{1}, -\frac{2}{3})$
	\bar{d}	\tilde{d}_R^*	d_R^\dagger	$(\bar{\mathbf{3}}, \mathbf{1}, \frac{1}{3})$
leptons, sleptons ($\times 3$ generations)	L	$(\tilde{\nu}, \tilde{e}_L)$	(ν, e_L)	$(\mathbf{1}, \mathbf{2}, \frac{1}{2})$
	\bar{e}	\tilde{e}_R^*	e_R^\dagger	$(\mathbf{1}, \mathbf{1}, 1)$
Higgs, higgsinos	H_u	(H_u^+, H_u^0)	$(\tilde{H}_u^+, \tilde{H}_u^0)$	$(\mathbf{1}, \mathbf{2}, +\frac{1}{2})$
	H_d	(H_d^0, H_d^-)	$(\tilde{H}_d^0, \tilde{H}_d^-)$	$(\mathbf{1}, \mathbf{2}, -\frac{1}{2})$

Table 2.1: Chiral Supermultiplets in the MSSM.

ing as a single Higgs Boson particle. In Supersymmetry, the single doublet causes gauge anomalies. Instead, a minimum of two complex doublets (8 degrees of freedom) are necessary, denoted by H_u and H_d , with the H_u coupling to the up-type quarks and the H_d coupling to the down-type quarks. After Electroweak symmetry breaking, both H_u^0 and H_d^0 get non-zero vacuum expectation values.

$$v_u = \langle H_u^0 \rangle \quad v_d = \langle H_d^0 \rangle \quad (2.5)$$

and their ratio is the important SUSY parameter:

$$\tan\beta \equiv \frac{v_u}{v_d} \quad (2.6)$$

Three of the eight degrees of freedom become the Goldstone Bosons, which are eaten by the Z^0 and W^\pm , becoming the longitudinal modes of the massive gauge bosons. This leaves five Higgs scalar mass eigenstates. There are two CP-even neutral scalars, called h^0 and H^0 ¹, one CP-odd neutral scalar, A^0 , and two charged scalars, H^\pm .

The superpartners to the bosons are named using the suffix “-ino”, so the fermionic partners to the Higgs are the Higgsinos, partners to the W bosons are winos, the partner to the B^0 , is the bino, and the partners to the gluons are the gluinos. The chiral multiplets including the Higgs and Higgsinos are shown in Table 2.1 and that showing the gauge supermultiplets is shown in Table 2.2.

¹by convention the h^0 is taken to be the lighter mass

Names	spin 1/2	spin 1	$SU(3)_C, SU(2)_L, U(1)_Y$
gluino, gluon	\tilde{g}	g	$(\mathbf{8}, \mathbf{1}, 0)$
winos, W bosons	$\tilde{W}^\pm \tilde{W}^0$	$W^\pm W^0$	$(\mathbf{1}, \mathbf{3}, 0)$
bino, B boson	\tilde{B}^0	B^0	$(\mathbf{1}, \mathbf{1}, 0)$

Table 2.2: Gauge Supermultiplets in the MSSM.

Because of Electroweak symmetry breaking, the partners of the Higgs and Electroweak Bosons are able to mix with one another. There are four neutral mass eigenstates called Neutralinos, $\tilde{\chi}_1^0, \tilde{\chi}_2^0, \tilde{\chi}_3^0, \tilde{\chi}_4^0$, numbered in increasing mass order. These result from the mixing of the two neutral Higgsinos, \tilde{H}_u^0 and \tilde{H}_d^0 , and the Bino and neutral Wino, \tilde{B} and \tilde{W}^0 . Similarly, the charged Higgsinos, \tilde{H}_u^\pm and \tilde{H}_d^\pm , mix with the charged Winos, \tilde{W}^\pm and \tilde{W}^\pm , to form two mass eigenstates called charginos, each with charge ± 1 . They are also numbered in increasing mass, giving $\tilde{\chi}_1^\pm$ and $\tilde{\chi}_2^\pm$. Collectively, the neutralinos and charginos are referred to as “gauginos”.

The mixing matrix for the neutral sector is given by:

$$\begin{pmatrix} M_1 & 0 & -m_Z \cos(\beta) \sin(\theta_W) & m_Z \sin(\beta) \sin(\theta_W) \\ 0 & M_2 & m_Z \cos(\beta) \cos(\theta_W) & -m_Z \sin(\beta) \cos(\theta_W) \\ -m_Z \cos(\beta) \sin(\theta_W) & m_Z \cos(\beta) \cos(\theta_W) & 0 & -\mu \\ m_Z \sin(\beta) \sin(\theta_W) & -m_Z \sin(\beta) \cos(\theta_W) & -\mu & 0 \end{pmatrix} \quad (2.7)$$

and for the charged sector:

$$\begin{pmatrix} M_2 & \sqrt{2} \sin(\beta) m_W \\ \sqrt{2} \cos(\beta) m_W & \mu \end{pmatrix} \quad (2.8)$$

where β is as previous defined, θ_W is the Weinberg angle, M_1 is the Bino mass term, M_2 is the Wino mass term, and μ is the Higgsino mass term.

2.2.3 The Case for Weakly-produced Supersymmetry

Through the end of the LHC's first run, no supersymmetric partners have been found so far. Searches in particular for strongly-produced colored superpartners, squarks and gluinos, have reached limits that are bound by the collider energy available. These limits set gluino masses above $\sim 1.1 - 1.7$ TeV and light squark masses above $0.8 - 1.7$ TeV, depending on the model and specific assumptions [39, 40, 41, 42].

The bounds on strongly-produced SUSY are high precisely because of their large production cross section. Particles produced via interaction with the weak force, that is through W or Z bosons, will have a much lower production rate. However, if the superpartners of the gauge bosons, the gauginos, are on the order of a few hundred GeV, and the squarks and gluinos are all much heavier (several TeV or more), weakly-produced SUSY could be the dominant production and thus discovery mode at the LHC running at $\sqrt{s} = 8$ TeV. In addition, there are some theoretical naturalness arguments that would point to gaugino masses having at most a few hundred GeV [43, 44]. The so-called naturalness requirement for the MSSM can be summarized as:

$$\frac{m_Z^2}{2} = -\mu^2 + |m_{H_u}^2| \quad (2.9)$$

with μ parameter controlling the Higgsino mass, forcing it to be light. Thus, it is likely that if gauginos exist, at least some of them would be light enough for detection at the LHC.

CHAPTER 3

The ATLAS Detector

The Atlas detector is one of two large, multi-purpose particle detectors located at the LHC; the other is the Compact Muon Solenoid (CMS). Both Atlas and CMS contain multiple detector technologies with complementary particle measurement abilities in order to accomplish a broad range of physics goals. The Atlas detector is comprised of an Inner Detector (ID) within a 2 Tesla solenoidal magnetic field, further sub-divided into a Pixel detector, Semi-Conductor Tracker, and a Transition Radiation Tracker; a liquid Argon Electromagnetic Calorimeter; Hadronic calorimeters based on liquid Argon and scintillating tiles; and a muon system providing both triggering and tracking capabilities located within an air-core toroidal magnetic field. The differing technologies of the Atlas sub-detectors were chosen in order to fulfill the broad-based goals common to many physics searches and measurements:

- Tracking of charged particles of transverse momentum greater than 500 MeV and $|\eta| \leq 2.5^2$
- Energy measurements and particle identification for electrons and photons with $|\eta| \leq 2.47$
- Identification and momentum measurement of muons with $|\eta| \leq 2.7$
- Jet energy measurements and determination of Missing Transverse Energy

The following chapter gives a cursory introduction to the components of the Atlas detector.

Much more detailed information about the as-built detector can be found in [45].

²ATLAS uses a right-handed coordinate system with its origin at the nominal interaction point (IP) in the center of the detector and the z -axis along the beam line. The x -axis points from the IP to the center of the LHC ring, and the y -axis points upward. Cylindrical coordinates (r, ϕ) are used in the transverse plane, ϕ being the azimuthal angle around the beam line. The pseudorapidity is defined in terms of the polar angle θ as $\eta = -\ln \tan(\theta/2)$.

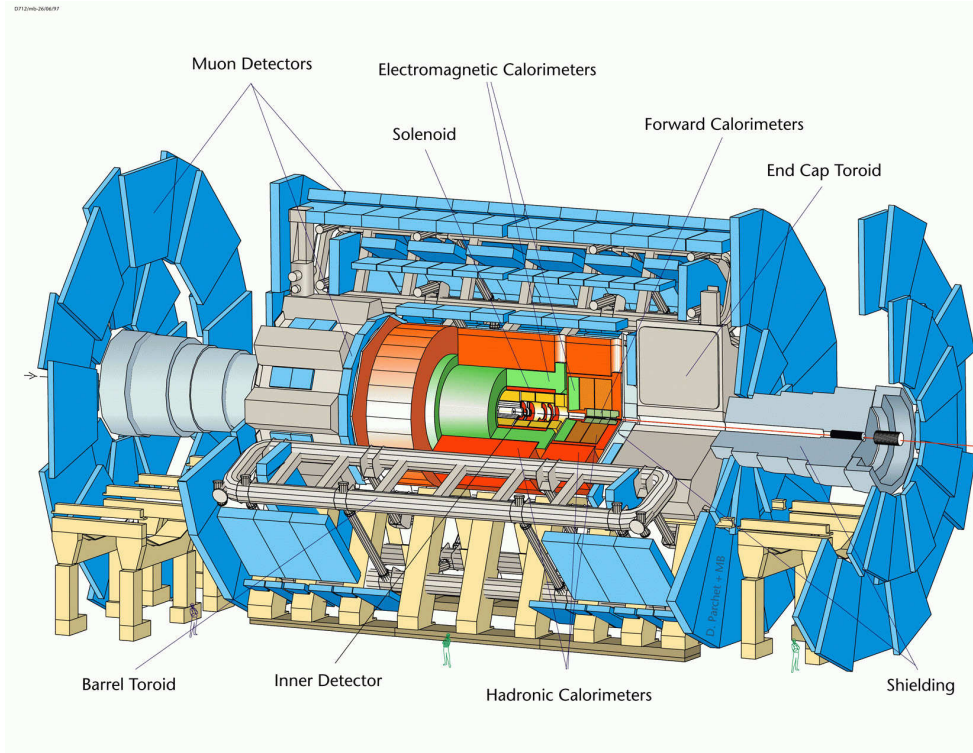


Figure 3.1: The full Atlas Detector with its individual sub detector elements visible

3.1 Trackers

The innermost Atlas detectors are two Silicon based trackers covering up to $|\eta| < 2.5$. Surrounding the beampipe is the extremely finely segmented Pixel detector. Outside of that is the Semi-Conductor tracker (SCT), with coarser segmentation. The final piece of the Atlas ID is the gaseous straw tube Transition Radiation Tracker (TRT). The entire ID is contained within a cylindrical space covering ± 3412 mm along the beampipe and a radius of 1150 mm. It is completely surrounded by the solenoid magnet, producing a 2 T field and causing charged particles to bend in the ϕ dimension. The arrangement of the ID sub-detectors is shown in Figures 3.2 and 3.3 and the individual subdetectors are described further in the following sections.

The Atlas tracking system is designed to perform several tasks. Its primary function is to provide position and momentum information for charged tracks. Each of the tracking systems is able to detect the deposit of energy caused by the passage of the charged particle (dE/dx) [46]. In

the silicon detectors, electron-hole pairs are created with minimum deposits of about 3 eV of energy, producing a large signal. In the TRT, energy deposits of about 30 eV ionize the active gas, producing electron-ion pairs. In both cases, the pairs are separated using electric fields, allowing for detectable electronic signals and giving position information within the ID via which locations show activity. The many position measurements are processed by sophisticated pattern recognition algorithms to identify the “tracks”, or the paths taken by the charged particles. As the charged particles traverse the detector, they are subject to the magnetic field, causing them to travel in helices, rather than straight lines. The curvature of the measured track is used to reconstruct the particle’s momentum.

The Atlas ID is able to reconstruct particle trajectories down to 500 MeV of transverse momentum in normal configuration, and down to 100 MeV in special cases, such as in the extremely low-luminosity environment. For high energy particles, relative momentum resolution $\sigma(p)/p = 4.83 \pm 0.16 \times 10^{-4} \text{ GeV}^{-1} \times p_T$ have been measured [47]. The precision detectors closest to the interaction point also allow for precise determination of the beamspot and reconstruction of secondary vertices from photon conversions or long-lived particles such as hadrons containing a b-quark. With the high pile-up environment of the LHC producing 20 or more primary vertices and large particle multiplicities, these capabilities are essential for the performance of the detector. The TRT, with less intrinsic accuracy per hit than the Silicon detectors, compensates by utilizing its long lever arm and large number of measurements for each track, thus providing a strong constraint on the particle momentum. The TRT also provides electron identification through the detection of transition radiation.

3.1.1 Pixel Detector

The Pixel Detector is the innermost and most finely segmented of all the Atlas sub-detectors. Containing a total of 80.4 million readout channels, the Pixel detector has a barrel section comprised of three cylindrical layers of detecting elements and two end-caps, each comprised of 3 disks oriented perpendicular to the beamline. A particle typically crosses 3 pixel layers. The innermost layer, also

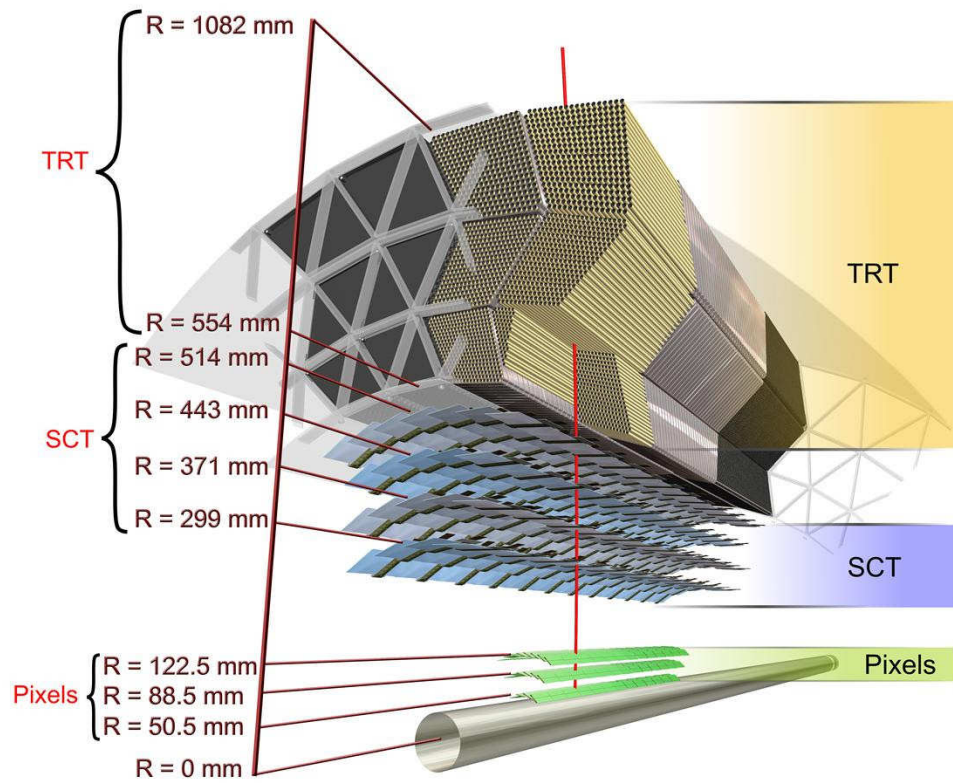


Figure 3.2: The ATLAS Inner Detector Barrel

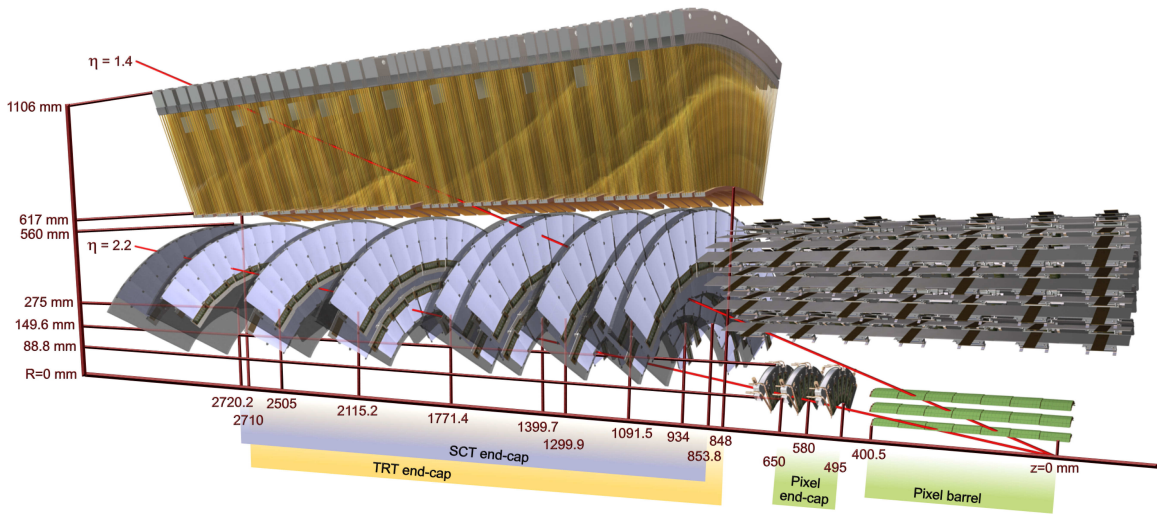


Figure 3.3: The ATLAS Inner Detector End-caps

known as the “vertexing” or “B” layer, is located at a radius of just 51 mm. Between the barrel and the end-cap, the sensitive modules are identical. The minimum pixel size is $50 \times 400 \mu\text{m}$ in $\phi \times z$ ($\phi \times r$) for the barrel (end-caps), and provides an intrinsic accuracy of $10 \mu\text{m}$ in $R - \phi$ and $115 \mu\text{m}$ in $z(r)$ for the barrel (end-caps).

3.1.2 Semi-Conductor Tracker

The SCT is also a central cylindrical barrel flanked by two end-caps comprised of disks. The barrel is composed of four double-sided layers of overlapping modules, designed to provide four space point measurements per track. The two sides of each module are rotated by 40 mrad, providing the stereo angle information. In the end-cap there are nine disk layers of stereo strips arranged radially, again with a 40 mrad angle, and designed to provide 4 space points per track. The intrinsic accuracy is $17 \mu\text{m}$ in $R - \phi$ and $115 \mu\text{m}$ in $z(r)$ for the barrel (end-caps).

3.1.3 Transition Radiation Tracker

The Transition Radiation Tracker (TRT) is the final and outer-most part of the Atlas Inner Detector. Containing 298,304 carbon-fiber reinforced Kapton[®] straws, it is a hybrid detector that combines the tracking capabilities of a straw tracker with the particle identification ability of a transition radiation detector. Its long lever arm provides strong constraints for the momentum measurement of charged particles, and TR detection allows for discrimination between electrons and hadrons. Typical charged particles within the fiducial acceptance cross about 36 straws, called colloquially “hits”. Each straw is 4 mm in diameter and has an intrinsic resolution of around $120 \mu\text{m}$. Position information is only available in two dimensions, $r - \phi$ in the barrel, and $z - \phi$ in the end-caps; that is, position of the hit along the length of the straw cannot be determined. The detector design also was optimized in order to reduce the material budget of the Inner Detector allowing for more accurate measurements by detectors outside the ID and to provide cost savings over an entirely silicon technology tracker.

3.1.3.1 Design

Like the rest of the ID, the TRT is composed of a central barrel section and two end-caps. The barrel is designed to fully contain tracks with $|\eta| < 0.7$, and provide some tracking ability for tracks up to $|\eta| < 1.0$. The end-caps extend coverage up to $|\eta| < 2.0$.

The barrel consists of 52,544 straws oriented parallel to the beamline in layers between $560 < R < 1080$ and $827 < |z| < 720$ mm. The wires are mechanically and electronically separated by a glass bead at $z = 0$, creating two channels, read out on each end of the detector. In order to decrease occupancy, the inner-most nine layers are similarly separated into three channels, with the central section not read out. These inner-most straws are known as the “short straws”. The barrel is mechanically separated into 96 modules, arranged in 3 concentric rings of 32 modules each in the ϕ direction. Oriented fibers of polypropylene are interwoven between the straws in order to provide radiating material for TR production [48].

Each end-cap contains 122,880 straws perpendicular to the beamline between $827 < |z| < 2744$ and $617 < R < 1106$ mm. The straws are arranged in radially oriented planes of 768 straws, with 8 planes forming one “wheel”. The first 12 wheels have a spacing of 4 mm between layers in the z-direction, and are known as “A-wheels”. The last 8 wheels, the “B-wheels” have a larger spacing of 11 mm between each of the layers, such that tracks at small polar (θ) angle cross approximately the same number of straws as those at larger angles. The space between each layer is filled with the radiating material, foils of polypropylene. Due to the larger spacing in the B-wheels, there is more radiating material present [49].

Each straw is 2 mm in radius and contains a 31 micron diameter, gold-plated tungsten wire in its center. The wires are kept at ground, while the straw walls are held at a potential of about -1530 Volts. The active gas in the straws is a mixture containing 70% Xe, 27% CO₂ and 3% O₂. Xenon is chosen for its high efficiency to absorb TR photons in the desired energy range. This can be seen in Figure 3.4. For the energy range ~ 10 keV, the absorption length for Xenon is about 5 mm, compared to 30-40 mm for Krypton. The 70% concentration was optimized to maximize performance, while

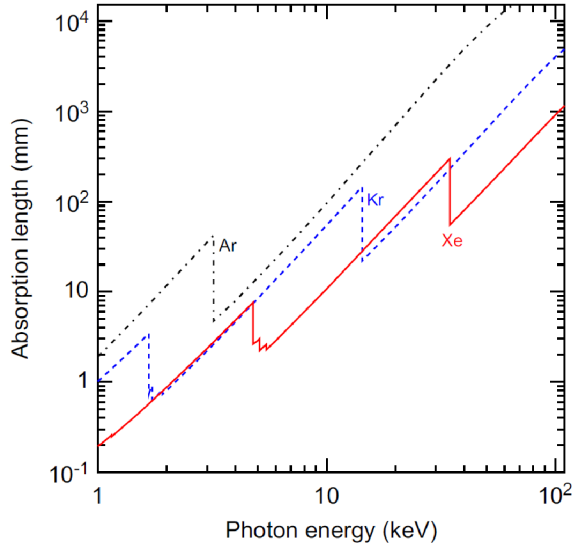


Figure 3.4: Transition radiation absorption length for potential gases in the TRT.

the additional gases stabilize the mixture and provide protection against streamers[50].

The read-out electronics for the TRT starts with two custom designed ASICs (application-specific integrated circuit) chips. The first performs Amplification and Shaping of the signal, followed by Discrimination against two thresholds (high for TR detection of about 5-6 keV and low for tracking of about 300 eV), and Baseline Restoration to compensate for the long signal tail due to relatively slow motion of the positive ions towards the cathode, thus the chip is known by the acronym ASDBLR. Each ASDBLR connects directly to eight straws and provides a ternary output to the second digital chip, the DTMROC (Drift-time measurement read-out chip). Each DTMROC is connected to 2 ASDBLRs, and thus reads out 16 straws separately. The DTMROC converts the ternary signal from each of the ASDBLR channels to a binary output. Eight bits for each bunch crossing of 25 ns contain the information from the low-threshold (3.12 ns per bit), and one bit for the high-threshold decision for each 25 ns bunch crossing. The DTMROC holds the information in a pipeline awaiting a signal from the level 1 trigger [51][52].

3.1.3.2 Tracking

The TRT operates as a gaseous straw tube tracking detector. When a charged particle traverses the active gas within the straw, the valence electrons from the gas are freed, ionizing the gas. This process, along with absorption of a TR photon, is depicted in Figure 3.5. The negatively charged electrons move along the electric potential away from the straw wall and toward the central wire, drifting at $50 \mu\text{m}/\text{ns}$. As the electrons approach the wire, they are able to induce a cascade effect, ionizing more gas in the presence of the high electric field. This characteristic amplification, or “gas gain” is on the order of 2×10^4 for the TRT and allows a large enough current on the wire to be detected by the front-end electronics and read out.

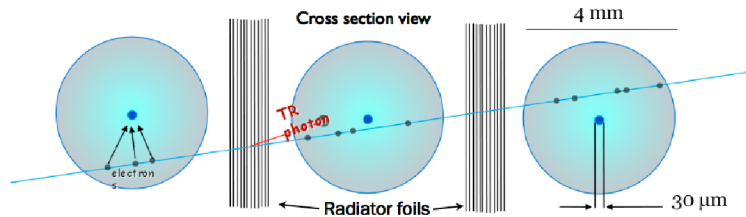


Figure 3.5: Illustration of a particle signal in one TRT straw.

The first ionization electrons to reach the wire will be those from the “distance of closest approach” to the wire, and will vary from roughly 0 to 2mm from wire depending on the path of the particle through the straw. The arrival time of the first electrons therefore varies from hit to hit. The arrival of the first ionization electrons creates the first $0 \rightarrow 1$ transition in the digital output, known as the “leading edge”, can therefore be transformed to a measurement of the distance of closest approach (also called track-to-wire distance), using the “R-T relationship”. Since the path of the particle will always traverse the straw wall, and that is the maximal distance from the wire, the last ionization electrons to arrive at the wire are produced nearest the straw wall, and their time of arrival will remain rather constant from hit to hit. After their arrival, the final $1 \rightarrow 0$ transition occurs, known as the “trailing edge”. The time difference between the leading and trailing edge is known as “time over threshold” [53]. This electronics response is illustrated in Figure 3.6.

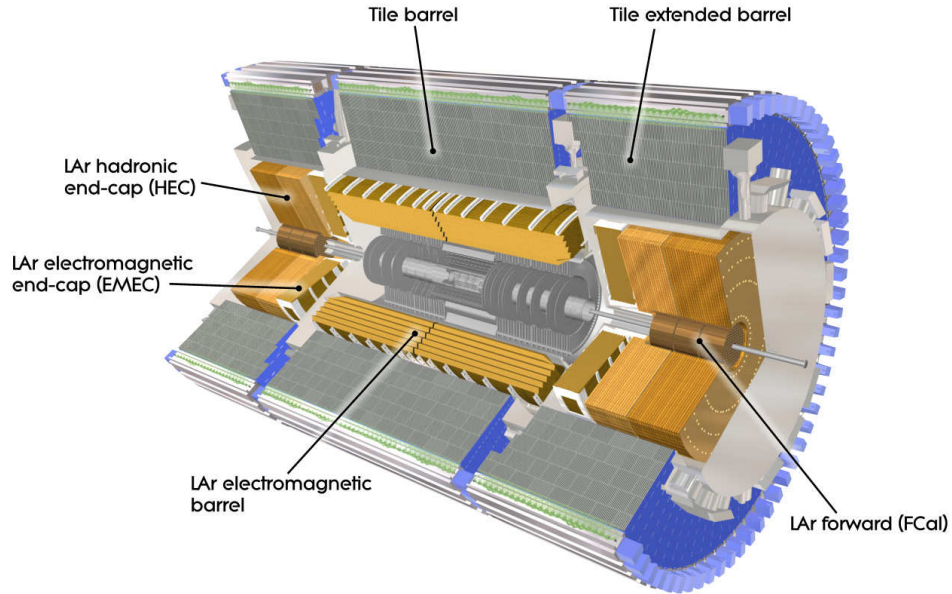


Figure 3.7: The Atlas Calorimeters

3.2 Calorimetry

The Atlas calorimeter system is designed to stop all Standard Model particles and provide a measurement of their energy, with the exception of muons and neutrinos. The calorimetry system is divided into an Electromagnetic Calorimeter, Hadronic Calorimeter and a Forward Calorimeter. A diagram of their layout is given in Figure 3.7. All the Atlas calorimeters are sampling calorimeters. Sampling calorimeters utilize two different materials to create the particle shower and to measure the deposited energy. However, because of some of the energy will be deposited in the showering material, not all the energy from the particle shower is able to be collected and thus, the true, total energy must be estimated from that collected.

3.2.1 ElectroMagnetic Calorimeter

The electromagnetic calorimeters are designed to measure energy from incoming photons or electrons. In a high- Z material, electrons lose energy by radiation of photons (bremsstrahlung), and energetic photons undergo pair-production to create e^+e^- . These two processes rapidly create a

“shower” of large numbers of electrons, positrons and photons. Muons and charged hadrons are too massive to lose energy this way. The radiation length is the distance for the electron to lose $1/e$ of its initial energy. For high- Z materials, such as lead, this is very short at 5-6 mm.

For the entire EM calorimeter, lead is used as an absorbing material to create the particle shower and liquid argon is utilized as the active medium to measure the energy deposits. Liquid argon provides radiation hardness, time-stability and linearity of energy measurement over a large energy range. The LAr calorimeters employ an accordion shaped geometry allowing for full ϕ coverage with no cracks, preventing missed energy deposits.

The central barrel detector extends to $|\eta|$ of 1.475 and is separated at $z = 0$ by a small gap into two halves. Each half of the barrel is 3.2 m long, with an inner radius of 1.4 m and an outer radius of 2 m, and provides greater than 22 radiation lengths of material. The two electromagnetic end-caps (EMEC) cover the region $1.375 < |\eta| < 3.2$, and are mechanically divided into an inner and outer wheel at $|\eta| = 2.5$. The end-caps provide more than 24 radiation lengths of material.

The EM Barrel is segmented longitudinally into three sections to take advantage of discriminating information in the shape of the showers. The innermost layer, known as the strips, is very finely segmented in η ($\Delta\eta \times \Delta\phi = 0.0031 \times 0.1$) in order to identify π^0 decays to $\gamma\gamma$, which have a small opening angle. The second layer is the bulk of the calorimeter, containing between 16.5-19 radiation lengths, and is segmented $\Delta\eta \times \Delta\phi = 0.025 \times 0.025$. The final layer is twice as wide in $\Delta\eta$ (0.05) and can help to distinguish electrons and photons from hadrons, which typically leave more energy in the back of the EM calorimeter. This arrangement can be seen in Figure 3.8

The EM End-caps are similarly segmented longitudinally, though geometric concerns make their arrangement somewhat more complicated than in the barrel. In the first layer, the strips become coarser in $\Delta\eta$ with increasing η (closer to the beamline) due to the practicality of having the width of the strips greater than a few mm. For the majority of the end-caps, the middle and last sampling layers have the same segmentation as the barrel (0.025×0.025 and 0.050×0.025 , respectively). The transition regions between the end-caps and the barrel have a somewhat coarser segmentation and

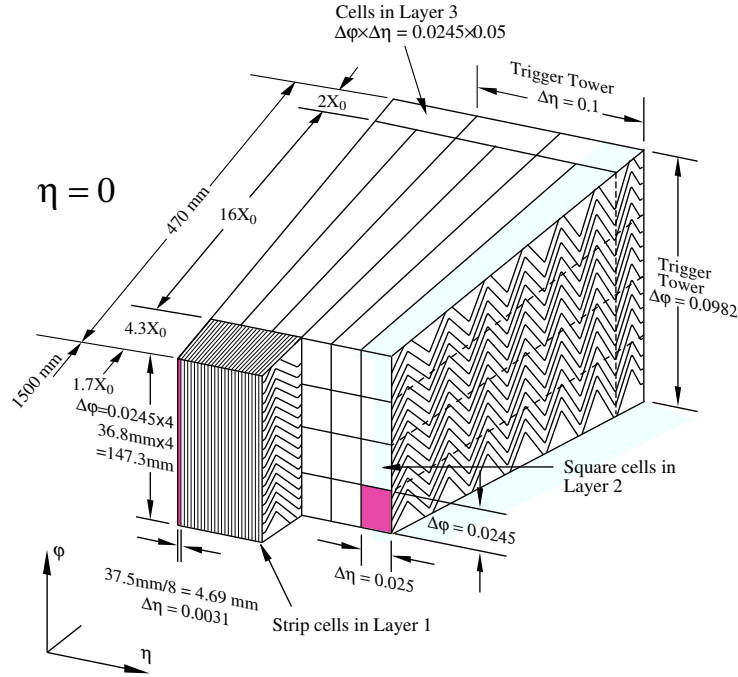


Figure 3.8: Sketch of the geometry of the liquid argon barrel calorimeter, clearly showing its segmentation in the different longitudinal layers.

no third layer. Because there is a large amount of inactive material in this region ($1.37 < |\eta| < 1.52$) leading to poorer energy measurements and identification power, it is often excluded from the fiducial region of the detector.

3.2.2 Hadronic Calorimeter

The hadronic calorimeter system is designed to measure energy from charged and neutral hadrons, interacting primarily through the strong force. The interaction length (or nuclear interaction length) is the mean distance a particle can traverse before undergoing a nuclear collision. For iron, this distance is about 170 mm.

The hadronic calorimeter systems is composed of two distinct technologies. In the central region is the Tile Calorimeter made of steel absorbers and scintillating tiles for active material to detect the passage of charged particles in the hadronic shower. The Tile Calorimeter is comprised of a barrel for $|\eta| < 1.0$ and two “extended barrels” from $0.8 < |\eta| < 1.7$. The tile calorimeter extends

from an inner radius of 2.28 meters to 4.25 m, and is segmented into three layers. At $\eta = 0$ the total material traversed is 9.7 interaction lengths.

At more forward parts of the detector the Hadronic End-cap (HEC) is located directly behind the EMEC, and extends to from $|\eta| = 1.5$ (slightly overlapping the tiles) to $|\eta| = 3.2$. Like the EM calorimeters, the HEC also utilizes liquid argon as its active material. It consists of two independent wheels for each end-cap, each of which contains two layers in depth (four total layers for each end-cap).

3.2.3 Forward Calorimeter

Finally, at the highest values of $|\eta|$ is the Forward Calorimeter (FCal), providing measurements up to $|\eta| = 4.9$ to ensure as uniform coverage as possible. The total depth of the FCal is approximately 10 interaction lengths and is segmented into three modules. The first, optimized for EM showers, is made of copper, while the second and third are made of tungsten and are most sensitive to hadronic interactions.

3.3 Muon System

Muons are too massive to lose significant energy by radiation and do not interact via the strong force, and so escape the calorimeters. The Atlas muon system is located outside of the calorimeters, is composed of four different detector technologies and is shown in Figure 3.9. Triggering on events that contain an energetic muon is provided by Thin Gap Chambers (TGCs) in the end-caps, and Resistive Plate Chambers (RPCs) in the barrel. Measurement of the muon's track in the η direction (the bending direction for the muon system) are provided by gaseous drift tubes, known as the Monitored Drift Tubes (MDTs) for most of the detector. As drift tubes, the MDTs operate on a similar principle as the TRT. This η measurement is augmented by ϕ information from the TGCs or the RPCs. In the most forward region of the end-caps ($2.0 < \eta < 2.7$), Cathode Strip Chambers (CSCs) are utilized instead due to the higher particle multiplicity.

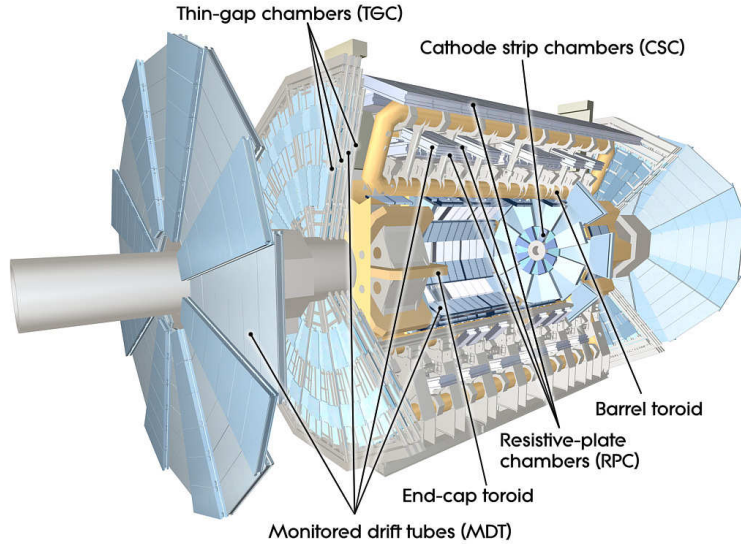


Figure 3.9: The Atlas Muon Spectrometer

Chambers in the barrel section containing the MDT and RPC detecting elements are arranged in 3 concentric layers, lying at radii of approximately 5 m, 7.5 m, and 10 m. In the end-cap, chambers containing the MDTs and TGCs are placed perpendicular to the beamline and are arranged in wheels, located at 7.4 m, 10.8 m, 14 m, and 21.5 m on either side of the interaction point. Each of these locations for the muon chambers are also referred to as “stations”.

Muons below about 4 GeV do not reach the muon system, however virtually all other particle types are stopped before the muon system. The designed momentum resolution of the muon system is 1% for a 1 TeV muon.

3.4 Trigger

In order to reduce the dataset from the high event-rate at the LHC to levels that are able to be stored permanently and distributed for further analysis, only potentially interesting events are saved. Atlas uses a three-level triggering system in order to perform this task, reducing the LHC’s designed bunch crossing rate of 40 MHz (in reality a maximum of 20 MHz for 2012 running) to a few hundred Hz output, the maximum that could be written out to permanent storage. The lowest level trigger

(Level 1 or L1) uses custom-built hardware on detector, while the Level 2 and Event Filter trigger utilize software based triggers. Level 1 uses information from the calorimeter and muon subsystems in order to reduce the event rate to a design value of 75 kHz with a latency of 2.5 μ s. After a successful L1 accept, information from the detector is passed to Readout Buffers (ROBs) for each subdetector to hold the data until a L2 decision is made. Information from Regions of Interest (ROI) identified at L1 are passed into the L2, which decides in an average of 40 ms per event and outputs at a rate of about 3 kHz. Accepted events are then passed to the event filter, which has access to full detector information and attempts to utilize algorithms as close to those used in offline reconstruction as possible. The Event filter makes a final trigger decision in approximately 4 s. Events are kept in collections called “trigger streams” according to what type of algorithms are run, usually related to the type of particle being selected for. The three main trigger streams for physics analyses are “Jet/Tau/ E_T^{miss} ”, “Egamma”, and “Muon” [45][56].

CHAPTER 4

Physics Object Reconstruction and Identification in ATLAS

Much of the design effort of the Atlas detector was centered around optimizing the identification capabilities and energy measurements of the several different particle types. The sub-detectors described in the previous chapter interact with different subsets of particle types, leading to distinct signatures in the detector as shown in Figure 4.1 for each particle type. For example, electrons can be identified by large energy deposits in the EM calorimeter, a track in the ID, but no activity in the HCAL or muon system; Photons behave similarly in the EM calorimeter, but will have no track in the ID. This chapter contains some details of the reconstruction and identification requirements for the physics objects used in this analysis – electrons, muons, hadron jets, and missing transverse energy (E_T^{miss}).

4.1 Identification of Electrons

4.1.1 Reconstruction

In the central region of the Atlas detector ($|\eta| < 2.47$) Electron objects are built from clusters of energy deposited in the EM Calorimeter and matched to a track from the Inner Detector. The EM clusters are found using a sliding-window algorithm, using a window size of 3×5 units of 0.025×0.025 in $\eta \times \phi$ space, and requiring total transverse energy greater than 2.5 GeV [57].

Tracks reconstructed in the Inner detector are then extrapolated into the calorimeter volume,

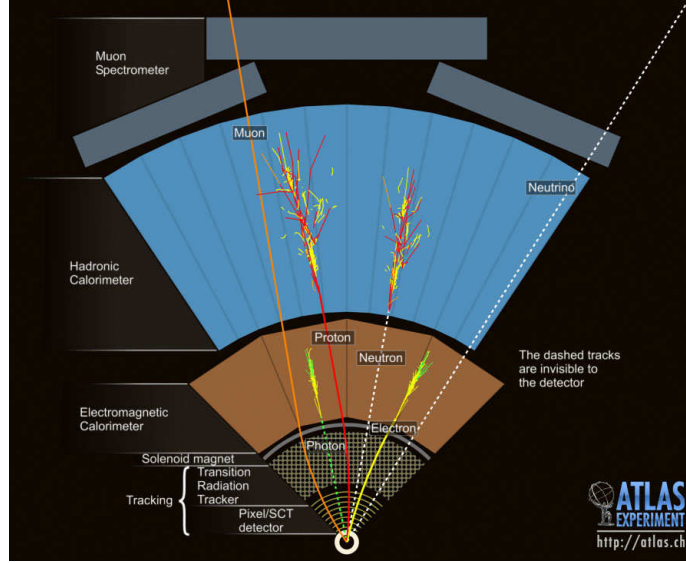


Figure 4.1: Diagram of the transverse view of a section of the ATLAS detector. Interactions with the various sub-detectors are shown for common particle types. The distinct interactions for different types of particles are used for identification.

and attempted to be matched to the identified EM clusters. A loose requirement of $\Delta\eta < 0.05$ is required, along with an asymmetric cut on $\Delta\phi$ of < 0.1 in the direction of bending, and < 0.05 on the other side. The loosened $\Delta\phi$ requirement allows electrons that have lost significant energy due to bremsstrahlung radiation to be recovered.

Tracks associated to electron candidates are then subjected to an improved tracking algorithm in order to better reflect energy losses due to bremsstrahlung radiation for electrons compared with the default tracking assumption of a pion. These tracks are refit using a Gaussian Sum Filter [58], providing, electron candidates with a better measurement of p_T , d_0 , d_0 significance ($d_0/\sigma(d_0)$), and ϕ .

4.1.2 Identification

After the electron candidates have been reconstructed, they are subject to a set of identification criteria to separate isolated, prompt, high p_T electrons from three main sources of background. The first background consists of jets misidentified as electrons. The last two sources involve real

electrons, but those coming from the leptonic decay of heavy quarks (b,c) or from the conversion of a photon into a electron-positron pair.

The default electron identification scheme for Run 1 is a selection utilizing rectangular cuts on discriminating variables from calorimeter shower information, track quality, transition radiation, and combined track-calorimeter information. These identification variables are given in Table 4.1. Certain identification variables are only useful for a subset of the possible background or fake electrons. For instance, the TRT high-threshold cut, further described in Section 4.1.3, can only distinguish between electrons and hadrons and is not able to reject non-prompt electrons coming from conversions of heavy-flavor decays or photon conversions.

The original schema defined three different working points, *Loose*, *Medium*, *Tight*, in order of increasing background rejection power and decreasing isolated electron efficiency. The *Loose* reference point utilized calorimeter variables in the second sampling layer as well as discrimination due to leakage into the hadronic calorimeter. Identification at the *Medium* level added requirements based on the first sampling layer of the EM calorimeter, requirements on track quality in the Silicon detectors and a loose requirement on the matching between the cluster and the track. The *Tight* working point further required the remaining identification variables, including those based on information from the TRT which are further elaborated in the next section. This framework unfortunately had the undesirable feature of very different mixes of the three background types at the different ID levels, leading to difficulties for many analyses which use extrapolations from a less stringent identification level to predict background contributions. For example, if using *Medium* selections to predict *Tight* lepton backgrounds, the hadron fake component could be too high compared to that from heavy flavor or conversions, because electron ID uses TRT information at *Tight*, but not *Medium*.

Since mid-2011, the selection has been optimized and reorganized into what is known as the “plusplus” menus. The plusplus menus differ from the old identification scheme in philosophy. Instead of adding additional cuts for each reference point, the plusplus menu generally utilizes a more

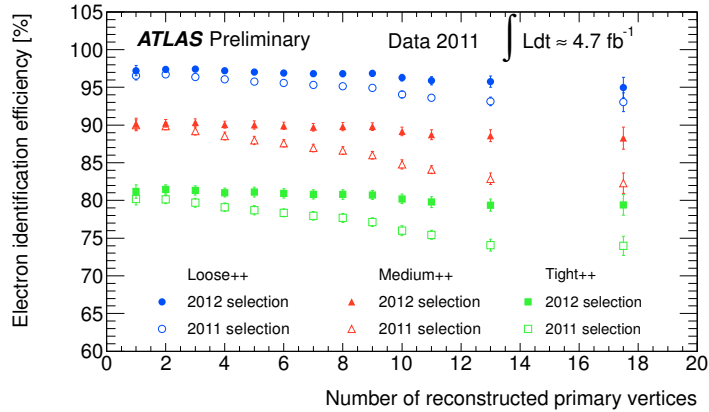


Figure 4.2: Efficiency for real isolated electrons using the new plusplus selection menu.

inclusive set of cuts at each working points, but allows for different cut values at each identification level for the same discriminating variable. This reorganization of the menu accomplished several goals. First, due to the increasing need for better background rejection to control trigger rates for medium identification level as the data-taking rate increased, it was found that the current scheme could not accommodate increased background rejection without also causing unacceptably large real electron efficiency losses. Allowing more discriminating variables all with somewhat looser cuts allowed an acceptable signal efficiency for the needed background rejection and acceptable trigger rates. Secondly, the plusplus menus greatly reduced the differences in background types between ID levels as described earlier, allowing for more reliable background estimates in analyses. Additionally, cuts on identification variables that are particularly affected by the presence of pile-up vertices in the 2012 dataset were able to be tuned to help mitigate this dependence. This effect can be seen in Figure 4.2.

4.1.3 Electron Identification in the TRT

The Atlas TRT provides an additional method of electron discrimination from the hadron background by detection of transition radiation. This capability provides an important complement to identification in the calorimeters, since it is almost completely uncorrelated. In contrast, several

Table 4.1: Definition of electron discriminating variables [57] that are used in the 2012 electron cut-based menus.

Type	Description	Name
Hadronic leakage	Ratio of E_T in the first layer of the hadronic calorimeter to E_T of the EM cluster (used over the range $ \eta < 0.8$ and $ \eta > 1.37$)	R_{Had1}
	Ratio of E_T in the hadronic calorimeter to E_T of the EM cluster (used over the range $ \eta > 0.8$ and $ \eta < 1.37$)	R_{Had}
Third layer of EM calorimeter	Ratio of the energy in the third layer to the total energy	f_3
Middle layer of EM calorimeter	Ratio of the energy in 3×7 cells over the energy in 7×7 cells centered at the electron cluster position	R_η
	Ratio of the energy in 3×3 cells over the energy in 3×7 cells centered at the electron cluster position	R_ϕ
	Lateral width of the shower	$W_{\eta 2}$
Strip layer of EM calorimeter	Total shower width	W_{stot}
	Ratio of the energy difference between the largest and second largest energy deposits in the cluster over the sum of these energies	E_{ratio}
	Ratio of the energy in the strip layer to the total energy	f_1
Track quality	Number of hits in the pixel detector	nPixHits
	Number of total hits in the pixel and SCT detectors	nSiHits
	Transverse impact parameter	d_0
	Significance of transverse impact parameter	σ_{d_0}
Track-cluster matching	$\Delta\eta$ between the cluster position in the strip layer and the extrapolated track	$\Delta\eta_1$
	$\Delta\phi$ between the cluster position in the middle layer and the extrapolated track	$\Delta\phi_2$
	Ratio of the cluster energy to the track momentum	E/p
TRT	Total number of hits in the TRT	nTRTHits
	Ratio of the number of high-threshold hits to the total number of hits in the TRT	F_{HT}
Conversions	Number of hits in the Blayer	nBlayerHits
Bremsstrahlung (GSF output)	Momentum difference of refitted and original track divided by original momentum	$\Delta p/p$
	Same as $\Delta\phi_2$, but after track refitting	$\Delta\phi_{\text{Res}}$

of the calorimeter variables listed in Table 4.1 are correlated with one another. In addition, the discrimination power of the TRT is particularly useful for energies below about 25 GeV, where the calorimeters are not as powerful for particle identification. For many analyses, such as that contained in this thesis and Higgs decaying via ZZ , leptons in this lower energy range are critical for maintaining good sensitivity. However, transition radiation is unable to separate prompt electrons from “background” electrons coming from photon conversion and heavy-flavor decays, the latter of which are not desirable for most physics searches and measurements.

The simplest way to exploit the increased energy deposits from absorption of TR (example shown in Figure 4.3) is to utilize the high-threshold of the TRT (see Section 3.1.3). However, hadrons may still produce some hits that pass the high-threshold by virtue of large energy deposits in the Landau

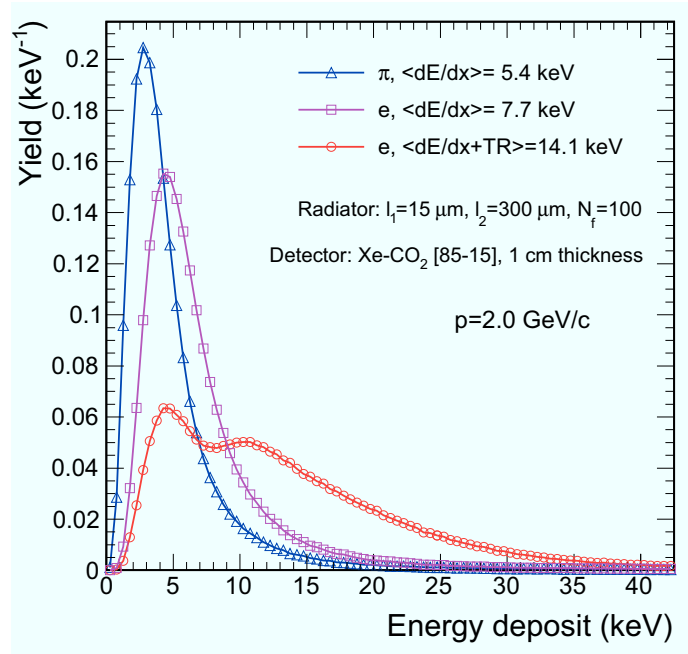


Figure 4.3: Distribution of energy deposits for pions, electrons without TR, and electrons producing TR for a single measurement. Large energy deposits are more likely to have come from electrons, but the Landau shape of the pion distribution means that some pions would also deposit energy comparable with electrons. The large number of measurement points in the TRT allows for better discrimination than a single measurement. Figure taken from Ref. [55].

tail. Thus, on a hit by hit basis, it is impossible to tell whether the large energy deposit is due to absorption of a TR photon or not. However, because of the large number of measurement points in the TRT (usually 30 or more), the ratio of hits passing the high-threshold to total hits on a track provides a good discriminant between electrons and hadrons. This quantity, known as either the high-threshold ratio or the high-threshold fraction, is shown in Figure 4.4 for a selection of electrons and pions.

Another way of showing the characteristic production and detection of TR in the Atlas detector is using the so-called “turn-on curves”, plotting the high-threshold probability against the Lorentz gamma factor. Here high-threshold probability is defined as an ensemble quantity of the ratio of total high-threshold hits to all hits summed over all tracks; that is, it is not a track quantity. In

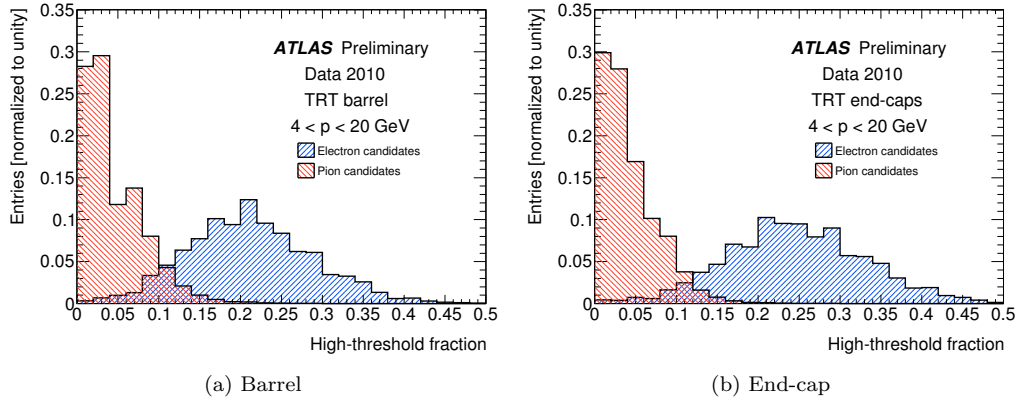


Figure 4.4: Distribution of fraction of TRT high-threshold hits over total hits for electrons in blue and pions in red. Good separation is observed between the two samples in both the TRT barrel and end-caps.

order to traverse a large range of values of Lorentz gamma factors, multiple particle types are used, such that even though their energy distribution are similar, their unique masses provide coverage over a large range of Lorentz gamma. Figure 4.5 shows the turn-on curves for different areas of the TRT detector, utilizing pions for low values of Lorentz gamma and electrons from conversions and Z boson decays for high values of Lorentz gamma. The pion candidates are observed to have a very low probability of having a high-threshold hit, just around 5%, slightly increasing with particle energy as expected. The rapid rise of the high-threshold probability around $\gamma = 1000$, indicates the onset of TR production in the energy range that can be detected by the Xenon gas. The rise then generally levels off and plateaus somewhere above $\gamma = 10^4$. The turn-on curves are divided into five different regions in η , comprising the three different radiator types in the TRT (Barrel, A-wheels, and B-wheels) and the overlap between them.

4.1.3.1 Quantifying Pion Rejection

The ability to separate electrons from hadrons is used in the Atlas electron identification as a cut on the minimum fraction of high-threshold hits to total hits. The values used for such a cut are shown in Table 4.2, where the values given for the plus plus menu reflect a optimization of the cut

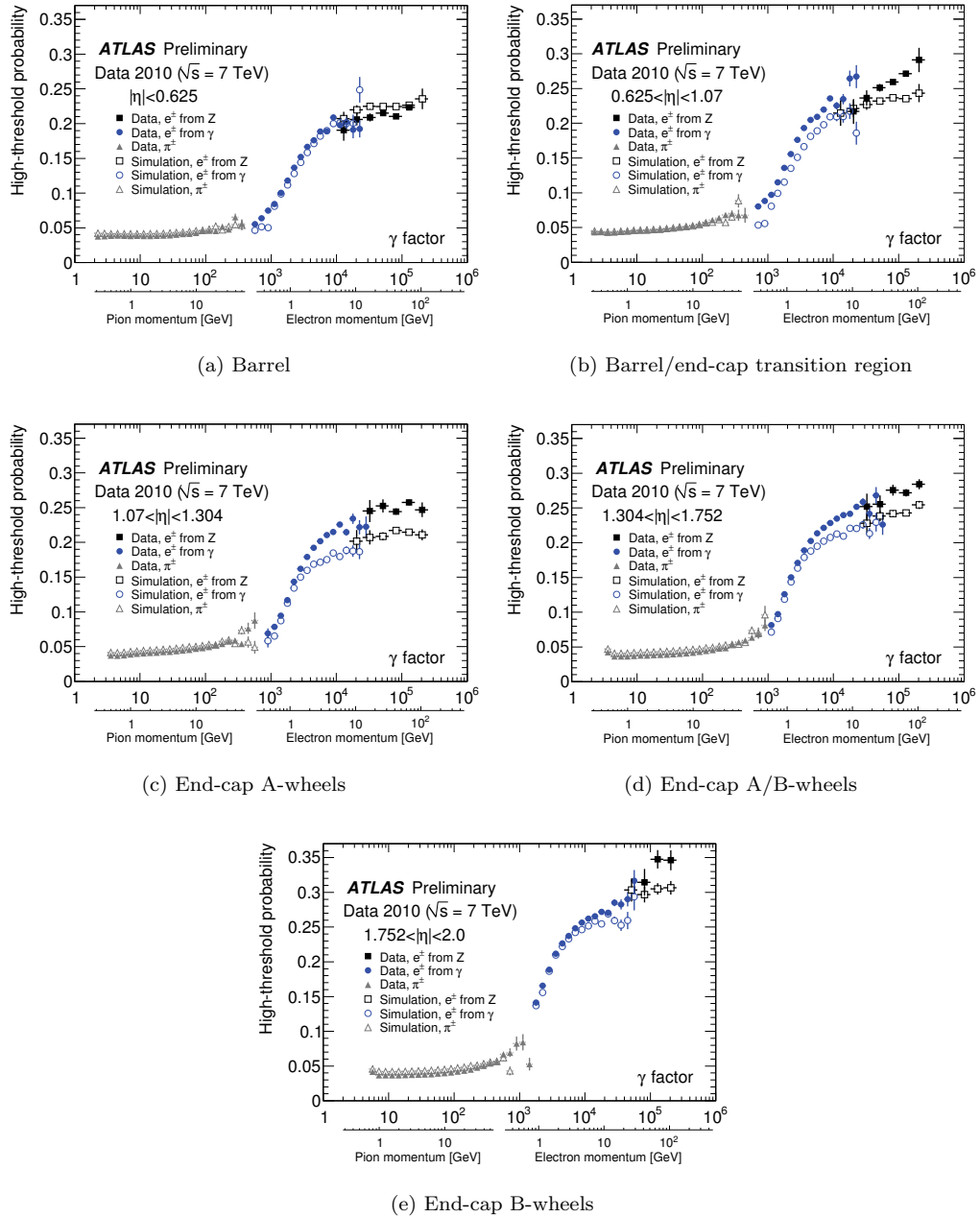


Figure 4.5: TRT high-threshold turn-on curves as observed in the 2010 dataset for five different regions of η . Pions are taken from generic tracks and electrons from both photon conversions and $Z \rightarrow ee$ decays.

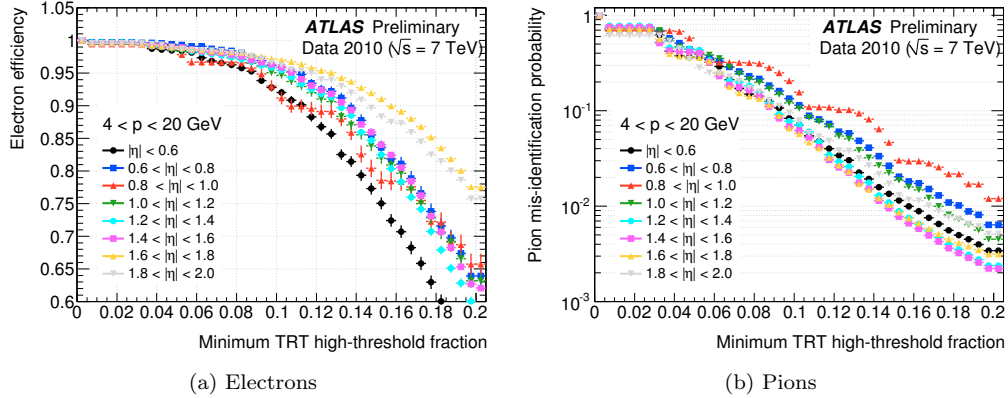


Figure 4.6: The efficiency for electron and pion candidates to pass a varying cut on high-threshold ratio for multiple η regions measured in 2010 data. The steps in the transition region at $0.8 < |\eta| < 1.0$ are due to the discrete distribution of the number of HT hits on track in the region where the spread in the number of all hits on tracks is small.

values. These cut values were changed in order to reflect the change in hardware settings described in Sec. 4.1.3.2 and implemented for data-taking in 2012. The *Medium* ++ cuts were chosen to be more than 98% efficient for electrons and the *Tight* ++ cuts chosen to be more than 95% efficient.

The efficiency for both electrons and pion candidates to pass a varying cut on high-threshold ratio is shown in Figure 4.6 for several different η regions. The two plots are combined in Figure 4.7, showing both the efficiencies as a function of one another and pion mis-id probability (rejection factor⁻¹) as a function of η for a fixed benchmark of 90% electron efficiency, as typically done for most TRDs.

$ \eta $ Range	HT ratio cut value		
	Tight	Medium++	Tight++
0 → 0.625	0.085	0.08	0.105
0.625 → 1.07	0.085	0.075	0.11
1.07 → 1.304	0.115	0.09	0.125
1.304 → 1.752	0.13	0.105	0.145
1.752 → 2.0	0.155	0.11	0.16

Table 4.2: Current high-threshold cut values for isEM tight electron selection (2010) and *medium* ++ and *tight* ++ (2012)

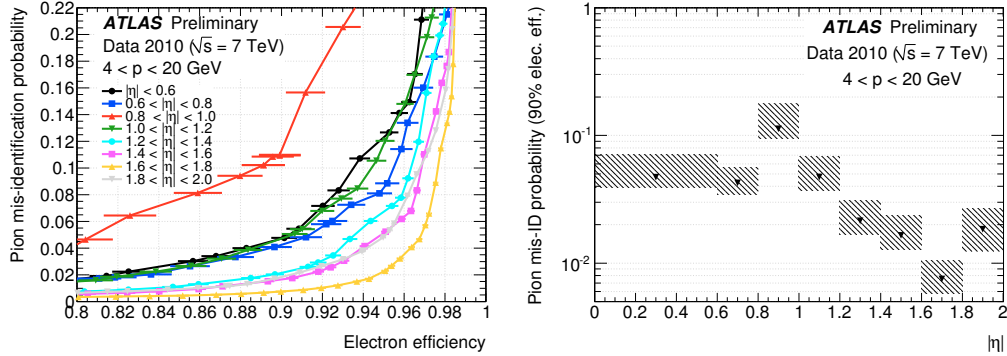


Figure 4.7: Pion misidentification probability as a function of electron efficiency for several different η regions and as a function of η for the set benchmark of 90% electron efficiency.

4.1.3.2 Validating Hardware High-threshold Settings

High-thresholds are set on the ASDBLR chip by selecting a setting for the Digital to Analog Converter (DAC counts), which vary by steps of about 60 eV. For the beginning of data-taking in 2009 and 2010, the high-thresholds across the detector were set to the value giving the best performance during the combined test beam, and adjusted to correct for variations in ground offsets.

In order to validate that the high-threshold setting in hardware was set to the optimal value, a dedicated run during July 2010 took data with varying hardware settings. Collecting a total integrated luminosity of 20 nb^{-1} , six different hardware settings were used: nominal, ± 15 DAC counts from nominal, ± 25 DAC counts from nominal, and -8 DAC counts from nominal. An electron trigger with a low energy threshold and very loose identification requirements was utilized in order to facilitate the collection of electron candidates from photon conversions. The results are shown in Figure 4.8, demonstrating the dependence of the high-threshold probability on hardware setting for identified electron and pion candidates.

To select the optimal hardware operating point, a further analysis determining the pion-rejection power for each of the DAC count settings in different η regions was performed. As described in Section 4.1.3, a cut on high-threshold fraction is utilized giving 90% electron efficiency is used, and the pion misidentification probability ($p_{\pi \rightarrow e}$) is plotted in Figure 4.9. For every η region, the

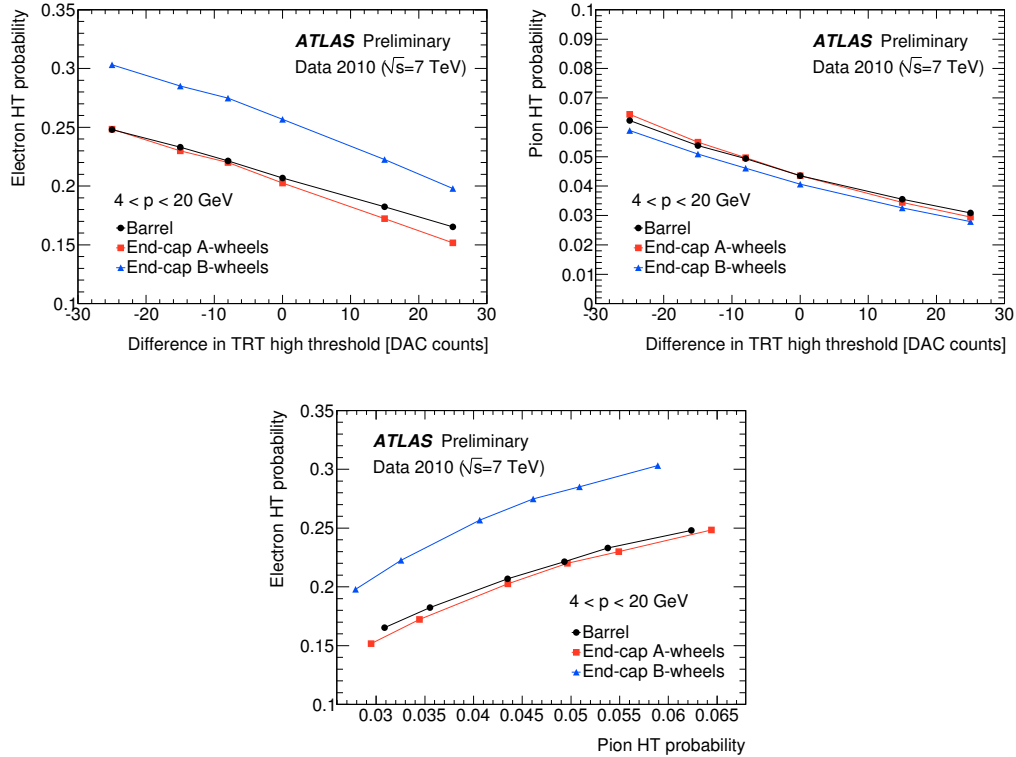


Figure 4.8: Results from special runs with differing TRT high-threshold hardware settings

performance of the TRT pion rejection is approximately constant for the nominal setting of 2010 and lower values, while it degrades for higher settings (higher values of $p_{\pi \rightarrow e}$). Based on this study, it was recommended that the hardware thresholds be lowered slightly, in order to ensure stable particle identification performance. Doing so, allows confidence that any slight operational problem, such as varying gas gain, would not cause the effective performance to degrade by ensuring that the hardware is set firmly near the center of the “plateau” of optimal performance.

4.2 Identification of Muons

A muon’s interaction within the Atlas detector is often much simpler than other particle types. As charged particles, they will leave tracks in both the Inner Detector and Muon Spectrometer, but minimal energy deposits in the calorimeters. Because of the large amounts of material in the

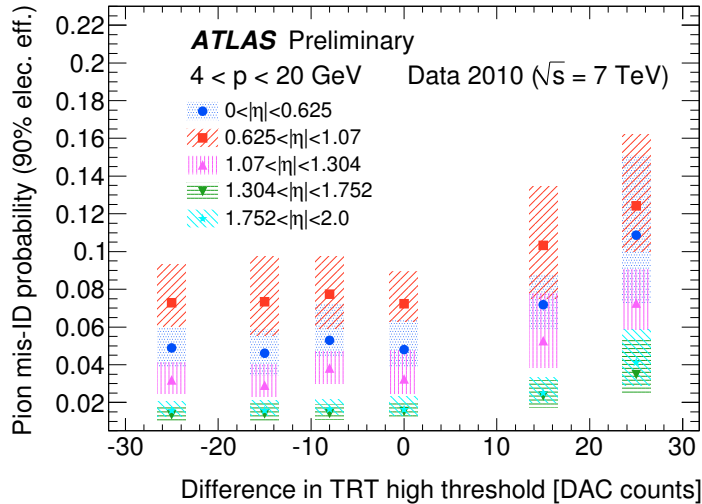


Figure 4.9: Results of the run in summer 2010 with differing TRT high-threshold hardware values. Pion mis-identification probability is plotted for the benchmark of 90% electron efficiency for a cut on high-threshold fraction. Performance is seen to be stable for the nominal hardware setting and for lower values, while performance decreases for higher threshold settings.

calorimeters, muons are typically the only standard model particles to interact in the MS³. Due to this fact, identification of muons is more straightforward than for electrons, and their backgrounds tend to come from non-prompt muons coming from heavy-flavor decays or decays in flight of pions and kaons.

Reconstruction of muons begins with track finding separately in the ID and the MS. In the MS, the algorithms for track-finding are referred to as “stand-alone” muons and start by building track segments from hits in each of the three muon stations. The segments from each of the stations are then combined to form stand-alone tracks, which are then extrapolated back into the other Atlas sub-detectors, applying corrections to account for multiple scattering and energy-loss in the calorimeters. In the ID, the standard tracking algorithm is used as with other particle types. Tracks in the ID and the MS are then matched and a χ^2 test is performed to determine the best pairings, forming a “combined track”.

An additional search for “tagged” muons is performed starting with energetic tracks in the ID.

³Neutrinos will also reach and, in fact, escape the MS, but do not interact, their presence can only be inferred by an imbalance of momentum, explained further in Section 4.4

These tracks are projected into the first station of the muon system and nearby track segments are searched for.

4.3 Identification of Jets

Due to color confinement, strongly-charged particles (quarks and gluons) do not propagate individually through the Atlas detector. Instead, they undergo a process called “hadronization”, where the additional production of quark-antiquark pairs is more energetically favorable in QCD. This process produces complicated collections of colorless particles: mesons and baryons plus their decay products, traveling roughly in the initial direction of the colored particle. These groups of particles are referred to as “jets” and are the reconstructable physics object in the detector, not the initiating quark or gluon. However, the jet objects are able to give some information about the initial quark or gluon.

Jets are reconstructed from energy clusters in the calorimeter using the anti- k_t algorithm [59], using the distance parameter $R = 0.4$. The energy of these reconstructed jets are calibrated, usually referred to as “Jet Energy Scale” (JES) and “Jet Energy Resolution” (JER). For this analysis, there are no final state quarks or gluons, so many events should have no jets. However, the presence of a single jet resulting from initial state radiation is also used for discrimination by boosting the SUSY system, see Sections 8.4.2 and 8.4.3.

Because of the complicated nature of jets, whether the initiating particle is a gluon or a specific flavor quark can not be determined easily, with the exception of initiating b-quarks. Because of their relatively long-life times, B-hadrons typically travel a few millimeters before decaying. This decay can lead to a “secondary vertex” several millimeters transverse to the beamline, a distance which can be resolved by the Atlas tracking system. Dedicated algorithms are used to identify jets consistent with having a secondary vertex and other properties consistent with jets initiated from a B-hadron, called “b-tagging”. The most commonly used b-tagging algorithm in Atlas is a multivariate discriminant called MV1. In this analysis, vetoing events with one or more b-tagged

jets is useful in reducing possible backgrounds from $t\bar{t}$ or single-top events, which can also produce high p_T isolated leptons.

4.4 Identification of Missing Transverse Energy

Particles that can not be directly detected by Atlas can be inferred by an imbalance in momentum. In a hadron collider like the LHC, the objects colliding are the constituent quarks or gluons of the protons, which may have an unknown boost along the beam axis (the z-direction). Because of this unknown initial condition, momentum balance can not be computed along this direction, and so instead, only the components transverse to the beamline are considered. Any possible imbalance is referred to as “missing transverse energy” or E_T^{miss} .

In the Standard Model, the only particles which would give rise to E_T^{miss} are neutrinos, which escape the detector. In BSM scenarios, E_T^{miss} can also be a sign of possible new particles. In this search, E_T^{miss} arises from the two LSPs, which will be stable and traverse the detector without interacting.

The starting point for E_T^{miss} calculations begins by simply taking the vector sum of p_T for all the calorimeter clusters and muons. Better estimates of E_T^{miss} take into account calibrations for identified high-level objects (electrons, photons, jets, etc.), separately for each particle type. Care must be taken to remove possible sources of fake E_T^{miss} arising from hot or dead detector channels or inactive regions of the detector (i.e. “cracks” between detector elements). Many variations of the E_T^{miss} variable exist based on the requirements of the constituent objects in the calculation.

This analysis uses MET_Egamma10NoTau. This E_T^{miss} definition includes contributions from electrons passing medium identification level with $p_T > 10$ GeV, tight photons with $p_T > 10$ GeV, jets with $p_T > 20$ GeV and muons with $p_T > 10$ GeV. Additional corrections, known as “soft terms” are computed from clusters and tracks which are not associated to any reconstructed objects. The hadronic taus are included either in the jet term or in the soft term, not calibrated separately.

CHAPTER 5

Analysis Motivation

There have been several previous searches for the direct production of supersymmetric charginos and neutralinos, in Atlas in the 3 Lepton channel [1] and the 2 Lepton opposite-sign channel [60] and similarly in CMS [61]. Particularly in the case of the trilepton search, strong limits have been placed on much of the allowed parameter space accessible during Run 1 of the LHC. However, some regions do remain difficult for the existing analyses to consider. It is the goal of this thesis analysis to specifically target these remaining regions still allowable.

Searches for weakly-produced SUSY generally concentrate on three production diagrams: pair production of $\tilde{\chi}_1^\pm$ and $\tilde{\chi}_2^0$, pair production of $\tilde{\chi}_1^+$ and $\tilde{\chi}_1^-$, or pair production of $\tilde{\ell}^+$ and $\tilde{\ell}^-$. Of these, the production of $\tilde{\chi}_1^\pm \tilde{\chi}_2^0$ is particularly attractive as it has the highest cross section of the group and its decay products provide up to three high p_T leptons to allow triggering on the event and separation from background.

As will be further explained in Chapter 6, there are two main modes of decay for the $\tilde{\chi}_1^\pm \tilde{\chi}_2^0$ pair. In the first scenario, the $\tilde{\chi}_1^\pm$ decays to a W boson and $\tilde{\chi}_1^0$ (the LSP), while the $\tilde{\chi}_2^0$ decays to a Z boson and $\tilde{\chi}_1^0$. When both resulting bosons decay leptonically, a final state signature with three energetic leptons plus E_T^{miss} from the two LSPs results. The Feynman diagram for this process is shown in the left of Figure 5.1. This diagram is of particular interest as it requires no additional SUSY particles to have small masses, only the gauginos. The current limits for this scenario from the trilepton analysis is shown in the right of Figure 5.1. The limits cover much of the $\tilde{\chi}_1^\pm, \tilde{\chi}_1^0$ parameter

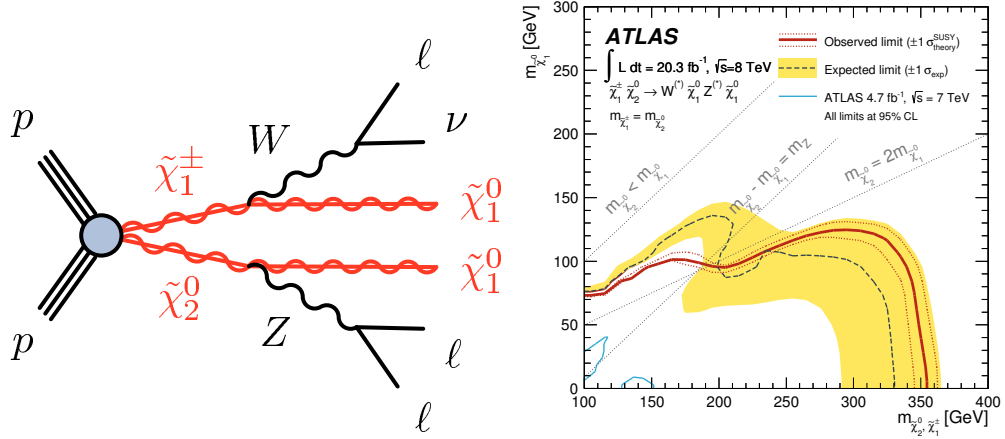


Figure 5.1: Feynman diagram for $\tilde{\chi}_1^\pm \tilde{\chi}_2^0$ decaying via W and Z bosons (left) and previous limits on this signature from the three lepton search[1]

space, extending up to nearly 350 GeV limits on the $\tilde{\chi}_1^\pm$ mass⁴ in the case of low mass $\tilde{\chi}_1^0$. However, in the region of parameter space where the mass of the $\tilde{\chi}_1^0$ is close to that of $\tilde{\chi}_1^\pm$, about 40 – 50 GeV less than the W or Z mass, the intermediate vector bosons will be produced off-shell⁵. This region is also often referred to as a “compressed scenario”, due to the low mass splitting. In such an instance, one or more of the resulting leptons from the vector boson decays will generally be low p_T , and often fail to be reconstructed or identified, resulting in a final state with less than 3 leptons. In the case that only one of the leptons from the Z decay is lost, the remaining lepton pair could be either same-sign or opposite-sign. The Atlas 2 lepton opposite sign analysis can be interpreted for this scenario. However, in order to reduce these large SM backgrounds, the two leptons are required to have $m(\ell\ell)$ within 10 GeV of the Z mass, in other words, requiring that the Z is on-shell. This requirement eliminates any possibility that a 2 lepton opposite-sign analysis could be useful in the compressed region as can be seen in the left plot of Figure 5.3. Instead, the same-sign signature is preferred to the oppositely charged two lepton signature due to its drastically lower backgrounds.

In the second decay scenario of the $\tilde{\chi}_1^\pm \tilde{\chi}_2^0$ pair, the superpartners of the leptons are additionally

⁴For the rest of this thesis, the mass of the $\tilde{\chi}_1^\pm$ and $\tilde{\chi}_2^0$ is assumed to be degenerate, and the common mass will generally be referred to as $m_{\tilde{\chi}_1^\pm}$

⁵The region $m_{\tilde{\chi}_1^\pm} \geq m_{\tilde{\chi}_1^0}$, indicated by the top diagonal line on Figure 5.1, is forbidden by construction as the neutralinos are numbered by their mass.

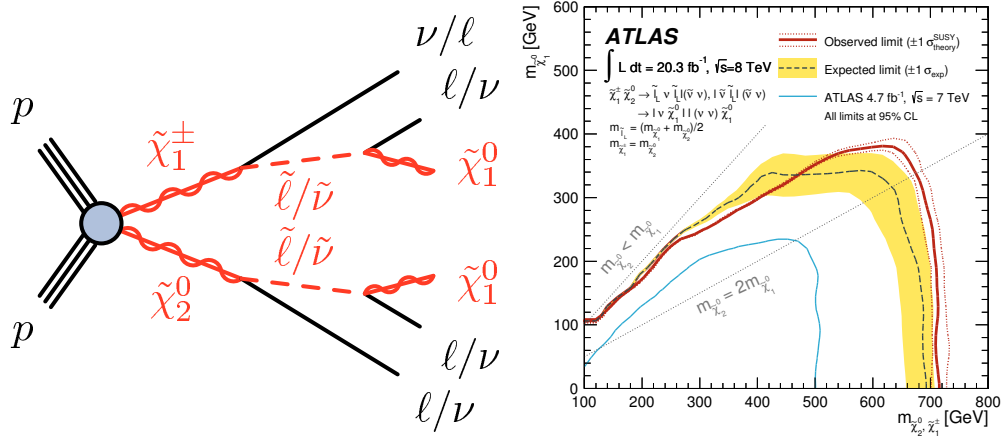


Figure 5.2: Previous limits on the direct production of $\tilde{\chi}_1^\pm$ $\tilde{\chi}_2^0$, decaying via W and Z bosons

assumed to be low mass (< 1 TeV). This allows the $\tilde{\chi}_1^\pm$ to decay either to a charged slepton and a neutrino, or to a sneutrino and a charged lepton. The $\tilde{\chi}_2^0$ is similarly allowed to decay to either a charged slepton and charged lepton, or a sneutrino and neutrino. The slepton (sneutrino) then subsequently decays to a charged lepton (neutrino) and $\tilde{\chi}_1^0$. In the case where the $\tilde{\chi}_2^0$ decays via the charged particles, the final state again has three leptons and 2 LSPs. This decay is shown in the Feynman diagram in Figure 5.2, along with the tripleton limits for this diagram. In comparison to the decays via W and Z bosons, the tripleton analysis is able to exclude a much larger region of parameter space (note the differing axes ranges between the two plots), with limits > 700 GeV for low mass $\tilde{\chi}_1^0$. This is primarily due to the increased branching fraction to charged leptons for the intermediate SUSY particles compared with the low branching fractions to charged leptons for the vector bosons ($\sim 11\%$ for the $W \rightarrow l\nu$, and $\sim 3\%$ for the $Z \rightarrow \ell\ell$). Full details on the assumptions on the branching fractions are given in Chapter 6. Additionally, the tripleton limits are able to approach the region near the $m_{\tilde{\chi}_1^\pm} = m_{\tilde{\chi}_1^0}$ diagonal much closer than in the vector boson case. Here, the tripleton search is able to exclude a mass splitting between $\tilde{\chi}_1^\pm$ and $\tilde{\chi}_1^0$ of 10 GeV for 100 GeV $\tilde{\chi}_1^\pm$ up to ~ 25 GeV splittings for 200 GeV $\tilde{\chi}_1^\pm$. In this region, the intermediate slepton mass is halfway between the $\tilde{\chi}_1^\pm$ and $\tilde{\chi}_1^0$ mass, allowing a reasonable amount of energy available to their decay products, even in the compressed region.

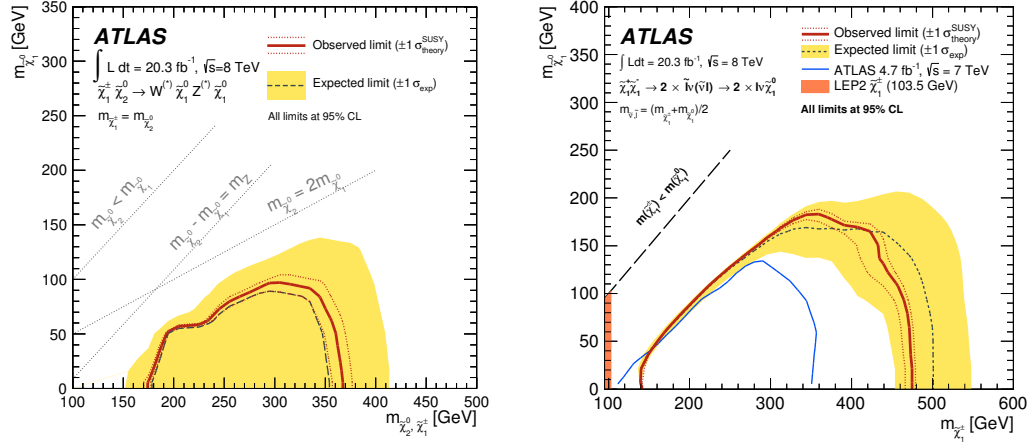


Figure 5.3: Previous limits on the direct production of $\tilde{\chi}_1^\pm \tilde{\chi}_2^0$, decaying via W and Z bosons (left) and sleptons (right) from the 2L opposite-sign analysis. The two lepton opposite-sign searches are not able to extend the trilepton search in the compressed region.

However, the mass of the intermediate slepton being exactly halfway between the two gaugino masses is an additional assumption of the model; there is no necessity for such a requirement. If the mass of the intermediate slepton is instead allowed to vary, the analysis acceptance, and thus the exclusion regions, can change. An example of this is shown for a similar situation in the 2L opposite sign analysis in Figure 5.4, with acceptance rates lowered by roughly 30% (relative) for slepton masses closer to the $\tilde{\chi}_1^\pm$ mass. In such an instance, there is again a compressed mass spectrum, this time between the gaugino and the slepton, rather than between two gauginos. Similarly to the first scenario, the selection criteria used in the two lepton opposite sign analysis renders it unable to contribute in a compressed scenario. This can be seen in the right plot of Figure 5.3. Again, a dedicated same-sign lepton search can be used to complement the three lepton search.

One limitation of this analysis constructed as a complement to the existing trilepton analysis is that in order to be easily combined, the two analyses must not have any event overlap between them. Practically, this means that the same-sign analyses must be exclusive in lepton number. Because of this requirement and the fact that the separation based on number of leptons is done at a fairly early stage of event selection, there are could unfortunately be events that are not considered by either analysis.

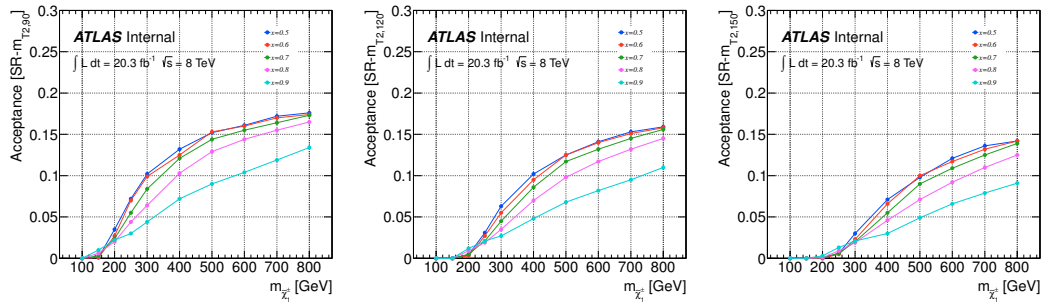


Figure 5.4: Effect of varying the intermediate slepton mass on acceptance for the 2L opposite sign analysis. The assumption that the slepton is halfway between the $\tilde{\chi}_1^\pm$ and $\tilde{\chi}_1^0$ maximizes the analysis acceptance for the majority of phase space.

CHAPTER 6

Signal Models

Like previous analyses searching for weakly-produced SUSY, this search utilizes simplified models for optimization and interpretation of the results [62][63]. Simplified models are not full Supersymmetric models, but deliberately reduce the large number of free parameters to only a relevant few, usually the masses of the new SUSY particles involved in the decay. The goal is to reproduce the relevant kinematics and particle multiplicities of the SUSY decay, and provide a framework for possible early discoveries, without the overhead of a full SUSY model.

For this analysis, we concentrate on simplified models involving the direct pair production of $\tilde{\chi}_1^\pm$ and $\tilde{\chi}_2^0$. For these simplified models, the most relevant parameters are the masses of the $\tilde{\chi}_1^\pm$ and the $\tilde{\chi}_2^0$, which are assumed to be degenerate, the mass of any intermediate SUSY particles, and the mass of the LSP. The mixing matrix that determines whether the gauginos are bino-like, wino-like or higgsino-like is an addition assumption, which would affect the cross-section and the branching fractions, but not the event kinematics.

The direct pair production of $\tilde{\chi}_1^\pm$ and $\tilde{\chi}_2^0$ are considered in two different scenarios. In the first scenario, the $\tilde{\chi}_1^\pm$ and $\tilde{\chi}_2^0$ are allowed to decay via $\tilde{\ell}_L$ (1/6 branching fraction to each $\tilde{e}_L, \tilde{\mu}_L, \tilde{\tau}_L, \tilde{\nu}_e, \tilde{\nu}_\mu, \tilde{\nu}_\tau$). The mass of sleptons and sneutrinos are assumed to be degenerate and their mass relative to the masses of the $\tilde{\chi}_1^\pm$ (or $\tilde{\chi}_2^0$) and the $\tilde{\chi}_1^0$ is given by $m_{\tilde{\nu}_\ell} = m_{\tilde{\ell}_L} = x \times m_{\tilde{\chi}_1^\pm} + (1-x) \times m_{\tilde{\chi}_1^0}$.

Previous searches involving this decay, as mentioned in Chapter 5, have interpreted their results assuming that the intermediate slepton has a mass exactly halfway between the $\tilde{\chi}_1^\pm$ or $\tilde{\chi}_2^0$ and the

LSP, also referred to as $x=0.5$ or 50%. This assumption emphasizes final decays containing three reconstructed leptons that can be discovered via searches such as in [1] by maximizing the energy available to the final state particles. Signal models using these assumptions are listed in Tables 6.1 and 6.2, giving the masses of the SUSY particles, the expected cross section and its uncertainty.

However, if this assumption for the value of x is changed in either direction, a greater fraction of events will include at least one lepton that has a low p_T and is not reconstructed. Such scenarios could escape previous search limits. This analysis concentrates on a signal model where there is such a small mass splitting between the slepton and $\tilde{\chi}_1^\pm$ ($x = 0.95$). An entire new simplified model grid in $m_{\tilde{\chi}_1^0}, m_{\tilde{\chi}_1^\pm}$ plane was produced to evaluate this scenario. These signal models are shown in Table 6.3. Scenarios where the mass difference between the slepton and the LSP is small (such as $x=0.05$) were also considered, but in this situation for $\tilde{\chi}_1^\pm$ masses accessible currently, the sleptons have low masses that are ruled out by direct slepton searches at LEP[64] or the LHC[60].

In the second scenario for the decay of the $\tilde{\chi}_1^\pm, \tilde{\chi}_2^0$ pair, the slepton and sneutrino masses are assumed to be very heavy, and thus inaccessible for the decay of the gauginos. The $\tilde{\chi}_1^\pm$ and $\tilde{\chi}_2^0$ therefore decay via W and Z bosons (respectively). Because of the low branching fraction to leptons for the W and Z boson, this decay is less sensitive than the decays via sleptons. Additionally, for this search, the kinematics of the decay tend not to favor a same-sign dilepton reconstructed final state. In this scenario, unlike the compressed slepton scenario, one of the leptons from the Z decay is not preferentially lost. Because of its slightly higher mass than the W, the leptons from the Z will also be slightly more energetic. Additionally, the Vector-Axial weak decay of the W prefers the charged lepton to be softer than the neutrino, leading to a higher likelihood of it failing to be reconstructed. However, This scenario is still considered in order to be combined with the stronger trilepton analysis to maximize discovery potential or limit setting ability. These signal models are shown in Tables 6.4 and 6.5.

In principle, the vector bosons in the decay diagram could also be replaced by Higgs (of which there are at minimum 5 in SUSY). Due to the varied decay possibilities of the Higgs bosons, they

are not considered as intermediate particles in this analysis. Instead, dedicated searches for weakly produced SUSY involving the new discovered Higgs Boson in the decay are presented in [65].

For all simplified models, the mass of the $\tilde{\chi}_1^\pm$ and $\tilde{\chi}_2^0$ are assumed to be degenerate and the particles assumed to be pure wino. The $\tilde{\chi}_1^0$ is assumed to be pure bino.

Signal cross sections in all tables are calculated to next-to-leading order in the strong coupling constant (NLO) using PROSPINO2 [66]. They are in agreement with the NLO calculations matched to resummation at the next-to-leading logarithmic accuracy (NLO+NLL) within $\sim 2\%$ [67, 68]. Signal processes are generated using HERWIG++ 2.5.2 [69].

Table 6.1: Cross-section and Relative uncertainty for simplified model with sleptons $x=0.50$. $\tilde{\chi}_1^\pm$ and $\tilde{\chi}_2^0$ are assumed to be mass degenerate and pure wino. The $\tilde{\chi}_1^0$ is the LSP and is assumed to be pure bino.

Dataset id	$m_{\tilde{\chi}_1^\pm}$ [GeV]	$m_{\tilde{\chi}_1^0}$ [GeV]	Cross-Section [pb]	Relative Uncertainty
179578	117.5	82.5	6.223	0.072
179579	142.5	107.5	2.983	0.065
179580	192.5	157.5	0.933	0.064
179581	135	115	3.667	0.068
179582	185	165	1.090	0.065
179583	260	240	0.273	0.067
144871	112.5	12.5	7.326	0.073
144873	130	30	4.244	0.068
144874	155	5	2.160	0.064
144876	150	50	2.453	0.067
144877	175	25	1.353	0.066
144879	175	75	1.353	0.066
144880	200	50	0.802	0.065
144883	225	125	0.501	0.064
144881	250	0	0.323	0.069
144884	250	100	0.323	0.069
144885	300	50	0.148	0.067
144888	300	200	0.148	0.067
144889	325	175	0.104	0.072
144886	350	0	0.074	0.072
144890	375	125	0.055	0.076
144891	425	75	0.030	0.079
144894	425	325	0.030	0.079
144895	450	300	0.022	0.084
144892	500	0	0.013	0.084
144896	500	250	0.013	0.084
157461	550	200	0.008	0.085
157464	625	125	0.004	0.088
157467	750	0	0.001	0.093

Table 6.2: Cross-section and Relative uncertainty for additional simplified models with sleptons $x=0.50$. $\tilde{\chi}_1^\pm$ and $\tilde{\chi}_2^0$ are assumed to be mass degenerate and pure wino. The $\tilde{\chi}_1^0$ is the LSP and is assumed to be pure bino.

Dataset id	$m_{\tilde{\chi}_1^\pm}$ [GeV]	$m_{\tilde{\chi}_1^0}$ [GeV]	Cross-Section [pb]	Relative Uncertainty
157957	267.5	232.5	0.245	0.067
157958	392.5	357.5	0.044	0.076
157959	517.5	482.5	0.011	0.085
157960	550	450	0.008	0.085
157961	575	425	0.006	0.085
157962	625	375	0.004	0.088
157963	675	325	0.002	0.089
157964	750	250	0.001	0.093
157965	642.5	607.5	0.003	0.090
157966	675	575	0.002	0.089
157967	700	550	0.002	0.096
157968	750	500	0.001	0.093
176531	110	90	7.983	0.074
176535	455	420	0.021	0.082
176536	112.5	47.5	7.326	0.073
176537	132.5	67.5	3.945	0.072
176538	157.5	92.5	2.042	0.069
176539	207.5	142.5	0.693	0.064
176540	282.5	217.5	0.193	0.067
176541	407.5	342.5	0.036	0.078
176542	470	405	0.018	0.082
176543	532.5	467.5	0.009	0.086
176544	562.5	312.5	0.007	0.088
176545	487.5	387.5	0.015	0.085
176546	512.5	362.5	0.011	0.085
176547	612.5	262.5	0.004	0.090
176548	800	450	0.001	0.094
176549	687.5	187.5	0.002	0.091
176550	875	375	0.001	0.098
176551	625	0	0.004	0.088
176552	687.5	62.5	0.002	0.091
176553	750	125	0.001	0.093
176554	812.5	187.5	0.001	0.097
176555	812.5	62.5	0.001	0.097
176556	875	125	0.001	0.098
176557	875	0	0.001	0.098

Table 6.3: New signal samples used in 2LSS analysis : simplified model with sleptons $x=0.95$. $\tilde{\chi}_1^\pm$ and $\tilde{\chi}_2^0$ are assumed to be mass degenerate and pure wino. The $\tilde{\chi}_1^0$ is the LSP and is assumed to be pure bino.

Dataset id	$m_{\tilde{\chi}_1^\pm}$ [GeV]	$m_{\tilde{\chi}_1^0}$ [GeV]	Cross-Section [pb]	Relative Uncertainty
186283	117.5	82.5	6.223	0.072
186284	135	115	3.667	0.068
186285	142.5	107.5	2.983	0.065
186287	192.5	157.5	0.933	0.064
186288	260	240	0.273	0.067
186289	110	90	7.983	0.074
186296	157.5	92.5	2.042	0.069
186300	207.5	142.5	0.693	0.064
186301	225	125	0.501	0.064
186302	250	0	0.323	0.069
186303	250	100	0.323	0.069
186304	267.5	232.5	0.245	0.067
186305	282.5	217.5	0.193	0.067
186306	300	200	0.148	0.067
186307	300	50	0.148	0.067
186308	325	175	0.104	0.072
186309	350	0	0.074	0.072
186310	375	125	0.054	0.076
186311	392.5	357.5	0.044	0.076
186312	407.5	342.5	0.036	0.078
186313	425	325	0.030	0.079
186314	425	75	0.030	0.079
186315	450	300	0.022	0.084
186319	500	0	0.013	0.084
186320	500	250	0.013	0.084
186322	517.5	482.5	0.011	0.085
186323	532.5	467.5	0.009	0.086
186324	550	200	0.008	0.085
186325	550	450	0.008	0.085
186327	575	425	0.006	0.085
186328	612.5	262.5	0.004	0.089
186330	625	125	0.004	0.088
186331	625	375	0.004	0.088
186332	642.5	607.5	0.003	0.090
186334	675	575	0.002	0.089
186335	687.5	187.5	0.002	0.091
186336	687.5	62.5	0.002	0.091
186340	750	250	0.001	0.093
186341	750	500	0.001	0.093

Table 6.4: Cross-section and Relative uncertainty for Simplified models with WZ bosons. $\tilde{\chi}_1^\pm$ and $\tilde{\chi}_2^0$ are assumed to be mass degenerate and pure wino. The $\tilde{\chi}_1^0$ is the LSP and is assumed to be pure bino. Cross sections do not include the branching fraction to leptons.

Dataset id	$m_{\tilde{\chi}_1^\pm}$ [GeV]	$m_{\tilde{\chi}_1^0}$ [GeV]	Cross-Section [pb]	Relative Uncertainty
127994	100	75	11.484	0.075
127995	125	100	4.911	0.069
127996	200	150	0.802	0.065
164274	100	0	11.484	0.075
164275	100	50	11.484	0.075
164276	150	0	2.456	0.067
164277	150	50	2.453	0.067
164278	150	100	2.453	0.067
164279	200	0	0.802	0.065
164280	200	50	0.802	0.065
164281	200	100	0.802	0.065
164282	200	150	0.802	0.065
164283	250	0	0.323	0.069
164284	250	50	0.323	0.069
164285	250	100	0.323	0.069
164286	250	150	0.323	0.069
164287	250	200	0.323	0.069
164288	300	0	0.148	0.067
164289	300	50	0.148	0.067
164290	300	100	0.148	0.067
164291	300	150	0.148	0.067
164292	300	200	0.148	0.067
164293	300	250	0.148	0.067

Table 6.5: Cross-section and Relative uncertainty for additional simplified models with WZ bosons. $\tilde{\chi}_1^\pm$ and $\tilde{\chi}_2^0$ are assumed to be mass degenerate and pure wino. The $\tilde{\chi}_1^0$ is the LSP and is assumed to be pure bino. Cross sections do not include the branching fraction to leptons.

Dataset id	$m_{\tilde{\chi}_1^\pm}$ [GeV]	$m_{\tilde{\chi}_1^0}$ [GeV]	Cross-Section [pb]	Relative Uncertainty
164294	350	0	0.074	0.072
164295	350	50	0.074	0.072
164296	350	100	0.074	0.072
164297	350	150	0.074	0.072
164298	350	200	0.074	0.072
164299	350	250	0.074	0.072
164300	350	300	0.074	0.072
164301	400	0	0.034	0.078
164302	400	50	0.040	0.078
164303	400	100	0.040	0.078
164304	400	150	0.040	0.078
164305	400	200	0.040	0.078
164306	400	250	0.040	0.078
164307	400	300	0.040	0.078
164308	400	350	0.040	0.078
164309	450	0	0.022	0.084
164310	450	50	0.022	0.084
164311	450	100	0.022	0.084
164312	450	150	0.022	0.084
164313	450	200	0.022	0.084
164314	450	250	0.022	0.084
164315	450	300	0.022	0.084
164316	450	350	0.022	0.084
164317	450	400	0.022	0.084
164318	500	0	0.013	0.084
164319	500	100	0.013	0.084
164320	500	200	0.013	0.084
164321	500	300	0.013	0.084
164322	500	400	0.013	0.084
164323	500	450	0.013	0.084

CHAPTER 7

Background Estimation

There are three major background to a search for same-sign leptons:

- Standard Model same-sign
- Charge misidentification of electrons
- Misidentifying Jets as leptons

Standard model backgrounds from true same-sign events or from three lepton events where one lepton fails to be identified are rare compared with opposite-sign events and are taken from Monte Carlo simulation estimates, described fully in Section 7.1. The possibility for charge misidentification for electrons results in true opposite-sign events being falsely reconstructed as same-sign events. The charge mis-id rates for electrons are measured in data from the Z-peak and used to weight OS data events. The charge misidentification rate for muons is negligible for the lepton p_T range used in this search. This procedure is described further in Section 7.2. Other particle types mis-identified as leptons, as well as non-prompt leptons, also referred to collectively as “fakes”, are estimated using the matrix method with efficiencies and fake rates measured in data with details given in Section 7.3

7.1 Standard Model Same-sign Leptons

The prompt same-sign backgrounds are taken from Monte Carlo simulation using the generators and cross-sections given in Tables 7.1-7.5. The dominant background comes from diboson production,

particularly WZ production where both bosons decay leptonically and one lepton from the Z boson decay is not identified. Smaller contributions come from triboson production (WWW, WWZ, ZZZ), $t\bar{t}$ +Vector boson production, and Higgs production.

For standard model backgrounds using simulated data, generated events are modeled with the Atlas simulation framework [70], using GEANT4 [71] to mimic the digital signals produced by the Atlas detector. Simulated events are then reconstructed using the same software framework used to reconstruct the data directly from the detector, described in Chapter 4.

The estimates are normalized to the best available theory calculations and are subject to theoretical and experimental systematics further described in Section 9.1.

7.1.1 $W/Z + \gamma^*$

In addition to the standard model backgrounds which contain at least 2 real, prompt leptons, events that contain a vector boson (W or Z) produced in association with an isolated photon are also considered using estimates from Monte Carlo background. In this event type, the photon can convert to an electron positron pair and be misidentified as an electron candidate. While normally this class of events should be classified as “fakes”, since there is only one real lepton, the rate at which these photons fake electrons can be quite different than those considered in the matrix method described in Section 7.3. The primary difference comes from these photons being isolated compared with the non-isolated photons considered by the matrix method, as they are generally produced within hadronic jets, for instance from the decay of a π^0 . In addition, the Monte Carlo simulation estimates for these fake processes are better modeled than those including non-isolated photons. Thus, this class of events are taken from the simulation estimates and their expected contribution to matrix method and charge flip backgrounds are subtracted. The datasets used for this estimate are given in Table 7.5.

Table 7.1: Diboson samples used for the analyses. The LO cross-section, k-factors (for NLO normalization) and filter efficiencies are reported. The integrated luminosities corresponding to the total statistics in each sample are also given.

Process (ID)	σ [pb]	k-factor	filter efficiency	$\int \mathcal{L} dt$ [fb $^{-1}$]
ZZ (4e) Powheg (126937)	0.08	1	0.91	8600.6
ZZ (4 μ) Powheg (126938)	0.18	1	0.83	4131.3
ZZ (2e2 μ) Powheg (126939)	0.18	1	0.58	5868.7
ZZ (2 μ 2 τ) Powheg (126940)	0.08	1	0.91	8554.6
ZZ (2e2 τ) Powheg (126941)	0.18	1	0.59	5825.0
ZZ (4 τ) Powheg (126942)	0.08	1	0.11	36813.5
WZ ($e^- \bar{\nu}_e e^+ e^-$) Powheg (129477)	1.41	1.12	0.29	408.5
WZ ($e^- \bar{\nu}_e \mu^+ \mu^-$) Powheg (129478)	0.94	1.12	0.35	512.6
WZ ($e^- \bar{\nu}_e \tau^+ \tau^-$) Powheg (129479)	0.17	1.12	0.17	2325
WZ ($\mu^- \bar{\nu}_\mu e^+ e^-$) Powheg (129480)	1.40	1.12	0.29	412.3
WZ ($\mu^- \bar{\nu}_\mu \mu^+ \mu^-$) Powheg (129481)	0.95	1.12	0.35	505.4
WZ ($\mu^- \bar{\nu}_\mu \tau^+ \tau^-$) Powheg (129482)	0.17	1.12	0.17	2300.6
WZ ($\tau^- \bar{\nu}_\tau e^+ e^-$) Powheg (129483)	1.40	1.12	0.14	336.1
WZ ($\tau^- \bar{\nu}_\tau \mu^+ \mu^-$) Powheg (129484)	0.94	1.12	0.18	395.4
WZ ($\tau^- \bar{\nu}_\tau \tau^+ \tau^-$) Powheg (129485)	0.17	1.12	0.06	1683.5
WZ ($e^+ \nu_e e^+ e^-$) Powheg (129486)	0.98	1.14	0.30	570.7
WZ ($e^+ \nu_e \mu^+ \mu^-$) Powheg (129487)	0.64	1.14	0.35	736.2
WZ ($e^+ \nu_e \tau^+ \tau^-$) Powheg (129488)	0.11	1.14	0.16	3697.9
WZ ($\mu^+ \nu_\mu e^+ e^-$) Powheg (129489)	0.94	1.14	0.30	596.1
WZ ($\mu^+ \nu_\mu \mu^+ \mu^-$) Powheg (129490)	0.65	1.14	0.35	722.8
WZ ($\mu^+ \nu_\mu \tau^+ \tau^-$) Powheg (129491)	0.11	1.14	0.16	3685.5
WZ ($\tau^+ \nu_\tau e^+ e^-$) Powheg (129492)	0.94	1.14	0.15	479.5
WZ ($\tau^+ \nu_\tau \mu^+ \mu^-$) Powheg (129493)	0.64	1.14	0.19	557.2
WZ ($\tau^+ \nu_\tau \tau^+ \tau^-$) Powheg (129494)	0.11	1.14	0.06	2648.4
WW (ee) Powheg (126928)	0.60	1.08	1	277.9
WW (μe) Powheg (126929)	0.60	1.08	1	278.0
WW (τe) Powheg (126930)	0.60	1.08	1	278.0
WW ($e\mu$) Powheg (126931)	0.60	1.08	1	278.1
WW ($\mu\mu$) Powheg (126932)	0.60	1.08	1	277.9
WW ($\tau\mu$) Powheg (126933)	0.60	1.08	1	278.0
WW ($e\tau$) Powheg (126934)	0.60	1.08	1	277.8
WW ($\mu\tau$) Powheg (126935)	0.60	1.08	1	278.1
WW ($\tau\tau$) Powheg (126936)	0.60	1.08	1	278.1
ZZ (4 ℓ) Sherpa (126894)	8.74	1.11	1	434.9
ZW (3 ℓ) Sherpa (126893)	9.75	1.05	1	263.6
ZZ (2 ℓ 2 ν) Sherpa (126895)	0.50	1.05	1	1727.2
WW (2 ℓ 2 ν) Sherpa (126892)	5.50	1.06	1	463.2
VV (eeqq) Sherpa (157814)	1.70	1	1	117.5
VV ($\mu\mu$ qq) Sherpa (157815)	1.69	1	1	118.5
VV ($\tau\tau$ qq) Sherpa (157816)	1.70	1	1	117.5
$\ell\ell\nu\nu jj$ Sherpa (126988)	0.018	1	1	2756.9
$\ell\ell\nu\nu jj$ Sherpa (126989)	0.021	1	1	4808.6

Table 7.2: Triboson samples used for the analyses. The LO cross-section, k-factors (for NLO normalization) and filter efficiencies are reported. The integrated luminosities corresponding to the total statistics in each sample are also given.

Process (ID)	σ [pb]	k-factor	filter efficiency	$\int \mathcal{L} dt$ [fb $^{-1}$]
WWW^* MadGraph (167006)	0.0051	1	1	9803.9
ZWW^* MadGraph (167007)	0.0016	1	1	32258
ZZZ^* MadGraph (167008)	0.0003	1	1	151515

Table 7.3: The top+boson samples used for this analyses. The LO cross-section, k-factors (for NLO normalisation) and filter efficiencies are reported. The integrated luminosities corresponding to the total statistics in each sample are also given.

Process	σ [pb]	k-factor	$\int \mathcal{L} dt$ [fb $^{-1}$]
$t\bar{t} W$ Madgraph (119353)	0.10	1.18	3270.1
$t\bar{t} W + jet$ Madgraph (119354)	0.09	1.18	3647.1
$t\bar{t} Z$ Madgraph (119355)	0.07	1.34	4409.9
$t\bar{t} Z + jet$ Madgraph(119356)	0.09	1.34	3416.9
$t\bar{t} WW$ Madgraph(119583)	0.00092	1.0	10869.5

Table 7.4: SM higgs (Higgs mass 125 GeV) samples used for the the analysis. The integrated luminosities corresponding to the total statistics in each sample are also given.

Process (ID)	σ [pb]	filter efficiency	$\int \mathcal{L} dt$ [fb $^{-1}$]
$H \rightarrow WW^* \rightarrow \nu\bar{\nu}\nu$ ggF PowhegPythia8 (161005)	4.41×10^{-1}	0.491	2311
$H \rightarrow WW^* \rightarrow \nu\bar{\nu}\nu$ VBF PowhegPythia8 (161055)	3.56×10^{-2}	0.507	16600
$H \rightarrow WW^* \rightarrow \nu\bar{\nu}\nu$ WH Pythia8 (161105)	1.50×10^{-1}	0.105	1270
$H \rightarrow WW^* \rightarrow \nu\bar{\nu}\nu$ ZH Pythia8 (161155)	8.90×10^{-3}	1.000	2250
$t\bar{t}H \rightarrow WW^*$ Pythia8 (161305)	2.80×10^{-2}	1.000	6700
$H \rightarrow ZZ^* \rightarrow \ell\bar{\ell}\nu\nu$ ggF PowhegPythia8 (160655)	4.67×10^{-2}	0.446	2400
$H \rightarrow ZZ^* \rightarrow \ell\bar{\ell}\nu\nu$ VBF PowhegPythia8 (160705)	3.77×10^{-3}	0.446	17800
$H \rightarrow ZZ^* \rightarrow \ell\bar{\ell}\nu\nu$ WH Pythia8 (160755)	1.67×10^{-3}	0.446	26900
$H \rightarrow ZZ^* \rightarrow \ell\bar{\ell}\nu\nu$ ZH Pythia8 (160805)	1.04×10^{-2}	0.040	48000
$H \rightarrow ZZ^* \rightarrow 4\ell$ ggF PowhegPythia8 (160155)	5.26×10^{-3}	1.000	37000
$H \rightarrow ZZ^* \rightarrow 4\ell$ VBF PowhegPythia8 (160205)	4.25×10^{-4}	1.000	460000
$H \rightarrow ZZ^* \rightarrow 4\ell$ WH Pythia8 (160255)	1.88×10^{-4}	1.000	520000
$H \rightarrow ZZ^* \rightarrow 4\ell$ ZH Pythia8 (160305)	1.04×10^{-2}	0.010	780000

Table 7.5: SM $V\gamma$ samples used for the the analysis. The integrated luminosities corresponding to the total statistics in each sample are also given.

Process (ID)	σ [pb]	filter efficiency	$\int \mathcal{L} dt$ [fb $^{-1}$]
$W\gamma(e\nu)$ Sherpa (126739)	163.11	1	11.0
$W\gamma(\mu\nu)$ Sherpa (126742)	162.74	1	11.0
$W\gamma(\tau\nu)$ Sherpa (126856)	162.00	1	11.0
$V\gamma(ee\nu)$ Sherpa (145161)	32.26	1	495
$V\gamma(\mu\mu\nu)$ Sherpa (145162)	32.317	1	495
$V\gamma(\tau\tau\nu)$ Sherpa (126854)	32.332	1	124

7.2 Charge Misidentification

Final states which include same-sign di-electrons or a same-sign electron and muon pair are also subject to an additional background from charge misidentification for the electron, turning an opposite-sign event into a same-sign one. This charge misidentification is predominately due to the “trident” process, where an electron undergoes a hard bremsstrahlung, followed by an asymmetric pair production of the resulting photon, $e_{\text{hard}}^{\mp} \rightarrow \gamma_{\text{hard}} e_{\text{soft}}^{\mp} \rightarrow e_{\text{soft}}^{\mp} e_{\text{soft}}^{\mp} e_{\text{hard}}^{\pm}$. The final hard particle, which is the one reconstructed, then has the opposite charge from the incident electron.

Since muons do not undergo such a trident process, their rate of charge misidentification is much lower and generally due to problems in the tracking reconstruction. The rate for charge misidentification for muons has been shown to be negligible (around 10^{-8}) for the particle energies considered in this search [42].

The background from charge misidentification is reduced as much as possible by tightening the d_0 significance cut to 3 from 5 as used in [60]. The transverse impact parameter d_0 measures the distance of closest approach of the reconstructed particle track to the beamline. The d_0 significance divides this quantity by the uncertainty on its measurement (d_0/σ_{d_0}). Electrons undergoing the trident process generally have less well-constructed tracks than those that traverse the detector unhindered. The effect of this can be seen in Figure 7.1. The left plot shows electrons from within the Z boson mass window, with the same-sign events (candidates for charge flip events) showing a much wider distribution). By tightening the selection on this variable for electrons, a reduction of the background by a factor of 2, with minimal corresponding loss of prompt, signal electrons can be seen in the right plot of Figure 7.1. The tight++ electron identification and strict isolation cuts also help to reduce this background.

Because the bremsstrahlung and photon conversion processes are directly related to the amount of material traversed by the particle, the charge flip rate is highly variable as a function of η . In addition, this dependence is not expected to be well modeled in the simulation, due to poor modeling of the detector material and its precise location. Previous results have show the rates to

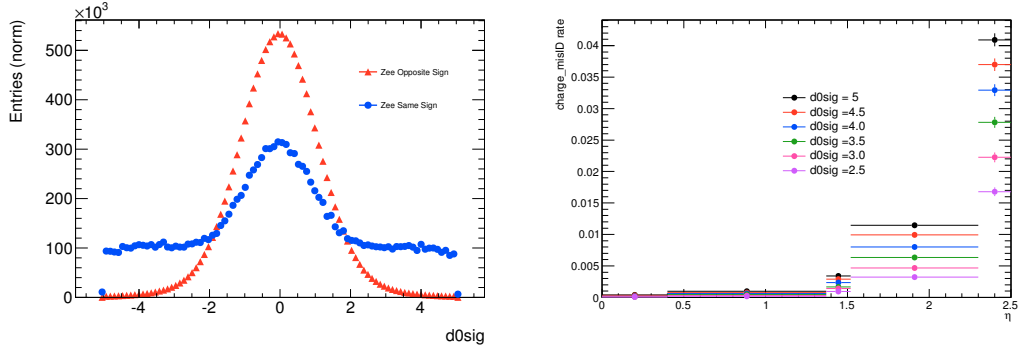


Figure 7.1: (Left) The d_0 significance distribution for opposite-sign (red) and same-sign (blue) $Z \rightarrow ee$ events, normalized to equal area. The same-sign events show a much broader distribution do to the poorly measured track coming from the trident process. (Right) Charge-flip rate for varying cut values of d_0 significance.

be approximately 20% too high compared to those determined directly in the data [72][73]. Because of this, the charge flip rate is measured in a dedicated data region enriched in charge-flip events and applied to opposite-sign data to estimate the contribution from charge misidentification. The flip rate is also dependent on the p_T of the lepton (though to a lower degree than the η dependence), so rates are extracted in bins of both $|\eta|$ and p_T .

7.2.1 Method

The charge flip rate is extracted in Z boson $\rightarrow ee$ events, requiring $75 < m(\ell\ell) < 100$ GeV. A slightly asymmetric $m(\ell\ell)$ window is chosen because the trident process often results in an underestimated electron energy, resulting in the $m(\ell\ell)$ for same-sign Z events being smeared and shifted slightly lower than the expected value.

In the Z window, the background from fake leptons is low, and what backgrounds remain are removed using the sideband subtraction method, shown in Figure 7.2. Here, the two sidebands are chosen to be $[50,75]$ and $[100,125]$ and the average of the two regions is subtracted from the charge flip extraction region.

The charge flip rate in a given $|\eta|$, p_T bin, ϵ_i is assumed to be independent from the other $|\eta|$, p_T bins. The chance for both electrons to undergo a charge flip is assumed to be a negligible correction.

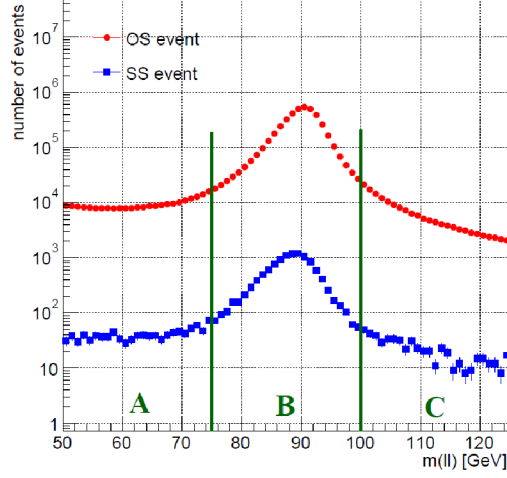


Figure 7.2: Sideband regions used to remove background from the charge-flip extraction region.

Therefore, the number of same sign events in with electrons in bins i and j (N_{SS}^{ij}), can be given as a function of the total number of Z candidates and the probability for each electron to undergo a charge flip (ϵ_i and ϵ_j) :

$$N_{SS}^{ij} = N^{ij}(\epsilon_i + \epsilon_j) \quad (7.1)$$

Thus, the probability to observe N_{SS}^{ij} , given the observed N^{ij} and the true values of ϵ_i and ϵ_j can be written as:

$$P(\epsilon_i, \epsilon_j | N_{SS}^{ij}, N^{ij}) = \frac{[N^{ij}(\epsilon_i + \epsilon_j)]^{N_{SS}^{ij}} e^{-N^{ij}(\epsilon_i + \epsilon_j)}}{N_{SS}^{ij}!} \quad (7.2)$$

The value of ϵ_i that maximizes the probability is taken as the best-fit value. To ease computation, the probability maximization is converted to a minimization of the negative natural log of the likelihood:

$$-\ln L \propto - \sum_{i,j} \left\{ \ln [N_{ij}(\epsilon_i + \epsilon_j)] N_{SS}^{ij} - N_{ij}(\epsilon_i + \epsilon_j) \right\} \quad (7.3)$$

The best fit values of ϵ as a function of $|\eta|$ and p_T are thus determined from data.

7.2.2 Results

The charge flip rates determined are shown in Figures 7.3 for signal electrons and Figure 7.4 for loose electrons. The rates for loose electrons are used only in the removal of charge flip events from the matrix method as described in Section 7.3, not in the final estimation of same-sign events in the signal or validation regions. As expected, the flip rates are highest for high η leptons, which cross the most detector material, and high p_T electrons. The rates are also noticeably lower than rates determined in previous analyses, as expected from the tightened electron selection [42][72].

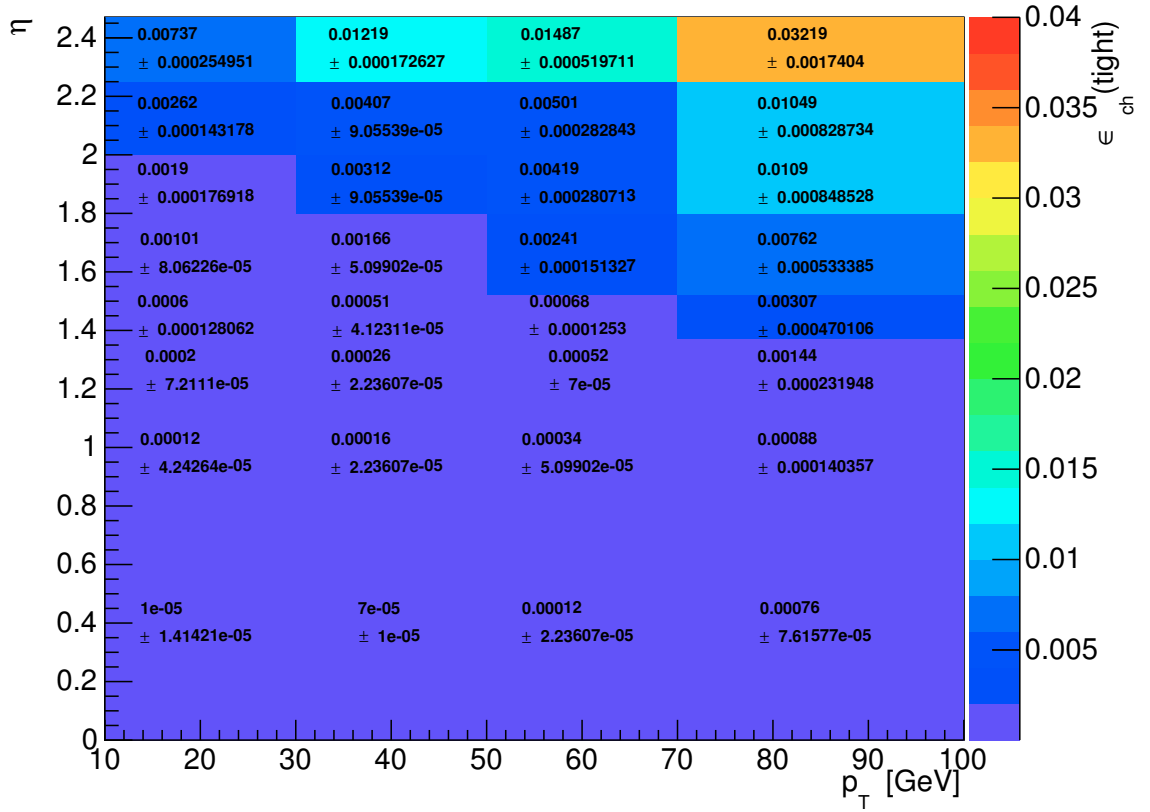


Figure 7.3: Charge-flip rate for signal electrons as a function of p_T and η .

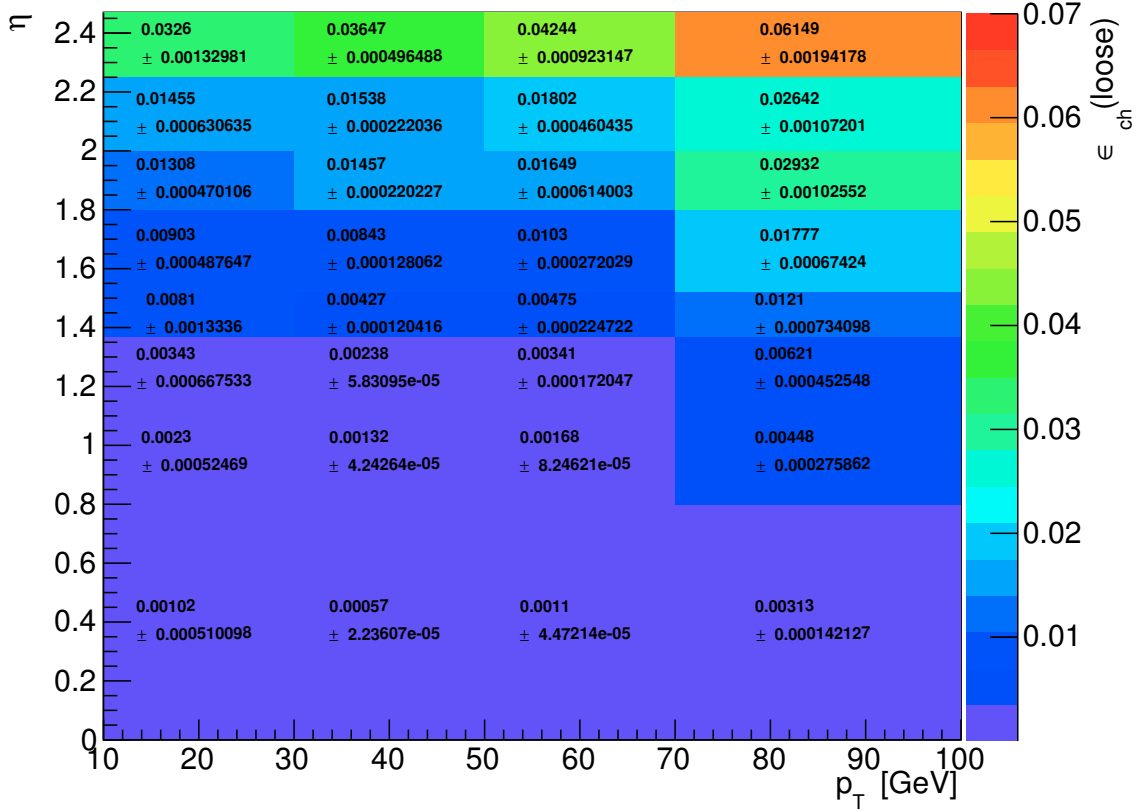


Figure 7.4: Charge flip rate for baseline electrons as a function of p_T and η . These rates are used to remove the charge flip contribution to the matrix method estimate of fake leptons.

7.2.3 Uncertainties

Several uncertainties are considered for the charge flip background.

The first uncertainty is due to the limited statistics in the charge flip rate extraction region. For central η values where the statistics are low, these can be up to 70%. However, because of the much smaller rates, this region's contribution to the overall estimate and its total uncertainty is small. For the dominant high η region, the statistical uncertainty is $< 1\%$.

An uncertainty on the background subtraction is measured by varying the size of the sidebands by 5 GeV. For the central η region, this gives an uncertainty of about 50%, again where the overall contribution to the same-sign estimate is small. For the high η region which dominates the estimate,

this uncertainty is around 1%.

A closure test is also performed using the Z window extraction region to test the performance of the likelihood method. An example of the results are shown in Figure 7.5, the black points show the same-sign data distribution, and the red circles are opposite-sign data events weighted using rates measured in simulation. The rates determined in simulation show a clear over-prediction of the same-sign estimate, motivating the need for a fully data-driven estimate. The green diamonds show opposite-sign data events weighted by rates measured in data, showing much better agreement in overall normalization. The same-sign data events do show the expected smeared and shifted $m(\ell\ell)$ distribution, which is not reproduced by the weighted opposite-sign events. The uncertainty of the closure test is approximately 1%.

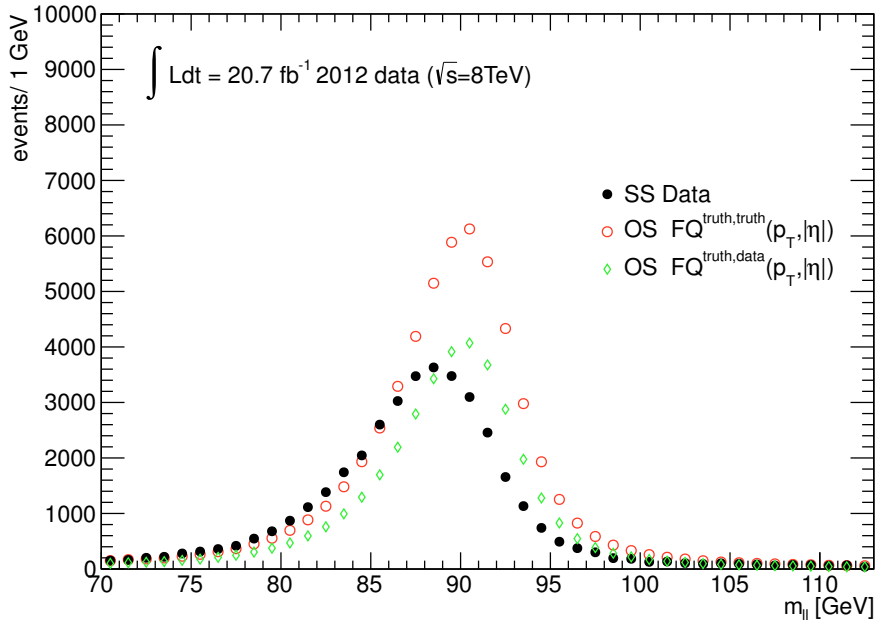


Figure 7.5: Charge-flip rate closure test results.

Finally, the charge flip rate is evaluated using a finer binning in p_T and η . The estimates in the validation regions with this finer binning are in agreement with the coarser binning within systematic uncertainties. The difference between the two estimates is taken as an additional systematic and

ranges between 1% and 10%. This systematic attempts to mitigate any potential differences arising from different η and p_T distributions in the extraction region and the signal and validation regions, which cannot be correctly modeled due to the fixed bin width. These differences are shown in Figure 7.6; the red points show the extraction region, while the other points show the different same-sign validation regions.

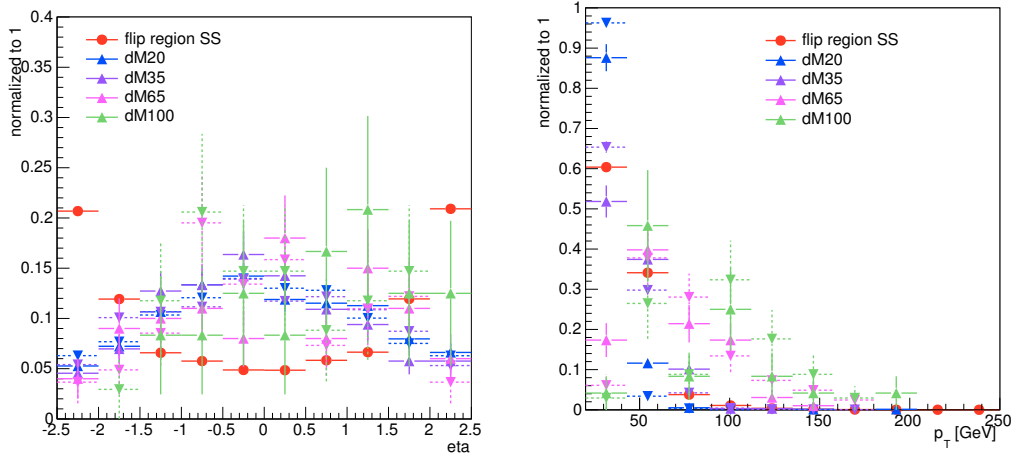


Figure 7.6: η (left) and p_T (right) spectrum for the ee validation regions and the charge-flip extraction region.

7.3 Lepton Misidentification

As previously stated, the final background for same-sign dilepton searches is due to particles misidentified as prompt leptons. As with the charge-flip background, the lepton selection requirements are tightened in comparison with previous complementary analyses, in order to reduce this background as much as possible (described in Section 8.1). Their impact is estimated using a fully data-driven implementation of the Matrix Method, described in this section.

7.3.1 Matrix Method

This method uses a 2×2 matrix that links pairs of real and fake leptons⁶ to pairs of “loose” and “tight” leptons[74]. Tight leptons correspond to the signal leptons while loose leptons correspond to the baseline leptons, which are described in Sec. 8, with the additional requirement on d0 significance to reduce the overlap between the fake estimate and the charge-flip.⁷

$$\begin{pmatrix} N_{TT} \\ N_{TL} \\ N_{LT} \\ N_{LL} \end{pmatrix} = \Lambda \times \begin{pmatrix} N_{RR} \\ N_{RF} \\ N_{FR} \\ N_{FF} \end{pmatrix} \quad (7.4)$$

If ϵ_i and ζ_j are the ratios for real and fake loose lepton to satisfy the tighter set of criteria, and $i, j = 1, 2$ are the leading and subleading lepton respectively, the matrix Λ is given by:

$$\Lambda = \begin{pmatrix} \epsilon_1 \epsilon_2 & \epsilon_1 \zeta_2 & \zeta_1 \epsilon_2 & \zeta_1 \zeta_2 \\ \epsilon_1 (1 - \epsilon_2) & \epsilon_1 (1 - \zeta_2) & \zeta_1 (1 - \epsilon_2) & \zeta_1 (1 - \zeta_2) \\ (1 - \epsilon_1) \epsilon_2 & (1 - \epsilon_1) \zeta_2 & (1 - \zeta_1) \epsilon_2 & (1 - \zeta_1) \zeta_2 \\ (1 - \epsilon_1)(1 - \epsilon_2) & (1 - \epsilon_1)(1 - \zeta_2) & (1 - \zeta_1)(1 - \epsilon_2) & (1 - \zeta_1)(1 - \zeta_2) \end{pmatrix} \quad (7.5)$$

The ϵ_i and ζ_j values are measured in dedicated extraction regions as described in Sections 7.3.2 and 7.3.3, respectively. The values for $N_{TT}, N_{TL}, N_{LT}, N_{LL}$ for a given region (i.e. validation region, signal region) can easily be determined. Then, the system of equations can then be inverted to retrieve the proportions of real and fake leptons in the sample:

⁶In this section “fake” leptons is used as a synonym for the collection of “non-prompt” leptons and hadrons misidentified as a lepton.

⁷Throughout this section “loose” (“tight”) will refer to loose(tight) selection for the matrix method and not loose or tight PID requirements as described in Chapter 4.

$$\begin{pmatrix} N_{RR} \\ N_{RF} \\ N_{FR} \\ N_{FF} \end{pmatrix} = \Lambda^{-1} \times \begin{pmatrix} N_{TT} \\ N_{TL} \\ N_{LT} \\ N_{LL} \end{pmatrix} \quad (7.6)$$

The final estimated for fake background in a given region is then simply:

$$N_{fakes} = N_{RF} + N_{FR} + N_{FF}. \quad (7.7)$$

7.3.2 Real efficiency measurements

Real efficiency measurements are assessed in samples of high purity electrons or muons, with little contamination from fake backgrounds. The Z-boson decaying to ee or $\mu\mu$ pairs is chosen. A tag and probe method is employed to further increase the purity. For this method, events with two opposite-sign, same-flavor, loose leptons are selected. As the probability for a lepton to pass the identification cuts should be largely independent of the rest of the event kinematics, there is no reason to require same-sign leptons for this measurement. The invariant mass of the dileptons is then required to be within the Z peak ($80 < m(\ell\ell) < 100$ GeV). One lepton (the tag) is required to pass tight identification (again as defined in Section 8.1). The second lepton (the probe) is then used to determine the probability for the baseline lepton to also pass the tight criteria. In the case where both leptons are “tight”, each is allowed to be considered as the tag lepton, to remove bias and increase statistics. The measurement is performed as a function of η and p_T . The differences of the values measured in the data and in the Monte Carlo simulation is taken as a systematic uncertainty. The determined efficiencies are shown in Figure 7.7. The real lepton efficiencies measured in data and simulation agree well – largest discrepancies of a few percent, and the overall efficiencies are high, plateauing near 90% for electrons and just under 100% for muons.

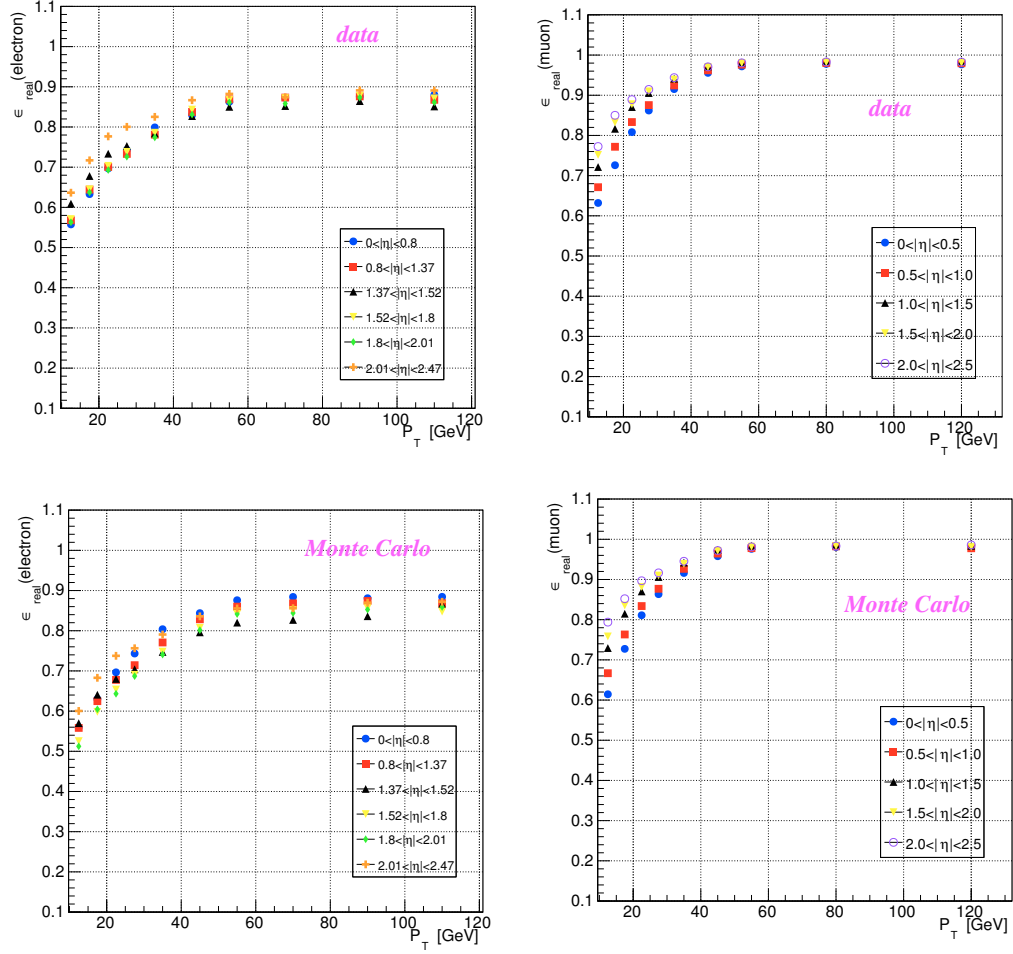


Figure 7.7: Real lepton identification efficiency from loose to tight selection measured in data (top) and MC (bottom), for electrons (left) and muons (right).

7.3.3 Fake rate extraction

As opposed to the real efficiency extraction region, there is not an obvious region that preferentially selects fake leptons while excluding real leptons. The region where the fake rates are extracted must balance providing a high fake lepton fraction (and thus a low real lepton composition) with event properties similar to those found in the signal selection.

After much study, for this analysis the following region is used:

- same-sign lepton (more details below),
- b -jet veto
- $H_T > 50$ GeV
- $m_{Tr1} > 50$ GeV.

This region is preferentially selected by the BDT training, so will provide a good estimate in the signal and validation regions, but has a small overlap with the the validation regions themselves ($< 1\%$ contamination) and a low contamination from possible signal models (also $< 1\%$). Contributions from sources of real leptons (diboson, $t\bar{t}+V$, Higgs production) are estimated in the Monte Carlo simulation and subtracted. Similarly, contributions from $W+\gamma$ and charge misidentified electrons are also removed.

For the measurement of muon fake rates, $\mu\mu$ events are used and the leading muon is required to have $p_T > 40$ GeV and pass signal muon cuts, leading to a very high probability that it is real. The subleading muon is then considered for measuring the fake rate in four bins of p_T : $[10, 15]$, $[15, 20]$, $[20, 25]$, and $[25, 40]$ GeV. For muons with > 40 GeV, an extrapolation factor measured in $t\bar{t}$ Monte Carlo is applied to the $[25, 40]$ GeV measurements, though the contribution from muons in this p_T range is expected to be small.

For the measurement of electron fake rates, $e\mu$ events are used, with the same requirements for the muon as the muon fake rate measurement. Note that ee events are not considered due to the high contamination from the charge flip background. A larger statistical sample allows eight bins in p_T from 10 GeV to 65 GeV (or more) and two bins in η , $|\eta| < 1.5$ and $1.5 < |\eta| < 2.5$, to be employed.

The measured rates are shown in Figure 7.8. The fake rates for electrons are generally lower than those for muons due to the additional identification requirements moving from loose to tight

(medium++ to tight++ PID). Overall, the fake rates are found to be lower than those in previous searches [1], by roughly a factor of 2 due to the tightened isolation and impact parameter requirements.

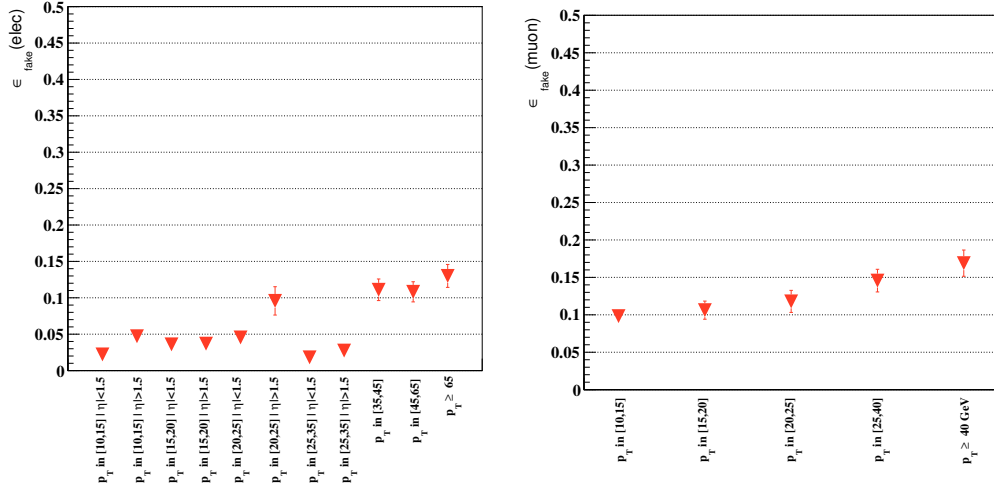


Figure 7.8: Lepton fake rate from loose to tight selection for electrons (left) and muons (right). This rate is presented for different $(p_T, |\eta|)$ bins for electrons and p_T bins for muons. Only the statistical uncertainties are shown.

7.3.4 Uncertainties for fake rate extractions

The uncertainties for the measurement of the fake rates are much larger than for the real efficiency measurement. The largest contributions are explained below.

The statistical uncertainty from the regions of extraction is significant. Additionally, there is a systematic uncertainty arising from the choice of extraction region to account for potential differences in composition between the extraction region and the signal and validation regions. This is estimated by taking the difference between the measured rates in the extraction region described and those determined in an inclusive same-sign selection with no additional event level cuts. Finally, the uncertainty of the subtraction of real lepton, charge flip and $W+\gamma$ events is also considered. The charge flip uncertainty is varied by the uncertainties determined in Section 7.2. For the other Monte Carlo samples, diboson, Higgs and $W\gamma$ samples are varied by 30%, and $t\bar{t}+V$ is varied by a

conservative 50%.

The resulting rates and uncertainties are shown in Tables 7.6 and 7.7. The dominant uncertainty is due to the varying of the subtraction of real lepton contribution from the fake extraction region.

electron bin	[10-15][0-1.5]	[10-15][1.5-2.5]	[15-20][0-1.5]	[15-20][1.5-2.5]	[20-25][0-1.5]
stat	12%	14%	15%	18%	18%
syst	14%	8%	11%	8%	17%
tot	19%	16%	18%	20%	24%
[20-25][1.5-2.5]	[25-35][0-1.5]	[25-35][1.5-2.5]	[35-45]	[45-65]	[65-++]
20%	15%	18%	13%	12%	14%
6%	27%	12%	18%	21%	18%
21%	31%	22%	22%	24%	23%

Table 7.6: Uncertainties on the electron fake rate. In the first row, the first and second of set of numbers give the p_T (in GeV) and η range of the bin. For the last three bins there is only one η bin used.

muon bin	[10-15]	[15-20]	[20-25]	[25-40]	[40-++]
stat	8%	11%	14%	14%	14%
syst	5%	14%	29%	29%	29%
tot	9%	18%	32%	32%	32%

Table 7.7: Uncertainties on the muon fake rate. The p_T range of the bin is provided in the first row (in GeV).

CHAPTER 8

Event Selection

This chapter describes the selection process used to separate SUSY signal-like events from the backgrounds described in the previous chapter.

This thesis uses the full Atlas 2012 dataset, corresponding to 20.3 fb^{-1} of integrated luminosity taken at $\sqrt{s} = 8 \text{ TeV}$, after requiring good data quality from a correctly functioning detector. Events are selected from the E/Gamma or Muon trigger streams, requiring trigger accept signals that are further explained in Sec. 8.2.

Selection is then performed at the object (electron, muon, jet) level and is described in Section 8.1. The event-level requirements on the identified high-level objects, is described in Section 8.3. Finally, the multi-variate analysis utilizing boosted decision trees is described in Section 8.4.

8.1 Object Selection

For leptons two identification levels are utilized, baseline and signal. The baseline selection is determined in accordance with several other searches targeting complementary signatures [60][1][75]. The number of leptons (e, μ, τ) is determined at the baseline level, assigning events to a particular analysis and ensuring orthogonality, so that results from the several searches can be easily combined.

Baseline electrons are required to have $p_T > 10 \text{ GeV}$, $|\eta| < 2.47$, and pass the medium++ criteria. To improve the purity at the signal electron level, electrons are now required to pass the tight++ requirements. To reduce the impact of the charge flip and to a smaller extent the fake backgrounds,

strict track quality cuts are imposed, requiring impact parameter significance $|d_0/\sigma(d_0)| < 3$, and $|z_0 \sin \theta| < 0.4$ mm. Isolation requirements are also quite strict in comparison with the previous searches to reduce the fake background. The isolation requirements were optimized based on the Zn significance value, and require track isolation $p_T^{cone30}/\min(p_T, 60\text{GeV}) < 0.07$ and calorimeter isolation $E_T^{cone30}/\min(p_T, 60\text{GeV}) < 0.13$.

Baseline muons are also required to have $p_T > 10$ GeV, and similar $|\eta|$ requirements of < 2.5 . They are reconstructed with the STACO algorithm allowing either a combined muon spectrometer track with a matched inner detector track (combined muon) or an inner detector seeded identification (segment tagged). They are required to pass the “loose” muon identification. Additional requirements are made on the number of inner detector hits and the impact parameter significance $|d_0/\sigma(d_0)| < 5$ to ensure well measured muon tracks. Signal muons tighten these track requirements to $|d_0/\sigma(d_0)| < 3$ and also require $|z_0 \sin \theta| < 1.0$ mm to reduce non-prompt muons. The isolation requirements are also optimized to require track isolation $p_T^{cone30}/\min(p_T, 60\text{GeV}) < 0.06$ and calorimeter isolation $E_T^{cone30}/\min(p_T, 60\text{GeV}) < 0.14$.

Hadronically decaying taus are not included as part of the final state signatures for this paper, but signal taus are vetoed in order to remain orthogonal to other analyses. Baseline taus must satisfy $p_T > 20\text{GeV}$, $|\eta| < 2.47$, nTrack= 1 or 3 (1 or 3-prong), and a charge of ± 1 . Two separate boosted decision trees are used for tau identification; one to discriminate against jets and the other to discriminate against electrons.

Jets are clustered with the anti- k_T algorithm with $\Delta R = 0.4$ as described in 4.3. We require central jets to have $p_T > 20$ GeV for $|\eta| < 2.4$ and forward jets to have $p_T > 30$ GeV for $2.4 < |\eta| < 4.5$. Central jets ($|\eta| < 2.4$) with $p_T < 50$ GeV must have $JVF > 0$ to reduce the impact of pileup. We veto events containing any identified b jets using an 80% efficiency working point ($MV1 > 0.3511$).

grid		No Slepton	Slepton	
mass (C1N2,N1) GeV		(100,75)	(120,80)	(260,240)
Z_n	Old Iso	0.10	0.10	4.87
	Iso 07	0.37	0.13	6.84

Table 8.1: Comparison of the analysis sensitivity before and after optimizing the isolation selection for leptons.

8.1.1 Isolation

As mentioned in Section 7.3, the best discriminating variable to reduce the contribution from misidentified leptons is isolation. For this analysis, it was necessary to tighten the isolation requirements for both electrons and muons as the fake background is generally either the dominant or sub-dominant background. Previous analyses, such as [60], used the following isolation requirements: $p_T^{cone30}/\min(p_T, 60) < 0.16(0.12)$ for electrons (muons) and $e_T^{cone30}/\min(p_T, 60) < 0.18$ for electrons. For this analysis, calo isolation is added to the muon requirements and both the calo and track isolation cuts are tightened. The optimized requirements are: $p_T^{cone30}/\min(p_T, 60) < 0.07(0.06)$ for electrons (muons) and $e_T^{cone30}/\min(p_T, 60) < 0.13(0.14)$ for electrons (muons). More restrictive cuts than those used in this analysis were not possible to avoid a loss of efficiencies for signal leptons. The gain in the expected significance can be seen in Table 8.1, demonstrating close to 30% improvement.

8.2 Trigger

Events are required to pass one of several dilepton triggers depending on the p_T of each of the two leptons. For the dielectron channel, events are required to pass either a symmetric trigger requiring 2 loosely identified electrons each with $p_T > 12$ GeV or the asymmetric trigger requiring 2 electrons passing medium identification with $p_T > 24$ GeV and > 7 GeV. In the dimuon channel, the symmetric trigger requires two muons both with $p_T > 13$ GeV and the asymmetric trigger requires the leading muon have $p_T > 18$ GeV and the sub-leading muon to be > 8 GeV. In the opposite flavor channels, two asymmetric triggers are utilized with $(p_T^e, p_T^\mu) > (12, 8)$ or $(7, 18)$ GeV.

In order to ensure the triggers are fully efficient, offline p_T requirements are imposed on the candidate leptons in the event, which may be higher than the stated trigger thresholds. These requirements are summarized in Table 8.2. Additionally, the leptons are required to pass a “Phase Space” requirement, ensuring that a specific trigger is passed given the particular p_T of the two leptons. This phase space requirement is used to allow for weighting of simulation events to properly model trigger efficiencies and is shown in Figure 8.1, with definitions are given in Table 8.3. Finally, the two leptons in the event must be matched in $\Delta R < 0.1$ to the two objects that fired the trigger.

trigger	L1	Offline p_T Threshold
EF_2e12Tvh_loose1	L1_2EM10VH	$p_T(e_1) > 14$ GeV, $p_T(e_2) > 14$ GeV
EF_e24vh_medium1_e7_medium1	L1_EM18VH	$p_T(e_1) > 25$ GeV, $p_T(e_2) > 8$ GeV
EF_2mu13	L1_2MU10	$p_T(\mu_1) > 14$ GeV, $p_T(\mu_2) > 14$ GeV
EF_mu18_tight_mu8_EFFS	L1_MU15	$p_T(\mu_1) > 18$ GeV, $p_T(\mu_2) > 8$ GeV
EF_e12Tvh_medium1_mu8	L1_EM10VH_MU6	$p_T(e) > 14$ GeV, $p_T(\mu) > 8$ GeV
EF_mu18_tight_e7_medium1	L1_MU15	$p_T(e) > 8$ GeV, $p_T(\mu) > 18$ GeV

Table 8.2: The list of lowest p_T un-prescaled di-lepton triggers.

		efficiency	
		b-b	e-e
<i>ee</i> channel			
region A	symmetric only: EF_2e12Tvh_loose1	0.98	0.94
region B	asymmetric only: EF_e24vh_medium1_e7_medium1	0.93	0.85
<i>$\mu\mu$</i> channel			
region A	asymmetric only: EF_mu18_tight_mu8_EFFS	≈ 0.8	≈ 0.98
region B	either: EF_mu18_tight_mu8_EFFS or EF_2mu13	≈ 0.6	≈ 0.9
region C	asymmetric only: EF_mu18_tight_mu8_EFFS	0.66	0.95
region D	symmetric only: EF_2mu13	0.52	0.77
<i>eμ</i> channel			
region A	EF_e12Tvh_medium1_mu8	0.71	0.82
region B	EF_mu18_tight_e7_medium1	0.65	0.81

Table 8.3: Di-lepton triggers used in different regions of lepton p_T phase space. The definition of the regions for different channels is shown in Fig. 8.1. The trigger efficiencies shown are meant to be informative rather than exact, and are based on the single lepton trigger efficiencies. Label b-b (e-e) stands for both leptons being in the barrel (end-cap) detector region.

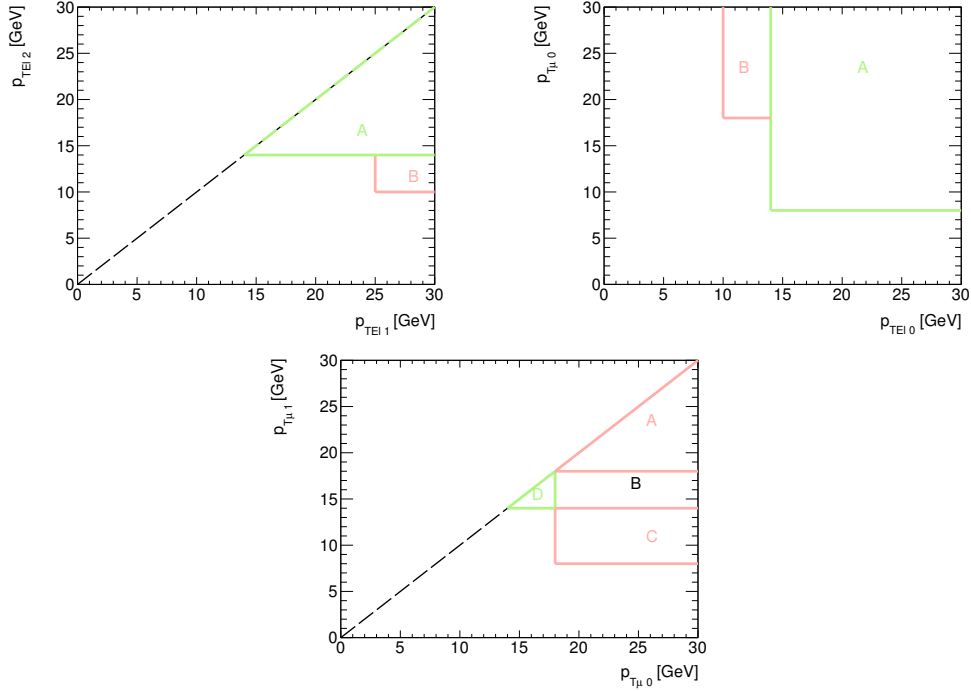


Figure 8.1: Phase space requirements for the dilepton triggers in the ee (left), $e\mu$ (center), $\mu\mu$ (right) channels

8.3 Event Level Selection

After the selection of two same-sign signal leptons passing the trigger requirements, further requirements are made at the event level.

To reduce the contribution from charge flip electrons and remove the region used for rate determination, ee events consistent with coming from a Z boson decay are removed by vetoing $75 < m(\ell\ell) < 100$ GeV.

Candidate events are further required to pass cleaning cuts to ensure that the full detector is functioning correctly at the time of data taking and that any objects are not contained in known trouble regions of the detector (such as known dead or hot channels).

Events must also contain a primary vertex, selected as the vertex with the highest $\sum p_T^2$ of the associated tracks. All muons in the event are checked for consistency with coming from a cosmic ray, and such events are vetoed.

8.4 Signal Selection using Boosted Decision Trees

For this scenario, particularly in the compressed region where the same-sign signature is the most powerful, discriminating variables typically used by the 2L and 3L gaugino searches, such as m_{T2} and $E_T^{\text{miss,rel}}$, are not as powerful. Particularly when the mass difference between $\tilde{\chi}_1^\pm$ and $\tilde{\chi}_1^0$ is small, any square cuts used for discrimination would lead to either poor signal efficiency or high background contamination. Instead a multivariate technique is used to better separate background and signal events. This analysis has decided to use a Boosted Decision Tree (BDT) as its multivariate of choice. The theory and structure of Boosted Decision Trees in general are described in Section 8.4.1, while the specific implementation for this analysis is given in Sections 8.4.2 and 8.4.3. The results after the BDT training are given in Section 8.4.4.

8.4.1 Boosted Decision Trees

Decision trees attempt to solve the inefficiency of rectangular cuts by allowing events which would have failed a cut on a particular variable to be considered further. Structurally, a decision tree is an ordered series of binary decisions, called nodes. Beginning with the primary node, the input variable and cut value are determined for optimal separation (explained below). Each event then passes or fails this criterion and events are separated into two daughter nodes (left and right). For each of the daughter nodes, the next variable and cut value are determined, both of which may be different for the left and right nodes, and the events are again separated, yielding four nodes. This procedure continues until a stopping criteria is reached, and the final node is denoted as a “leaf”. Such stopping criteria include a signal or background purity greater than a set threshold, a minimum number of events populating a node, or a maximum branch depth. The ending leaves are then classified as signal or background by the majority of training events contained. This structure is shown in Figure 8.2.

To optimally choose the next variable and cut value for a given node, the criterion that maximally changes the gini index is computed. The gini index is defined as

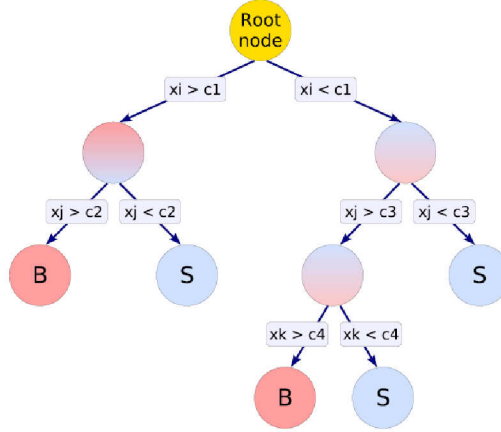


Figure 8.2: Illustration of Decision Tree structure

$$gini = p * (1 - p), \quad (8.1)$$

where p is the purity, defined as the ratio of signal events to total events. Thus, gini is maximized when the node is completely mixed (50% signal, 50% background) and falls to 0 when a node is completely signal or background (purity of 1 or 0, respectively).

While the clear structure and decision path for a tree is much more straightforward than for other multivariate techniques such as Artificial Neural Networks, they can suffer from instability due to statistical fluctuations in the training dataset.

In order to combat this problem, the training set is analyzed many times producing a “forest” of decision trees. After one iteration of decision tree creation, misclassified events are given a higher weight than those correctly classified for the next iteration of training, using a procedure known as “boosting”. The weights of all of the events are then renormalized to maintain a constant total sum of weights, and the decision tree algorithm is run again. Thus, subsequent iterations emphasize events that have been previously misclassified.

The most widely used boosting algorithm is the *AdaBoost* (adaptive boost) [76]. The weight used to boost the events is determined from the misclassification rate, err of the previous tree,

$$\alpha = \frac{1 - err}{err}. \quad (8.2)$$

The final output (y_{Boost}) of the BDT classifier is taken as a weighting of all of the individual decision trees (the forest), given by

$$y_{Boost}(\mathbf{x}) = \frac{1}{N_{collection}} * \sum_i^{N_{collection}} \ln(\alpha_i) * h_i(\mathbf{x}) \quad (8.3)$$

where $h(\mathbf{x})$ is the result of an individual tree (+1 for signal, -1 for background) and \mathbf{x} is the ensemble of input discriminating variables. Small values for y_{Boost} are indicative of background-like events, while large values are indicative of signal-like events.

8.4.2 BDT Training

We focus on the compressed region close to the diagonal with low p_T leptons, where we want to increase the limit determined by the 3L analysis. We optimize and define the signal regions with the 95% grid where 3L has little sensitivity and we interpret the result on other Susy scenarios: for example $\tilde{\chi}_1^\pm \tilde{\chi}_2^0$ grid with $x=50\%$ sleptons and $\tilde{\chi}_1^\pm \tilde{\chi}_2^0$ production without sleptons, decaying via W and Z boson.

For training our BDTs we utilize the Toolkit for MultiVariate Analysis (TMVA), integrated into the ROOT framework [77].

Due to the lack of MC signal statistics, it is not possible to train a separate BDT for each signal point available on the $\tilde{\chi}_1^\pm, \tilde{\chi}_1^0$ mass grid, nor to train the BDT separately for $ee, e\mu$ and $\mu\mu$ flavor events. To solve this problem, all flavor channels are combined and signal samples with the same mass splitting between $\tilde{\chi}_1^0$ and $\tilde{\chi}_1^\pm$ are grouped together as a single signal region. These BDT signal regions defined by the mass splitting are $\Delta m = 20, 35, 65, 100$ GeV and are shown in Figure 8.3. Larger values of Δm are not considered for individual BDT training, as the gain from a tailored BDT is not significant over the performance of the $\Delta m=100$ BDT. In addition, for $\Delta m > 100$ GeV

all three final state leptons are generally energetic enough to be reconstructed, leading to a better sensitivity for the 3L analysis compared with the 2LSS analysis.

In such scenarios with small mass splittings, the two SUSY particles are produced back-to-back and their LSP daughters from the decay continue in the same direction. This means that generally the momentum carried by the two LSPs would add destructively in the calculation of E_T^{miss} , giving a very low value. Unfortunately, many of the backgrounds to this search, also contain low expected values of E_T^{miss} , making this signature difficult to discriminate. If there is some initial state radiation (ISR) giving a transverse boost to the entire system, then at least some component of the the E_T^{miss} from the two LSPs can add to a value higher than that expected from the background, allowing for separation. This scenario is depicted in Figure 8.4.

Thus, the samples are split into orthogonal regions based on the presence of at least one central, light-flavored jet into ISR regions and no ISR regions to maximize the selection power of the analyses. Combining this with the four Δm regions gives a total of 8 BDT decisions and 8 signal regions: SRm20ISR, SRm35ISR, SRm65ISR, SRm100ISR, SRm20noISR, SRm35noISR, SRm65noISR, SRm100noISR. The rationale for splitting into ISR and no ISR regions is explained in the next section. The grouping by mass splitting and presence of an ISR jet also accomplishes a compromise between optimal separation power for all possible signal models and an unwieldy number of boosted decision trees to train, maintain, and evaluate.

In order to have more statistics and include the training events in the final result in a completely unbiased way, we divide the events into two subsamples for both background and signal using even and odd event numbers. The two subsamples were confirmed to have very similar normalization and shapes. We use subsample 1(2) from signal and background to train the BDT and apply the weights onto subsample 2(1) from signal and background.

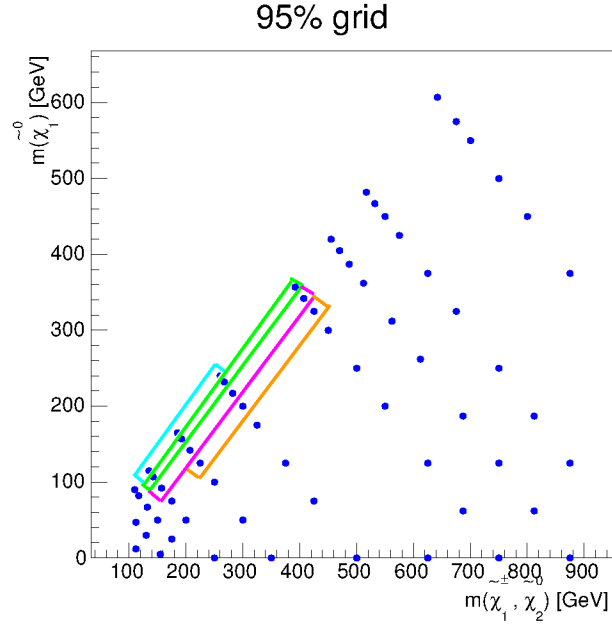


Figure 8.3: Signal points with identical mass splitting are combined for BDT training

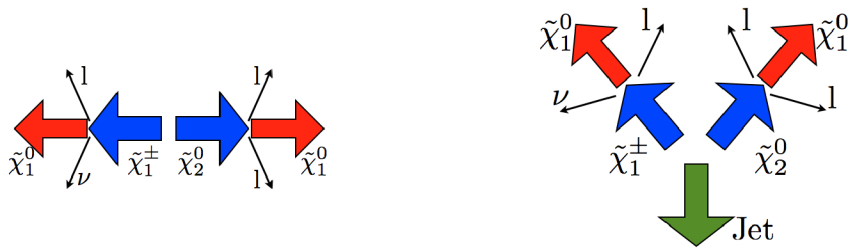


Figure 8.4: Cartoon depicting E_T^{miss} in the case of no ISR (left) and ISR (right). For the no ISR case, the two escaping LSPs are produced nearly back to back, so their E_T^{miss} sums to near 0. In the ISR case, their E_T^{miss} adds constructively.

8.4.3 Discriminating Variables

For all 8 BDT regions, the following variables are used:

- m_{T2} (described below)
- $p_{T_{li}} = \sqrt{(px_1 + px_2)^2 + (py_1 + py_2)^2}$
- $E_T^{\text{miss,rel}}$ (described below)
- $H_T = p_T(\text{lep}_1) + p_T(\text{lep}_2) + \sum p_T(\text{jets})$
- $m_{T\text{lep}1}$ - Transverse mass using leading lepton
- $m_{T\text{lep}2}$ - Transverse mass using sub-leading lepton
- $\Delta\phi_{\ell\ell}$ - Azimuthal angle between the two leptons

In addition, for the ISR Regions the following variables are also included. These variables are chosen to exploit the kinematics of the SUSY system with a small mass splitting including the ISR boost [78].

- $\Delta\phi(E_T^{\text{miss}}, \text{leading jet})$
- $E_T^{\text{miss}} / p_T(\text{leading jet})$
- $p_T(\text{leading lepton}) / p_T(\text{leading jet})$

The ‘‘Stransverse Mass’’ or ‘‘Cambridge MT2’’ variable m_{T2} is a function of the reconstructed lepton momenta and the missing transverse momentum. It is calculated as

$$m_{T2} = \min_{\mathbf{q}_T} [\max(m_T(\mathbf{p}_T^{\ell 1}, \mathbf{q}_T), m_T(\mathbf{p}_T^{\ell 2}, \mathbf{p}_T^{\text{miss}} - \mathbf{q}_T))], \quad (8.4)$$

where $\mathbf{p}_T^{\ell 1}$ and $\mathbf{p}_T^{\ell 2}$ are the transverse momenta of the two leptons, and \mathbf{q}_T is a transverse vector that minimizes the larger of the two transverse masses m_T . The latter is defined by:

$$m_T(\mathbf{p}_T, \mathbf{q}_T) = \sqrt{2(p_T q_T - \mathbf{p}_T \cdot \mathbf{q}_T)}. \quad (8.5)$$

It is designed for estimating masses of pair produced particles which each decay via both visible and invisible particles. For standard model backgrounds involving the decay of W boson to a visible lepton and an invisible neutrino, the m_{T2} distribution has an upper endpoint near the W mass. For signal events, the $\mathbf{p}_T^{\text{miss}}$ comes from the escaping LSP and the endpoint of m_{T2} is related to mass difference between the $\tilde{\chi}_1^\pm$ or $\tilde{\chi}_2^0$ and the $\tilde{\chi}_1^0$. So for compressed scenarios, the m_{T2} variable is generally shifted to smaller values than for Standard Model background as can be seen in Figures 8.5 and 8.7, for ISR and no-ISR events, respectively. Further details can be found in [79, 80].

The $E_T^{\text{miss,rel}}$ variable is constructed from E_T^{miss} . It is designed to reduce instrumental contributions to the missing transverse momentum and is computed the following way:

$$E_T^{\text{miss,rel}} \begin{cases} E_T^{\text{miss}} & \text{if } \Delta\phi_{l,j} \geq \pi/2 \\ E_T^{\text{miss}} \times \sin\Delta\phi_{l,j} & \text{if } \Delta\phi_{l,j} < \pi/2 \end{cases} \quad (8.6)$$

where $\Delta\phi_{l,j}$ is the azimuthal angle between the direction of $\mathbf{p}_T^{\text{miss}}$ and that of the nearest electron, muon, or central jet. So if a lepton or jet is within $\frac{\pi}{2}$ of the E_T^{miss} , the E_T^{miss} is reduced to only to component perpendicular to the lepton or jet.

The shape of these discriminating variables for the signal and the background before any cuts on the BDT output are shown Fig 8.5 to 8.7. For many of the variables, differences in shapes can be seen, but no clear boundary is seen to allow for simple rectangular cuts. For this reason, the BDT is used.

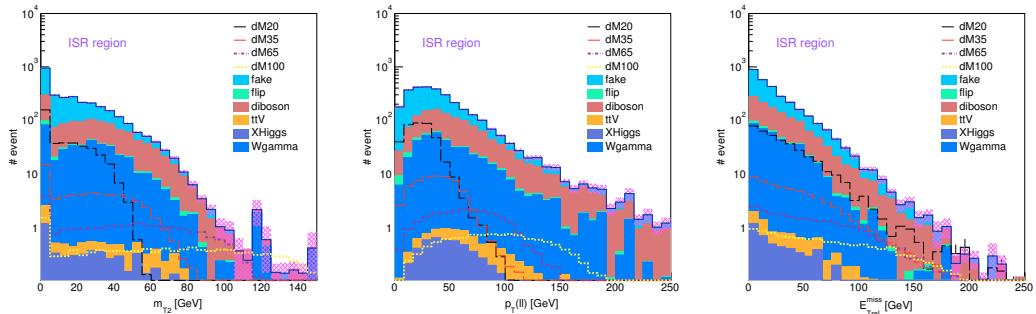


Figure 8.5: Distribution of m_{T2} (left), $p_{T(l)}$ (center) and $E_T^{\text{miss,rel}}$ (right) for ISR region.

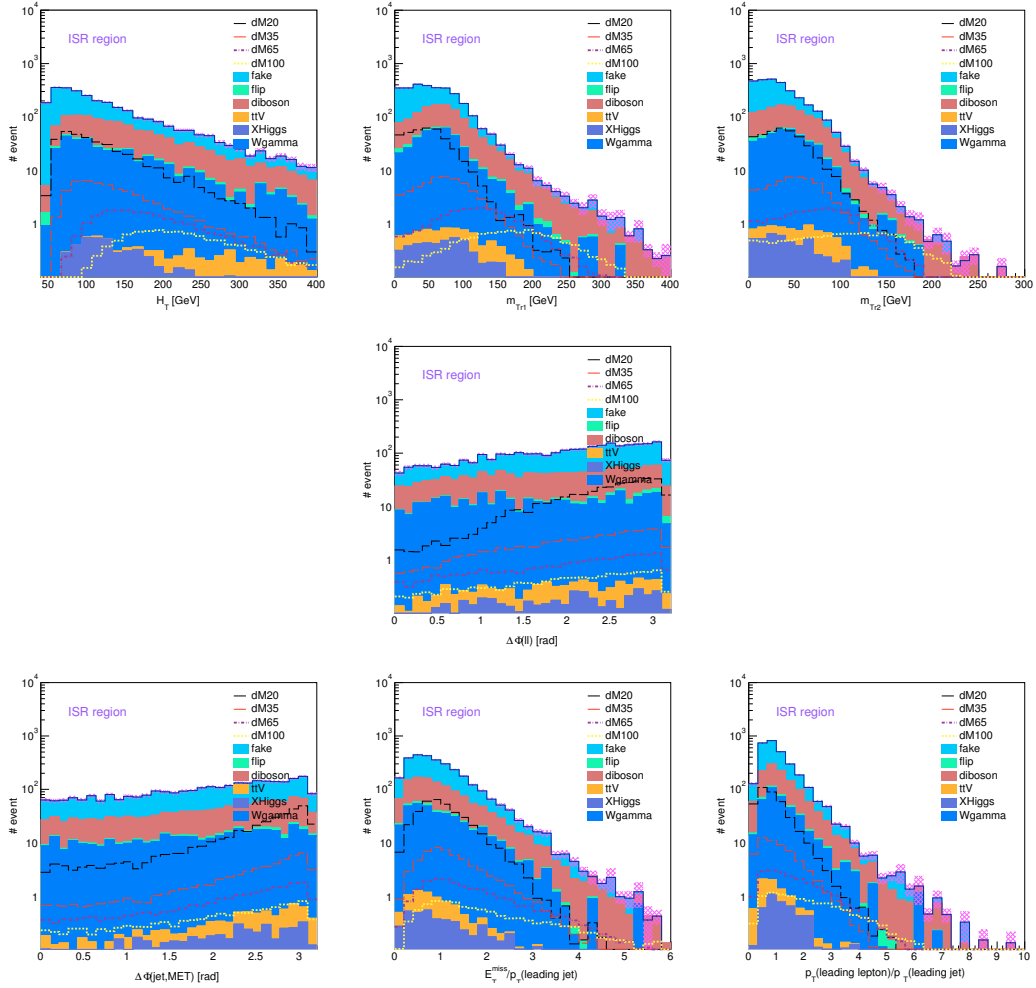


Figure 8.6: Distribution of H_T (top-left), m_{Tlep1} (top-center), m_{Tlep2} (top-right), $\Delta\phi_{\ell\ell}$ (center), $\Delta\phi(E_T^{\text{miss}}, \text{leading jet})$ (bottom-left), $E_T^{\text{miss}}/p_T(\text{leading jet})$ (bottom-center) and $p_T(\text{leading lepton})/p_T(\text{leading jet})$ (bottom-right) for the signal and the background for ISR region.

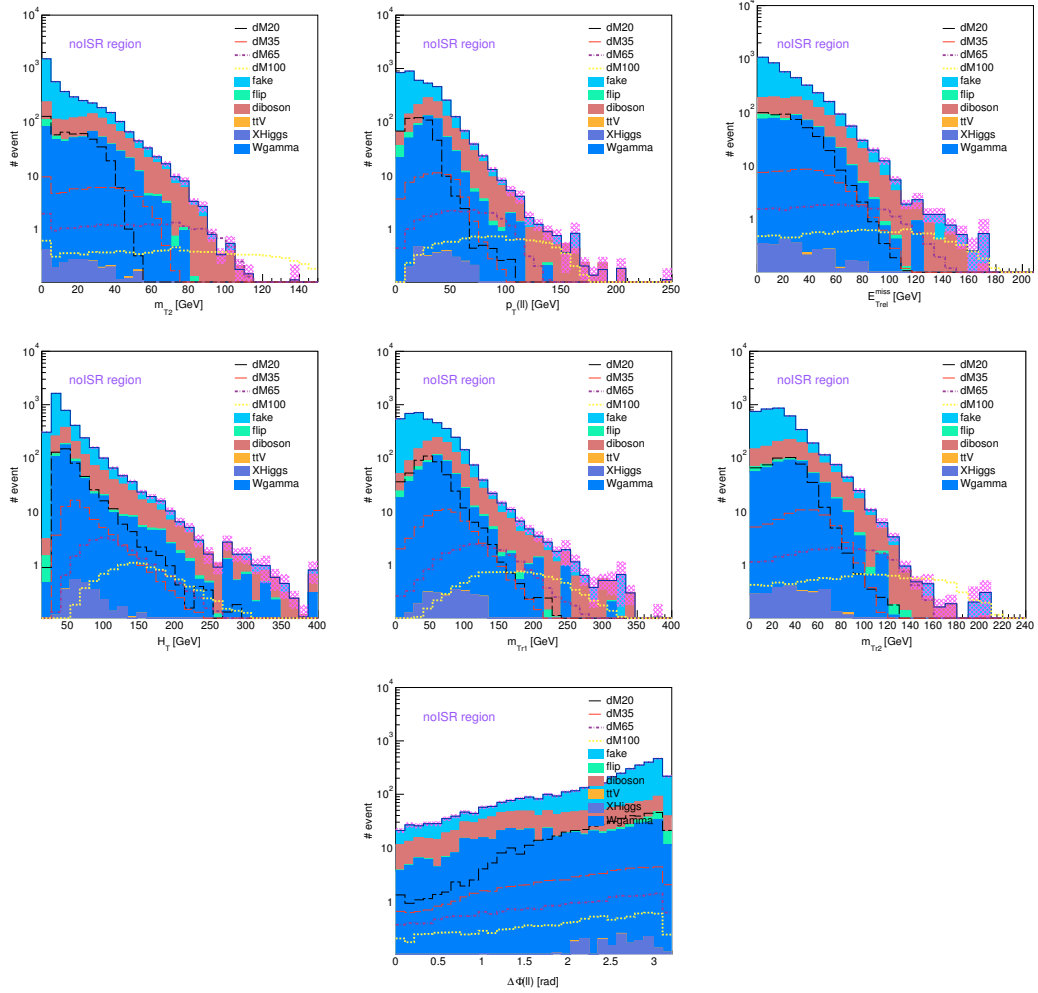


Figure 8.7: Distribution of m_{T2} (top-left), p_{Tl} (top-center) and $E_T^{\text{miss,rel}}$ (top-right) H_T (middle-left), m_{Tlep1} (middle-center), m_{Tlep2} (middle-right) and $\Delta\phi_{\ell\ell}$ (bottom) for the signal and the background for region without an ISR jet.

8.4.4 BDT Output and testing

The training samples represents 75% of the available MC statistics. The remainder are reserved for testing after the training of the BDTs using a Kolmogorov-Smirnov test [81] to evaluate the goodness of the fit and check for overfitting. An example of this testing is shown in Figure 8.8. In this case, the training and the testing sample show similar BDT responses for both background and signal samples and thus small values (good agreement) for KS test, demonstrating a well-trained BDT and no overfitting.

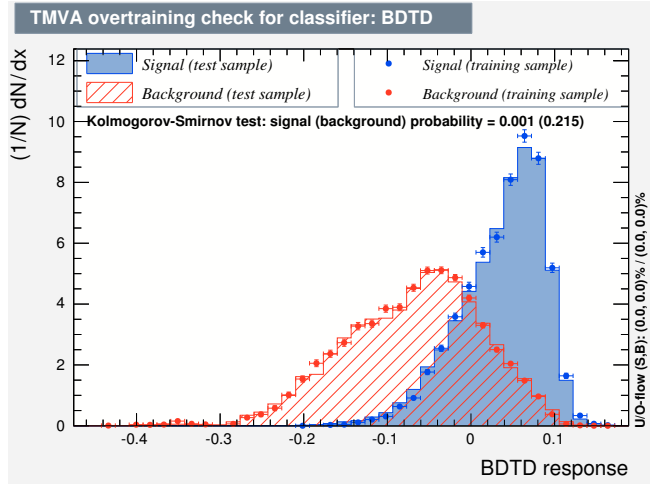


Figure 8.8: Results of the Kolmogorov-Smirnov test for the BDT on the training and testing samples

The ranking of variables in the BDT by discriminatory power is shown in Table 8.4 for the different boosted decision trees in the ISR signal regions.

Table 8.4: Importance of the variables used for the BDT training

$\Delta M=20$ GeV	$\Delta M=35$ GeV	$\Delta M=65$ GeV	$\Delta M=100$ GeV
ISR	ISR	ISR	ISR
$\Delta\Phi(MET, jet)$	m_{Tr2}	m_{Tr2}	$\Delta\Phi(MET, jet)$
$\Delta\phi(ll)$	m_{Tr1}	m_{Tr1}	H_T
$p_T(ll)$	E_{Trel}^{miss}	H_T	m_{Tr1}
m_{T2}	$\Delta\phi(ll)$	$\Delta\Phi(MET, jet)$	$\Delta\phi(ll)$
m_{Tr1}	$p_T(ll)$	E_{Trel}^{miss}	m_{Tr2}
m_{Tr2}	$p_T(lep)/p_T(jet)$	$\Delta\phi(ll)$	E_{Trel}^{miss}
H_T	$\Delta\Phi(MET, jet)$	$E_{Trel}^{miss}/p_T(jet)$	$p_T(lep)/p_T(jet)$
E_{Trel}^{miss}	H_T	$p_T(lep)/p_T(jet)$	m_{T2}

8.4.5 Signal Region definitions

Cut values on the respective BDT outputs are chosen to maximize the Z_N figure of merit for each of the 8 signal regions (four mass splittings for each ISR and no ISR). The cut values on the eight BDT discriminants used to define the signal regions are given in Table 8.5.

Table 8.5: Signal Region BDT cuts

$\Delta\mathbf{m}(\tilde{\chi}_1^\pm, \tilde{\chi}_2^0; \tilde{\chi}_1^0)$	20	35	65	100
ISR	> 0.071	> 0.087	> 0.103	> 0.119
no ISR	> 0.071	> 0.087	> 0.135	> 0.135

CHAPTER 9

Systematic Uncertainties

9.1 Systematic Uncertainties for background estimates

The list of systematics considered in this analysis are listed in Table 9.1. The backgrounds for charge misidentification and non-prompt leptons are determined from weighted data events and are therefore only correlated among signal regions ($CT = 1$). More details on the uncertainties considered for these backgrounds can be found in Sections 7.3 and 7.2, respectively. Theory uncertainties for MC backgrounds including cross-section, renormalization scale and MC generator are process dependent and thus only correlated between regions ($CT = 1$). All other systematics are correlated among both regions and processes ($CT = 3$). The type of systematic: weight or tree indicates whether the basic selection or rejection of an event can occur. For weights, the relative importance of an event can change, but its selection or rejection for a given signal or validation region is not affected. Other systematics such as those affecting the energy scales of each of the particle types, can move individual objects above or below a cut value, leading to differing raw (unweighted) Monte Carlo event yields.

A list showing the dominant overall systematics is shown in Table 9.2, the top systematics are quite constant among all the sub-channels. The uncertainty on the fake background, specifically on the fake rate determination, and the lack of MC statistics are generally dominant uncertainties, followed closely by the generator uncertainty for the WZ and $W\gamma$ processes and the Jet Energy Resolution.

Table 9.1: Correlation Type (CT) : None=0, Regions=1, Processes=2, Regions and Processes=3. HistFitter Type (HFT) : Tree or weight.

Source	CT	HFT
jet energy scale (JES)	3	tree
jet energy resolution (JER)	3	tree
b-jet tagging weight (BJET)	3	weight
c-jet tagging weight (CJET)	3	weight
light-jet tagging weight (BMISTAG)	3	weight
pileup (PILEUP)	3	weight
electron energy scale (LOW,MAT,PS,Z)	3	tree
electron energy resolution (EER)	3	tree
electron scale factor (ESF)	3	weight
muon ID (MID)	3	tree
muon MS (MMS)	3	tree
muon efficiency (MEFF)	3	weight
tau energy scale (TES)	3	tree
MET soft term scale (SCALEST)	3	tree
MET soft term resolution (RESOST)	3	tree
trigger reweight (TRIGREW)	3	weight
fake rate (FAKE)	1	weight
charge misid rate (FLIP)	1	weight
generator (proc_GEN)	1	weight
cross section (proc_XS)	1	weight
luminosity (LUMI)	3	weight

Table 9.2: Overview of the dominant systematic uncertainties on background estimates in the various signal regions. The percentages show the size of the uncertainty relative to the total expected background and the range show the variation among the flavor channels.

	SR ΔM_{20}		SR ΔM_{35}		SR ΔM_{65}		SR ΔM_{100}	
	ISR	no-ISR	ISR	no-ISR	ISR	no-ISR	ISR	no-ISR
Reducible background								
- Fake lepton composition	7-14%	15-20%	4-14%	5-17%	5-17%	21%	9-24%	20-22%
- Real lepton subtraction	13-32%	12-25%	10-20%	18-26%	8-18%	26%	15-32%	22-33%
- Statistical uncertainty on data	5-8%	9-12%	3-7%	4-8%	3-9%	9%	5-11%	9-11%
Statistical uncertainty on MC	15-37%	7-12%	15-28%	8-16%	15-43%	16-32%	30-45%	35-74%
Choice of generator for WZ	9-17%	4-20%	15-17%	5-11%	13-20%	6-21%	3-27%	4-20%
Choice of generator for $W\gamma$	2-3%	3-7%	2%	4-8%	3-9%	-	-	-
Jet energy resolution	1-18%	1-7%	1-7%	6-12%	1-10%	1-6%	5-70%	4-35%
Total	28-81%	18-32%	28-48%	22-37%	33-47%	33-50%	39-67%	55-71%

9.2 Systematic Uncertainties for Signal Models

For uncertainties on the cross sections for considered signal models, a procedure standard to all Atlas SUSY searches is used.

This procedure can result in asymmetric uncertainties. The CTEQ PDF, scale, and α_s uncertainties are combined in quadrature for the upward shifts and for the downward shifts. This is also done for the MSTW PDF and scale uncertainties. The maximum value of the CTEQ and MSTW uncertainties is then chosen as the upper and lower systematic uncertainties. The average ($0.5 \times (a + b)$) is used as the central value of the cross section, and the relative difference $[(a - b)/(a + b)]$ as a symmetric uncertainty. The total signal cross section uncertainty is around 7-10% and is listed with the individual signal samples in Tables 6.1-6.4.

9.3 Initial State Radiation

An additional systematic is added to the signal variation to account for uncertainty due to the presence of an ISR jet. The yields obtained from the default sample generated with Herwig++ are compared with those using Madgraph, with 0 or 1 additional parton in the hard scatter. Because of this ability to include additional partons via matrix element calculations, Madgraph is expected to better model ISR. For the Madgraph samples, the Scale, ISR and Q parameters were varied, and the total uncertainty was taken as their sum in quadrature. These values are shown in Table 9.3.

Total Uncertainty	$\Delta M20$	$\Delta M35$	$\Delta M65$	$\Delta M100$
ISR	+5.2	+5.7	+6.7	+8.7
	-14.6	-12.3	-7.9	-4.7
No ISR	+7.4	+7.	+8.6	+10.1
	-4.8	-4.8	-4.7	-4.6

Table 9.3: Systematic applied to signal models to account for modeling of Initial State Radiation

CHAPTER 10

Validation of Background Estimates

Before examining the signal regions, several validation regions are defined in order to evaluate the performance of the background estimation techniques defined in Section 7 in a region where little signal is expected. Two types of validation regions are defined, one is a general same-sign region based on the BDT output, which is described in Section 10.1; the other is selected to target diboson events specifically, and is described in Section 10.2.

10.1 General Same-sign Validation Regions

It is desirable to define the validation regions as close to the signal regions as possible while maintaining a minimal amount of signal contamination in the validation regions. For the $\Delta M=65$ and 100 GeV scenarios, the validation regions are able to share an upper boundary with the lower boundary of the signal region with minimal signal contamination. For the $\Delta M=35$ and 20 GeV scenarios, this is not possible due to the signal contamination and a small buffer between the upper boundary of the validation region and the lower boundary of the signal region is needed. The validation regions are all defined to be 0.10 in width in BDT output to collect sufficient statistics. The validation region definition is given in Table 10.1. The contamination of signal points with the highest cross section in the validation regions is given in Table 10.2. For all validation regions and sub-channels, the level of maximum contamination is less than 30%, with most less than 10%.

Table 10.1: Validation Region BDT cuts

$\Delta m(\tilde{\chi}_1^\pm, \tilde{\chi}_2^0, \tilde{\chi}_1^0)$	20	35	65	100
ISR	[-0.049;0.051]	[-0.023;0.077]	[0.003;0.103]	[0.019;0.119]
no ISR	[-0.049;0.051]	[-0.023;0.077]	[0.035;0.135]	[0.035;0.135]

The BDT output distributions inside the validation regions are shown Fig 10.1 to Fig 10.4. Good agreement is observed between the expected and observed events. This can also be seen in the pull distributions, shown in Figure 10.5. While there is a systematic overestimate in the ee regions, all estimates are well within the uncertainties. Additional plots for each of the kinematic variables used in the BDTs are shown for all the validation regions in Appendix A.

ΔM [GeV]	20						35					
C1N2 [GeV]	135			260			142			192		
chan	ee	$e\mu$	$\mu\mu$									
ISR [%]	5	12	25	<1	1	3	10	22	28	3	10	12
no ISR [%]	4	11	21	<1	<1	2	7	15	29	2	9	12
ΔM [GeV]	65						100					
C1N2 [GeV]	207			282			300			425		
chan	ee	$e\mu$	$\mu\mu$									
ISR [%]	7	16	20	2	4	7	5	9	13	<1	1	2
no ISR [%]	9	21	28	3	8	11	6	11	14	<1	2	2

Table 10.2: Signal contamination (in %) in each validation region for each channel.

-	$\Delta M = 20$ ISR			$\Delta M = 20$ no ISR		
	ee	$e\mu$	$\mu\mu$	ee	$e\mu$	$\mu\mu$
fake	$263.84 \pm 16.98 \pm 138.24$	$671.85 \pm 52.64 \pm 327.16$	$155.17 \pm 65.99 \pm 91.02$	$410.55 \pm 21.56 \pm 183.99$	$1052.41 \pm 63.64 \pm 394.54$	$309.75 \pm 78.89 \pm 154.87$
flip	$289.18 \pm 4.51 \pm 13.84$	$15.04 \pm 0.84 \pm 0.89$	-	$711.18 \pm 6.87 \pm 33.36$	$28.13 \pm 1.13 \pm 1.59$	-
diboson	$58.37 \pm 4.90 \pm 22.21$	$154.54 \pm 7.21 \pm 35.99$	$110.04 \pm 6.16 \pm 25.30$	$67.18 \pm 5.38 \pm 24.16$	$199.24 \pm 8.40 \pm 42.67$	$154.36 \pm 7.39 \pm 33.56$
higgs	$0.42 \pm 0.20 \pm 0.22$	$0.74 \pm 0.25 \pm 0.38$	$0.69 \pm 0.28 \pm 0.36$	$0.23 \pm 0.13 \pm 0.12$	$0.59 \pm 0.21 \pm 0.30$	$0.50 \pm 0.22 \pm 0.25$
ttV	$0.23 \pm 0.12 \pm 0.13$	$0.66 \pm 0.19 \pm 0.36$	$0.44 \pm 0.17 \pm 0.24$	$0.01 \pm 0.01 \pm 0.02$	$0.01 \pm 0.01 \pm 0.02$	$0.01 \pm 0.01 \pm 0.02$
$W\gamma$	$61.11 \pm 13.87 \pm 21.09$	$93.92 \pm 16.25 \pm 16.21$	$0.99 \pm 0.85 \pm 0.17$	$124.19 \pm 19.92 \pm 43.05$	$197.96 \pm 24.16 \pm 34.77$	$2.27 \pm 2.00 \pm 0.40$
total	$673.15 \pm 22.92 \pm 142.27$	$936.75 \pm 55.56 \pm 329.53$	$267.33 \pm 66.29 \pm 94.47$	$1313.34 \pm 30.62 \pm 193.40$	$1478.34 \pm 68.60 \pm 398.37$	$466.88 \pm 79.26 \pm 158.47$
data	585.00	799.00	363.00	1134.00	1349.00	612.00

Table 10.3: Expected and observed number of events in the validation regions with $\Delta M = 20$ GeV and with or without ISR jets. The first uncertainty is statistical and the second is from systematics.

-	$\Delta M = 35$ ISR			$\Delta M = 35$ no ISR		
	ee	$e\mu$	$\mu\mu$	ee	$e\mu$	$\mu\mu$
fake	$200.14 \pm 15.31 \pm 99.28$	$310.29 \pm 30.71 \pm 136.71$	$177.04 \pm 36.51 \pm 99.52$	$267.79 \pm 18.14 \pm 117.63$	$359.72 \pm 35.35 \pm 150.46$	$155.58 \pm 40.15 \pm 108.51$
flip	$219.22 \pm 3.93 \pm 10.18$	$12.56 \pm 0.85 \pm 0.74$	-	$400.83 \pm 5.37 \pm 17.42$	$15.22 \pm 0.92 \pm 0.80$	-
diboson	$72.31 \pm 5.50 \pm 26.41$	$182.87 \pm 7.87 \pm 40.04$	$132.12 \pm 6.85 \pm 28.95$	$67.29 \pm 5.55 \pm 24.05$	$186.76 \pm 8.17 \pm 37.77$	$147.32 \pm 7.45 \pm 30.77$
higgs	$0.58 \pm 0.25 \pm 0.29$	$1.09 \pm 0.35 \pm 0.55$	$0.95 \pm 0.34 \pm 0.48$	$0.37 \pm 0.20 \pm 0.19$	$0.87 \pm 0.32 \pm 0.44$	$0.74 \pm 0.28 \pm 0.38$
ttV	$0.38 \pm 0.15 \pm 0.20$	$0.82 \pm 0.21 \pm 0.44$	$0.67 \pm 0.21 \pm 0.36$	$0.01 \pm 0.01 \pm 0.02$	$0.03 \pm 0.03 \pm 0.04$	$0.00 \pm 0.00 \pm 0.00$
$W\gamma$	$73.55 \pm 15.30 \pm 25.21$	$90.27 \pm 15.00 \pm 15.14$	$0.80 \pm 0.63 \pm 0.13$	$122.58 \pm 20.25 \pm 42.44$	$156.90 \pm 21.51 \pm 27.43$	$1.87 \pm 1.65 \pm 0.33$
total	$566.17 \pm 22.68 \pm 106.27$	$597.90 \pm 35.08 \pm 143.26$	$311.59 \pm 37.15 \pm 103.64$	$858.87 \pm 28.27 \pm 128.53$	$719.51 \pm 42.19 \pm 157.54$	$305.51 \pm 40.87 \pm 112.79$
data	452.00	557.00	233.00	737.00	684.00	288.00

Table 10.4: Expected and observed number of events in the validation regions with $\Delta M = 35$ GeV and with or without ISR jets. The first uncertainty is statistical and the second is from systematics.

-	$\Delta M = 65$ ISR			$\Delta M = 65$ no ISR		
-	ee	$e\mu$	$\mu\mu$	ee	$e\mu$	$\mu\mu$
fake	$81.10 \pm 10.23 \pm 43.09$	$89.78 \pm 13.42 \pm 42.86$	$32.03 \pm 12.26 \pm 14.05$	$42.76 \pm 7.71 \pm 20.93$	$57.48 \pm 11.35 \pm 27.05$	$13.72 \pm 9.56 \pm 8.93$
flip	$72.33 \pm 2.44 \pm 4.15$	$7.65 \pm 0.73 \pm 0.54$	-	$35.37 \pm 1.77 \pm 2.03$	$4.45 \pm 0.54 \pm 0.29$	-
diboson	$42.05 \pm 4.13 \pm 15.57$	$104.23 \pm 5.79 \pm 23.41$	$74.39 \pm 5.11 \pm 16.82$	$15.21 \pm 2.48 \pm 5.44$	$55.63 \pm 4.28 \pm 10.59$	$50.22 \pm 4.34 \pm 9.87$
higgs	$0.38 \pm 0.21 \pm 0.19$	$0.73 \pm 0.29 \pm 0.37$	$0.58 \pm 0.30 \pm 0.29$	$0.21 \pm 0.14 \pm 0.11$	$0.42 \pm 0.23 \pm 0.22$	$0.50 \pm 0.24 \pm 0.25$
ttV	$0.33 \pm 0.14 \pm 0.18$	$0.84 \pm 0.20 \pm 0.46$	$0.59 \pm 0.19 \pm 0.33$	$0.00 \pm 0.00 \pm 0.00$	$0.03 \pm 0.02 \pm 0.01$	$0.00 \pm 0.00 \pm 0.00$
$W\gamma$	$21.87 \pm 6.93 \pm 7.45$	$39.09 \pm 9.80 \pm 6.41$	$0.08 \pm 0.08 \pm 0.01$	$21.09 \pm 7.34 \pm 7.31$	$23.87 \pm 6.45 \pm 4.18$	$0.00 \pm 0.00 \pm 0.00$
total	$218.06 \pm 13.26 \pm 46.60$	$242.32 \pm 17.62 \pm 49.27$	$107.67 \pm 13.28 \pm 21.92$	$114.64 \pm 11.07 \pm 22.92$	$141.88 \pm 13.75 \pm 29.35$	$64.43 \pm 10.50 \pm 13.31$
data	165.00	210.00	97.00	82.00	117.00	69.00

Table 10.5: Expected and observed number of events in the validation regions with $\Delta M = 65$ GeV and with or without ISR jets. The first uncertainty is statistical and the second is from systematics.

-	$\Delta M = 100$ ISR			$\Delta M = 100$ no ISR		
-	ee	$e\mu$	$\mu\mu$	ee	$e\mu$	$\mu\mu$
fake	$27.35 \pm 6.21 \pm 17.54$	$35.16 \pm 7.68 \pm 17.42$	$6.14 \pm 3.91 \pm 2.51$	$21.69 \pm 5.11 \pm 11.24$	$18.08 \pm 5.51 \pm 9.44$	$6.10 \pm 4.16 \pm 2.51$
flip	$24.77 \pm 1.44 \pm 1.62$	$4.38 \pm 0.53 \pm 0.33$	-	$18.00 \pm 1.30 \pm 1.11$	$2.52 \pm 0.41 \pm 0.18$	-
diboson	$19.35 \pm 2.61 \pm 7.32$	$45.05 \pm 3.57 \pm 10.78$	$32.28 \pm 3.21 \pm 7.63$	$7.28 \pm 1.66 \pm 2.63$	$26.61 \pm 2.88 \pm 5.20$	$23.29 \pm 2.78 \pm 4.58$
higgs	$0.17 \pm 0.11 \pm 0.09$	$0.35 \pm 0.17 \pm 0.18$	$0.27 \pm 0.16 \pm 0.14$	$0.14 \pm 0.10 \pm 0.07$	$0.25 \pm 0.18 \pm 0.13$	$0.22 \pm 0.15 \pm 0.11$
ttV	$0.23 \pm 0.11 \pm 0.12$	$0.54 \pm 0.14 \pm 0.29$	$0.39 \pm 0.14 \pm 0.21$	$0.00 \pm 0.00 \pm 0.00$	$0.02 \pm 0.02 \pm 0.03$	$0.00 \pm 0.00 \pm 0.00$
$W\gamma$	$9.09 \pm 4.37 \pm 3.10$	$13.26 \pm 4.59 \pm 2.17$	$0.08 \pm 0.08 \pm 0.01$	$8.11 \pm 3.98 \pm 2.81$	$8.81 \pm 3.48 \pm 1.54$	$0.00 \pm 0.00 \pm 0.00$
total	$80.97 \pm 8.16 \pm 19.32$	$98.73 \pm 9.65 \pm 20.60$	$39.16 \pm 5.06 \pm 8.03$	$55.21 \pm 6.82 \pm 11.93$	$56.29 \pm 7.14 \pm 10.89$	$29.60 \pm 5.01 \pm 5.23$
data	75.00	71.00	32.00	41.00	50.00	31.00

Table 10.6: Expected and observed number of events in the validation regions with $\Delta M = 100$ GeV and with or without ISR jets. The first uncertainty is statistical and the second is from systematics.

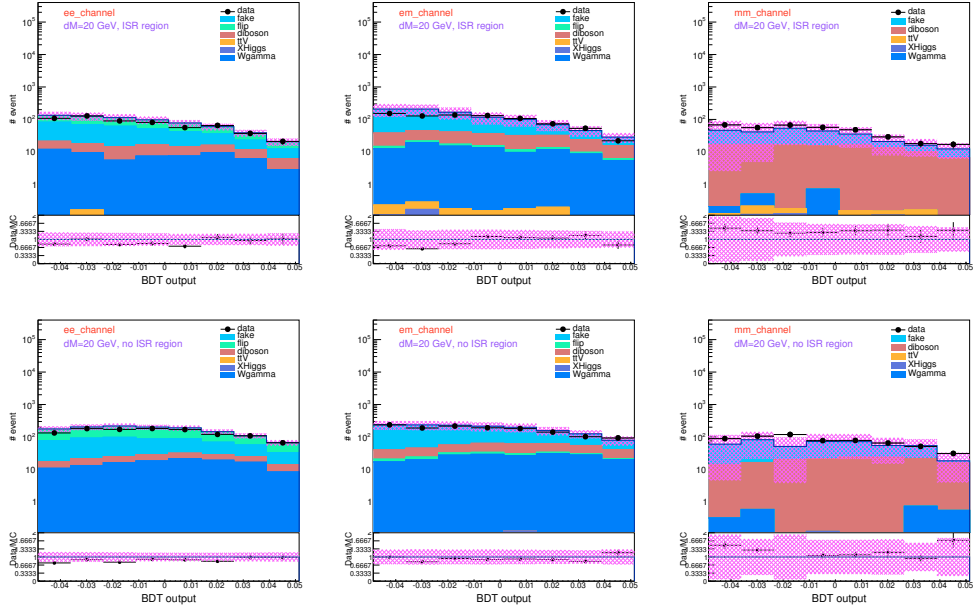


Figure 10.1: BDT output distribution inside the Validation Region for $\Delta M=20$ GeV with (top) and without (bottom) an ISR jet for the three channels (ee at left, $e\mu$ in the middle and $\mu\mu$ at right).

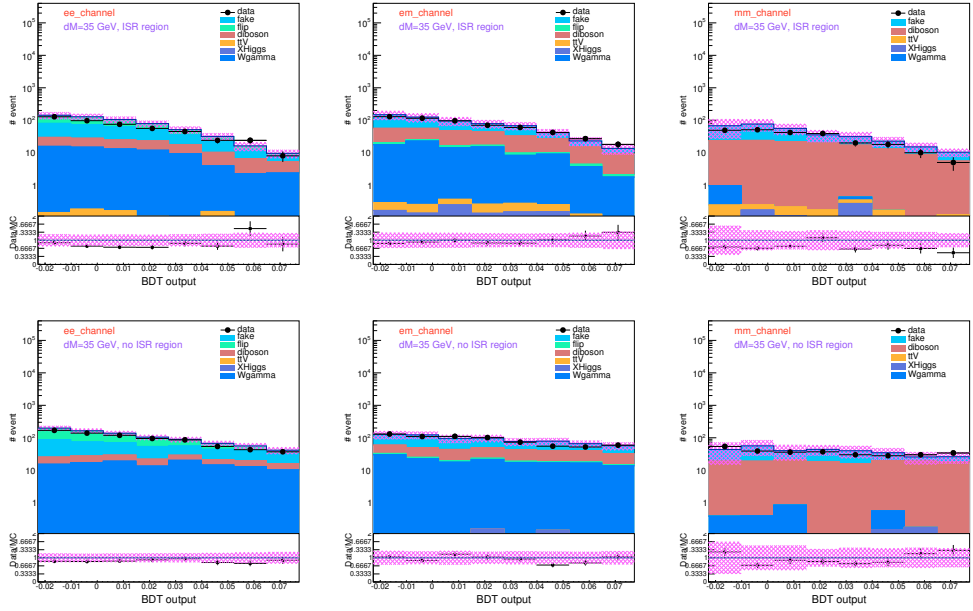


Figure 10.2: BDT output distribution inside the Validation Region for $\Delta M=35$ GeV with (top) and without (bottom) an ISR jet for the three channels (ee at left, $e\mu$ in the middle and $\mu\mu$ at right).

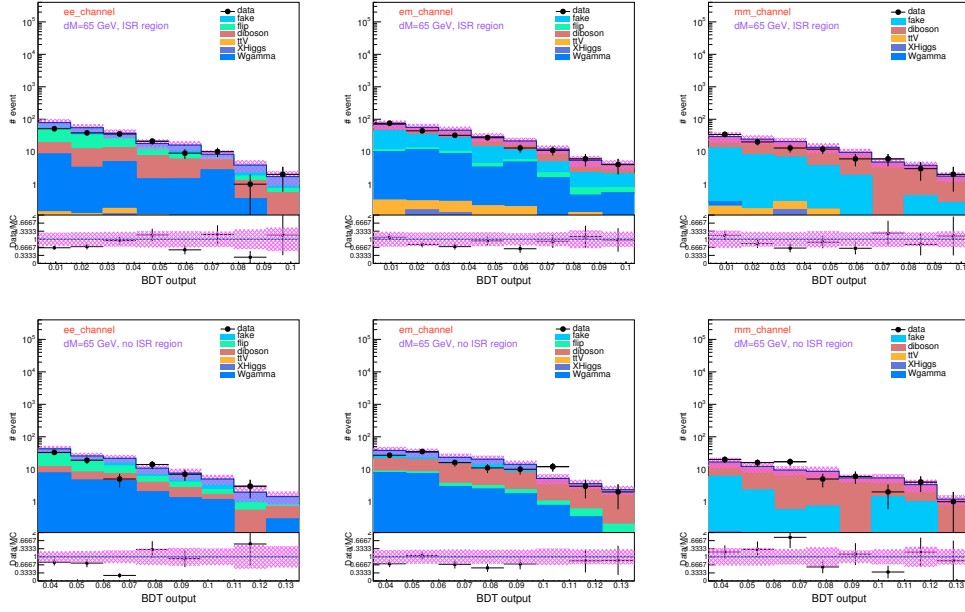


Figure 10.3: BDT output distribution inside the Validation Region for $\Delta M=65$ GeV with (top) and without (bottom) an ISR jet for the three channels (ee at left, $e\mu$ in the middle and $\mu\mu$ at right).

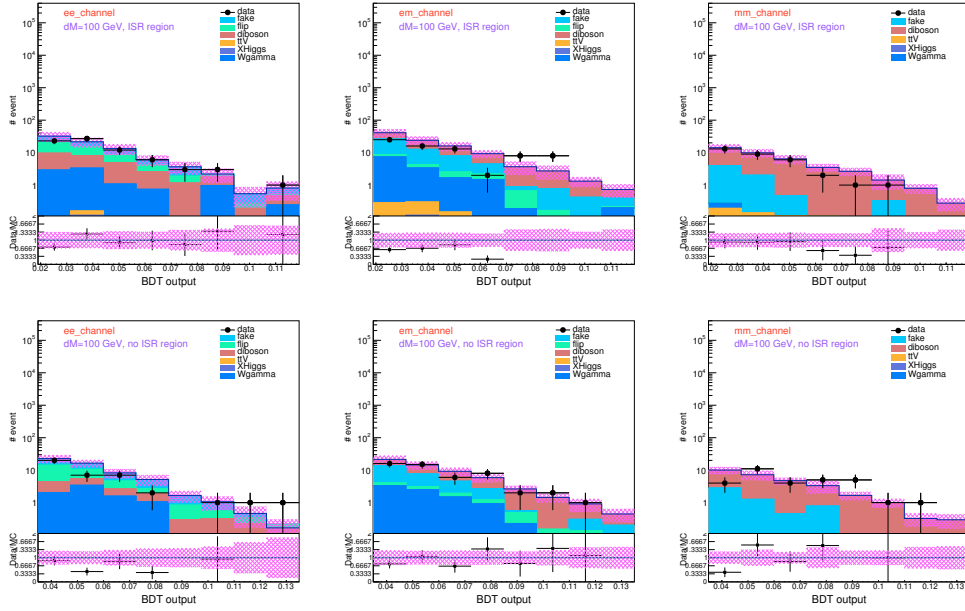


Figure 10.4: BDT output distribution inside the Validation Region for $\Delta M=100$ GeV with (top) and without (bottom) an ISR jet for the three channels (ee at left, $e\mu$ in the middle and $\mu\mu$ at right).

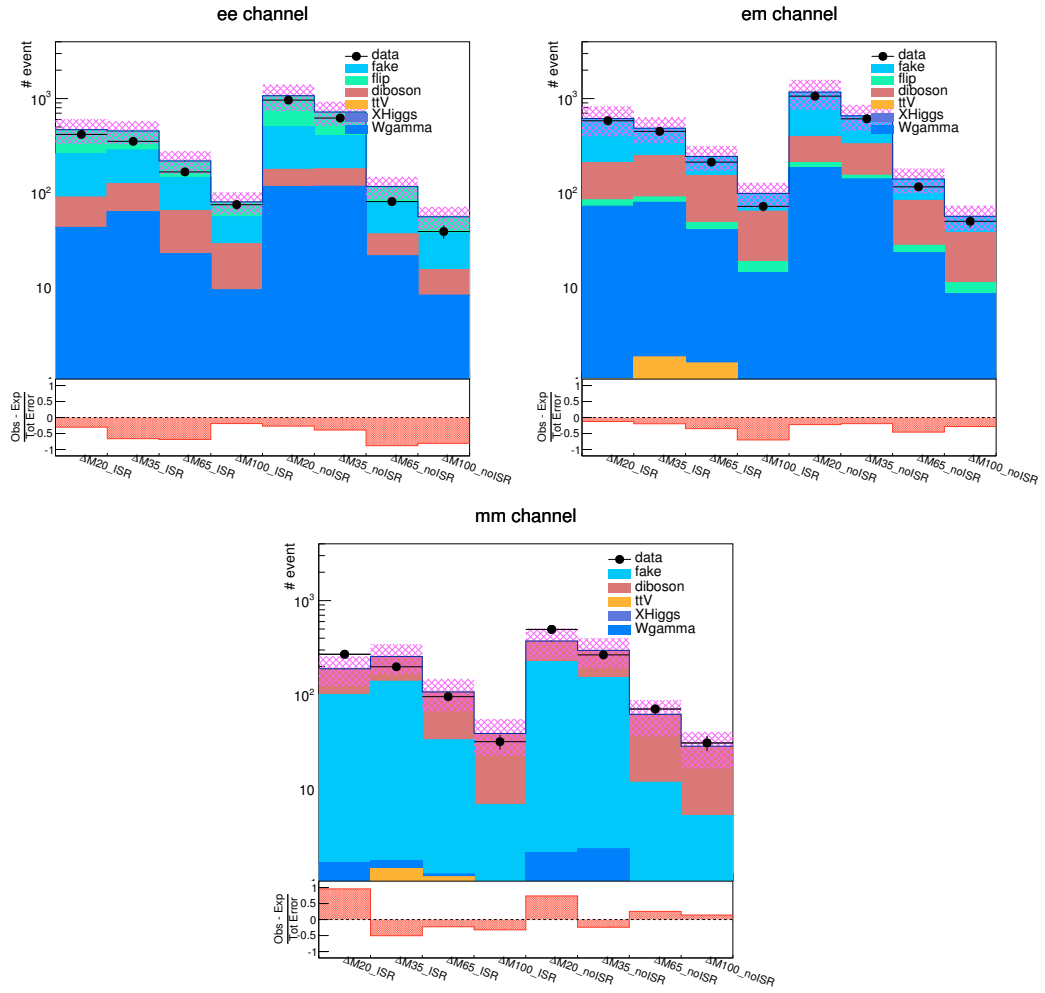


Figure 10.5: Pull plot per channel for all the 8 validation regions for the ee channel (top left), $e\mu$ channel (top right) and $\mu\mu$ channel (bottom).

10.2 Dedicated Regions for Validation of Diboson Background

Because the diboson contribution is the dominant background source for many of the signal regions, but several of the validation regions disproportionately contain fake or charge-flip background, addition dedicated diboson validation regions are also defined.

The following diboson region is chosen:

- $p_T(\text{leading lepton}) > 35 \text{ GeV}$
- $p_T(\text{subleading lepton}) > 30 \text{ GeV}$
- ISR region
- $e\mu$ or $\mu\mu$ event
- BDT score given by Table 10.7 :

Table 10.7: Validation Region BDT cuts.

$\Delta m(\tilde{\chi}_1^\pm, \tilde{\chi}_2^0, \tilde{\chi}_1^0)$	20	35	65	100
ISR	[-0.009;0.051]	[0.017;0.077]	[0.043;0.103]	[0.059;0.119]
no ISR	[-0.009;0.051]	[0.017;0.077]	[0.075;0.135]	[0.075;0.135]

Both the increased p_T requirements and the BDT score shifted to higher values attempt to reduce the contribution from fakes. The results for some of the kinematic distributions for the WZ validation region are shown in Figures 10.6-10.9. Good agreement is seen, providing assurance that the estimate from the WZ background is understood.

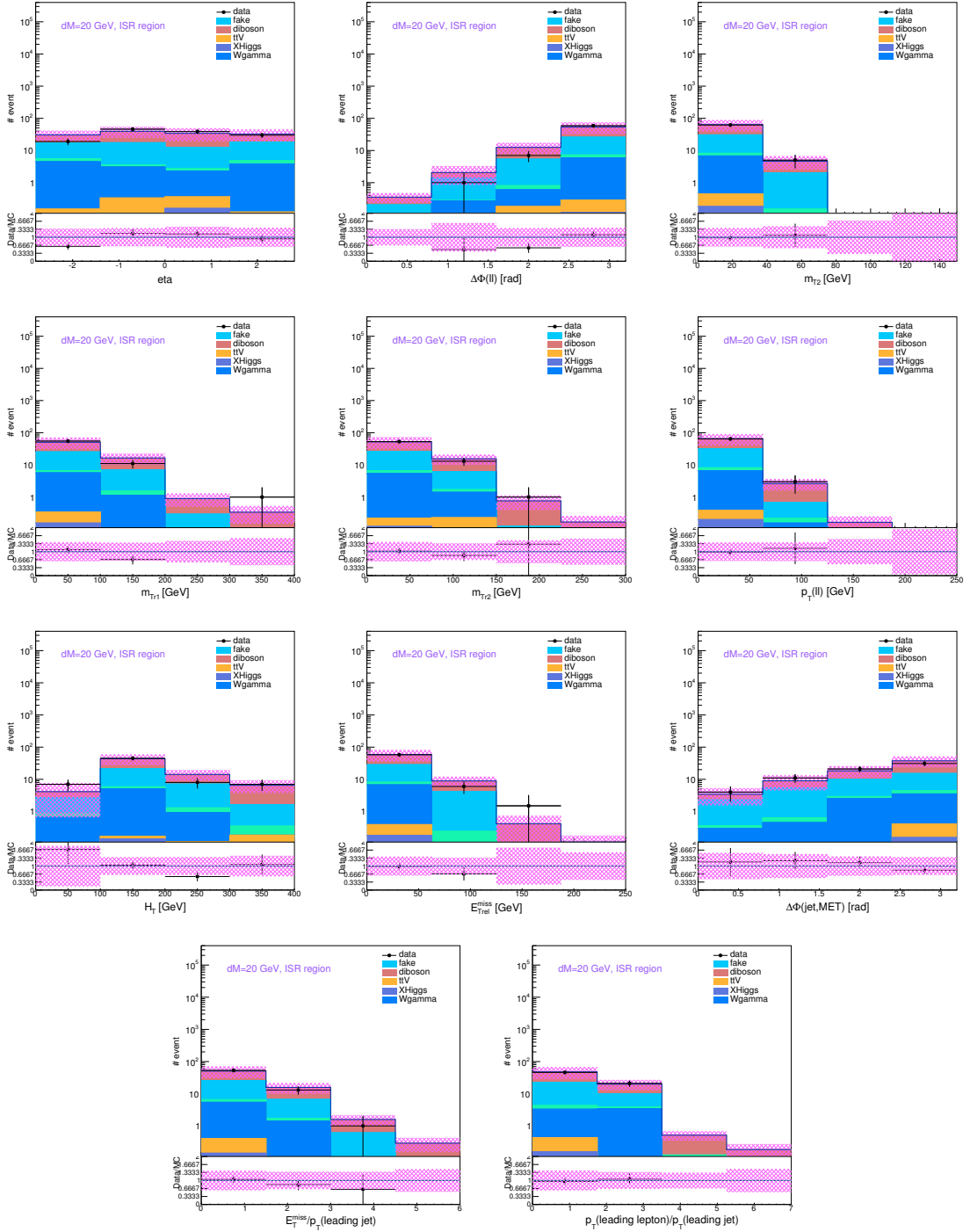


Figure 10.6: Distribution of $|\eta|$, $\Delta\phi_{\ell\ell}$, m_{T2} , m_{Tlep1} , m_{Tlep2} , p_{Tl} , H_T , $E_T^{\text{miss,rel}}$, $\Delta\phi(E_T^{\text{miss}}, \text{leading jet})$, $E_T^{\text{miss}}/p_T(\text{leading jet})$ and $p_T(\text{leading lepton})/p_T(\text{leading jet})$ for $\Delta M=20$ GeV.

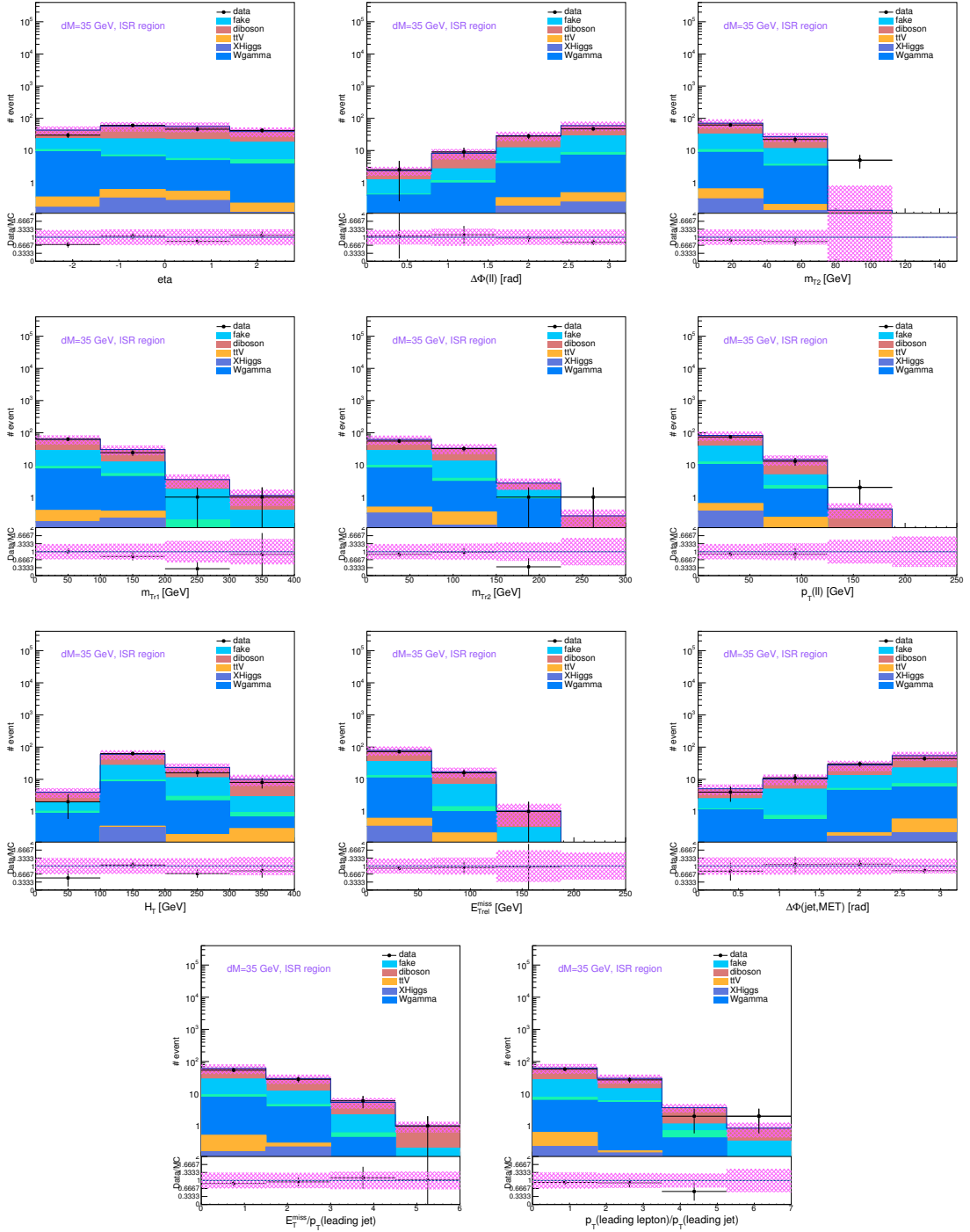


Figure 10.7: Distribution of $|\eta|$, $\Delta\phi_{\ell\ell}$, m_{T2} , m_{Tlep1} , m_{Tlep2} , p_{Tl} , H_T , $E_T^{\text{miss,rel}}$, $\Delta\phi(E_T^{\text{miss}}, \text{leading jet})$, $E_T^{\text{miss}}/p_T(\text{leading jet})$ and $p_T(\text{leading lepton})/p_T(\text{leading jet})$ for $\Delta M=35$ GeV.

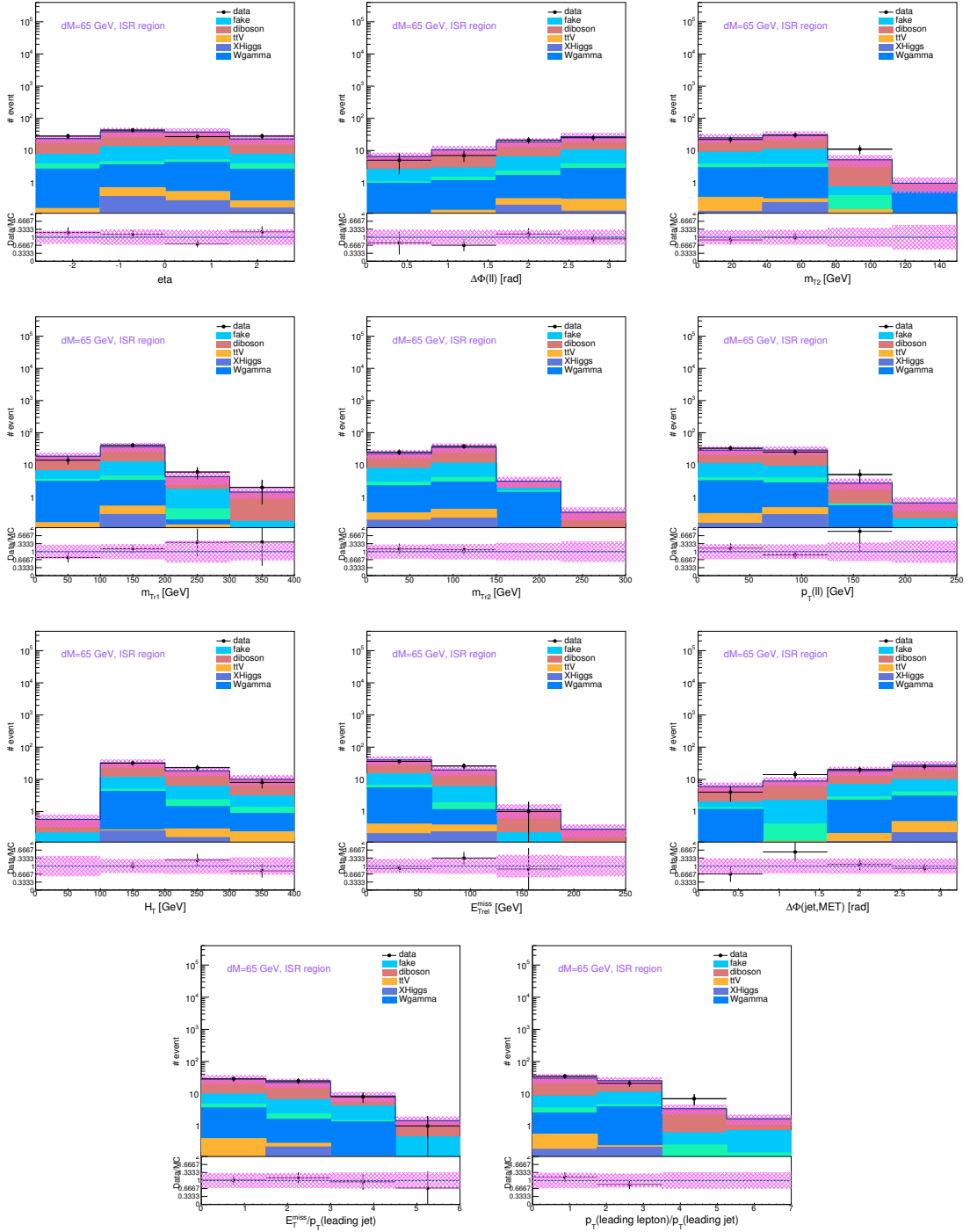


Figure 10.8: Distribution of $|\eta|$, $\Delta\phi_{\ell\ell}$, m_{T2} , m_{Tlep1} , m_{Tlep2} , p_{Tl} , H_T , $E_T^{\text{miss,rel}}$, $\Delta\phi(E_T^{\text{miss}}, \text{leading jet})$, $E_T^{\text{miss}}/p_T(\text{leading jet})$ and $p_T(\text{leading lepton})/p_T(\text{leading jet})$ for $\Delta M=65$ GeV.

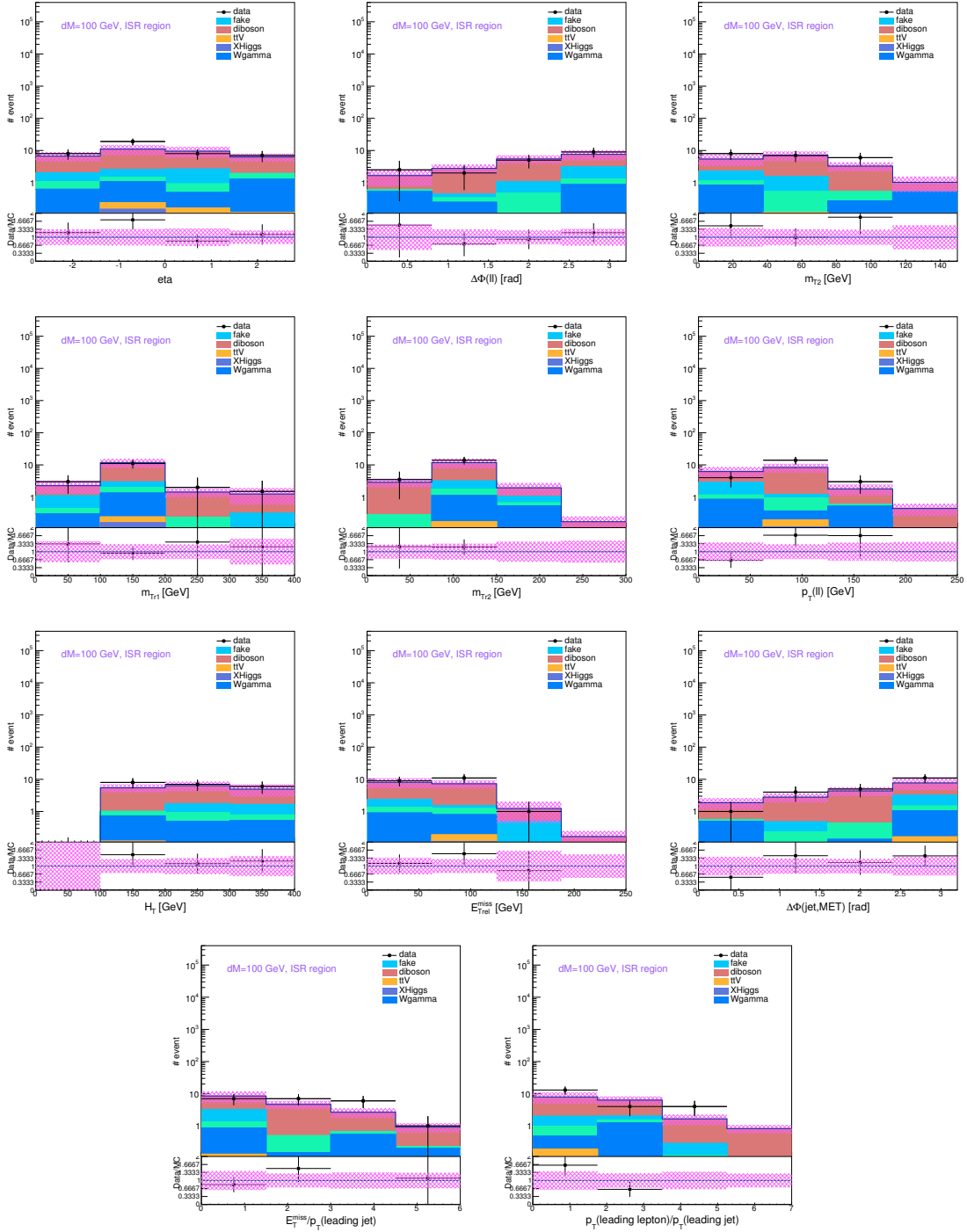


Figure 10.9: Distribution of $|\eta|$, $\Delta\phi_{\ell\ell}$, m_{T2} , m_{Tlep1} , m_{Tlep2} , p_{Tl} , H_T , $E_T^{\text{miss,rel}}$, $\Delta\phi(E_T^{\text{miss}}, \text{leading jet})$, $E_T^{\text{miss}}/p_T(\text{leading jet})$ and $p_T(\text{leading lepton})/p_T(\text{leading jet})$ for $\Delta M=100$ GeV.

CHAPTER 11

Results

The expected number of background events for each of the sources is compared to the observed number of events in data in Tables 11.1-11.4. Results are grouped by the signal region's mass splitting and numbers are shown separated for the three flavor channels and for ISR and no-ISR regions. Uncertainties shown are statistical and systematic, respectively.

The same results are shown for the output value of the Boosted Decision trees in Figures 11.1-11.4. Here it is easier to see that there are no disagreements larger than the associated uncertainties.

As no significant excesses are found to indicate the presence of our signal from $\tilde{\chi}_1^\pm \tilde{\chi}_2^0$ production and decay, the analysis proceeds to limit setting with these results.

-	$\Delta M = 20$ ISR			$\Delta M = 20$ no ISR		
	ee	$e\mu$	$\mu\mu$	ee	$e\mu$	$\mu\mu$
fake	$0.63 \pm 0.39 \pm 0.40$	$4.13 \pm 1.80 \pm 1.62$	$1.60 \pm 3.30 \pm 0.80$	$8.10 \pm 1.27 \pm 3.77$	$8.72 \pm 2.79 \pm 6.81$	$0.32 \pm 0.24 \pm 0.22$
flip	$0.91 \pm 0.09 \pm 0.04$	$0.24 \pm 0.05 \pm 0.01$	-	$10.65 \pm 0.34 \pm 0.53$	$0.51 \pm 0.06 \pm 0.03$	-
diboson	$1.49 \pm 0.34 \pm 0.51$	$3.46 \pm 0.53 \pm 0.88$	$2.70 \pm 0.46 \pm 0.64$	$3.22 \pm 0.50 \pm 0.93$	$8.97 \pm 0.78 \pm 1.87$	$7.24 \pm 0.71 \pm 1.53$
higgs	$0.00 \pm 0.00 \pm 0.00$	$0.00 \pm 0.00 \pm 0.00$	$0.00 \pm 0.00 \pm 0.00$	$0.05 \pm 0.04 \pm 0.03$	$0.03 \pm 0.02 \pm 0.01$	$0.06 \pm 0.04 \pm 0.03$
ttV	$0.00 \pm 0.00 \pm 0.00$	$0.03 \pm 0.01 \pm 0.02$	$0.03 \pm 0.02 \pm 0.02$	$0.00 \pm 0.00 \pm 0.00$	$0.00 \pm 0.00 \pm 0.00$	$0.00 \pm 0.00 \pm 0.00$
W γ	$0.19 \pm 0.19 \pm 0.07$	$1.88 \pm 1.04 \pm 0.32$	$0.00 \pm 0.00 \pm 0.00$	$5.68 \pm 1.55 \pm 1.97$	$6.84 \pm 1.94 \pm 1.20$	$0.00 \pm 0.00 \pm 0.00$
total	$3.23 \pm 0.56 \pm 0.66$	$9.74 \pm 2.15 \pm 1.87$	$4.34 \pm 3.33 \pm 1.03$	$27.70 \pm 2.10 \pm 4.38$	$25.06 \pm 3.49 \pm 7.16$	$7.62 \pm 0.75 \pm 1.55$
data	5.00	9.00	5.00	23.00	29.00	12.00

Table 11.1: Expected and observed number of events in the signal regions with $\Delta M = 20$ GeV and with or without ISR jets. The first uncertainty is statistical and the second is from systematics.

-	$\Delta M = 35$ ISR			$\Delta M = 35$ no ISR		
	ee	$e\mu$	$\mu\mu$	ee	$e\mu$	$\mu\mu$
fake	$1.80 \pm 0.56 \pm 0.74$	$1.47 \pm 0.96 \pm 0.79$	$2.02 \pm 2.13 \pm 1.12$	$9.31 \pm 1.47 \pm 4.12$	$19.95 \pm 3.46 \pm 9.54$	$12.38 \pm 5.45 \pm 7.46$
flip	$0.40 \pm 0.07 \pm 0.02$	$0.23 \pm 0.06 \pm 0.02$	-	$4.53 \pm 0.29 \pm 0.19$	$0.91 \pm 0.12 \pm 0.05$	-
diboson	$1.63 \pm 0.44 \pm 0.67$	$4.13 \pm 0.60 \pm 1.04$	$3.24 \pm 0.53 \pm 0.87$	$3.20 \pm 0.60 \pm 1.19$	$14.69 \pm 1.08 \pm 2.79$	$14.75 \pm 1.19 \pm 2.90$
higgs	$0.03 \pm 0.02 \pm 0.02$	$0.02 \pm 0.02 \pm 0.01$	$0.08 \pm 0.04 \pm 0.04$	$0.04 \pm 0.03 \pm 0.02$	$0.03 \pm 0.02 \pm 0.01$	$0.13 \pm 0.05 \pm 0.07$
ttV	$0.02 \pm 0.01 \pm 0.01$	$0.03 \pm 0.02 \pm 0.02$	$0.05 \pm 0.02 \pm 0.03$	$0.00 \pm 0.00 \pm 0.00$	$0.00 \pm 0.00 \pm 0.00$	$0.01 \pm 0.01 \pm 0.01$
$W\gamma$	$0.00 \pm 0.00 \pm 0.00$	$0.56 \pm 0.45 \pm 0.09$	$0.00 \pm 0.00 \pm 0.00$	$5.50 \pm 1.75 \pm 1.90$	$10.75 \pm 2.62 \pm 1.88$	$0.00 \pm 0.00 \pm 0.00$
total	$3.88 \pm 0.71 \pm 1.00$	$6.45 \pm 1.22 \pm 1.31$	$5.39 \pm 2.20 \pm 1.42$	$22.58 \pm 2.39 \pm 4.70$	$46.33 \pm 4.47 \pm 10.11$	$27.27 \pm 5.58 \pm 8.00$
data	1.00	10.00	5.00	19.00	39.00	21.00

Table 11.2: Expected and observed number of events in the signal regions with $\Delta M = 35$ GeV and with or without ISR jets. The first uncertainty is statistical and the second is from systematics.

-	$\Delta M = 65$ ISR			$\Delta M = 65$ no ISR		
	ee	$e\mu$	$\mu\mu$	ee	$e\mu$	$\mu\mu$
fake	$0.49 \pm 0.51 \pm 0.34$	$0.10 \pm 0.47 \pm 0.21$	0.00 ± 0.07	$0.65 \pm 0.46 \pm 0.23$	0.00 ± 0.06	0.00 ± 0.04
flip	$0.25 \pm 0.06 \pm 0.02$	$0.30 \pm 0.07 \pm 0.02$	-	$0.19 \pm 0.07 \pm 0.01$	$0.20 \pm 0.07 \pm 0.01$	-
diboson	$0.56 \pm 0.20 \pm 0.21$	$1.74 \pm 0.43 \pm 0.46$	$1.38 \pm 0.39 \pm 0.35$	$0.33 \pm 0.20 \pm 0.10$	$1.08 \pm 0.39 \pm 0.29$	$1.51 \pm 0.41 \pm 0.31$
higgs	$0.01 \pm 0.01 \pm 0.01$	$0.03 \pm 0.03 \pm 0.02$	$0.01 \pm 0.01 \pm 0.01$	$0.00 \pm 0.00 \pm 0.00$	$0.02 \pm 0.02 \pm 0.01$	$0.01 \pm 0.01 \pm 0.00$
ttV	$0.01 \pm 0.01 \pm 0.00$	$0.00 \pm 0.00 \pm 0.00$	$0.03 \pm 0.02 \pm 0.01$	$0.00 \pm 0.00 \pm 0.00$	$0.00 \pm 0.00 \pm 0.00$	$0.00 \pm 0.00 \pm 0.00$
$W\gamma$	$0.39 \pm 0.39 \pm 0.13$	$0.21 \pm 0.21 \pm 0.03$	$0.00 \pm 0.00 \pm 0.00$			
total	$1.71 \pm 0.68 \pm 0.42$	$2.38 \pm 0.68 \pm 0.50$	$1.42 \pm 0.44 \pm 0.36$	$1.17 \pm 0.51 \pm 0.26$	$1.30 \pm 0.40 \pm 0.29$	$1.52 \pm 0.42 \pm 0.31$
data	4.00	4.00	2.00	0.00	2.00	2.00

Table 11.3: Expected and observed number of events in the signal regions with $\Delta M = 65$ GeV and with or without ISR jets. The first uncertainty is statistical and the second is from systematics.

-	$\Delta M = 100$ ISR			$\Delta M = 100$ no ISR		
	ee	$e\mu$	$\mu\mu$	ee	$e\mu$	$\mu\mu$
fake	$0.69 \pm 0.48 \pm 0.29$	$0.22 \pm 0.20 \pm 0.10$	0.00 ± 0.006	$0.19 \pm 0.20 \pm 0.07$	$0.16 \pm 0.22 \pm 0.09$	0.00 ± 0.05
flip	$0.08 \pm 0.06 \pm 0.00$	$0.03 \pm 0.02 \pm 0.00$	-	$0.09 \pm 0.05 \pm 0.01$	$0.04 \pm 0.02 \pm 0.00$	-
diboson	$0.12 \pm 0.03 \pm 0.02$	$0.30 \pm 0.14 \pm 0.10$	$0.36 \pm 0.14 \pm 0.06$	$0.03 \pm 0.02 \pm 0.01$	$0.33 \pm 0.16 \pm 0.07$	$0.25 \pm 0.15 \pm 0.07$
higgs	$0.00 \pm 0.00 \pm 0.00$	$0.02 \pm 0.02 \pm 0.01$	$0.00 \pm 0.00 \pm 0.00$			
ttV	$0.00 \pm 0.00 \pm 0.00$	$0.00 \pm 0.00 \pm 0.00$	$0.02 \pm 0.02 \pm 0.01$	$0.00 \pm 0.00 \pm 0.00$	$0.00 \pm 0.00 \pm 0.00$	$0.00 \pm 0.00 \pm 0.00$
$W\gamma$	$0.00 \pm 0.00 \pm 0.00$	$0.03 \pm 0.03 \pm 0.00$	$0.00 \pm 0.00 \pm 0.00$			
total	$0.90 \pm 0.48 \pm 0.29$	$0.57 \pm 0.25 \pm 0.15$	$0.38 \pm 0.14 \pm 0.06$	$0.31 \pm 0.21 \pm 0.08$	$0.55 \pm 0.28 \pm 0.11$	$0.25 \pm 0.15 \pm 0.07$
data	0.00	0.00	0.00	0.00	1.00	0.00

Table 11.4: Expected and observed number of events in the signal regions with $\Delta M = 100$ GeV and with or without ISR jets. The first uncertainty is statistical and the second is from systematics.

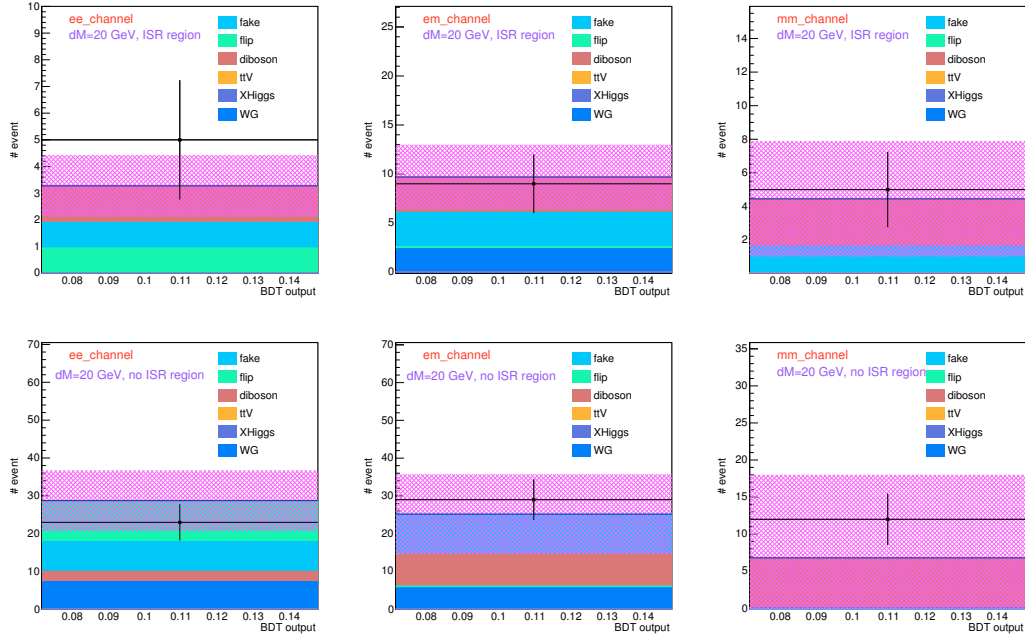


Figure 11.1: Output of Boosted Decision Tree for $\Delta M=20$ GeV for the ISR (top) and not ISR jet region (bottom) for the ee (left), $e\mu$ (middle) and $\mu\mu$ (right) channel.

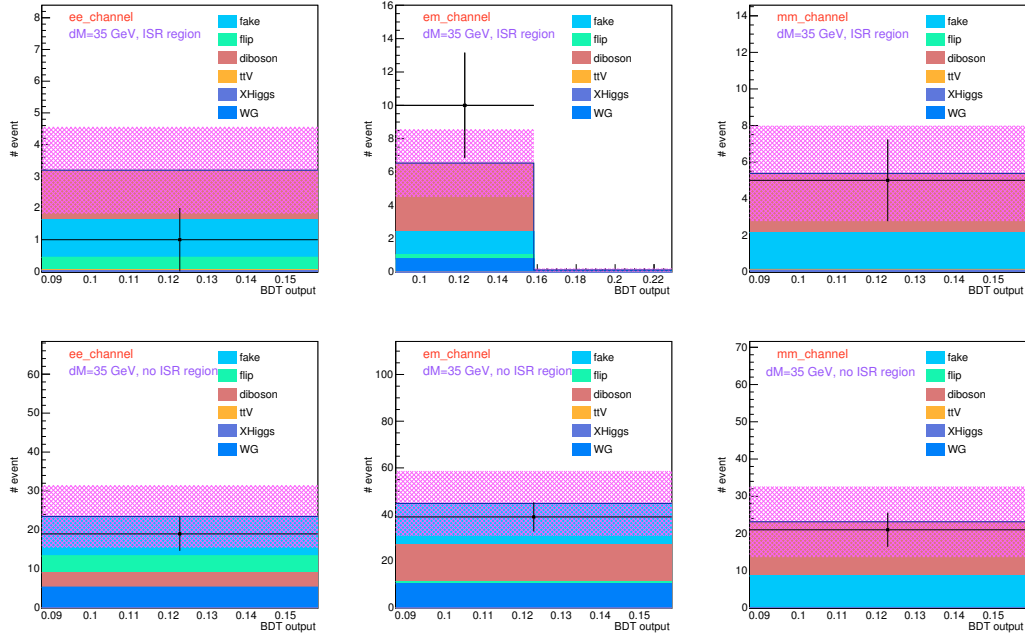


Figure 11.2: Output of Boosted Decision Tree for $\Delta M=35$ GeV for the ISR (top) and not ISR jet region (bottom) for the ee (left), $e\mu$ (middle) and $\mu\mu$ (right) channel.

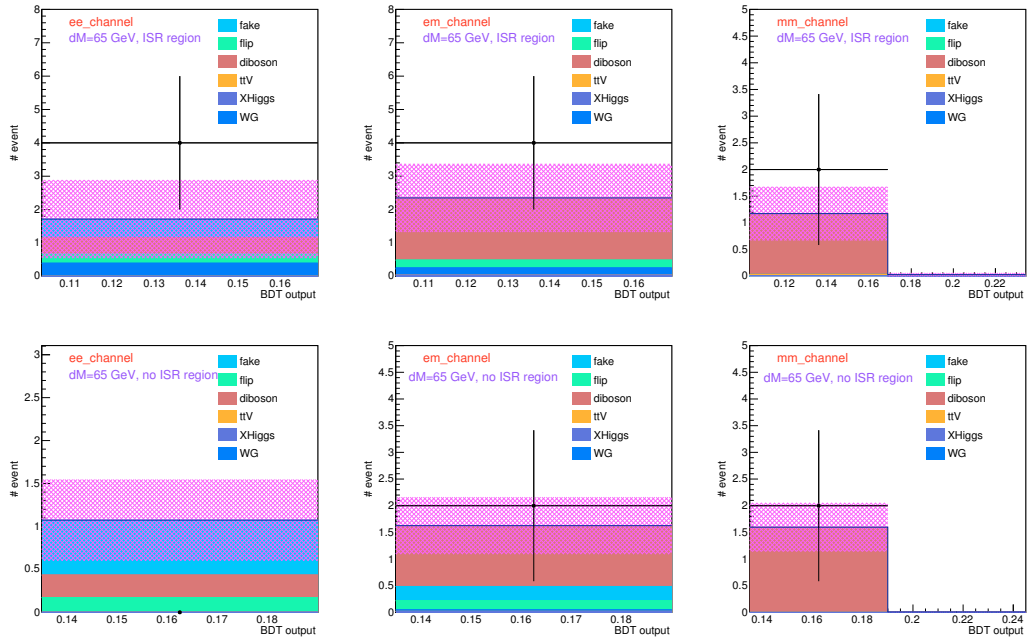


Figure 11.3: Output of Boosted Decision Tree for $\Delta M=65\text{GeV}$ for the ISR (top) and not ISR jet region (bottom) for the ee (left), $e\mu$ (middle) and $\mu\mu$ (right) channel.

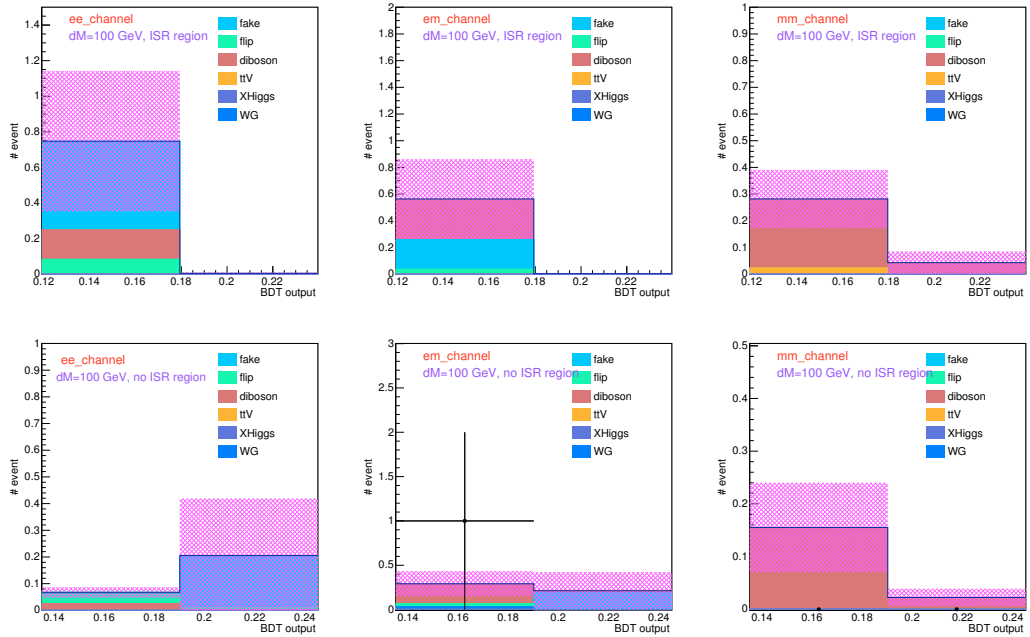


Figure 11.4: Output of Boosted Decision Tree for $\Delta M=100\text{GeV}$ for the ISR (top) and not ISR jet region (bottom) for the ee (left), $e\mu$ (middle) and $\mu\mu$ (right) channel.

CHAPTER 12

Limits

Since no significant excesses are seen above the Standard Model expectations, limits on the models described in Chapter 6 are calculated using the CL_s method [82]. The CL_s method is further explained in Section 12.1. Limits obtained for simplified models are given in Section 12.2, while model-independent limits are presented in Section 12.3. Finally, the results of a statistical combination with other analyses, primarily the trilepton search, are presented in Section 12.4.

12.1 Limit Setting Procedure

To compute limits, the three flavor channels, ee , $e\mu$, $\mu\mu$, and the ISR and no-ISR signal regions for a given mass splitting are able to be easily combined because all channels are independent. Because of the differing signal to background ratio for each of these six sub-channels, they are statistically combined rather than simply grouped together to maximally exploit the results. Among the four targeted mass splitting of dM20, dM35, dM65, and dM100, there is a possibility for event overlap between the signal regions, so they are not combined. In the case of model dependent limits, the signal region giving the best expected limit is chosen from the four possibilities. For the model independent limits, each is evaluated separately.

As stated previously, for this analysis the CL_s procedure is used. The CL_s method is simply the ratio of two pure frequentist confidence limits:

$$\text{CL}_s \equiv \frac{\text{CL}_{s+b}}{\text{CL}_b} \quad (12.1)$$

Here CL_b quantifies how well the data describes the background only hypothesis, while CL_{s+b} similarly describes the signal plus background hypothesis, and will be further described below. A signal model is viewed as excluded at a confidence level of $1 - \alpha$, when $\text{CL}_s < \alpha$. For all limits in this analysis the 95% CL ($\alpha = 0.05$), is used.

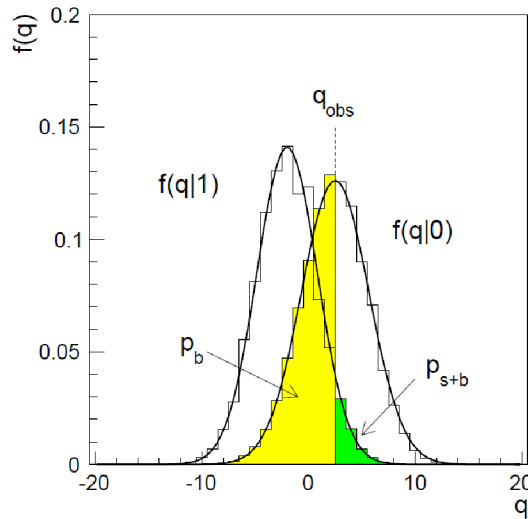


Figure 12.1: Illustration of p_b and p_{s+b} , values to the left of the plot are more signal-like, while values to the right are more background-like.

The frequentist confidence level CL_{s+b} starts with the construction of a test statistic q to distinguish between the background only hypothesis b and the signal plus background hypothesis, $s + b$. The choice of the test statistic q is open to some choice, and will be further explained below. The distributions $f(q|s + b)$ and $f(q|b)$ are then determined based on this choice of q , and the expected number of events given signal and background predictions. An example of these quantities can be seen in Figure 12.1 for a given test statistic q . For this choice of statistic, the signal+background hypothesis is shifted to lower values, while the background-only hypothesis is shifted to high values. If the actual data results show q_{obs} , the p-value of the signal+background hypothesis gives the probability to find q with equal or less compatibility than q_{obs} , shown in green in Figure 12.1. Writing

this explicitly gives:

$$p_{s+b} = P(q \geq q_{obs}|s+b) = \int_{q_{obs}}^{\infty} f(q|s+b)dq \quad (12.2)$$

The CL_{s+b} method then uses this p-value to determine if a particular model is excluded at a given confidence level as explained above, such that a model would be excluded by CL_{s+b} if $p_{s+b} < \alpha$, again with $\alpha = 0.05$ for 95% CL. So that both small values of CL_{s+b} and p_{s+b} indicate a strong exclusion.

Similarly, the p-value for the background-only hypothesis (shown in yellow in the figure) can be given by:

$$p_b = P(q \leq q_{obs}|b) = \int_{-\infty}^{q_{obs}} f(q|b)dq \quad (12.3)$$

This gives the probability that for the q test statistic to be equally or more discrepant with the background only hypothesis as the observed data. The quantity CL_b is then defined as $1 - CL_b = p_b$.

Then, CL_s can equally well be defined in terms of the underlying p-values:

$$CL_s \equiv \frac{p_{s+b}}{1 - p_b} \quad (12.4)$$

The main benefit of the CL_s method over CL_{s+b} or is that it prevents false exclusions in experiments where there should be no sensitivity. In the instance when the expected signal is very low and the observed number of events has a large fluctuation down from the expected background estimate, neither the background-only, nor the signal+background is favored. In this situation, the pure frequentist method CL_{s+b} may exclude such a hypothesis, even though there should be no sensitivity to it. By dividing by the CL_b value, which will also be small, such an exclusion is prevented. As a result, the false exclusion rate for the CL_s method is lower than the expected stated confidence limit (i.e. 95% CL would expect 5% of repeated experiments to make a false exclusion), but the limits are “conservative” in the case of no expected exclusion.

The choice of the test statistic has been undefined so far. Generally, likelihoods are used as a test statistic as they provide a straightforward representation of complex data and good signal discrimination. The likelihood of a hypothesis, H , with parameters θ , given the result x , is equal to the probability for outcome x , given the hypothesis:

$$L(H(\theta)|x) = P(x|H(\theta)) \quad (12.5)$$

For a counting experiment, the Poisson distribution is used

$$P(k; \lambda) = \frac{e^{-\lambda} \lambda^k}{k!} \quad (12.6)$$

where, k is the number of observed events and λ is the expected number.

It is also useful to define the signal strength variable μ , such that $\mu = 0$ represents the background only hypothesis, $\mu = 1$ represents the background + (nominal) signal hypothesis. Then the likelihood for observing N events, with s expected signal events and b expected background, is given by

$$L(N; \mu) = P(N; \mu \cdot s_{exp} + b_{exp}) \quad (12.7)$$

For comparing two or more possible hypothesis, H_0 with parameters θ_0 and H_1 with parameters θ_1 , a ratio between the two likelihoods can be used. In fact, in the case where the two hypotheses have no unknown parameters, the Neyman-Pearson Lemma states that the likelihood ratio is the most powerful test[83].

$$\lambda(x) = \frac{L(\theta_1|x)}{L(\theta_0|x)} \quad (12.8)$$

In reality for evaluating physics searches or measurements, there are many unknowns due to systematic errors, which enter these calculations as nuisance parameters. These nuisance parameters are represented by θ .

Like many Atlas searches, this analysis uses the one-sided profile likelihood, q_μ , as its test statistic [84]. The profile likelihood uses the ratio of the hypothesis under testing to the hypothesis

that maximizes the likelihood value, rather than the background-only hypothesis. It can be written as:

$$q_\mu = \begin{cases} -2 \ln \lambda(\mu) & \mu \geq \hat{\mu} \geq 0 \\ 0 & \text{Otherwise} \end{cases} \quad (12.9)$$

with

$$\lambda(\mu) = \frac{L(\mu, \hat{\boldsymbol{\theta}})}{L(\hat{\mu}, \hat{\boldsymbol{\theta}})} \quad (12.10)$$

where $\hat{\boldsymbol{\theta}}$ represents the value of $\boldsymbol{\theta}$ that maximizes the likelihood for the given μ value under study. In other words it is a function of μ , and also known as the conditional maximum-likelihood estimator. In the denominator, $\hat{\mu}$ and $\hat{\boldsymbol{\theta}}$ specify the maximum value of the likelihood.

This analysis uses the ‘‘HistFitter’’ [85] software framework to ease computation of the profile likelihood, CL_s and p-values and resulting limits.

12.2 Limits on Simplified Models

12.2.1 $x=0.50$ Intermediate Slepton Grid

Limits found for this analysis for the $\tilde{\chi}_1^\pm \tilde{\chi}_2^0$ decaying via intermediate sleptons in the nominal scenario with the slepton mass exactly halfway between $\tilde{\chi}_1^\pm, \tilde{\chi}_2^0$ and the LSP are presented in Figure 12.2. The 95% CL exclusion contour is shown in the upper left plot, and the chosen signal region giving the best expected CL_s value is shown in the upper right. The lower plots show the observed and expected CL_s values, respectively. The corresponding limits for the 3 lepton and two lepton opposite sign analysis can be found in Figures 5.2 and 5.3(right). As expected, the limits from this analysis are not competitive with those from the trilepton analysis for high mass $\tilde{\chi}_1^\pm$. Near the compressed diagonal, this analysis is able to exclude mass splittings of about 40 GeV for $\tilde{\chi}_1^\pm$ masses of less than about 140 GeV. However, the three lepton limit still is stronger, excluding mass splittings of around 20 GeV in this region.

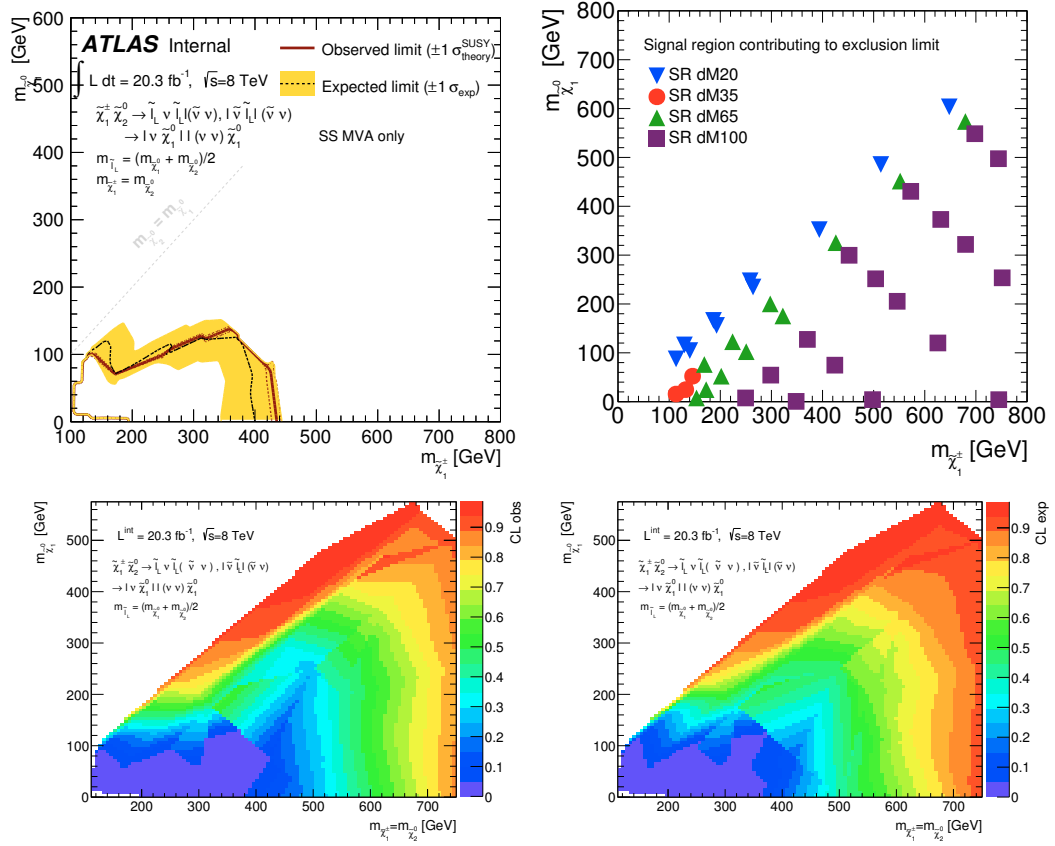


Figure 12.2: Exclusion contour for $\tilde{\chi}_1^\pm, \tilde{\chi}_2^0$ pair production with $x=0.50$ sleptons in the decay (left). Signal region with best expected CLs value used for each grid point (right).

12.2.2 $x=0.95$ Intermediate Slepton Grid

Limits found for this analysis for the $\tilde{\chi}_1^\pm, \tilde{\chi}_2^0$ decaying via intermediate sleptons in the compressed scenario are presented in Figure 12.3. While the exclusions in the high $\tilde{\chi}_1^\pm$ mass region are much stronger for the trilepton analysis versus this analysis, in the compressed region near the diagonal ($m_{\tilde{\chi}_1^\pm} \sim m_{\tilde{\chi}_2^0}$) this analysis provides the stronger limit. Close to the diagonal, we exclude mass splittings above 20 GeV for $\tilde{\chi}_1^\pm$ masses below 180 GeV, and we exclude mass splittings above 35 GeV for $\tilde{\chi}_1^\pm$ masses below 250 GeV.

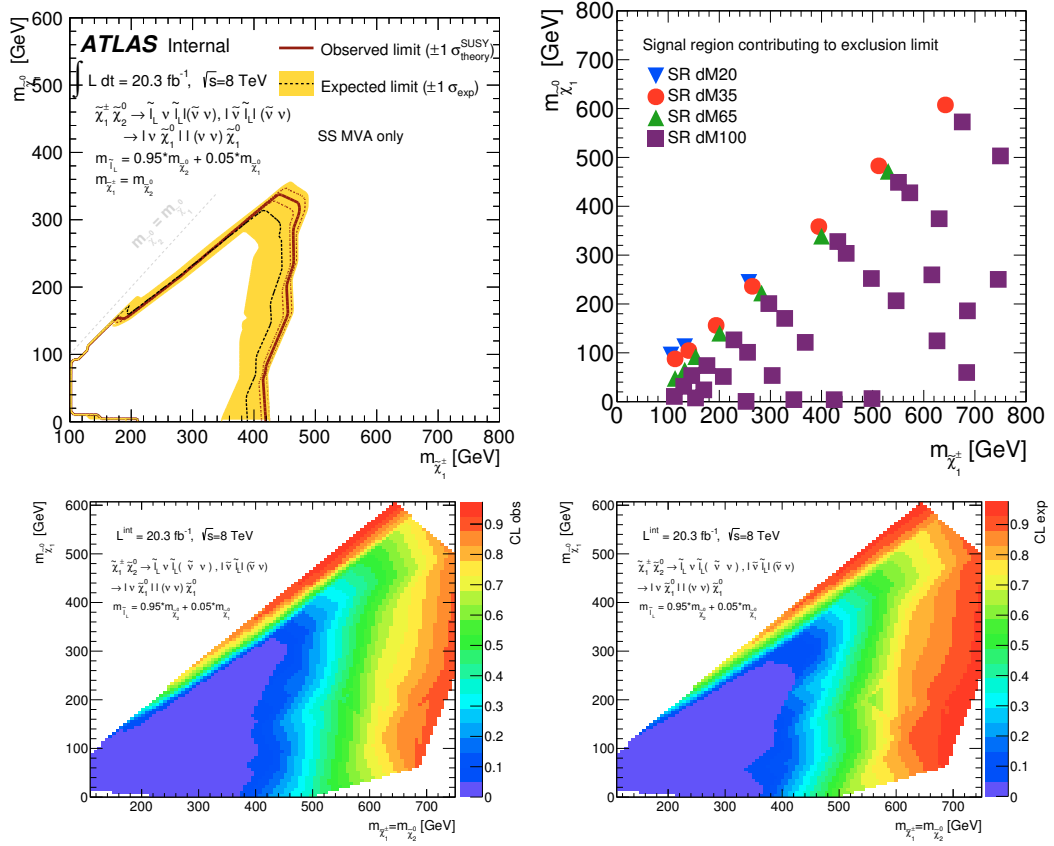


Figure 12.3: Exclusion contour for $\tilde{\chi}_1^\pm, \tilde{\chi}_2^0$ pair production with $x=0.95$ sleptons in the decay (top left) and the expected Zn value from the trilepton search (top right) for comparison. Signal region with best expected CLs value used for each grid point (bottom).

12.2.3 WZ Grid

The results for the $\tilde{\chi}_1^\pm \tilde{\chi}_2^0$ decaying via W and Z bosons are shown in Figure 12.4. For this grid scenario, no hypothesis points are able to be excluded by this analysis alone. The observed and the expected CL_s values are shown. While it is somewhat expected that the sensitivity to this grid is greatly diminished compared with those with intermediate sleptons due to the branching fraction to leptons, unfortunately the kinematics of this decay do not favor a same-sign final state. In the case of the intermediate sleptons, with the slepton mass near that of the $\tilde{\chi}_1^\pm$ and $\tilde{\chi}_2^0$, the lepton that is not reconstructed preferentially comes from the decay of the $\tilde{\chi}_2^0$, giving roughly a 50% chance that the final 2L state is same-sign. In the case of intermediate gauge bosons, this is not the case as both

the W and the Z are produced off-shell in the compressed region. This means that all of the three final state leptons are roughly equally probable to not be reconstructed. This unfortunately means that the same-sign channel is not expected to become particularly sensitive to this decay channel, even with increased data. Efforts to explore the compressed region in this scenario would be better spent using different analysis techniques, such as utilizing soft-leptons below the trigger thresholds used in this analysis.

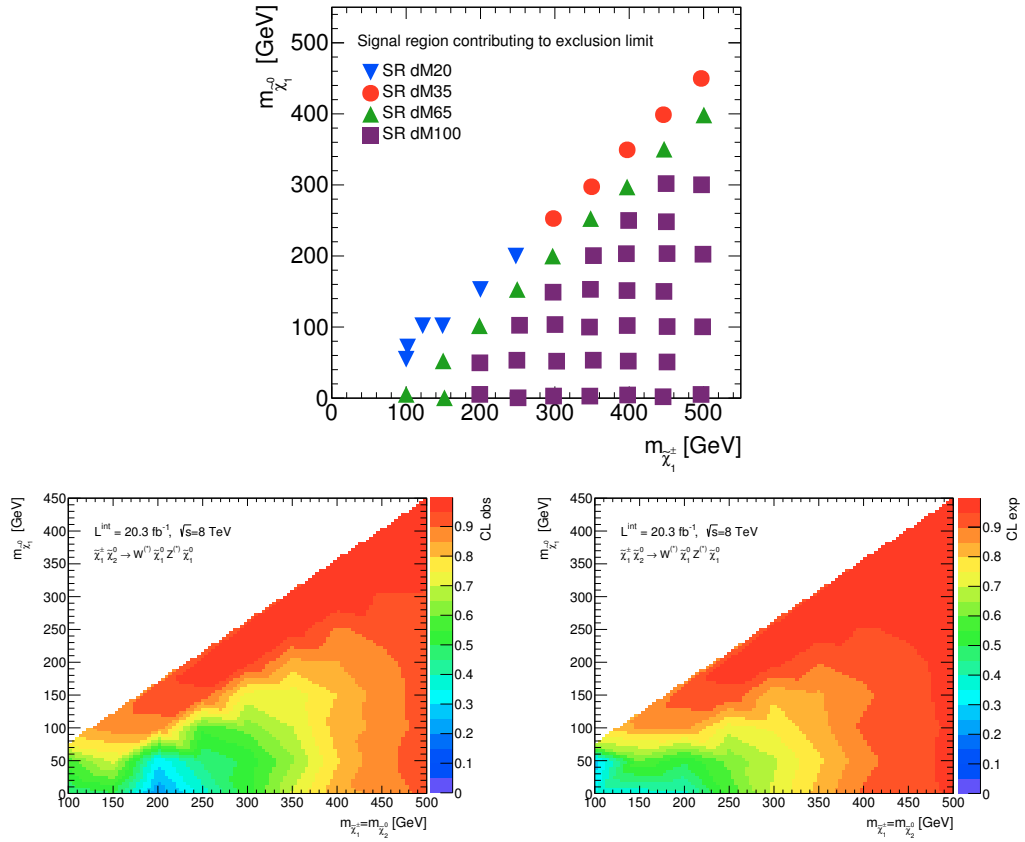


Figure 12.4: Exclusion contour for $\tilde{\chi}_1^\pm, \tilde{\chi}_2^0$ pair production with WZ bosons in the decay chain (left). Signal region with best expected CLs value used for each grid point (right).

12.3 Model independent limits

Tables 12.1-12.4 show the model independent limits for each of the sub-signal regions, as the acceptances are very different amongst them. Given are the numbers for the 95% upper confidence limit

Signal channel	$\langle\epsilon\sigma\rangle_{obs}^{95}$ [fb]	S_{obs}^{95}	S_{exp}^{95}	CL_B	p_0
ee ISR	0.33	6.9	$5.4^{+2.8}_{-1.8}$	0.72	0.33
em ISR	0.29	6.2	$6.3^{+4.1}_{-2.4}$	0.48	0.50
mm ISR	0.38	7.9	$8.4^{+3.5}_{-2.3}$	0.41	0.50
ee noISR	0.17	3.6	$5.0^{+2.7}_{-1.5}$	0.17	0.50
em noISR	0.27	5.7	$5.4^{+4.5}_{-2.3}$	0.54	0.21
mm noISR	0.59	12.3	$8.2^{+3.5}_{-2.2}$	0.88	0.09

Table 12.1: Model independent results for the dM20 signal regions. Left to right: 95% CL upper limits on the visible cross section ($\langle\epsilon\sigma\rangle_{obs}^{95}$) and on the number of signal events (S_{obs}^{95}). The third column (S_{exp}^{95}) shows the 95% CL upper limit on the number of signal events, given the expected number (and $\pm 1\sigma$ excursions on the expectation) of background events. The last two columns indicate the CL_B value, i.e. the confidence level observed for the background-only hypothesis, and the discovery p -value ($p(s=0)$).

Signal channel	$\langle\epsilon\sigma\rangle_{obs}^{95}$ [fb]	S_{obs}^{95}	S_{exp}^{95}	CL_B	p_0
ee ISR	0.19	4.1	$5.6^{+2.2}_{-1.5}$	0.06	0.50
em ISR	0.69	14.6	$9.2^{+3.1}_{-2.3}$	0.94	0.02
mm ISR	0.26	5.4	$5.8^{+3.4}_{-2.1}$	0.43	0.50
ee noISR	0.27	5.6	$6.2^{+5.1}_{-2.6}$	0.41	0.50
em noISR	0.26	5.6	$6.1^{+5.3}_{-2.6}$	0.43	0.50
mm noISR	0.24	5.1	$5.5^{+4.5}_{-2.4}$	0.45	0.50

Table 12.2: Model independent results for the dM35 signal regions. Left to right: 95% CL upper limits on the visible cross section ($\langle\epsilon\sigma\rangle_{obs}^{95}$) and on the number of signal events (S_{obs}^{95}). The third column (S_{exp}^{95}) shows the 95% CL upper limit on the number of signal events, given the expected number (and $\pm 1\sigma$ excursions on the expectation) of background events. The last two columns indicate the CL_B value, i.e. the confidence level observed for the background-only hypothesis, and the discovery p -value ($p(s=0)$).

on the visible cross section times acceptance, and limit on the number of observed and expected signal events, and the CL_B (observed confidence level for the background-only hypothesis), where large values of CL_b indicate less compatibility with the background-only hypothesis and finally the discovery p -value with signal strength set to 0. For the p -values, small values indicate disagreement with the background only hypothesis. The largest discrepancy is seen in the dM35 ISR *em* sub-channel, however the remaining dM35 sub-channels show good agreement.

Signal channel	$\langle\epsilon\sigma\rangle_{obs}^{95}$ [fb]	S_{obs}^{95}	S_{exp}^{95}	CL_B	p_0
ee ISR	0.36	7.5	$4.3^{+2.9}_{-1.3}$	0.86	0.09
em ISR	0.30	6.2	$6.1^{+2.2}_{-1.9}$	0.54	0.34
mm ISR	0.21	4.4	$4.2^{+2.0}_{-0.4}$	0.56	0.47
ee noISR	0.13	2.7	$3.9^{+2.1}_{-1.5}$	0.20	0.50
em noISR	0.22	4.7	$4.0^{+2.2}_{-1.2}$	0.62	0.36
mm noISR	0.23	4.8	$4.1^{+2.3}_{-1.2}$	0.62	0.39

Table 12.3: Model independent results for the dM65 signal regions. Left to right: 95% CL upper limits on the visible cross section ($\langle\epsilon\sigma\rangle_{obs}^{95}$) and on the number of signal events (S_{obs}^{95}). The third column (S_{exp}^{95}) shows the 95% CL upper limit on the number of signal events, given the expected number (and $\pm 1\sigma$ excursions on the expectation) of background events. The last two columns indicate the CL_B value, i.e. the confidence level observed for the background-only hypothesis, and the discovery p -value ($p(s=0)$).

Signal channel	$\langle\epsilon\sigma\rangle_{obs}^{95}$ [fb]	S_{obs}^{95}	S_{exp}^{95}	CL_B	p_0
ee ISR	0.12	2.4	$3.5^{+1.9}_{-1.4}$	0.29	0.50
em ISR	0.12	2.4	$3.5^{+1.9}_{-1.4}$	0.29	0.50
mm ISR	0.10	2.1	$2.9^{+1.7}_{-0.9}$	0.38	0.50
ee noISR	0.10	2.1	$2.9^{+1.7}_{-0.9}$	0.38	0.50
em noISR	0.19	3.9	$3.6^{+2.0}_{-1.5}$	0.61	0.36
mm noISR	0.10	2.1	$3.0^{+1.7}_{-0.9}$	0.37	0.50

Table 12.4: Model independent results for the dM100 signal regions. Left to right: 95% CL upper limits on the visible cross section ($\langle\epsilon\sigma\rangle_{obs}^{95}$) and on the number of signal events (S_{obs}^{95}). The third column (S_{exp}^{95}) shows the 95% CL upper limit on the number of signal events, given the expected number (and $\pm 1\sigma$ excursions on the expectation) of background events. The last two columns indicate the CL_B value, i.e. the confidence level observed for the background-only hypothesis, and the discovery p -value ($p(s=0)$).

12.4 Combined Limits

Since this analysis searches for the same decay hypothesis as the trilepton analysis, it is natural to combine the results from both analyses to provide the maximal exclusion (or discovery potential).

As the two analyses are designed to be completely orthogonal to one another based on the number of leptons in the events, a straightforward statistical combination can be done. This combination is again done using the HistFitter framework and the results are shown in Figure 12.5 for the $x=0.50$ slepton grid and the $x=0.95$ slepton grid. Because there is little expected gain from the combination of this analysis with the existing trilepton limits in the WZ-mediated grid, no combination is

performed. In both scenarios, the trilepton analysis dominates the result at high $\tilde{\chi}_1^\pm, \tilde{\chi}_2^0$ mass, but in the compressed region near the diagonal in the $x=0.95$ grid the 2LSS analysis provides stronger limits, shown in the pink contour.

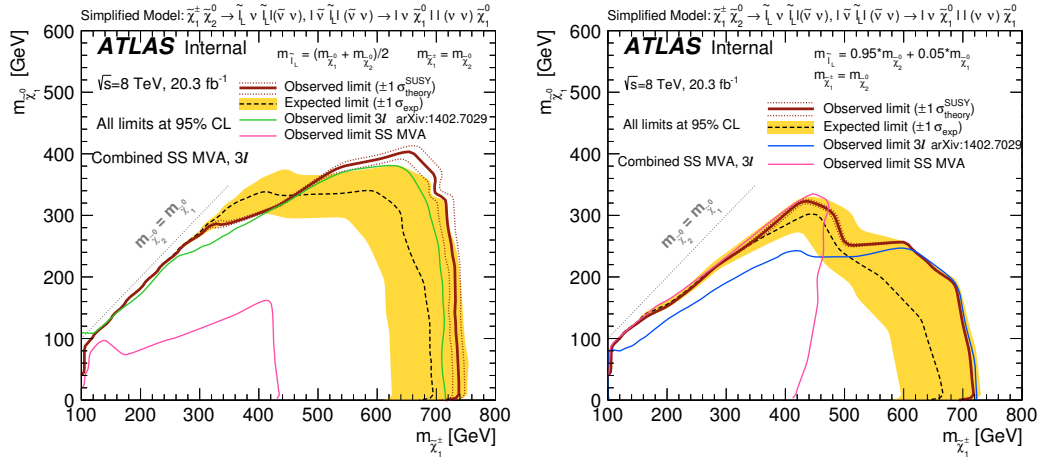


Figure 12.5: Exclusion contour for $\tilde{\chi}_1^\pm, \tilde{\chi}_2^0$ pair production with $x=0.50$ sleptons in the decay (left) and $x=0.95$ (right) sleptons in the decay, using the combination of the 2LSS analysis and the 3L analysis.

CHAPTER 13

Conclusions and Future Prospects

This thesis presented a search for $\tilde{\chi}_1^\pm \tilde{\chi}_2^0$ pair production, using same-sign leptons to extend the reach of the trilepton search for compressed scenarios. For this signature, particularly in the compressed scenarios where the mass splitting between $\tilde{\chi}_1^\pm$ and $\tilde{\chi}_1^0$ is small and the mass splitting between $\tilde{\chi}_1^\pm$ and an intermediate slepton is small, the usual discriminating variables do not show a clear separation between signal events and backgrounds. A multivariate analysis (BDT) is implemented to optimally separate signal and background events. BDTs are trained for four mass splittings of 20, 35, 65, and 100 GeV as well as separately trained for events without and with at least one jet from ISR. The sensitivity of the search has been optimized for decays with sleptons of intermediate mass set to 95% of the mass splitting plus the mass of the lightest neutralino, and applied to several signal hypotheses.

For $\tilde{\chi}_1^\pm \tilde{\chi}_2^0$ pair production with the intermediate slepton mass set to 95% of the mass splitting above the mass of the LSP, χ_1^\pm masses below 410 GeV are excluded for a massless LSP. Close to the diagonal $m_{\tilde{\chi}_1^\pm} = m_{\tilde{\chi}_1^0}$, mass splittings above 20 GeV for χ_1^\pm masses below 180 GeV are excluded, and mass splittings above 35 GeV for χ_1^\pm masses below 250 GeV are excluded. These exclusions are shown to be more powerful than the trilepton search, as shown by preliminary results in the combination.

For $\tilde{\chi}_1^\pm \tilde{\chi}_2^0$ pair production with the intermediate slepton mass exactly halfway between the LSP mass and the $\tilde{\chi}_1^\pm$ mass, χ_1^\pm masses below 425 GeV for low χ_1^0 mass are excluded and mass splittings

above 35 GeV only for χ_1^\pm masses below 160 GeV are excluded. While this analysis alone cannot set exclusions beyond the trilepton only search, the combination with trilepton does extend the reach. Additional signal models with mass splittings down to 5 GeV are currently being produced to further evaluate this situation. The poorer exclusion is expected since the number of expected same-sign dilepton (trilepton) events is smaller (larger) for the 50% mass splitting than for the 95% mass splitting.

For decays with W and Z bosons, no exclusion is set for the simplified models considered. Compared to decays with sleptons, the branching fractions for W and Z to leptons are smaller so the expected number of events with leptons is smaller. Compared to trilepton, the poorer sensitivity is expected since the structure of the decay (mass splittings) favors larger numbers of expected events for trilepton than for same-sign dilepton.

As of this writing, Run 2 at the LHC is in its first days, and much work is being done to further weakly-produced SUSY searches in the new dataset. With the center of mass energy increasing from 8 TeV to 13 TeV, the production cross section for $\tilde{\chi}_1^\pm \tilde{\chi}_2^0$ pairs increases by roughly a factor of 2, so the reach of analyses at 13 TeV should exceed those at 8 TeV with about 10 fb^{-1} of integrated luminosity. This amount of data is expected to be collected in the first year of running, and by the end of Run 2 a total of roughly 100 fb^{-1} is expected.

Additionally, many studies are being done to target the compressed regions still uncovered after this analysis, particularly in the decay proceeding through W and Z bosons. The kinematics of the decay in the compressed region do not favor the exclusive same-sign channel, and thus it does not seem prudent to expend extensive manpower on such an effort. Instead, analyses are exploring several other strategies. First, future analyses with Run 2 data are planning on exploiting ISR, similar to that used in this analysis. Further, by using the ISR jet as the triggering object, the p_T requirements on the leptons can be lowered. It is expected that such an analysis should be able to access mass splittings of $\sim 5 - 30 \text{ GeV}$. Clearly, with the large new dataset at world-record energies, the next few years should be exciting at the LHC and in the continued search for supersymmetry.

APPENDIX A

Kinematic plots for same-sign validation region

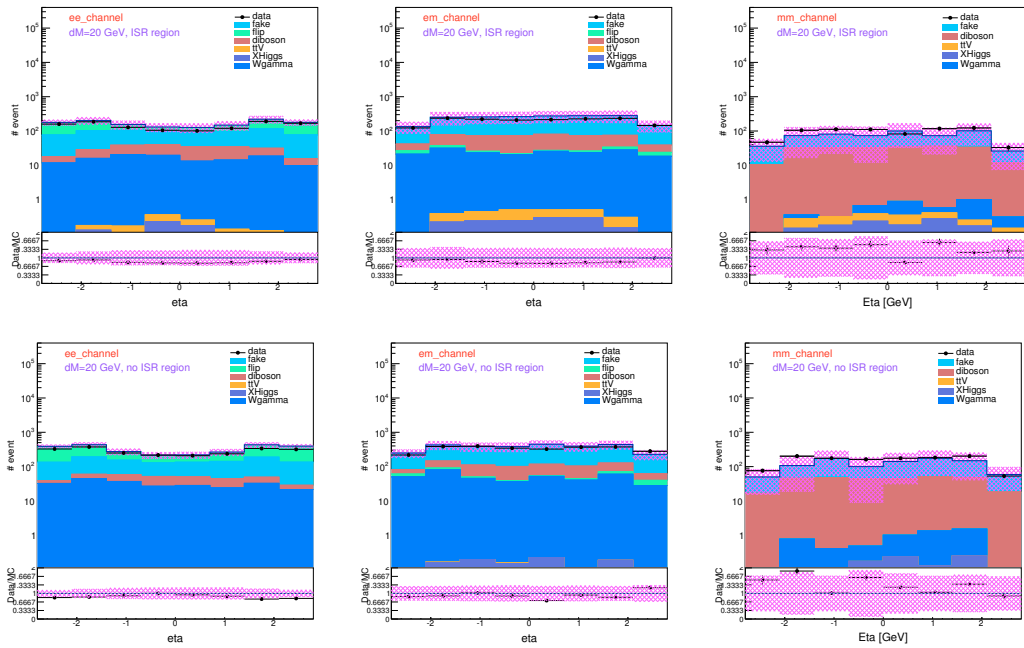


Figure A.1: Lepton η in the validation regions with $\Delta M=20$ GeV and with ISR (top) or without ISR jet (bottom), for ee (left), $e\mu$ (middle), and $\mu\mu$ (right) channel.

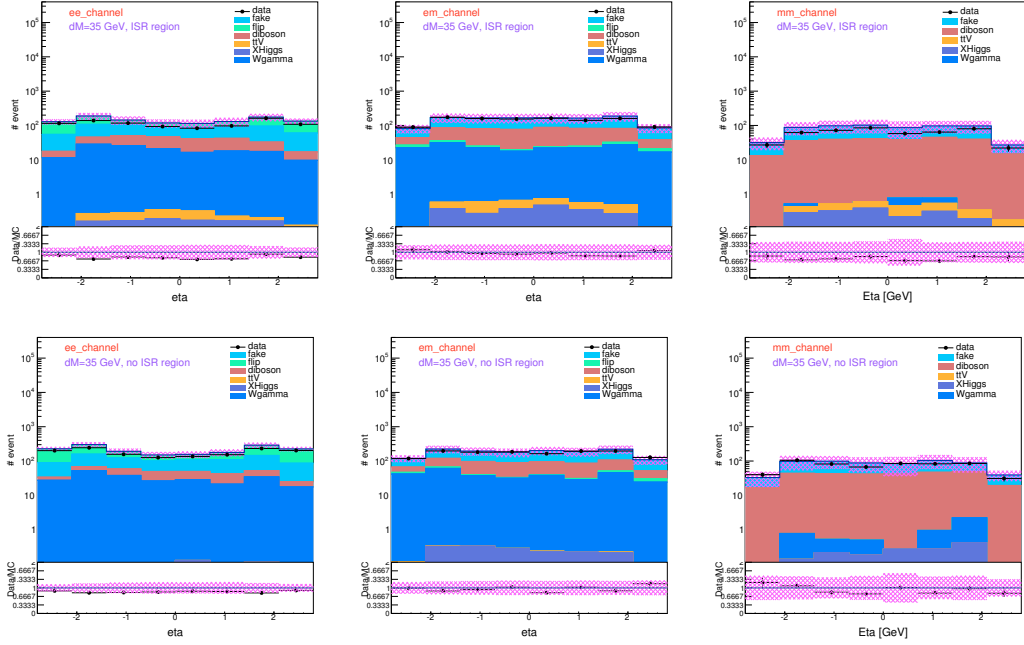


Figure A.2: Lepton η in the validation regions with $\Delta M=35$ GeV and with ISR (top) or without ISR jet (bottom), for ee (left), $e\mu$ (middle), and $\mu\mu$ (right) channel.

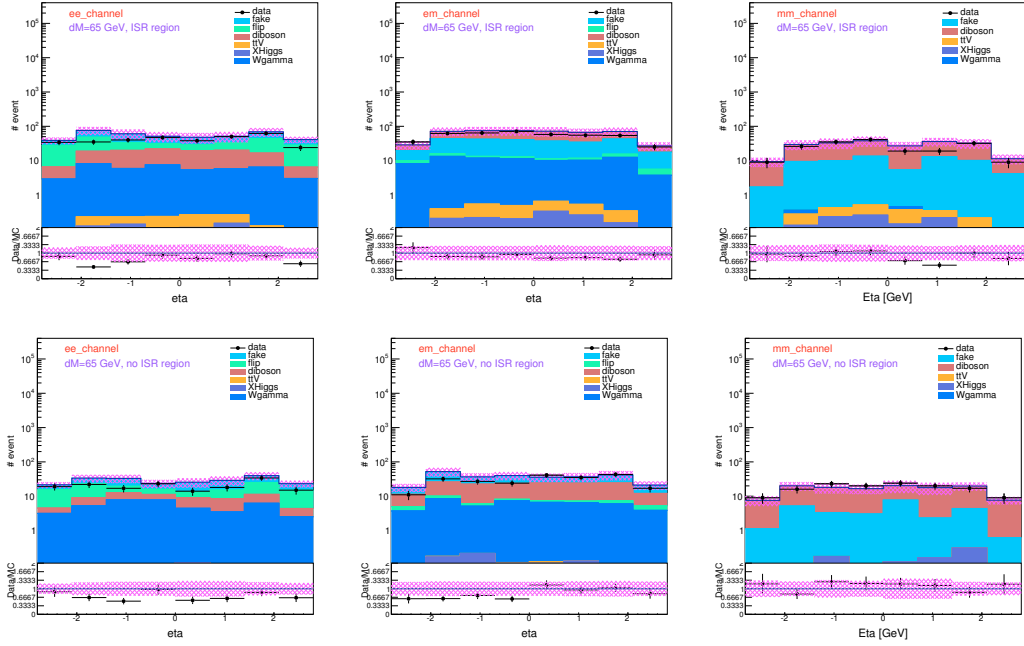


Figure A.3: Lepton η in the validation regions with $\Delta M=65$ GeV and with ISR (top) or without ISR jet (bottom), for ee (left), $e\mu$ (middle), and $\mu\mu$ (right) channel.

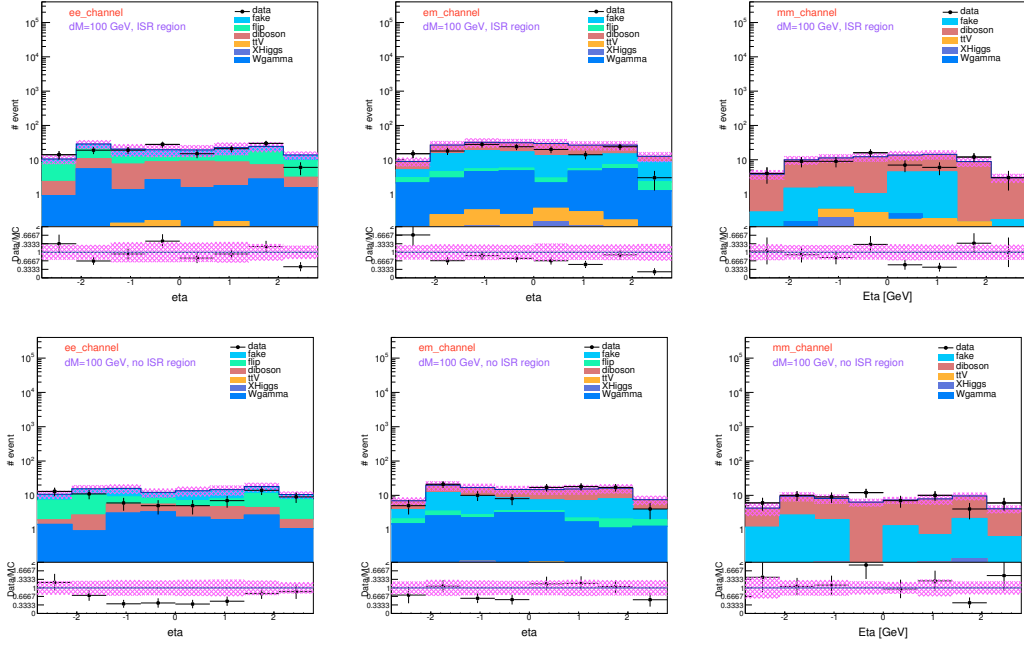


Figure A.4: Lepton η in the validation regions with $\Delta M=100$ GeV and with ISR (top) or without ISR jet (bottom), for ee (left), $e\mu$ (middle), and $\mu\mu$ (right) channel.

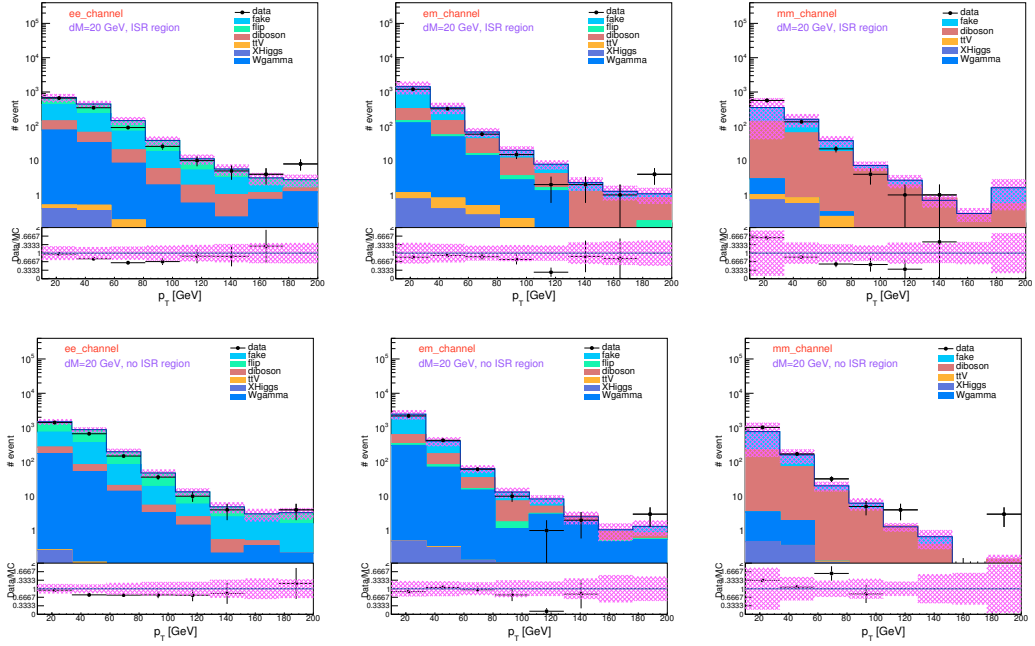


Figure A.5: Lepton p_T in the validation regions with $\Delta M=20$ GeV and with ISR (top) or without ISR jet (bottom), for ee (left), $e\mu$ (middle), and $\mu\mu$ (right) channel.

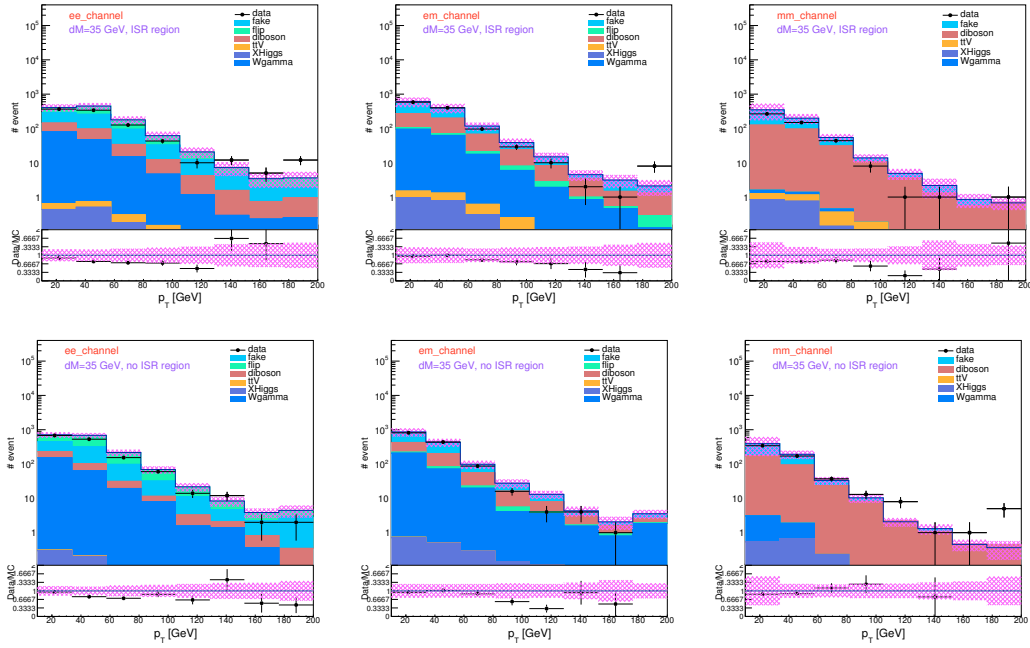


Figure A.6: Lepton p_T in the validation regions with $\Delta M=35$ GeV and with ISR (top) or without ISR jet (bottom), for ee (left), $e\mu$ (middle), and $\mu\mu$ (right) channel.

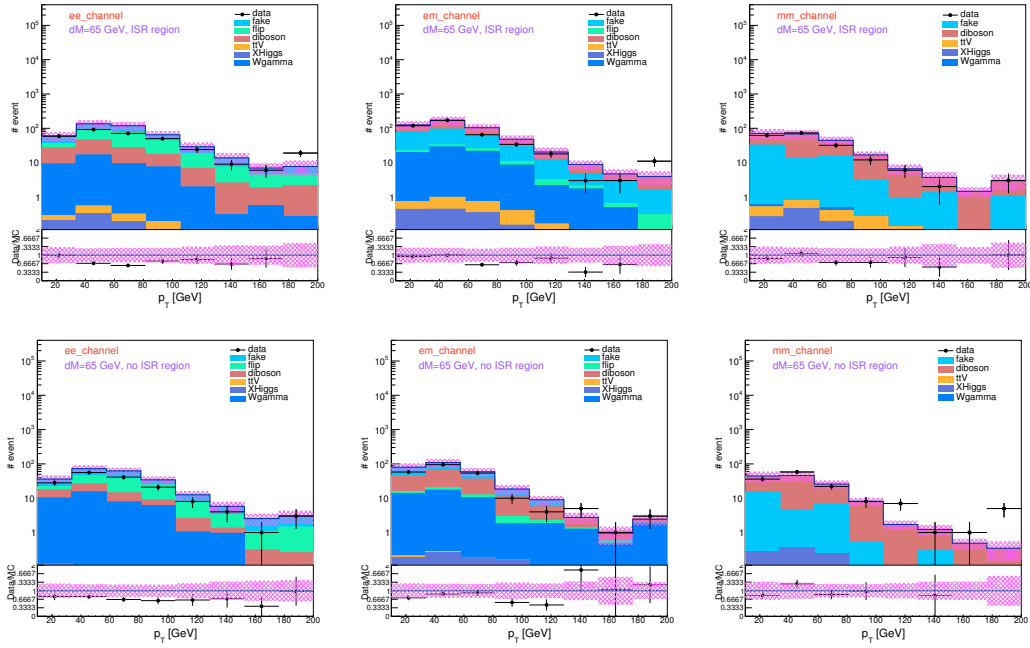


Figure A.7: Lepton p_T in the validation regions with $\Delta M=65$ GeV and with ISR (top) or without ISR jet (bottom), for ee (left), $e\mu$ (middle), and $\mu\mu$ (right) channel.

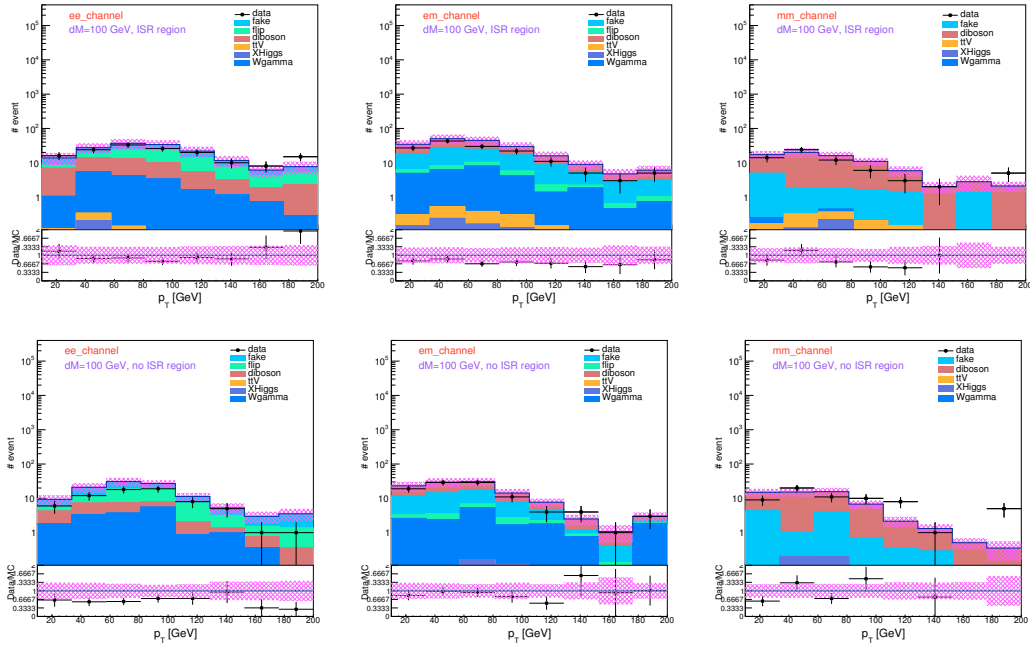


Figure A.8: Lepton p_T in the validation regions with $\Delta M=100$ GeV and with ISR (top) or without ISR jet (bottom), for ee (left), $e\mu$ (middle), and $\mu\mu$ (right) channel.

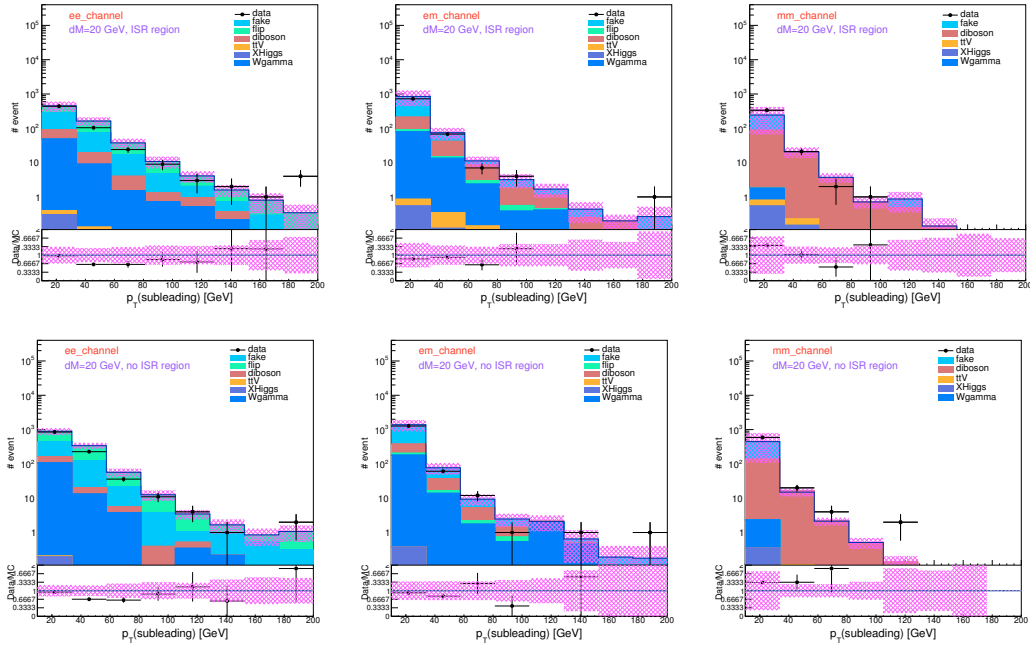


Figure A.9: Subleading lepton p_T in the validation regions with $\Delta M=20$ GeV and with ISR (top) or without ISR jet (bottom), for ee (left), $e\mu$ (middle), and $\mu\mu$ (right) channel.

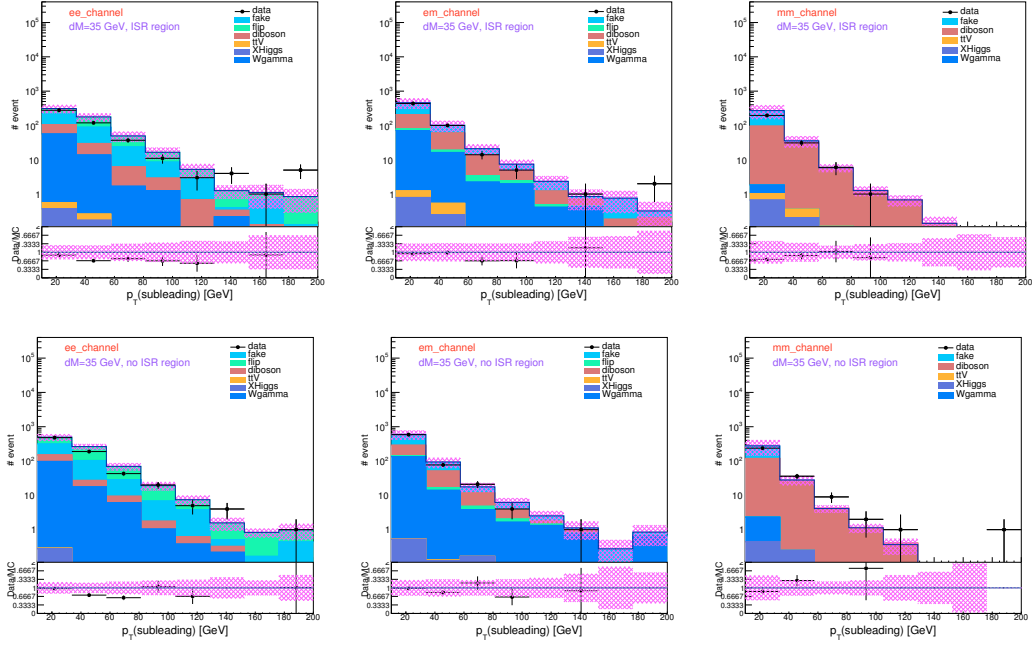


Figure A.10: Subleading lepton p_T in the validation regions with $\Delta M=35$ GeV and with ISR (top) or without ISR jet (bottom), for ee (left), $e\mu$ (middle), and $\mu\mu$ (right) channel.

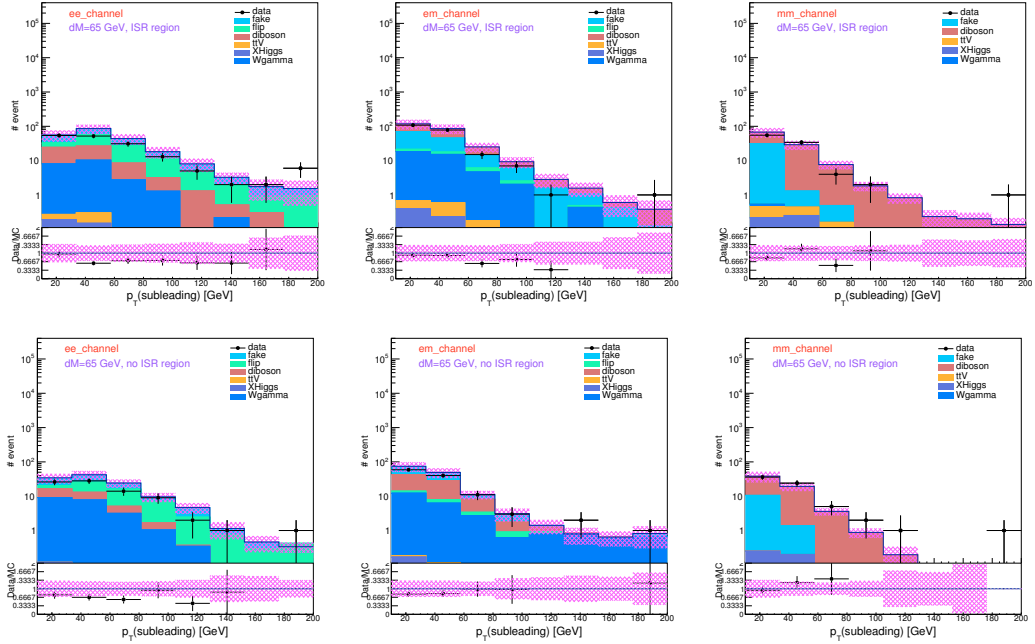


Figure A.11: Subleading lepton p_T in the validation regions with $\Delta M=65$ GeV and with ISR (top) or without ISR jet (bottom), for ee (left), $e\mu$ (middle), and $\mu\mu$ (right) channel.

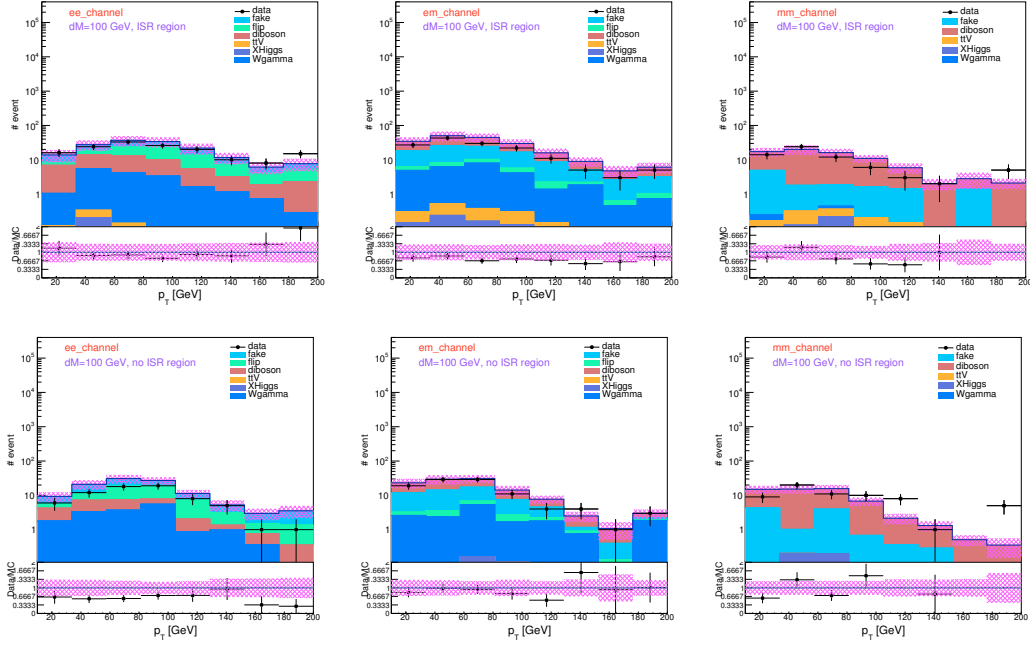


Figure A.12: Lepton p_T in the validation regions with $\Delta M=100$ GeV and with ISR (top) or without ISR jet (bottom), for ee (left), $e\mu$ (middle), and $\mu\mu$ (right) channel.

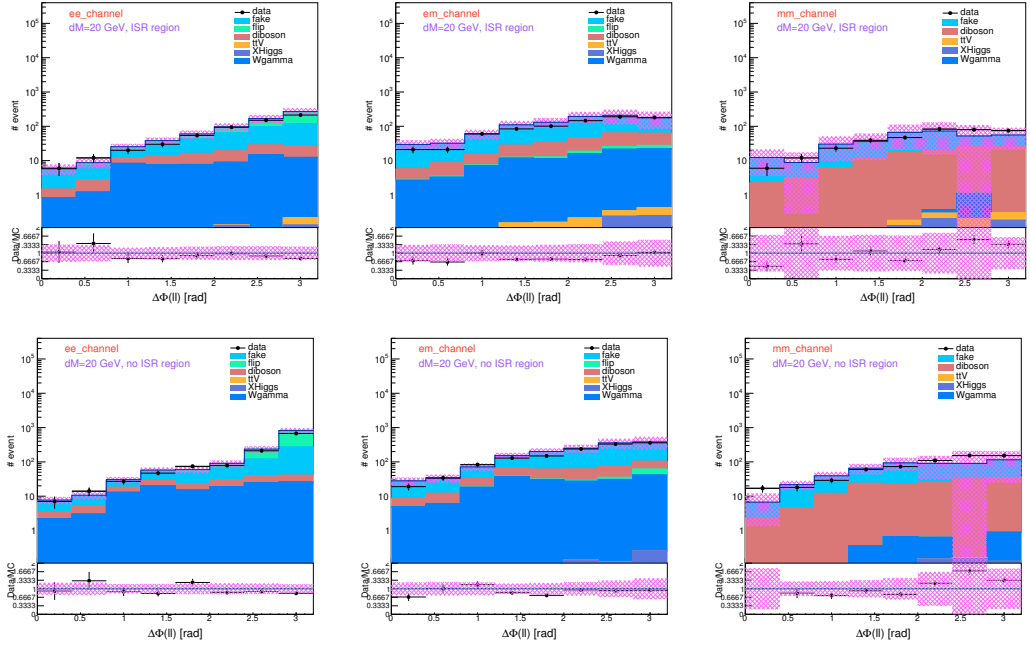


Figure A.13: Azimuthal angle between leptons in the validation regions with $\Delta M=20$ GeV and with ISR (top) or without ISR jet (bottom), for ee (left), $e\mu$ (middle), and $\mu\mu$ (right) channel.

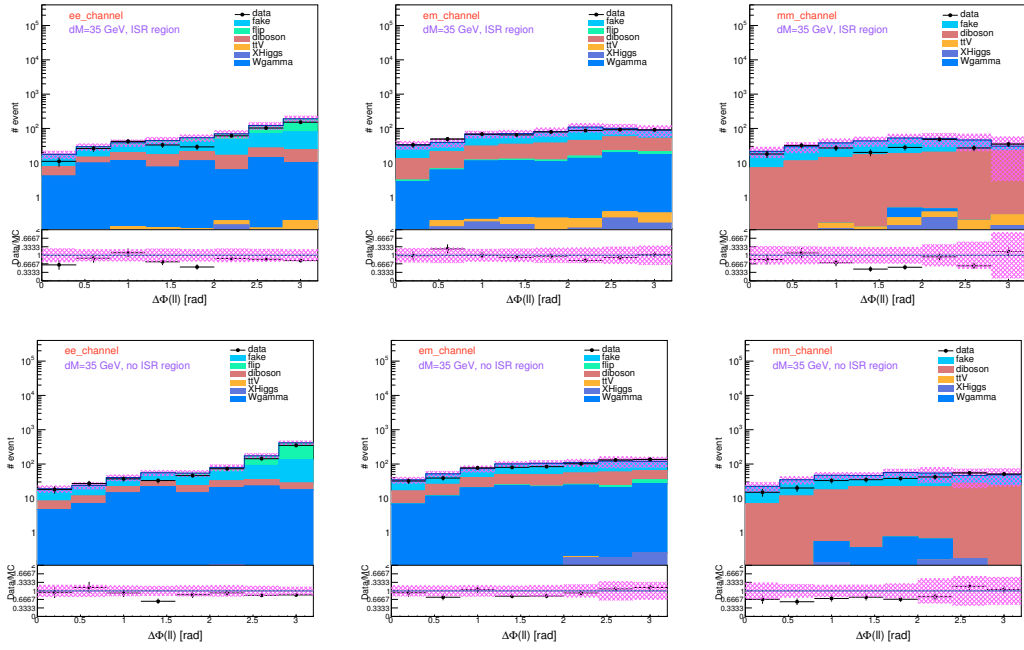


Figure A.14: Azimuthal angle between leptons in the validation regions with $\Delta M=35$ GeV and with ISR (top) or without ISR jet (bottom), for ee (left), $e\mu$ (middle), and $\mu\mu$ (right) channel.

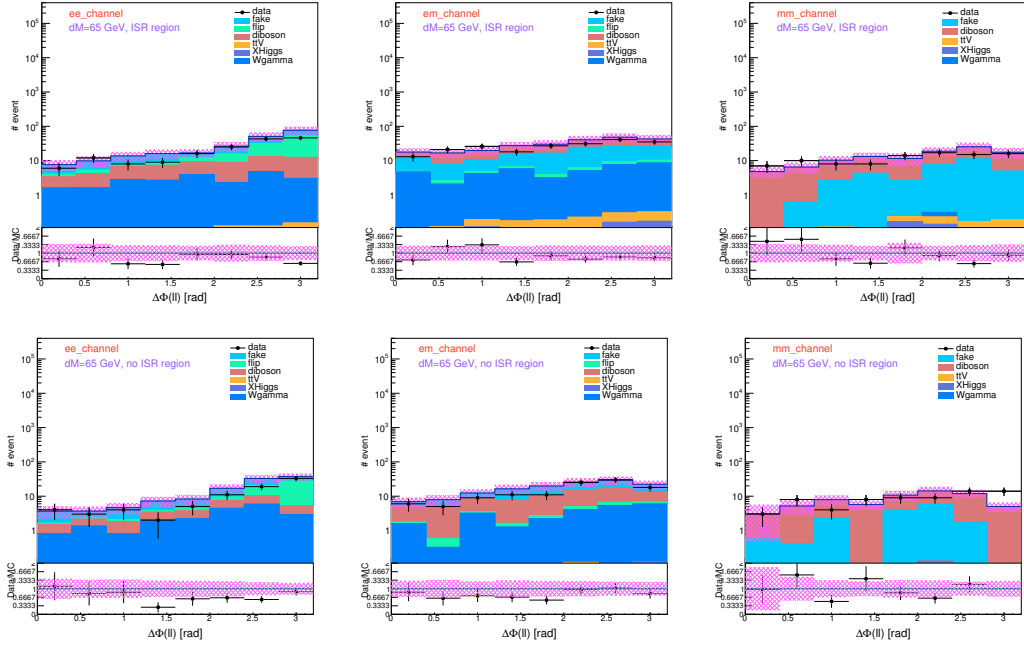


Figure A.15: Azimuthal angle between leptons in the validation regions with $\Delta M=65$ GeV and with ISR (top) or without ISR jet (bottom), for ee (left), $e\mu$ (middle), and $\mu\mu$ (right) channel.

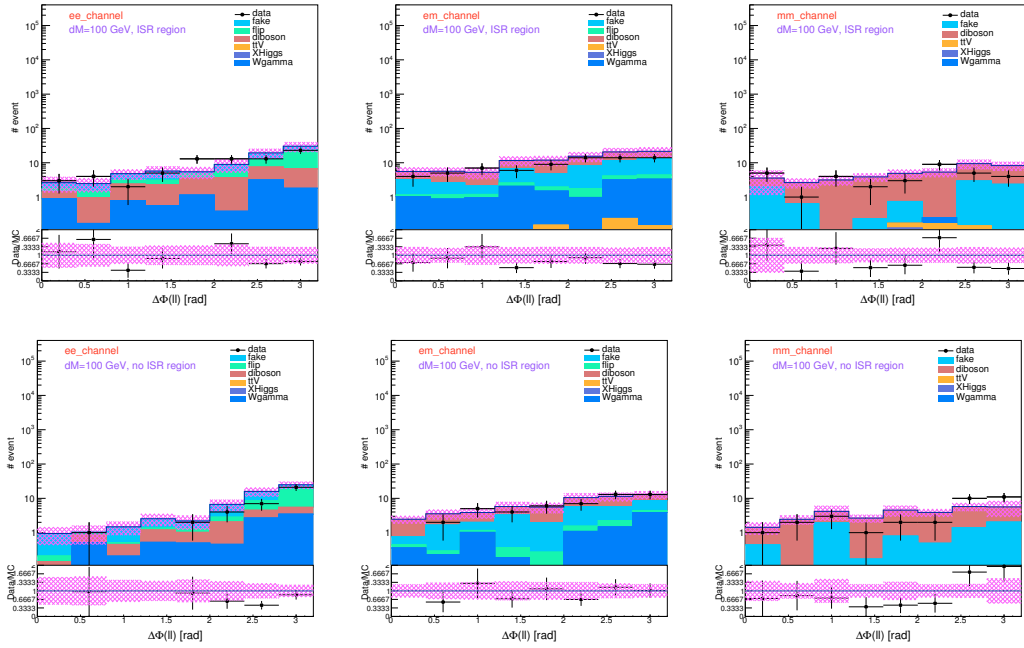


Figure A.16: Azimuthal angle between leptons in the validation regions with $\Delta M = 100$ GeV and with ISR (top) or without ISR jet (bottom), for ee (left), $e\mu$ (middle), and $\mu\mu$ (right) channel.

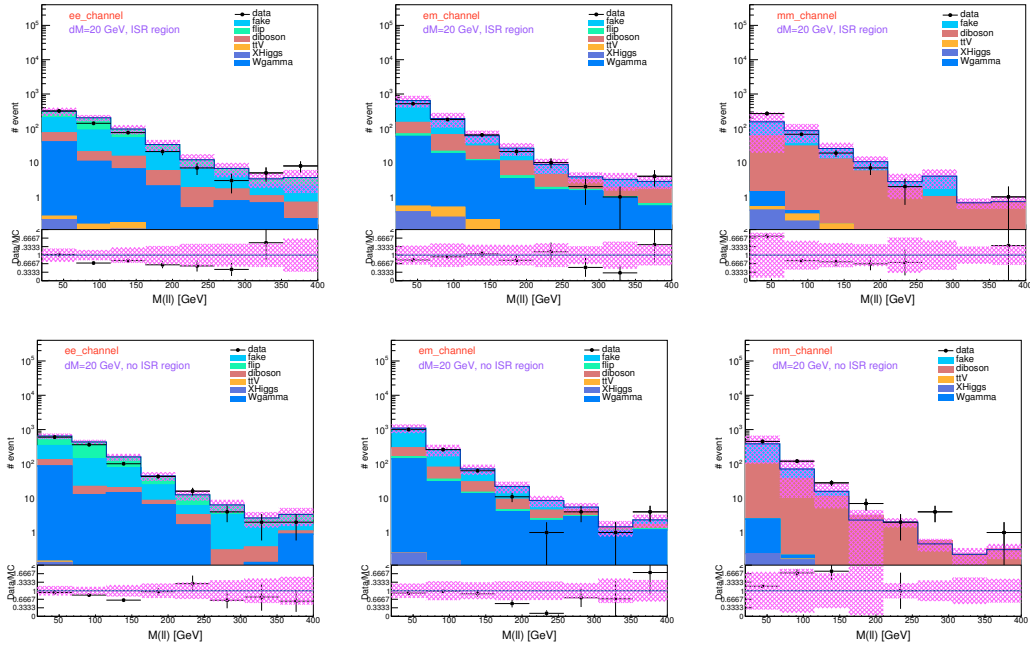


Figure A.17: Invariant mass of the 2 leptons in the validation regions with $\Delta M = 20$ GeV and with ISR (top) or without ISR jet (bottom), for ee (left), $e\mu$ (middle), and $\mu\mu$ (right) channel.

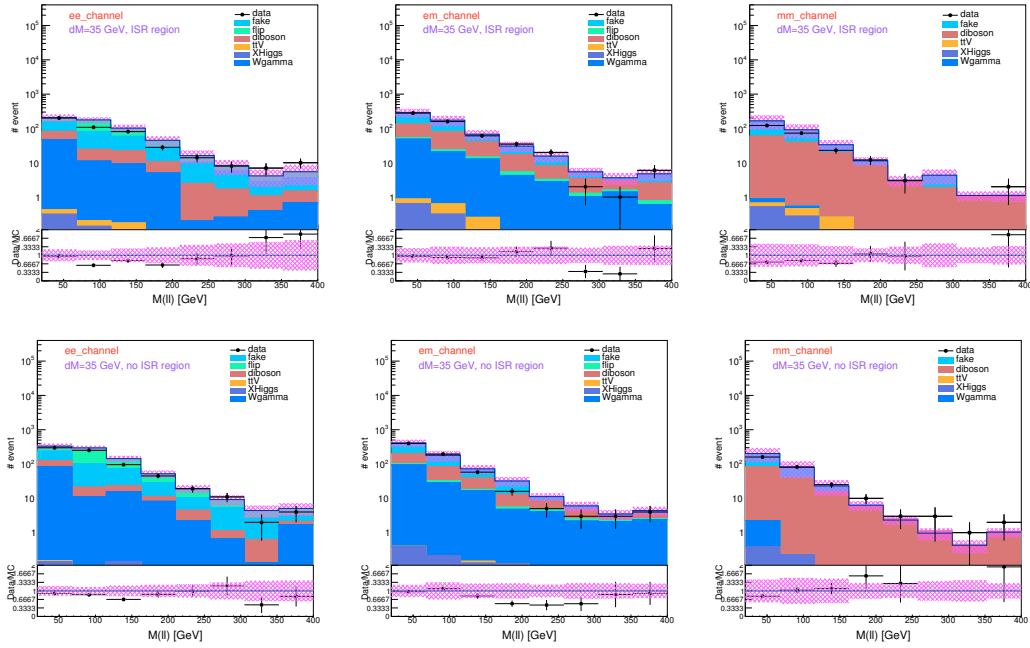


Figure A.18: Invariant mass of the 2 leptons in the validation regions with $\Delta M=35$ GeV and with ISR (top) or without ISR jet (bottom), for ee (left), $e\mu$ (middle), and $\mu\mu$ (right) channel.

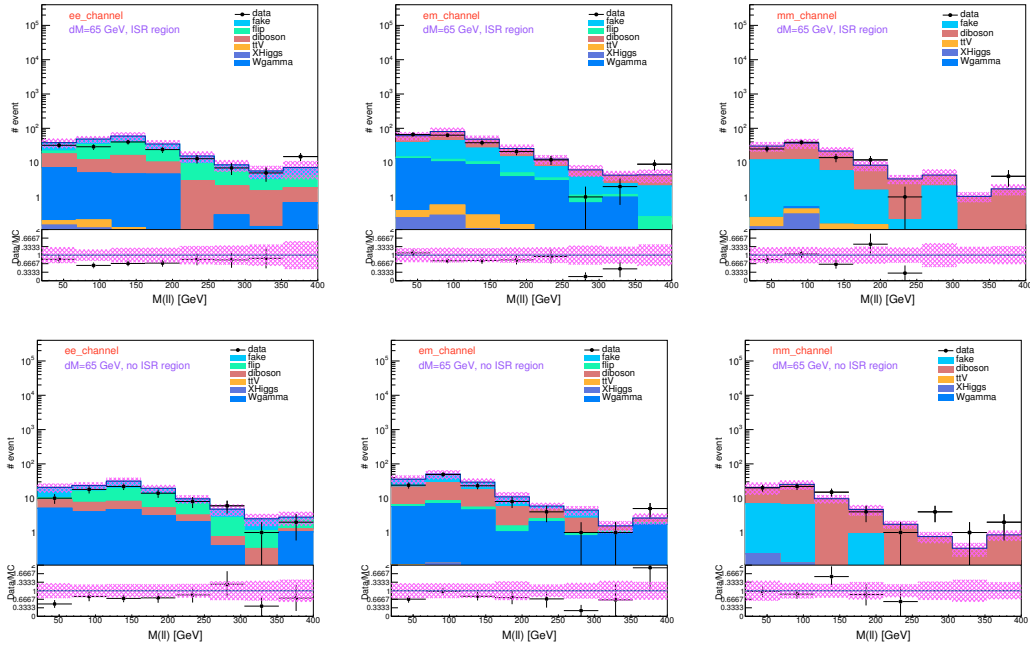


Figure A.19: Invariant mass of the 2 leptons in the validation regions with $\Delta M=65$ GeV and with ISR (top) or without ISR jet (bottom), for ee (left), $e\mu$ (middle), and $\mu\mu$ (right) channel.

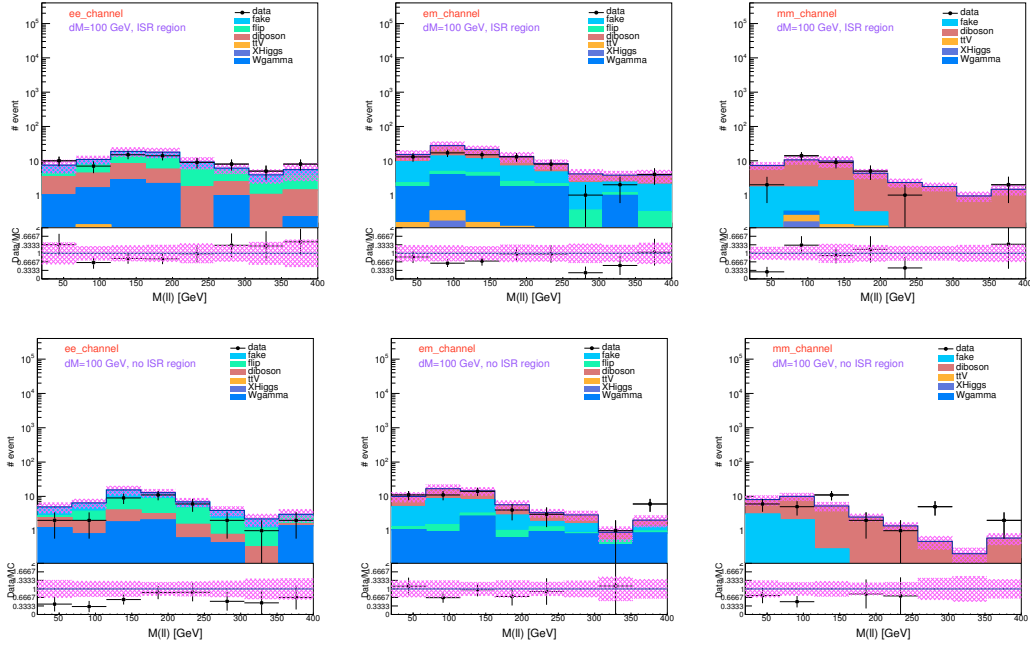


Figure A.20: Invariant mass of the 2 leptons in the validation regions with $\Delta M=100$ GeV and with ISR (top) or without ISR jet (bottom), for ee (left), $e\mu$ (middle), and $\mu\mu$ (right) channel.

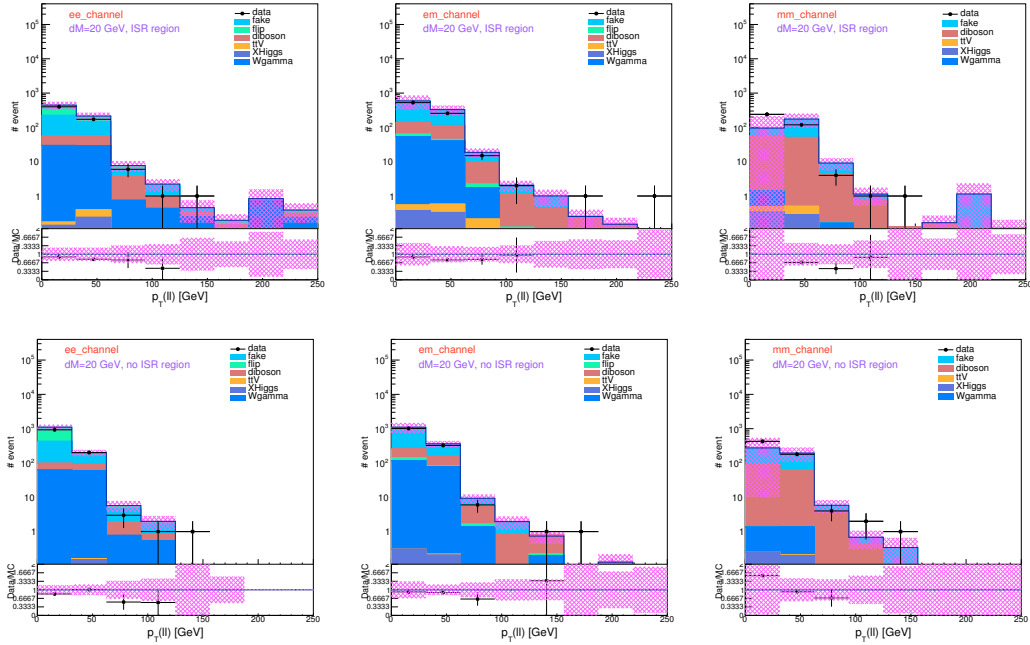


Figure A.21: Total transverse momentum of the 2 leptons in the validation regions with $\Delta M=20$ GeV and with ISR (top) or without ISR jet (bottom), for ee (left), $e\mu$ (middle), and $\mu\mu$ (right) channel.

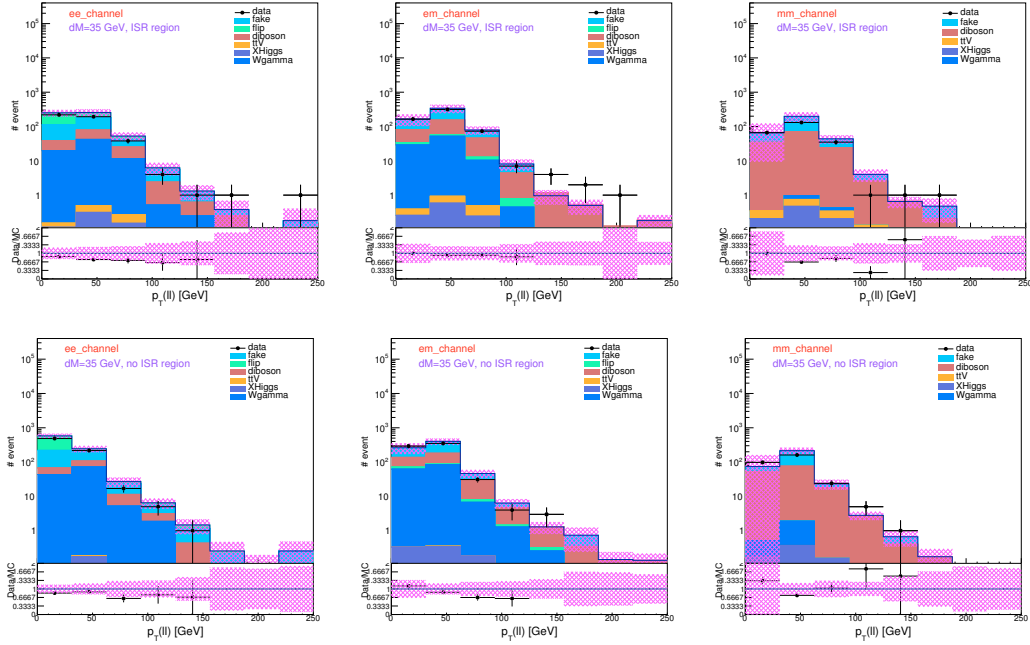


Figure A.22: Total transverse momentum of the 2 leptons in the validation regions with $\Delta M=35$ GeV and with ISR (top) or without ISR jet (bottom), for ee (left), $e\mu$ (middle), and $\mu\mu$ (right) channel.

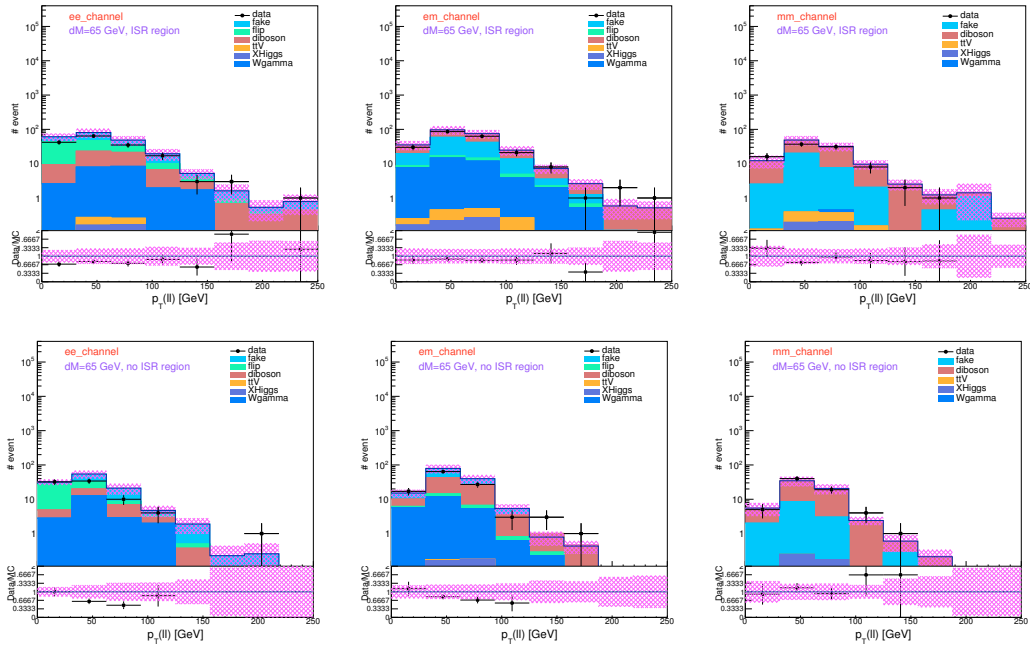


Figure A.23: Total transverse momentum of the 2 leptons in the validation regions with $\Delta M=65$ GeV and with ISR (top) or without ISR jet (bottom), for ee (left), $e\mu$ (middle), and $\mu\mu$ (right) channel.

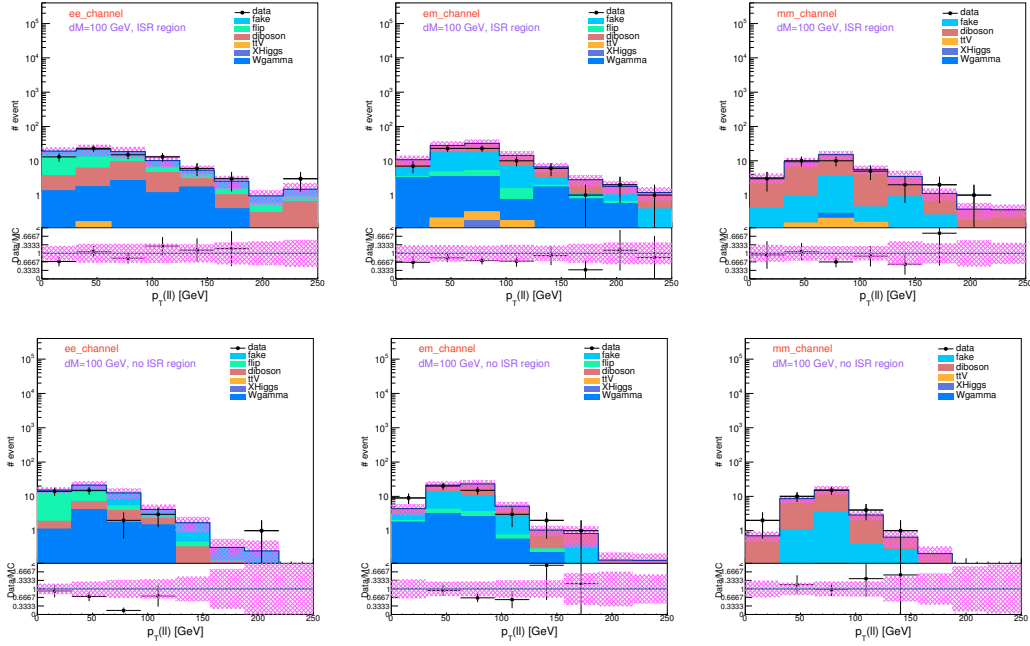


Figure A.24: Total transverse momentum of the 2 leptons in the validation regions with $\Delta M=100$ GeV and with ISR (top) or without ISR jet (bottom), for ee (left), $e\mu$ (middle), and $\mu\mu$ (right) channel.

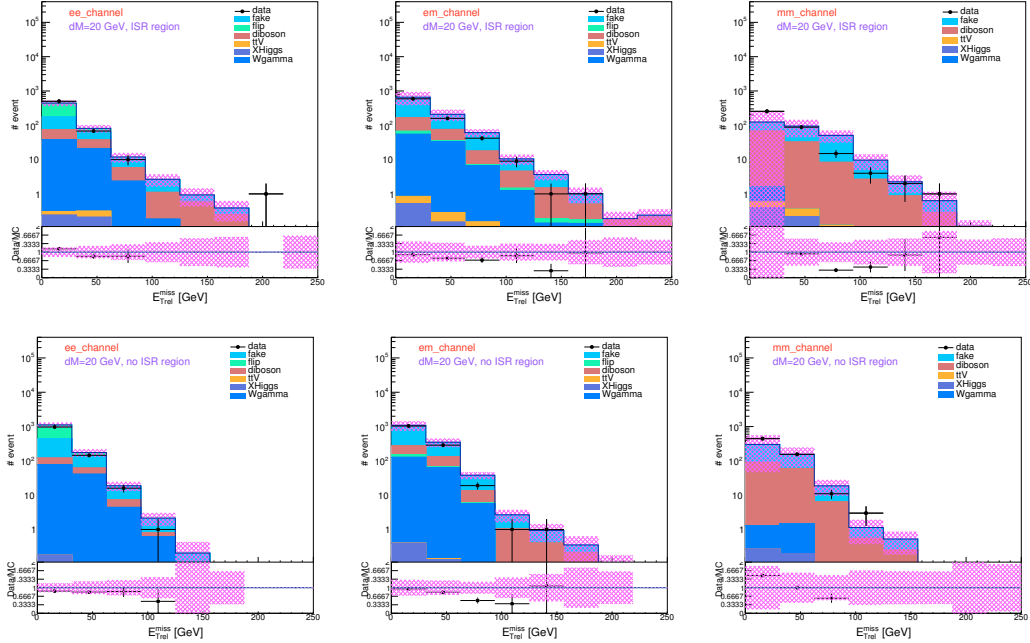


Figure A.25: Metrel in the validation regions with $\Delta M=20$ GeV and with ISR (top) or without ISR jet (bottom), for ee (left), $e\mu$ (middle), and $\mu\mu$ (right) channel.

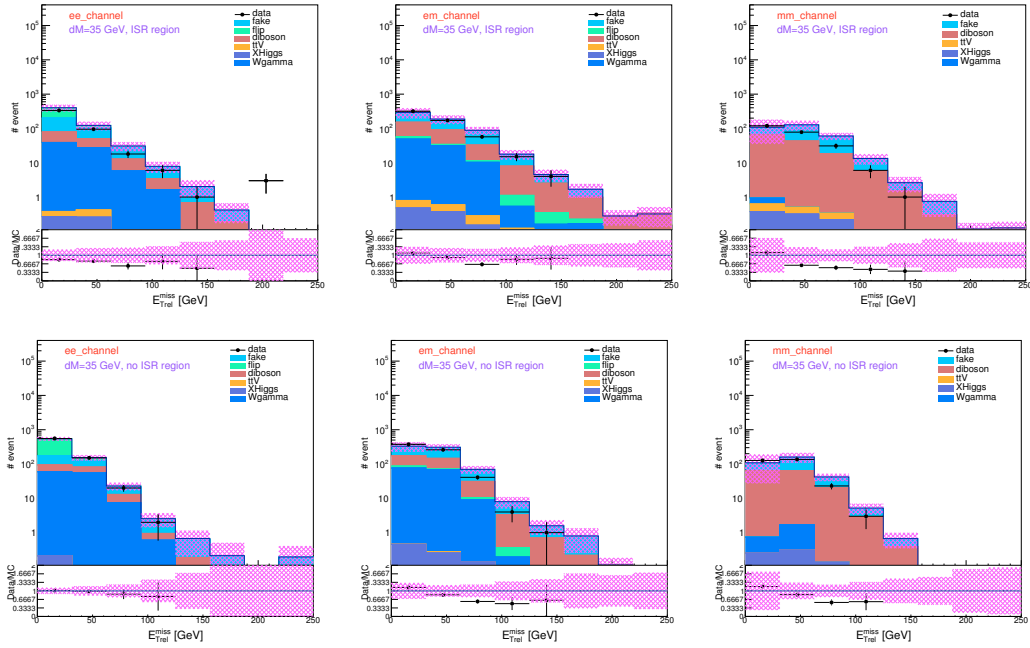


Figure A.26: Metrel in the validation regions with $\Delta M=35$ GeV and with ISR (top) or without ISR jet (bottom), for ee (left), $e\mu$ (middle), and $\mu\mu$ (right) channel.

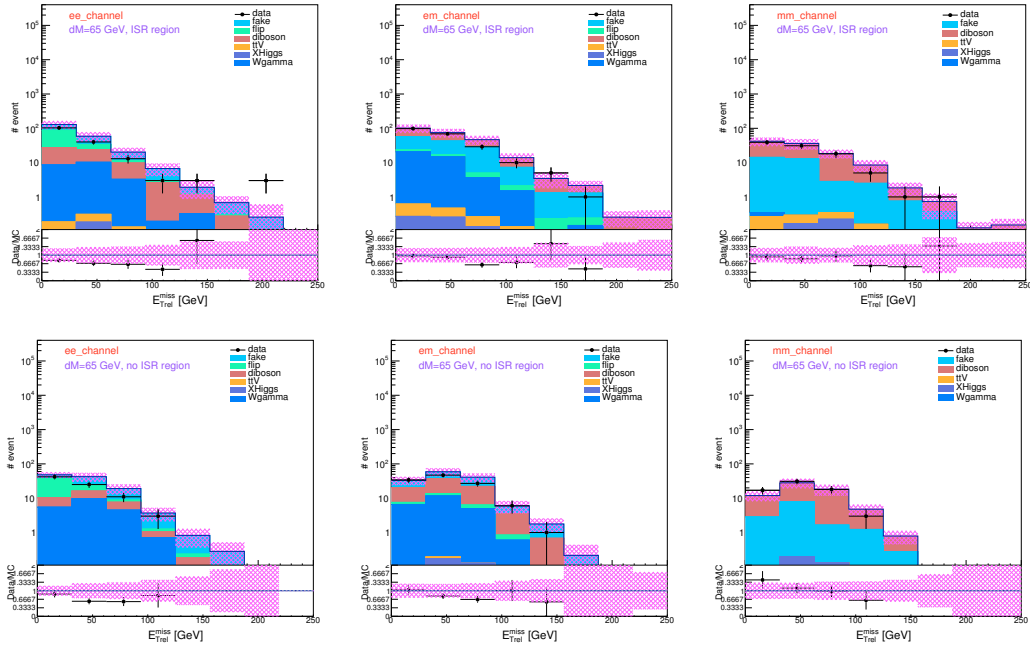


Figure A.27: Metrel in the validation regions with $\Delta M=65$ GeV and with ISR (top) or without ISR jet (bottom), for ee (left), $e\mu$ (middle), and $\mu\mu$ (right) channel.

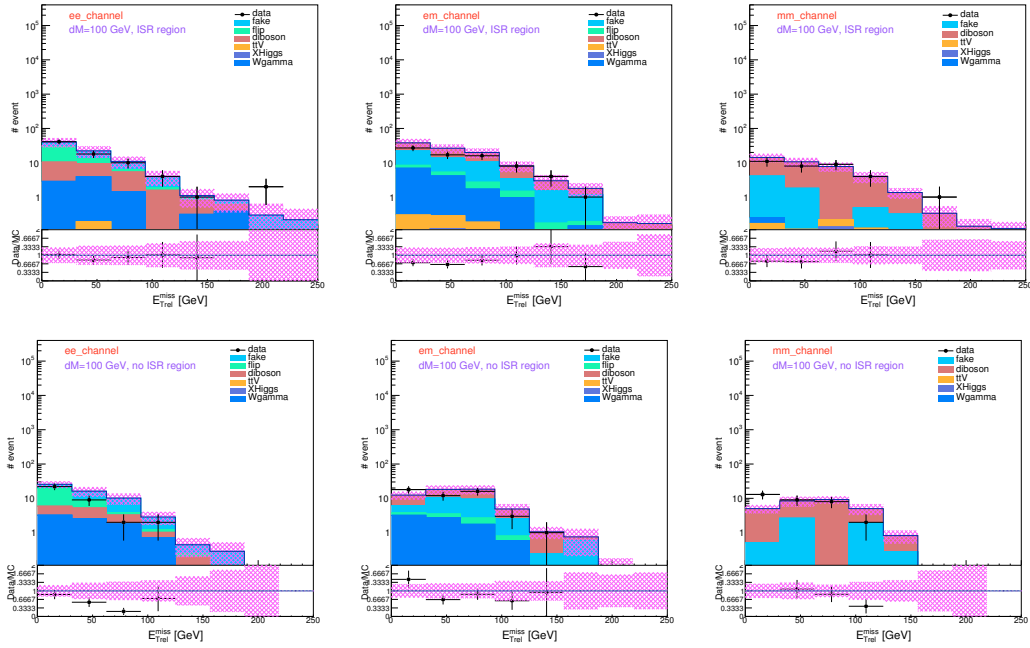


Figure A.28: Metrel in the validation regions with $\Delta M=100$ GeV and with ISR (top) or without ISR jet (bottom), for ee (left), $e\mu$ (middle), and $\mu\mu$ (right) channel.

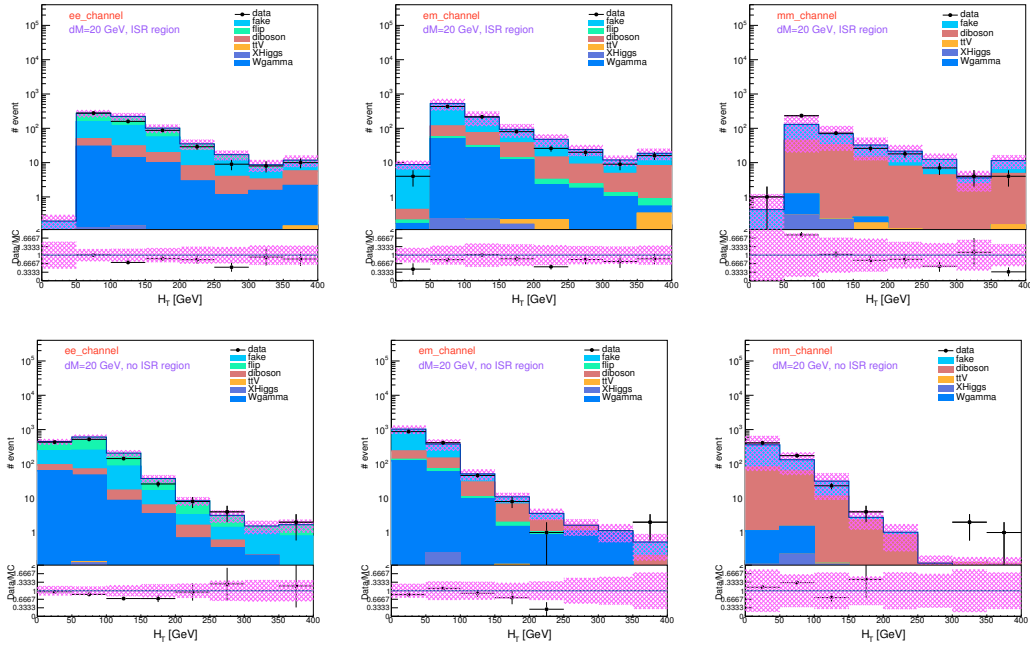


Figure A.29: H_T in the validation regions with $\Delta M=20$ GeV and with ISR (top) or without ISR jet (bottom), for ee (left), $e\mu$ (middle), and $\mu\mu$ (right) channel.

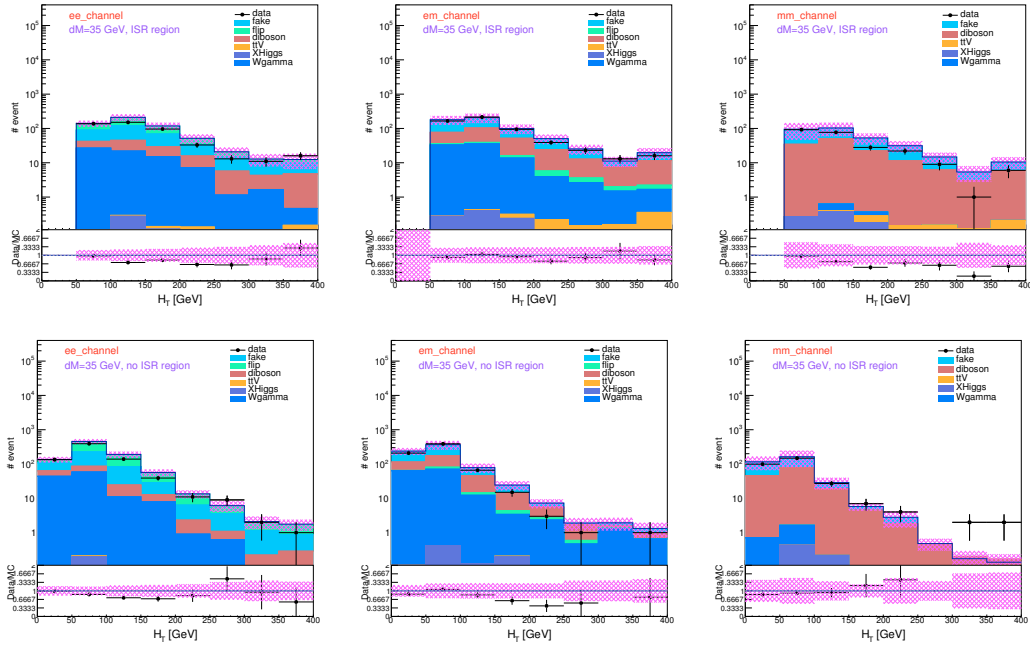


Figure A.30: H_T in the validation regions with $\Delta M=35$ GeV and with ISR (top) or without ISR jet (bottom), for ee (left), $e\mu$ (middle), and $\mu\mu$ (right) channel.

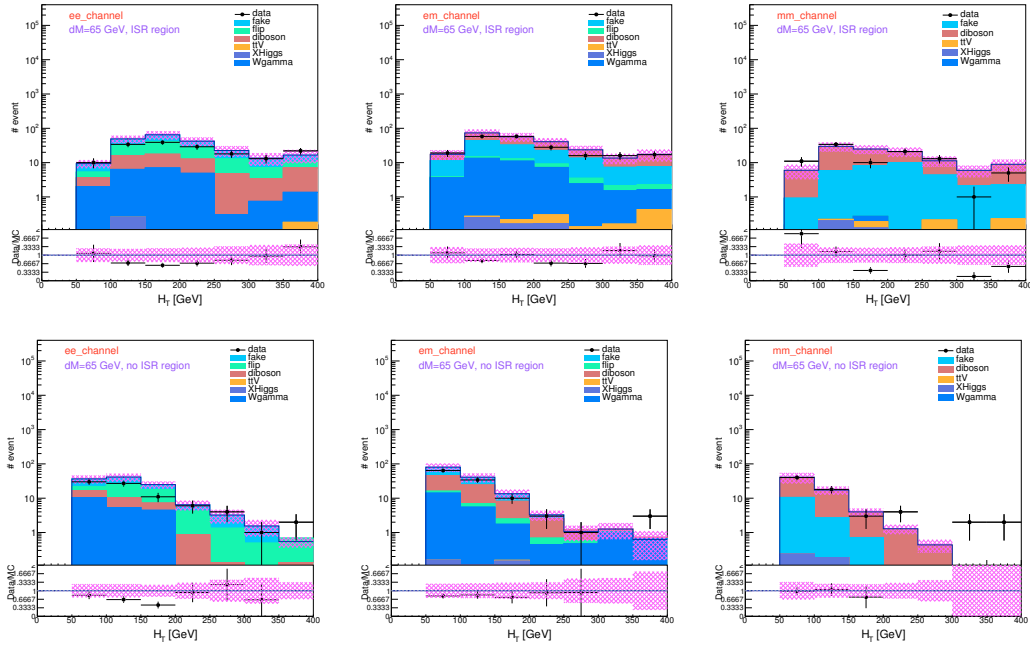


Figure A.31: H_T in the validation regions with $\Delta M=65$ GeV and with ISR (top) or without ISR jet (bottom), for ee (left), $e\mu$ (middle), and $\mu\mu$ (right) channel.

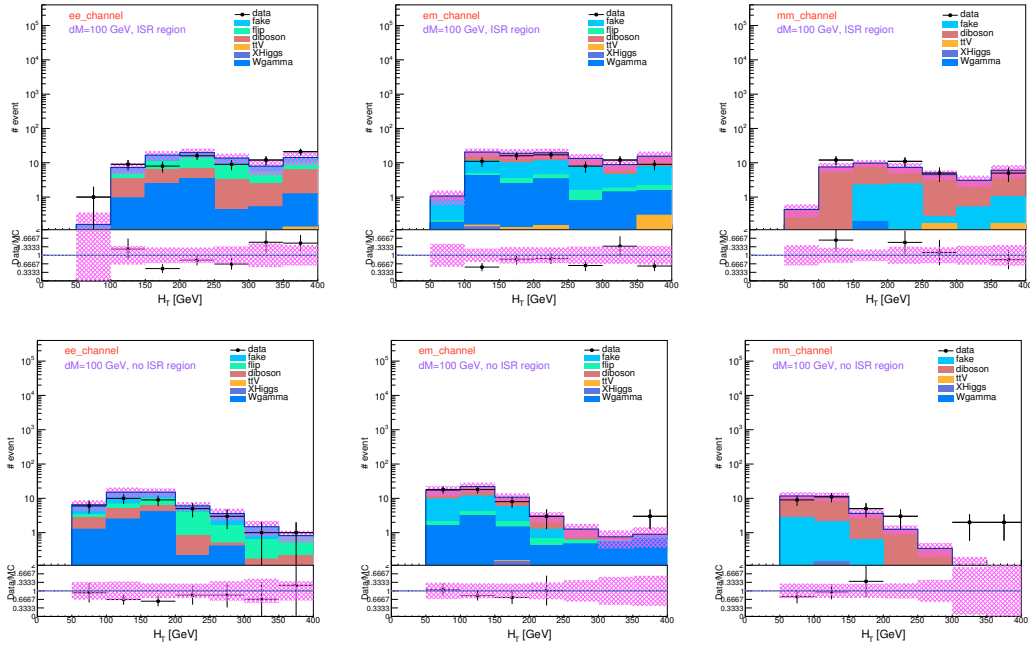


Figure A.32: H_T in the validation regions with $\Delta M=100$ GeV and with ISR (top) or without ISR jet (bottom), for ee (left), $e\mu$ (middle), and $\mu\mu$ (right) channel.

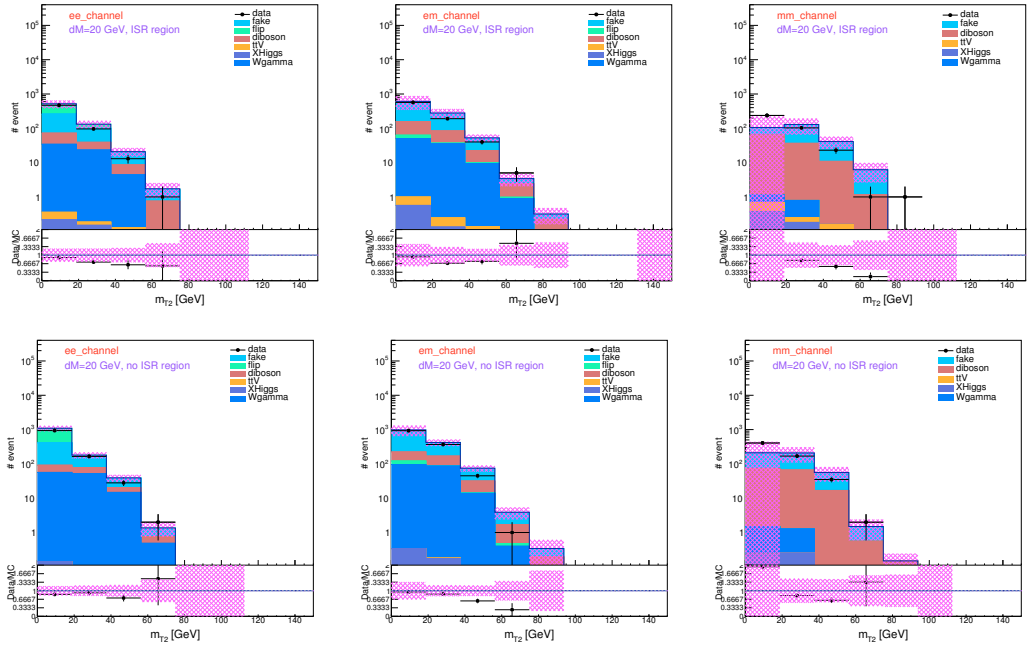


Figure A.33: m_{T2} in the validation regions with $\Delta M=20$ GeV and with ISR (top) or without ISR jet (bottom), for ee (left), $e\mu$ (middle), and $\mu\mu$ (right) channel.

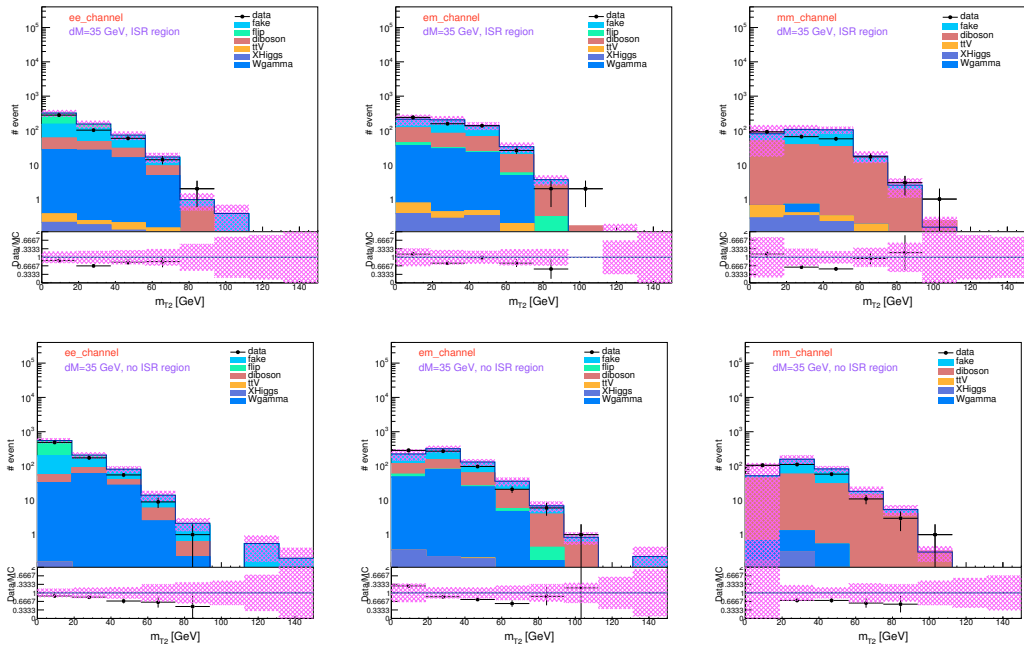


Figure A.34: m_{T2} in the validation regions with $\Delta M=35$ GeV and with ISR (top) or without ISR jet (bottom), for ee (left), $e\mu$ (middle), and $\mu\mu$ (right) channel.

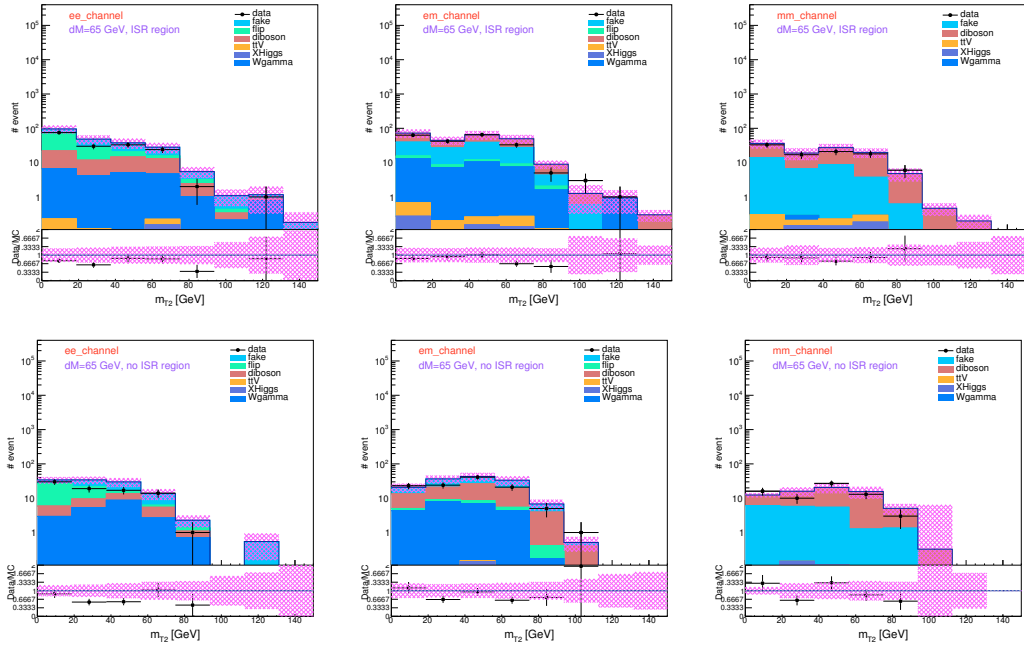


Figure A.35: m_{T2} in the validation regions with $\Delta M=65$ GeV and with ISR (top) or without ISR jet (bottom), for ee (left), $e\mu$ (middle), and $\mu\mu$ (right) channel.

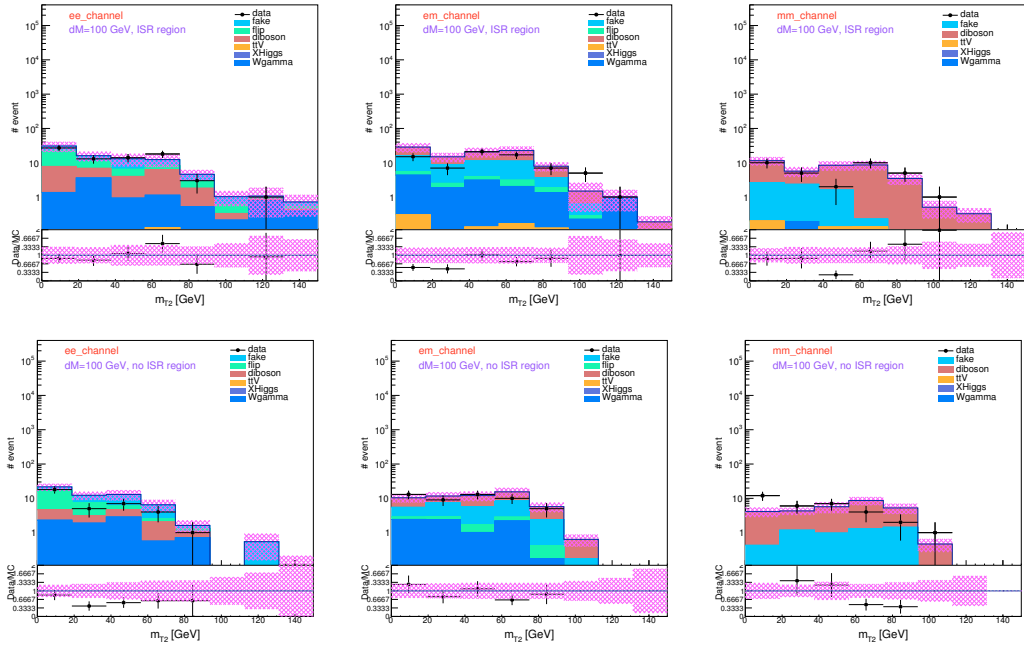


Figure A.36: m_{T2} in the validation regions with $\Delta M=100$ GeV and with ISR (top) or without ISR jet (bottom), for ee (left), $e\mu$ (middle), and $\mu\mu$ (right) channel.

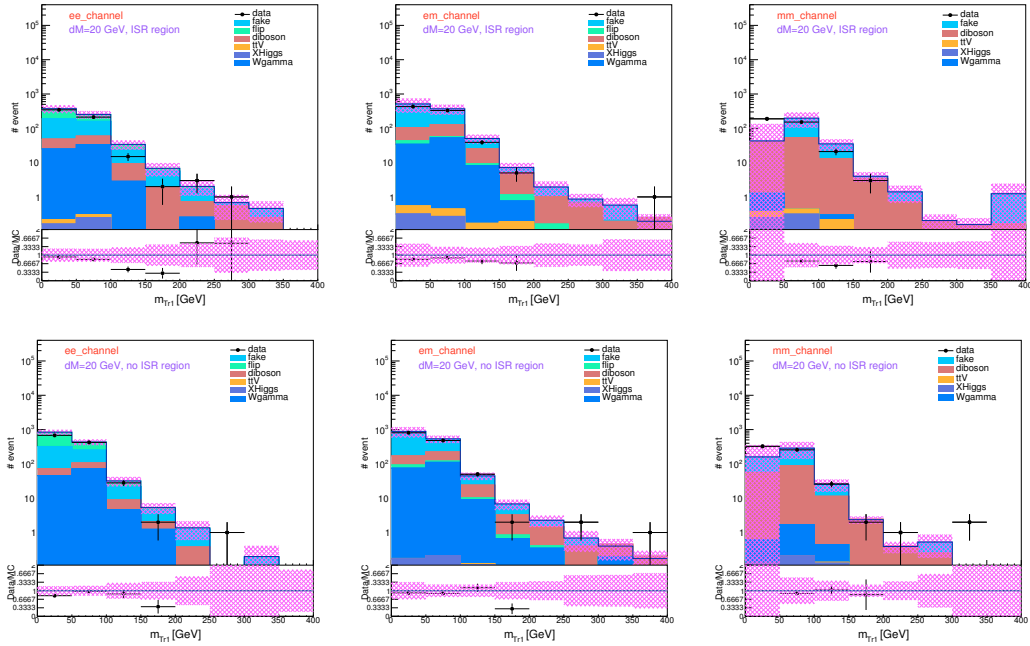


Figure A.37: m_{T1} in the validation regions with $\Delta M=20$ GeV and with ISR (top) or without ISR jet (bottom), for ee (left), $e\mu$ (middle), and $\mu\mu$ (right) channel.

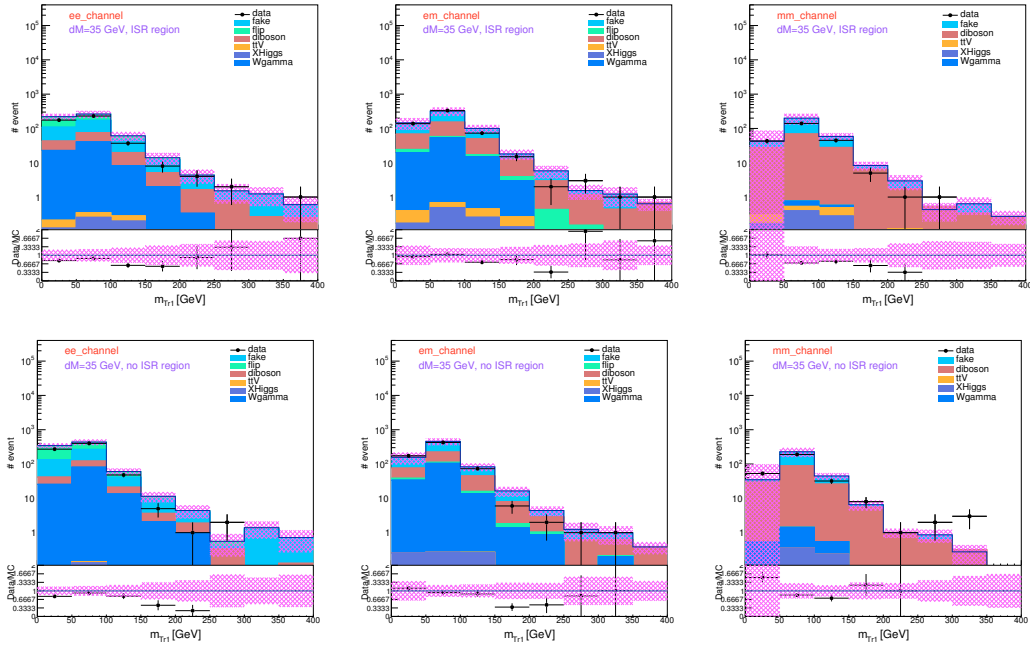


Figure A.38: $m_{T_{r1}}$ in the validation regions with $\Delta M=35$ GeV and with ISR (top) or without ISR jet (bottom), for ee (left), $e\mu$ (middle), and $\mu\mu$ (right) channel.

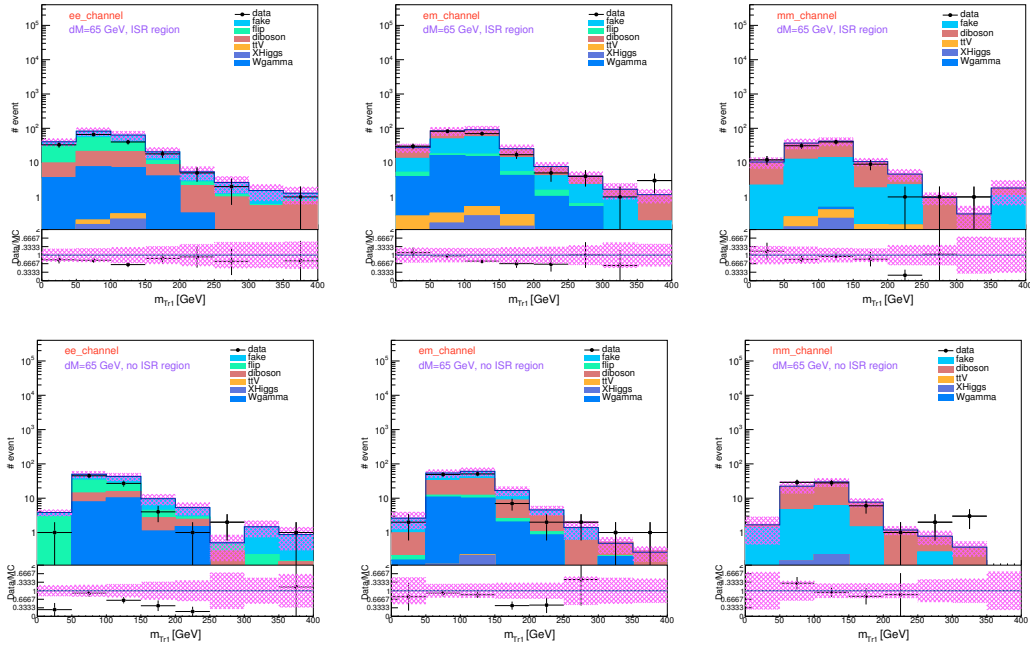


Figure A.39: $m_{T_{r1}}$ in the validation regions with $\Delta M=65$ GeV and with ISR (top) or without ISR jet (bottom), for ee (left), $e\mu$ (middle), and $\mu\mu$ (right) channel.

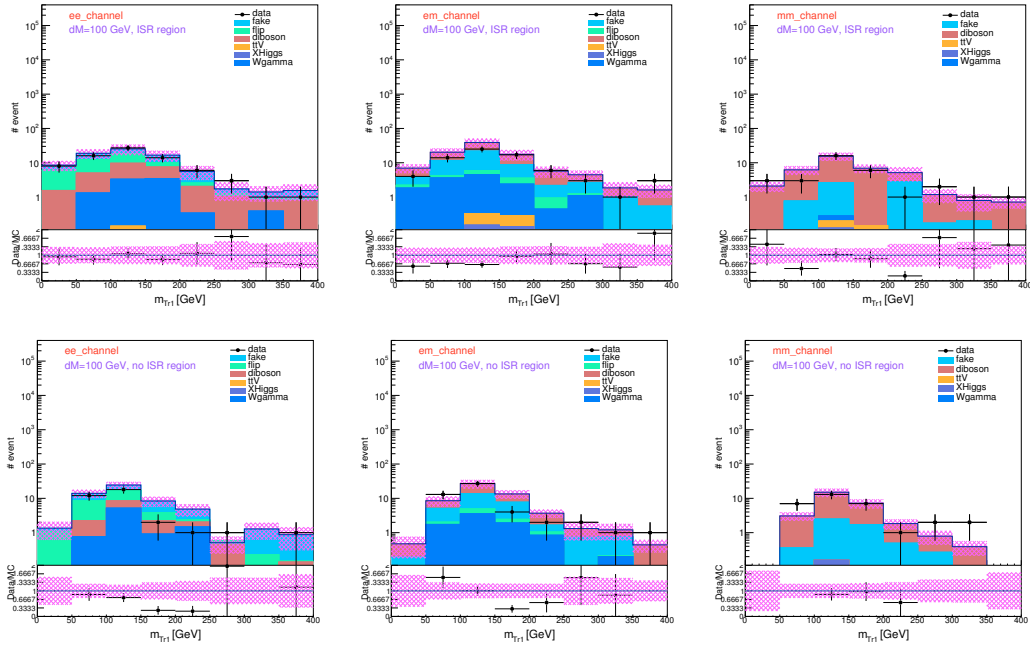


Figure A.40: $m_{T r_1}$ in the validation regions with $\Delta M=100$ GeV and with ISR (top) or without ISR jet (bottom), for ee (left), $e\mu$ (middle), and $\mu\mu$ (right) channel.

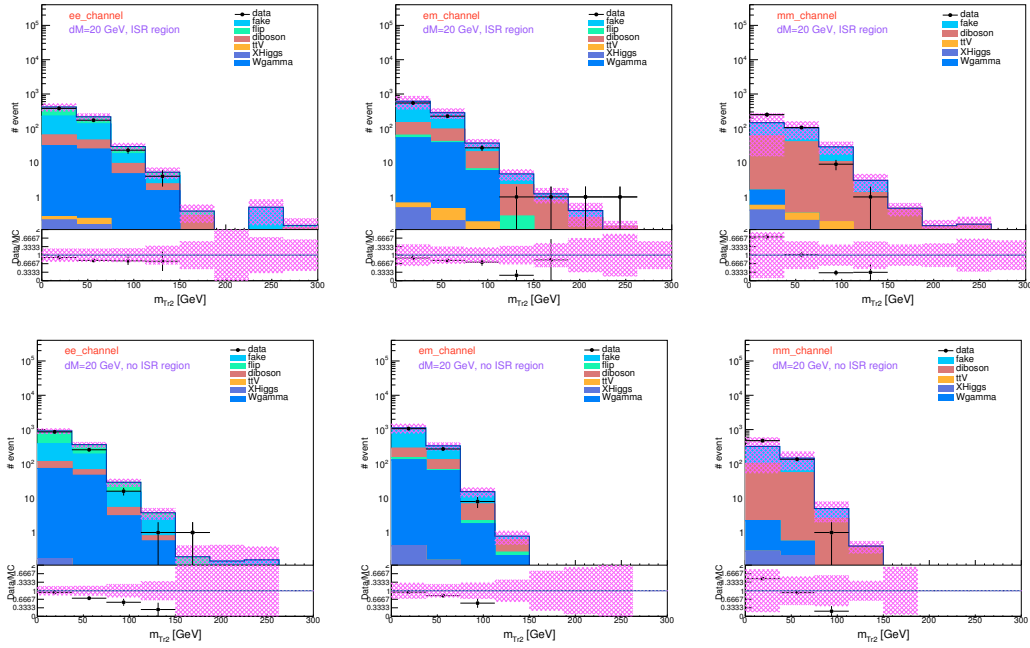


Figure A.41: $m_{T r_2}$ in the validation regions with $\Delta M=20$ GeV and with ISR (top) or without ISR jet (bottom), for ee (left), $e\mu$ (middle), and $\mu\mu$ (right) channel.

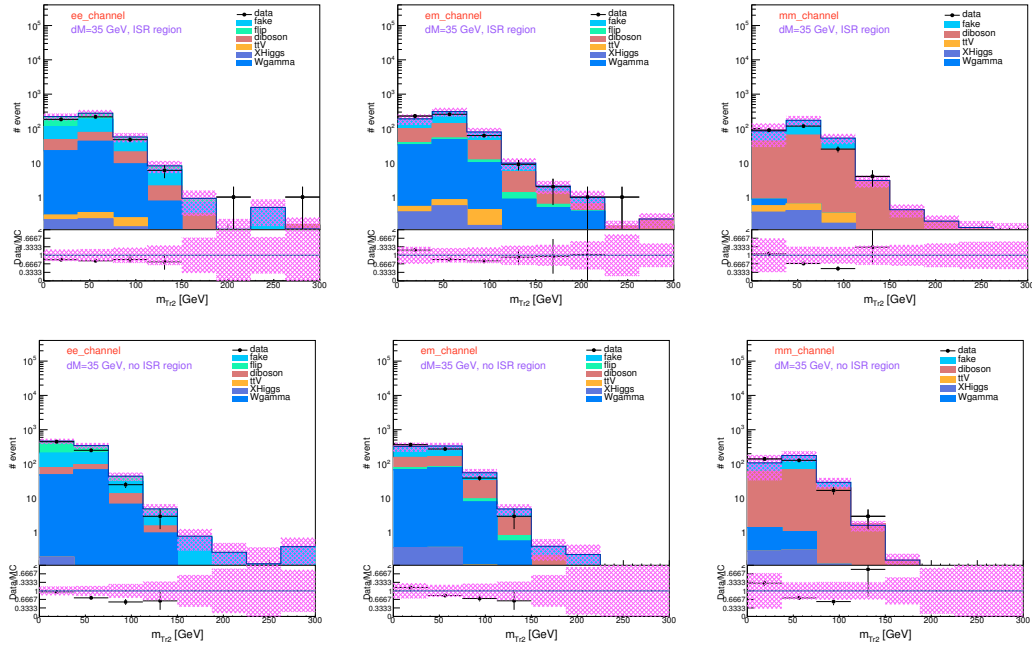


Figure A.42: $m_{T_{r2}}$ in the validation regions with $\Delta M=35$ GeV and with ISR (top) or without ISR jet (bottom), for ee (left), $e\mu$ (middle), and $\mu\mu$ (right) channel.

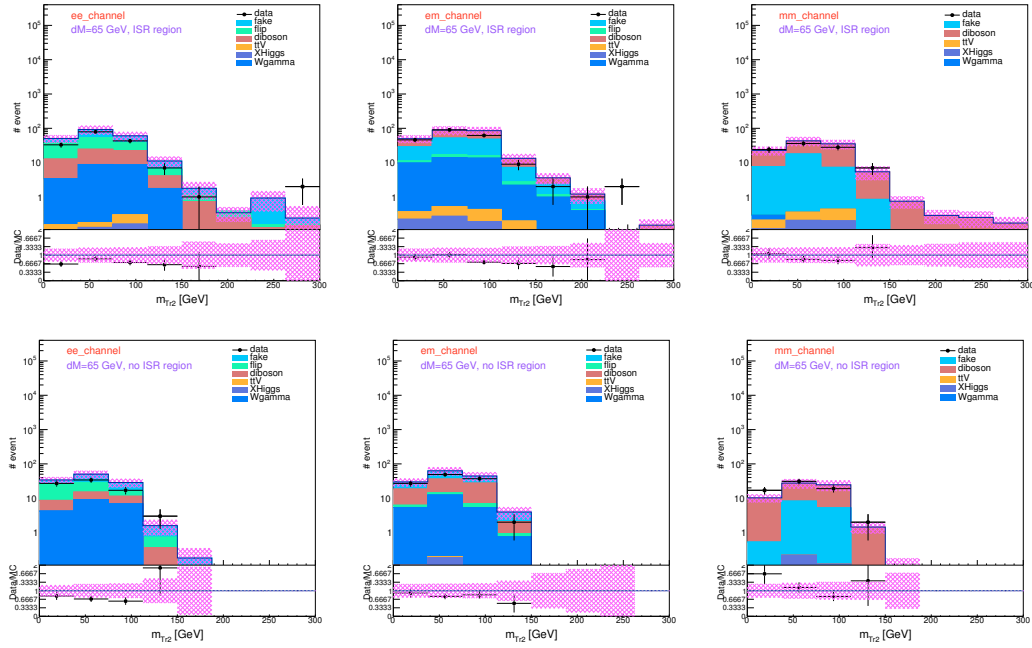


Figure A.43: $m_{T_{r2}}$ in the validation regions with $\Delta M=65$ GeV and with ISR (top) or without ISR jet (bottom), for ee (left), $e\mu$ (middle), and $\mu\mu$ (right) channel.

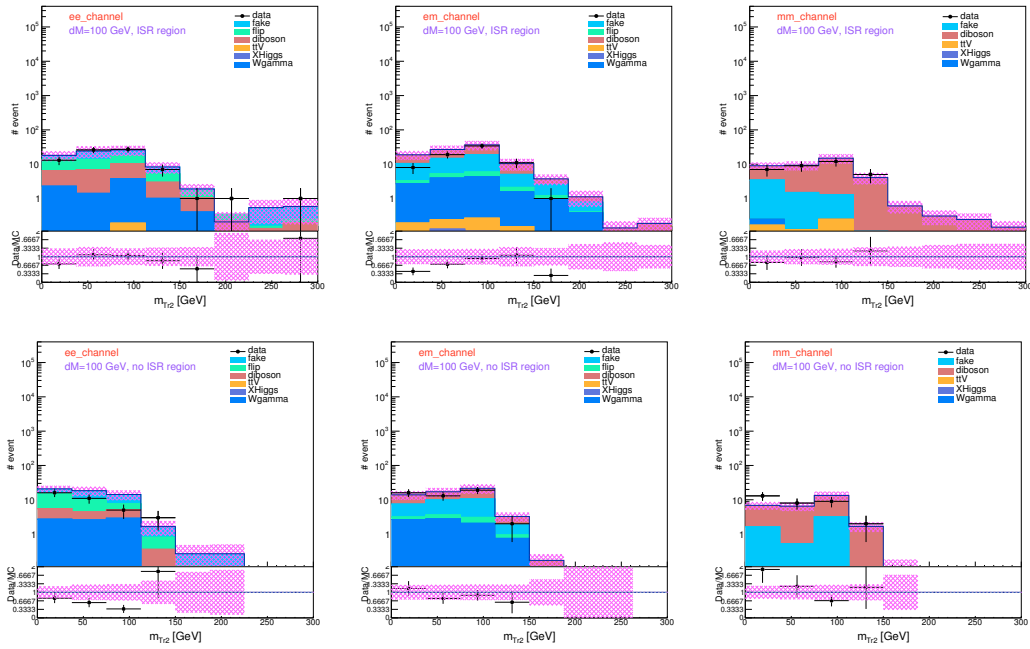


Figure A.44: $m_{T,2}$ in the validation regions with $\Delta M=100$ GeV and with ISR (top) or without ISR jet (bottom), for ee (left), $e\mu$ (middle), and $\mu\mu$ (right) channel.

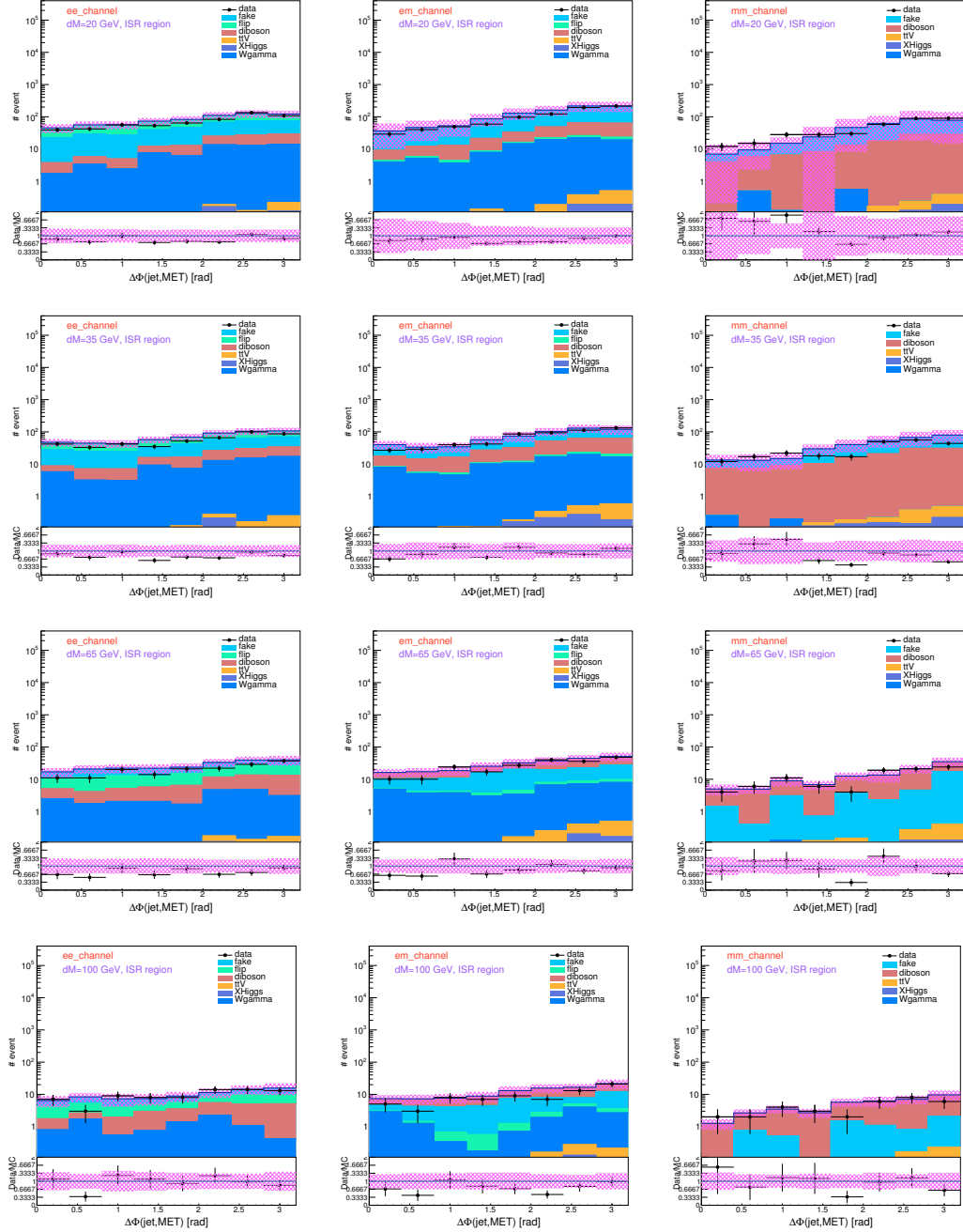


Figure A.45: The azimuthal angle between the leading jet and the missing transverse energy in the validation regions with ISR jet and $\Delta M=20$ GeV (top row), 35 GeV (second row), 65 GeV (third row), and 100 GeV (bottom row), for ee (left), $e\mu$ (middle), and $\mu\mu$ (right) channel.

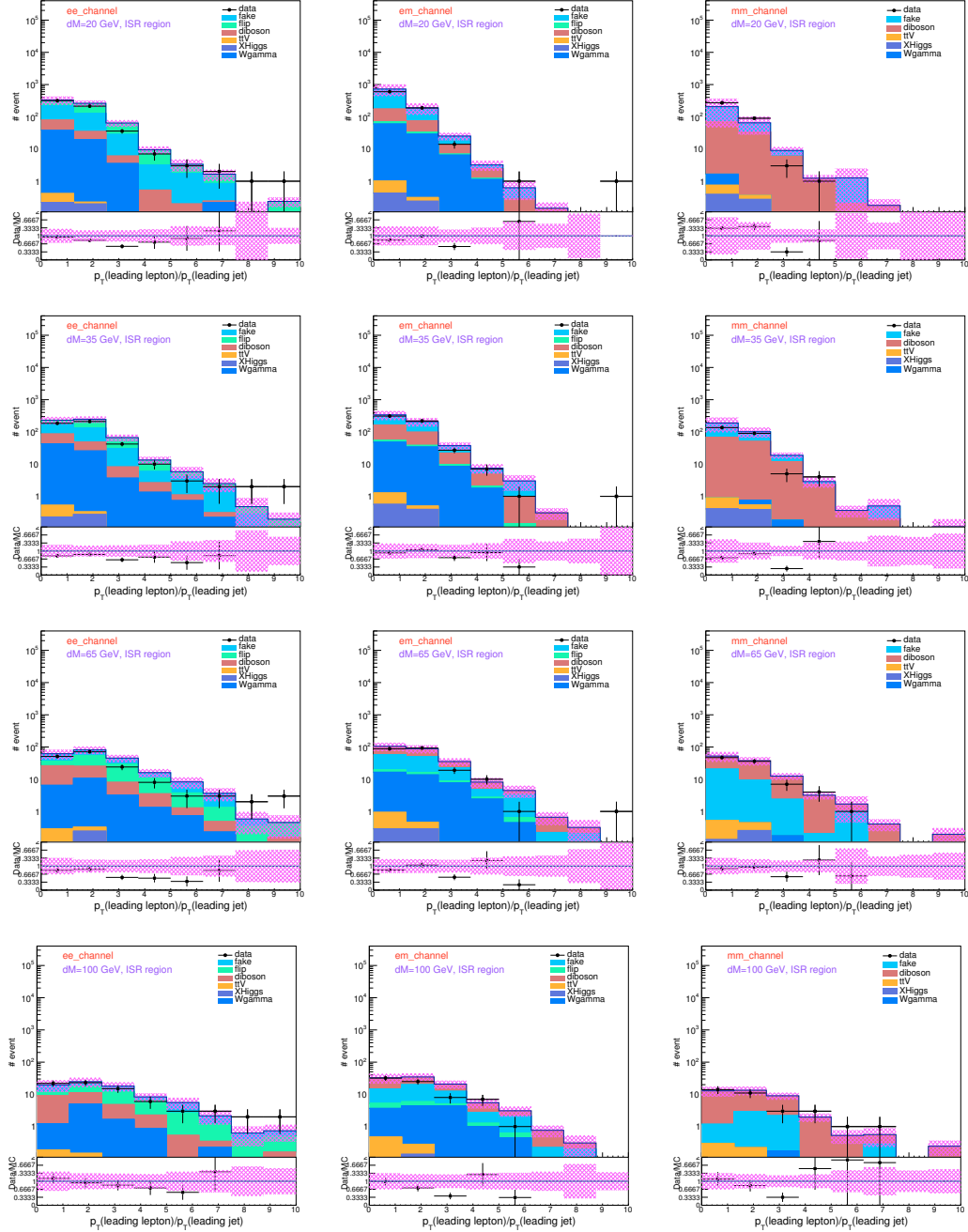


Figure A.46: The ratio of the p_T of the leading lepton and the p_T of the leading jet in the validation regions with ISR jet and $\Delta M=20$ GeV (top row), 35 GeV (second row), 65 GeV (third row), and 100 GeV (bottom row), for ee (left), $e\mu$ (middle), and $\mu\mu$ (right) channel.

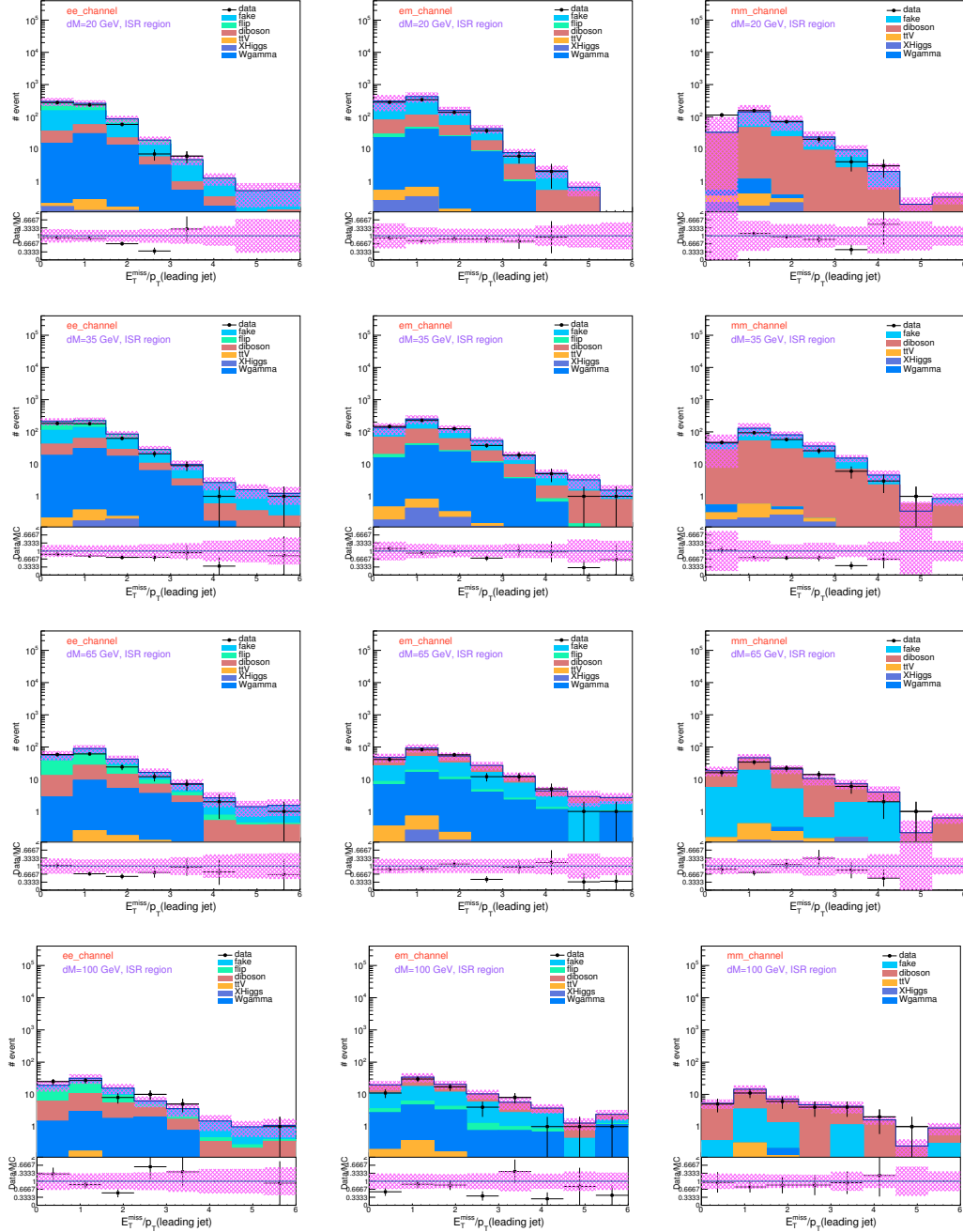


Figure A.47: The ratio of the missing transverse energy and the p_T of the leading jet in the validation regions with ISR jet and $\Delta M=20$ GeV (top row), 35 GeV (second row), 65 GeV (third row), and 100 GeV (bottom row), for ee (left), $e\mu$ (middle), and $\mu\mu$ (right) channel.

Bibliography

- [1] ATLAS Collaboration, G. Aad et al., *Search for direct production of charginos and neutralinos in events with three leptons and missing transverse momentum in $\sqrt{s} = 8\text{TeV}$ pp collisions with the ATLAS detector*, JHEP **1404** (2014) 169, arXiv:1402.7029 [hep-ex].
- [2] S. P. Martin, *A Supersymmetry primer*, arXiv:hep-ph/9709356 [hep-ph].
- [3] S. Glashow, *Partial Symmetries of Weak Interactions*, Nucl.Phys. **22** (1961) 579–588.
- [4] S. Weinberg, *A Model of Leptons*, Phys.Rev.Lett. **19** (1967) 1264–1266.
- [5] A. Salam, *Weak and Electromagnetic Interactions*, Conf.Proc. **C680519** (1968) 367–377.
- [6] ATLAS Collaboration, G. Aad et al., *Observation of a new particle in the search for the Standard Model Higgs boson with the ATLAS detector at the LHC*, Phys.Lett.B (2012) , arXiv:1207.7214 [hep-ex].
- [7] CMS Collaboration, S. Chatrchyan et al., *Observation of a new boson at a mass of 125 GeV with the CMS experiment at the LHC*, Phys.Lett.B (2012) , arXiv:1207.7235 [hep-ex].
- [8] S. Weinberg, *Implications of Dynamical Symmetry Breaking*, Phys. Rev. **D13** (1976) 974–996.
- [9] E. Gildener, *Gauge Symmetry Hierarchies*, Phys. Rev. **D14** (1976) 1667.
- [10] S. Weinberg, *Implications of Dynamical Symmetry Breaking: An Addendum*, Phys. Rev. **D19** (1979) 1277–1280.
- [11] L. Susskind, *Dynamics of Spontaneous Symmetry Breaking in the Weinberg- Salam Theory*, Phys. Rev. **D20** (1979) 2619–2625.
- [12] D. Clowe, M. Bradač, A. H. Gonzalez, M. Markevitch, S. W. Randall, C. Jones, and D. Zaritsky, *A Direct Empirical Proof of the Existence of Dark Matter*, ApJL **648** (2006) L109–L113, astro-ph/0608407.
- [13] H. Miyazawa, *Baryon Number Changing Currents*, Prog. Theor. Phys. **36** (6) (1966) 1266–1276.
- [14] P. Ramond, *Dual Theory for Free Fermions*, Phys. Rev. **D3** (1971) 2415–2418.
- [15] Y. A. Gol’fand and E. P. Likhtman, *Extension of the Algebra of Poincare Group Generators and Violation of p Invariance*, JETP Lett. **13** (1971) 323–326. [Pisma Zh.Eksp.Teor.Fiz.13:452-455,1971].

- [16] A. Neveu and J. H. Schwarz, *Factorizable dual model of pions*, Nucl. Phys. **B31** (1971) 86–112.
- [17] A. Neveu and J. H. Schwarz, *Quark Model of Dual Pions*, Phys. Rev. **D4** (1971) 1109–1111.
- [18] J. Gervais and B. Sakita, *Field theory interpretation of supergauges in dual models*, Nucl. Phys. **B34** (1971) 632–639.
- [19] D. V. Volkov and V. P. Akulov, *Is the Neutrino a Goldstone Particle?*, Phys. Lett. **B46** (1973) 109–110.
- [20] J. Wess and B. Zumino, *A Lagrangian Model Invariant Under Supergauge Transformations*, Phys. Lett. **B49** (1974) 52.
- [21] J. Wess and B. Zumino, *Supergauge Transformations in Four-Dimensions*, Nucl. Phys. **B70** (1974) 39–50.
- [22] S. Dimopoulos and H. Georgi, *Softly Broken Supersymmetry and SU(5)*, Nucl. Phys. **B193** (1981) 150.
- [23] E. Witten, *Dynamical Breaking of Supersymmetry*, Nucl. Phys. **B188** (1981) 513.
- [24] M. Dine, W. Fischler, and M. Srednicki, *Supersymmetric Technicolor*, Nucl. Phys. **B189** (1981) 575–593.
- [25] S. Dimopoulos and S. Raby, *Supercolor*, Nucl. Phys. **B192** (1981) 353.
- [26] N. Sakai, *Naturalness in Supersymmetric Guts*, Zeit. Phys. **C11** (1981) 153.
- [27] R. Kaul and P. Majumdar, *CANCELLATION OF QUADRATICALLY DIVERGENT MASS CORRECTIONS IN GLOBALLY SUPERSYMMETRIC SPONTANEOUSLY BROKEN GAUGE THEORIES*, Nucl. Phys. **B199** (1982) 36.
- [28] T. S.-K. Collaboration, *Search for Proton Decay via $p \rightarrow e^+\pi^0$ and $p \rightarrow \mu^+\pi^0$ in a Large Water Cherenkov Detector*, Phys. Rev. Lett. **102** (2009) 141801.
<http://link.aps.org/doi/10.1103/PhysRevLett.102.141801>.
- [29] H. Goldberg, *Constraint on the photino mass from cosmology*, Phys. Rev. Lett. **50** (1983) 1419.
- [30] J. Ellis, J. Hagelin, D. Nanopoulos, K. Olive, and M. Srednicki, *Supersymmetric relics from the big bang*, Nucl. Phys. **B238** (1984) 453–476.
- [31] S. Dimopoulos, S. Raby, and F. Wilczek, *Supersymmetry and the Scale of Unification*, Phys. Rev. **D24** (1981) 1681–1683.
- [32] L. E. Ibanez and G. G. Ross, *Low-Energy Predictions in Supersymmetric Grand Unified Theories*, Phys. Lett. **B105** (1981) 439.
- [33] M. B. Einhorn and D. R. T. Jones, *The Weak Mixing Angle and Unification Mass in Supersymmetric SU(5)*, Nucl. Phys. **B196** (1982) 475.
- [34] W. J. Marciano and G. Senjanovic, *Predictions of Supersymmetric Grand Unified Theories*, Phys. Rev. **D25** (1982) 3092.
- [35] C. Giunti, C. W. Kim, and U. Lee, *Running coupling constants and grand unification models*, Mod. Phys. Lett. **A6** (1991) 1745–1755.
- [36] J. Ellis, S. Kelley, and D. Nanopoulos, *Probing the desert using gauge coupling unification*, Phys. Lett. **B260** (1991) 131–137.

- [37] U. Amaldi, W. de Boer, and H. Furstenau, *Comparison of grand unified theories with electroweak and strong coupling constants measured at LEP*, Phys. Lett. **B260** (1991) 447–455.
- [38] P. Langacker and M.-X. Luo, *Implications of precision electroweak experiments for $M(t)$, $\rho(0)$, $\sin^2\theta(W)$ and grand unification*, Phys. Rev. **D44** (1991) 817–822.
- [39] A. Collaboration, *Search for new phenomena in final states with large jet multiplicities and missing transverse momentum at $\sqrt{s}=8$ TeV proton-proton collisions using the ATLAS experiment*, <http://arxiv.org/abs/1308.1841v3>.
- [40] A. Collaboration, *Search for squarks and gluinos with the ATLAS detector in final states with jets and missing transverse momentum using $\sqrt{s} = 8$ TeV proton-proton collision data*, <http://arxiv.org/abs/1405.7875v2>.
- [41] A. collaboration, *Search for squarks and gluinos in events with isolated leptons, jets and missing transverse momentum at $\sqrt{s} = 8$ TeV with the ATLAS detector*, Journal of High Energy Physics **2015** (2015) no. 4, . <http://dx.doi.org/10.1007/JHEP04%282015%29116>.
- [42] ATLAS, G. Aad et al., *Search for supersymmetry at $\sqrt{s}=8$ TeV in final states with jets and two same-sign leptons or three leptons with the ATLAS detector*, JHEP **1406** (2014) 035, arXiv:1404.2500 [hep-ex].
- [43] R. Barbieri and G. Giudice, *Upper Bounds on Supersymmetric Particle Masses*, Nucl.Phys. **B306** (1988) 63.
- [44] B. de Carlos and J. Casas, *One loop analysis of the electroweak breaking in supersymmetric models and the fine tuning problem*, Phys.Lett. **B309** (1993) 320–328, arXiv:hep-ph/9303291 [hep-ph].
- [45] ATLAS Collaboration, G. Aad et al., *The ATLAS Experiment at the CERN Large Hadron Collider*, JINST **3** (2008) S08003.
- [46] Particle Data Group, K. A. Olive et al., *Review of Particle Physics*, Chin. Phys. **C38** (2014) 090001.
- [47] "ATLAS Collaboration", G. "Aad and others", *The ATLAS Inner Detector commissioning and calibration*, The European Physical Journal C **70** (2010) no. 3, 787–821. <http://dx.doi.org/10.1140/epjc/s10052-010-1366-7>.
- [48] ATLAS TRT Collaboration, E. Abat et al., *The ATLAS TRT barrel detector*, JINST **3** (2008) P02014.
- [49] ATLAS TRT Collaboration, E. Abat et al., *The ATLAS TRT end-cap detectors*, JINST **3** (2008) P10003.
- [50] *ATLAS inner detector: Technical Design Report, 2*. Technical Design Report ATLAS. CERN, Geneva, 1997.
- [51] ATLAS TRT Collaboration, E. Abat et al., *The ATLAS TRT electronics*, JINST **3** (2008) P06007.
- [52] M. Hance, *Readout of the ATLAS Transition Radiation Tracker: Timing Parameters and Constraints*, Tech. Rep. ATL-INDET-PUB-2008-008. ATL-COM-INDET-2008-002, CERN, Geneva, Sep, 2007.
- [53] ATLAS Collaboration, *Calibration of the ATLAS Transition Radiation Tracker*, ATLAS-CONF-2011-006, 2011.

- [54] B. Dolgoshein, *Transition radiation detectors*, Nuclear Instruments and Methods in Physics Research A **326** (1993) no. 3, 434 – 469.
<http://www.sciencedirect.com/science/article/pii/016890029390846A>.
- [55] A. Andronic and J. P. Wessels, *Transition radiation detectors*, Nuclear Instruments and Methods in Physics Research A **666** (2012) 130–147, arXiv:1111.4188 [physics.ins-det].
- [56] ATLAS Collaboration, G. Aad et al., *Performance of the ATLAS Trigger System in 2010*, Eur.Phys.J. **C72** (2012) 1849, arXiv:1110.1530 [hep-ex].
- [57] ATLAS Collaboration, G. Aad et al., *Electron performance measurements with the ATLAS detector using the 2010 LHC proton-proton collision data*, Eur.Phys.J. **C72** (2012) 1909, arXiv:1110.3174 [hep-ex].
- [58] ATLAS Collaboration, *Improved electron reconstruction in ATLAS using the Gaussian Sum Filter-based model for bremsstrahlung*, ATLAS-CONF-2012-47, 2012.
- [59] M. Cacciari, G. P. Salam, and G. Soyez, *The anti- k_t jet clustering algorithm*, JHEP **0804** (2008) 063, arXiv:0802.1189 [hep-ph].
- [60] ATLAS Collaboration, G. Aad et al., *Search for direct production of charginos, neutralinos and sleptons in final states with two leptons and missing transverse momentum in pp collisions at $\sqrt{s} = 8$ TeV with the ATLAS detector*, JHEP **1405** (2014) 071, arXiv:1403.5294 [hep-ex].
- [61] C. Collaboration, *Searches for electroweak production of charginos, neutralinos, and sleptons decaying to leptons and W, Z, and Higgs bosons in pp collisions at 8 TeV*, <http://arxiv.org/abs/1405.7570v2>.
- [62] J. Alwall, P. C. Schuster, and N. Toro, *Simplified models for a first characterization of new physics at the LHC*, Phys. Rev. D **79** (2009) .
- [63] D. Alves, N. Arkani-Hamed, S. Arora, et al., *Simplified models for LHC new physics searches*, Journal of Physics G: Nuclear and Particle Physics **39** (2012) no. 10, 105005.
- [64] LEPSUSYWG, ALEPH, DELPHI, L3 and OPAL experiments, *Sleptons*, LEPSUSYWG/04-01.1 . <http://lepsusy.web.cern.ch/lepsusy/Welcome.html>.
- [65] A. collaboration, *Search for direct pair production of a chargino and a neutralino decaying to the 125GeV Higgs boson in $\sqrt{s} = 8$ TeV pp collisions with the ATLAS detector*, The European Physical Journal C **75** (2015) no. 5, .
<http://dx.doi.org/10.1140/epjc/s10052-015-3408-7>.
- [66] W. Beenakker et al., *The Production of charginos/neutralinos and sleptons at hadron colliders*, Phys. Rev. Lett. **83** (1999) 3780, arXiv:hep-ph/9906298 [hep-ph].
- [67] B. Fuks, M. Klasen, D. R. Lamprea, and M. Rothering, *Gaugino production in proton-proton collisions at a center-of-mass energy of 8 TeV*, JHEP **1210** (2012) 081, arXiv:1207.2159 [hep-ph].
- [68] B. Fuks, M. Klasen, D. R. Lamprea, and M. Rothering, *Precision predictions for electroweak superpartner production at hadron colliders with Resummino*, Eur.Phys.J. **C73** (2013) 2480, arXiv:1304.0790 [hep-ph].
- [69] M. Bahr, S. Gieseke, M. A. Gigg, D. Grellscheid, K. Hamilton, O. Latunde-Dada, S. Platzer, P. Richardson, M. H. Seymour, A. Sherstnev, J. Tully, and B. R. Webber, *Herwig++ Physics and Manual*, <http://arxiv.org/abs/0803.0883v3>.

- [70] ATLAS Collaboration, G. Aad et al., *The ATLAS Simulation Infrastructure*, Eur.Phys.J. **C70** (2010) 823–874, arXiv:1005.4568 [physics.ins-det].
- [71] GEANT4, S. Agostinelli et al., *GEANT4: A Simulation toolkit*, Nucl.Instrum.Meth. **A506** (2003) 250–303.
- [72] ATLAS, G. Aad et al., *Search for direct slepton and gaugino production in final states with two leptons and missing transverse momentum with the ATLAS detector in pp collisions at $\sqrt{s} = 7$ TeV*, Phys.Lett. **B718** (2013) 879–901, arXiv:1208.2884 [hep-ex].
- [73] ATLAS, G. Aad et al., *Search for same-sign top-quark production and fourth-generation down-type quarks in pp collisions at $\sqrt{s} = 7$ TeV with the ATLAS detector*, Journal of High Energy Physics **2012** (2012) no. 4, . <http://dx.doi.org/10.1007/JHEP04%282012%29069>.
- [74] T. Gillam and C. Lester, *Improving estimates of the number of fake leptons and other mis-reconstructed objects in hadron collider events: BoBs your UNCLE*, Journal of High Energy Physics **2014** (2014) no. 11, . <http://dx.doi.org/10.1007/JHEP11%282014%29031>.
- [75] ATLAS Collaboration, G. Aad et al., *Search for the direct production of charginos, neutralinos and staus in final states with at least two hadronically decaying taus and missing transverse momentum in pp collisions at $\sqrt{s} = 8$ TeV with the ATLAS detector*, J. High Energy Phys. **10** (2014) no. arXiv:1407.0350. CERN-PH-EP-2014-121, 096. 35 p.
- [76] Y. Freund and R. E. Schapire, *A Decision-Theoretic Generalization of On-Line Learning and an Application to Boosting*, Journal of Computer and System Sciences **55** (1997) no. 1, 119 – 139. <http://www.sciencedirect.com/science/article/pii/S002200009791504X>.
- [77] A. Hoecker, P. Speckmayer, J. Stelzer, J. Therhaag, E. von Toerne, and H. Voss, *TMVA: Toolkit for Multivariate Data Analysis*, PoS **ACAT** (2007) 040, arXiv:physics/0703039.
- [78] S. Gori, S. Jung, and L.-T. Wang, *Cornering electroweakinos at the LHC*, JHEP **1310** (2013) 191, arXiv:1307.5952.
- [79] C. G. Lester and D. J. Summers, *Measuring masses of semi invisibly decaying particles pair produced at hadron colliders*, Phys. Lett. **B463** (1999) 99, arXiv:hep-ph/9906349.
- [80] A. Barr, C. Lester, and P. Stephens, *m_{T2} : The Truth behind the glamour*, J. Phys. **G29** (2003) 2343, arXiv:hep-ph/0304226.
- [81] J. Massey, Frank J., *The Kolmogorov-Smirnov Test for Goodness of Fit*, Journal of the American Statistical Association **46** (1951) no. 253, pp. 68–78. <http://www.jstor.org/stable/2280095>.
- [82] A. L. Read, *Presentation of search results: The $CL(s)$ technique*, J.Phys. **G28** (2002) 2693–2704.
- [83] J. Neyman and E. S. Pearson, *On the Problem of the Most Efficient Tests of Statistical Hypotheses*, Phil. Trans. R. Soc. Lond. **A231** (1933) no. 694-706, 289–337.
- [84] G. Cowan, K. Cranmer, E. Gross, and O. Vitells, *Asymptotic formulae for likelihood-based tests of new physics*, Eur.Phys.J. **C71** (2011) 1–19.
- [85] M. Baak, G. Besjes, D. Ct, A. Koutsman, J. Lorenz, and D. Short, *HistFitter software framework for statistical data analysis*, The European Physical Journal C **75** (2015) no. 4, . <http://dx.doi.org/10.1140/epjc/s10052-015-3327-7>.